Institut für Theoretische Physik

Fakultät Mathematik und Naturwissenschaften

Technische Universität Dresden

QCD jet evolution at high and low scales

Dissertation

zur Erlangung des akademischen Grades

Doctor rerum naturalium

vorgelegt von

Jan-Christopher Winter

geboren am 10. Januar 1976 in Cottbus

Dresden   2007

Dedicated to the memory of Prof. Gerhard Soff, 1949 – 2004

Eingereicht am October 4, 2007

1. Gutachter: _____

2. Gutachter: _____

3. Gutachter: _____

Verteidigt am _____

Contents

0   Introduction

Present and future high-energy physics accelerators constitute a demanding challenge. They are the laboratories where high-energetic particles are brought to collision producing a multitude of (low-energetic) particles in the final state, which will be detected in the experiments. Examples for such machines are the Large Electron Positron Collider (LEP) at CERN, which operated up to centre-of-mass energies of 207 GeV until November 2000, or, the Tevatron at Fermilab, where proton–antiproton collisions at an energy of 1.96 TeV are still under investigation and corresponding data taking is under way. A new era will be heralded with the Large Hadron Collider (LHC) designed to provide proton–proton collisions at 14.0 TeV, the largest energy ever used in a particle-physics experiment. The LHC is currently under construction at CERN; once operating, it will allow enter a new energy, space and time domain, and is soon going to become the leading instrument in the exploration of particle physics, and, even beyond, for the next 15 years. In particular with this new machine physicists/mankind would like to gain insight into the present puzzle of elementary particle physics: its Standard Model (SM) is seen to be incomplete. Theoretical reasons for this are given through the quest for the deep origin of the electroweak symmetry breaking, the SM's family and gauge structure, the quest to know whether or not the hierarchy problem exists, and the fact that quantum gravity is outside the SM's applicability at all. Its incompleteness has been profoundly fortified by three compelling experimental observations, namely neutrino mixing, dark matter, and the baryon asymmetry of the Universe, all of which are unexplainable within the SM. Thus, progress will unavoidably come with the expected start of the LHC in 2008, since its design will further large production rates of SM particles (e.g. top–antitop pairs will emerge once per second, bottom–antibottom pairs will appear copiously, $5 \cdot 10^5/s$) and exploring, for the first time, the TeV energy scale, where new-physics effects and beyond-SM particles are expected to show up. The collection and understanding of LHC data (which will be enormous constituting a challenge on its own) will truly push forward confirm or rule out anticipated new-physics scenarios, which have been worked out through the last decades to possibly solve the problems left by the SM. In addition, the new era will strongly call for close collaborations of particle theorists, experimentalists, astrophysicists and cosmologists.

However, the first tasks are outlined as having to understand the new detectors in detail and rediscover known physics. These first signals have to be under control before the road to new discoveries can be followed and the discussion of possible signal-to-background puzzles (as in Higgs production via vector-boson fusion etc.) attains paramount importance. The hadronic intitial states of the LHC will invoke a presence of strong interactions and related phenomena in any production process. Unavoidably, this will manifest itself in jet and multihadron production [1, 2, 3]. With the large energies available at the LHC,

complications emerge, amongst them the tremendously large phase space available for such QCD (quantum chromodynamics) radiation. As a matter of fact, multijet events will then be the standard and not the exception, and appear much more likely w.r.t. the rates experienced by the Tevatron experiments. Together with the fact that the new measurements will be much more precise than before, there is a strong need to improve higher-order calculations in perturbative QCD and to provide advanced tools that adequately describe jet production and evolution plus the subsequent hadronization.

For a plethora of reasons, a full quantum-mechanical treatment is out of reach: first, fixed-order perturbative calculations are used to describe energetic scattering processes in collider experiments; in the context of QCD, in particular, the production of hard partons initiating the jets. This is in principle well understood, however the calculational costs rapidly increase even at the lowest, the tree level where the number of contributing Feynman diagrams already grows factorially with the number of particles involved. Moreover, higher-order calculations including virtual corrections will culminate in the evaluation of multileg loop integrals, which further complicates the task. Second, when it comes to non-perturbative phenomena, only a limited understanding of QCD exists. The de- and confinement of coloured partons off and into colourless hadrons, respectively, cannot be precisely predicted yet. Therefore, phenomena related to resolving the partonic substructure of the incoming hadron or hadronization of the outgoing quarks and gluons imply a need for phenomenological models.

Hence, a successful, even though in total approximate, description of the three "phases" – jet production, evolution and hadronization – relies, first, on a factorization, which permits the separation of the perturbative evolution from the non-perturbative development of an event. Second, jet production will be handled best through calculations of hard matrix elements, and, jet evolution manifests itself in subsequent multiple (softer) parton emissions. These, again, cannot be accurately calculated through fixed-order methods, however, the bulk of additional QCD activity emerges through factorizable collinear and soft emissions off the coloured (primary) partons. Such emissions are connected to large logarithms arising in the perturbative expansion to all orders of the strong coupling constant. A reliable prediction can then be achieved through a resummation taking these logarithms into account to all orders. This is best described by parton showers. By exploiting universal QCD splitting functions, parton showers encode this radiation pattern in a probabilistic fashion. They form a substantial part of and reside in Monte Carlo event generators, which simulate exclusive hadronic final states for a given collision process. Event generators deeply incorporate the – already indicated – principle of decomposing the full scattering process into a sequence of phases characterized by different energy scales. These phases can be modelled fairly independently of each other and underlying assumptions on the phase-specific dynamics of particle interactions can be tested or modified separately. Following this strategy, Monte Carlo generators have been very successful in the past in describing a full wealth of data, they are an indispensable tool for the accomplishment of the analyses of the currently running Tevatron experiments and they will, unquestionable, play an important rôle at the LHC, to gain comprehension of detector acceptances and data correction.

0.1   New era of Monte Carlo event generation

In the past decades, QCD shower programs, such as PYTHIA [4, 5, 6, 7, 8], HERWIG [9, 10], or ARIADNE [11] have been very successful in correctly describing, both qualitatively and quantitatively, a large range of QCD related phenomena at different colliders, at different energies, and with different initial states. Their success is based on good approximations in their treatment of logarithmically enhanced emission of QCD particles in soft and/or collinear regions of phase space. In conventional parton showers such as the ones in PYTHIA [12, 13, 14] and HERWIG [15], this is achieved by an expansion around the collinear limit. This manifests itself in the ordering of subsequent emissions through virtual masses supplemented with an explicit veto on increasing emission angles or through an ordering by emission angles. Rather than in terms of parton splittings, perturbative QCD cascades can also be formulated in a complementary way, namely in terms of colour dipoles [16, 17, 18]. The shower in ARIADNE is based on this colour-dipole model, and the splitting of the dipoles eventually is equivalent to an expansion around the soft limits of the radiation process. It is realized through ordering the emissions in relative transverse momenta of subsequent splittings. Furthermore such a dipole shower then quite naturally seems to fulfil the requirement of quantum coherence [16], which, for the parton showers, leads to the angular ordering, see e.g. [2].

In view of the upcoming LHC era, however, the parton-shower programs undergo an intensive overhaul, leading essentially to complete rewrites of the codes [19, 20, 21] in the modern, object-oriented programming language `C++`. Apart from issues related to maintenance, a number of improvements concerning physics simulation motivated the construction of new and better shower codes. First of all, the shower algorithms themselves have been improved: in PYTHIA, a $k_\perp$ ordered parton shower has been introduced [8, 22] in order to better account for coherence effects and for a dramatically extended model of multiple parton interactions; in HERWIG, a new formulation of angular ordering [23] better embeds Lorentz invariance and provides an improved treatment of those regions, where the original HERWIG parton-shower formulation over- or undercounted parton emissions. In addition, a new parton-shower formulation has been developed based on Catani–Seymour dipole factorization [24, 25, 26, 27], and first steps have been undertaken in the development of yet another QCD shower formulation which uses antenna subtraction kernels [28]. A common denominator for all these recent developments was to put more emphasis on the notion of a colour-connected partner of the splitting parton and thus an obliteration of the difference between parton and dipole showers. Especially the latter two, the showers based on either Catani–Seymour or antenna subtraction kernels [29, 30], aim at an improved matching or merging with exact higher-order matrix elements. In fact, this systematic inclusion of higher orders in the perturbative expansion of QCD has been a dramatic and recent improvement of the paradigm underlying building and using Monte Carlo event generators, i.e. in view of the need for increasing precision, the two approaches of matching and merging have been developed to directly incorporate higher-order corrections into the framework of multipurpose event generators.

In the first approach, the exact next-to-leading order matrix element result is consistently matched with the parton shower [31, 32, 33, 34] such that the overall result correctly reproduces the corresponding NLO cross section and the first additional hard QCD emis-

sion. This has been first implemented for specific processes in `MC@NLO` [35] on the basis of the Frixione–Kunszt–Signer subtraction. Of course, this method depends to some extent on the details of the parton shower, and it has some residual dependence on the process in question. Moreover, with `POWHEG` an approach and a proposal have been given to completely circumvent the appearance of negative weights – which are present in the former method – and to head towards a shower-independent matching solution [33, 34].

In alternative approaches, sequences of tree-level multileg matrix elements with increasing final-state multiplicity are merged with the parton shower to yield a fully inclusive sample with no double counting and correct at leading logarithmic accuracy. A first approach has been presented, known as the CKKW merging approach, for the case of electron–positron annihilations into jets [36]; later it has been extended to hadronic collisions [37] and it has been reformulated to a merging procedure in conjunction with a dipole shower (LCKKW) in [38]. A further method, the MLM method, has been developed also aiming at a merging of matrix elements and parton showers, however, uses a different way in generating the inclusive samples based on a geometric interpretation of the full radiation pattern in terms of cone jets [39, 40]. In a number of works, these different algorithms have been implemented in different variations on different levels of sophistication in conjunction with various matrix-element generators or already in full-fledged event generators [41, 42, 43, 44, 45, 46, 47, 48, 49, 50, 51]. Despite their differences they exhibit an assuring level of agreement [52].

Clearly, recapitulating this enormous research activity, the field of jet physics has undergone a multitude of improvements and refinements, most of which related to a better description of hard jets and jet–jet correlations as well as jet rates. During the last decade the understanding of simulating jets therefore has been considerably broadened, including the understanding of how jets should be defined in an infrared-safe manner [53, 54]. Eventually, the clear distinction between matrix-elements computation and showering gives way to a more intertwined treatment and combination of both matrix elements and parton showers, i.e. jet production and evolution, respectively. In particular, the tremendous progress in evaluating multileg tree-level squared amplitudes led to the advancements in the description dedicated to jet production, and, certainly, they have left their marks on the other side of simulating jet evolution. Therefore, it is no surprise that the progress on the one side initiated refinements and progress on the other side. However, in the prospect of the LHC approaching these new achievements will be of strong need.

0.2   The event generator SHERPA

The development of the Monte Carlo event generator SHERPA (Simulation of High Energy Reactions of PArticles) [41], entirely written in the object-oriented programming language `C++` right from the beginning, has been pursued in tight connection with and contributed to the improvements in jet and Monte Carlo physics outlined above. SHERPA constitutes a new multipurpose event generator providing a complete description of hadronic final states in high-energy lepton–lepton and hadron–hadron collisions. Its physics programme covers particle production at tree level in the SM, the Minimal Supersymmetric Standard Model (MSSM) and the ADD model of Large Extra Dimensions. The simulation of realistic jet-physics scenarios can be achieved, since SHERPA in its key feature provides an im-
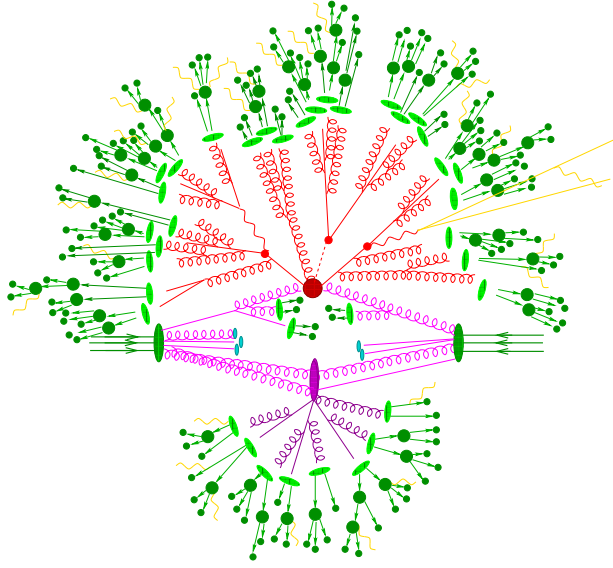
Figure 1: Paradigm of Monte Carlo event generation: split the simulation in parts; this constitutes the Monte Carlo ansatz to modelling full scattering processes. Here, the case of a proton–proton collision is visualized.

plementation of the Catani–Krauss–Kuhn–Webber (CKKW) merging approach [36, 37], yielding an improved description of multijet production through a consistent combination of multiparton tree-level matrix elements with the QCD initial- and final-state parton showers and the hadronization. SHERPA's CKKW "machinery" is supplemented by a multiple-interactions description, which respects the jet-production scales of the primary, leading, process.

The idea underlying CKKW is to separate the kinematical range of parton emission by a k_T algorithm [53, 54, 55] into a regime of jet production, covered by the appropriate matrix elements, and a regime of jet evolution, covered by the respective shower. Then, the matrix elements are reweighted through Sudakov form factors and hard emissions in the parton shower yielding another jet are vetoed such that there is only a residual dependence on the jet-resolution cut.

The construction of SHERPA fully reflects the paradigm or separation ansatz of Monte Carlo event generation of splitting the simulation into well-defined phases, cf. fig. 1. Accordingly, SHERPA provides physics modules each associated with a phase and in its own initializes them and steers their interplay. The main phases and their realizations within SHERPA are:

- Signal process (big red blob in fig. 1), provided by AMEGIC++; this is SHERPA's robust kernel [56] for internal matrix-element generation.

- Initial- and final-state parton showers (magenta and red parts in fig. 1), provided by APACIC++ [57].

- Matrix-element parton-shower merging combining the two previous phases according to CKKW [36, 37].

- Multiple parton interactions (violet parts in in fig. 1), provided by AMISIC++, mainly based on the ideas of [58], however an own model is under way [59].

- Hadronization or primary-hadron genesis (green parts in in fig. 1), will be provided by AHADIC++, following the ideas given in [60].

- Decays of unstable hadrons, will be provided by HADRONS++ (darkgreen) and PHOTONS++ (yellow parts in fig. 1).

Note that in its current version, version 1.0.10, SHERPA is still equipped with an interface to PYTHIA's string-fragmentation and hadron-decay routines.

0.3   Outline of this thesis

This thesis deals with a broad range of aspects that are deeply related to jet physics. In particular, phenomenological work has been accomplished in validating the CKKW merging approach, first, in a detailed comparison with other merging approaches using the testbed of W+jets production at hadron colliders, and, second, through a study of charged vector-boson pair production at Tevatron energies verifying SHERPA against a calculation at next-to-leading order in the strong coupling constant and other Monte Carlo generators. All of which is presented in ch. 1. Both studies led to a number of internal refinements of SHERPA's CKKW implementation, therefore, contributed to the further improvement of the event generator SHERPA.

As outlined above, new shower formalisms in close relation to subtraction methods are strongly motivated. Therefore, in ch. 2 the main project of this thesis is presented, dealing with the definition and realization of a new QCD colour-dipole cascade. In particular for the case of initial-state radiation, a completely orthogonal ansatz w.r.t. the Lund colour-dipole model [11] has been pursued. In the new model dipoles are also spanned with incoming partons and in turn treated fully perturbatively. At neither point of the shower evolution the hadron remnants will be included, which is in striking contrast to the Lund approach. All necessary steps to achieve a complete working shower algorithm are documented in ch. 2 together with very encouraging first results corroborating the feasibility of the approach.

Improvements in the description of jets not only touch their production through hard matrix elements and evolution through showering, but also concern the investigation of phenomenological hadronization models afresh. A new cluster-hadronization model is presented in ch. 3. Its specific features are the incorporation of soft colour reconnection, a more general treatment of diquarks including their spin and giving rise to clusters with baryonic quantum numbers, and a dynamic separation of the regimes of clusters and hadrons according to their masses and flavours. The distinction between the two regions automatically leads to different cluster decay and transformation modes and their extension w.r.t. previous versions of cluster fragmentation. The model presented here and its preliminary realization eventually have served as the basis and the testbed for the actual implementation of the AHADIC++ model in SHERPA.

The thesis closes with a summary given in ch. 4.

1 Multijets in hadronic collisions – validating the CKKW merging of SHERPA

1.1 Introduction

One of the most striking features of LHC final states will be the large number of events with several hard jets. Final states with 6 jets from $t\bar{t}$ decays will have a rate of almost 1 Hz, with 10-100 times more coming from prompt QCD processes. The immense amount of available phase space, and the large acceptance of the detectors, with calorimeters covering a region of almost 10 units of pseudo-rapidity (η), will lead to production and identification of final states with 10 or more jets. These events will hide or strongly modify all possible signals of new physics, which involve the chain decay of heavy coloured particles, such as squarks, gluinos or the heavier partners of the top, which appear in little-Higgs models. Being able to predict their features is therefore essential.

To achieve this, our calculations need to describe as accurately as possible both the full matrix elements for the underlying hard processes, as well as the subsequent development of the hard partons into jets of hadrons. However, for the complex final-state topologies one is interested in, no factorization theorem exists to rigorously separate these two components. The main obstacle is the existence of several hard scales, like the jet transverse energies and dijet invariant masses, which for a generic multijet event will span a wide range. This makes it difficult to unambiguously separate the components of the event, which belong to the "hard process" (to be calculated using a multiparton amplitude) from those developing during its evolution (described by the parton shower). A given $n + 1$ jet event can be obtained in two ways: from the collinear/soft-radiation evolution of an appropriate $n + 1$ parton final state, or from an n parton configuration where hard, large-angle emission during its evolution leads to the extra jet. A factorization prescription (in this context it is often called a "matching scheme" or "merging scheme") defines, on an event-by-event basis, which of the two paths should be followed. The primary goal of a merging scheme is therefore to avoid double counting (by preventing some events to appear twice, once for each path), as well as dead regions (by ensuring that each configuration is generated by at least one of the allowed paths). Furthermore, a good merging scheme will optimize the choice of the path, using the one, which guarantees the best possible approximation to a given kinematics.

One such scheme is given by the CKKW merging algorithm, which has been proposed for the first time in the realm of electron–positron annihilations into jets in [36]. Its extension
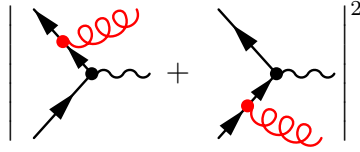
matrix element: *parton shower:*
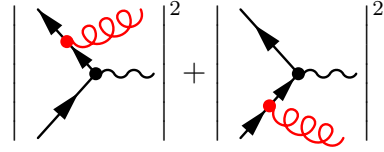
$$|A_R|^2 + |B_R|^2 + 2\,\mathrm{Re}(\mathrm{A_R B_R^*})$$ $$\sim\ |A_R|^2 + |B_R|^2$$

Figure 1.1: First gluon emission in hadronic vector boson production as described by the matrix element (left panel) or a parton shower (right panel).
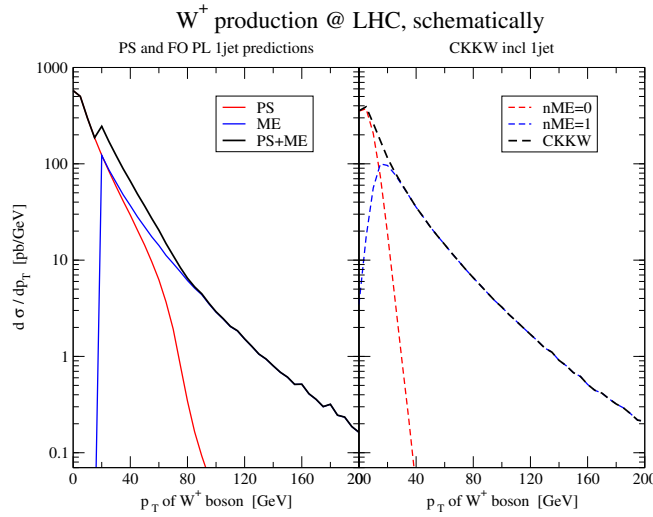
Figure 1.2: Schematic comparison of a naive merging of matrix elements and parton showers with the CKKW merging by means of the p_T distribution of W^+ bosons produced at the LHC.

to hadronic processes has been discussed in [37] and the approach has been validated for the former case [43, 57] and for the production of single vector bosons at the Fermilab Tevatron [42] and the CERN LHC [61].

The issue of double counting of phase-space regions can be easily exemplified schematically as in fig. 1.1. Considering this first QCD emission, it becomes apparent that a parton-shower approach will account for terms that are also present in the matrix element. In the CKKW method the general requirements on a merging scheme outlined above are obeyed as follows: first, a separation scale is introduced dividing the phase space into production, described by matrix elements, and evolution of multijets, described by parton showers. Second, the matrix elements are reweighted by a combined α_s coupling and Sudakov form factor weight and parton-shower configurations that have been already included through

the higher-order tree-level matrix elements are vetoed. This then removes double counting as well as the problem of missing phase-space regions. Furthermore it almost eliminates the "unphysical" dependence on the, in principle, "arbitrary" separation scale that regularized the matrix elements, and, it preserves the accuracy of the original parton shower. [1] Any unavoidable residual dependence can then be used for tuning less singular terms to obtain optimal agreement with data. Of course, for a successful and stable algorithm the notion of a jet must be clear and the corresponding jet measure infrared safe reflecting the characteristics of QCD dynamics. Fig. 1.2 schematically shows a comparison between a naive "merging" and the sophisticated CKKW approach.

After characterizing the fundamentals of merging schemes, sec. 1.2, these key issues of the CKKW merging and its implementation in SHERPA are reviewed in sec. 1.3 on a more technical and detailed level. Also, in sec. 1.4, two different approaches to the problem, namely the Lönnblad and the MLM schemes, are presented, such that in sec. 1.5 a first W+multijet comparison of Tevatron/LHC predictions of the three approaches can be discussed, with some focus on an assessment of their systematic uncertainties. Finally, in sec. 1.6 a CKKW study of charged-diboson+jets will be presented.

1.2 Fundamentals of merging procedures

In general, the different merging procedures follow a similar strategy:

1. A jet measure is defined and all relevant cross sections including jets are calculated for the process under consideration, i.e. for the production of a final state X in pp collisions, the cross sections for the processes $pp \rightarrow X + n$ jets with $n = 0, 1, \ldots, N = n_{\max}$ are evaluated.

2. Hard parton samples are produced with a probability proportional to the respective total cross section, in a corresponding kinematic configuration following the matrix element.

3. The individual configurations are accepted or rejected with a dynamical, kinematics-dependent probability that includes both effects of running coupling constants and of Sudakov form factors. In case the event is rejected, step 2 is repeated, i.e. a new parton sample is selected, possibly with a new number of jets.

4. The parton shower is invoked with suitable initial conditions for each of the legs. In some cases, like, e.g. in the MLM procedure described below, this step is performed together with the step before, i.e. the acceptance/rejection of the jet configuration. In all cases the parton shower is constrained not to produce any extra jet; stated in other words: configurations that would fall into the realm of matrix elements with a higher jet multiplicity are vetoed in the parton shower step.

The merging procedures discussed below differ mainly

- in the jet definition used in the matrix elements;

---

[1] The cancellation of the dependence on the separation scale has been proven analytically in the e^+e^- case up to next-to-leading logarithmic accuracy [36].

- in the way the acceptance/rejection of jet configurations stemming from the matrix element is performed;

- and in details concerning the starting conditions of and the jet vetoing inside the parton showering.

1.3   The method of CKKW merging

The merging prescription proposed in [36, 37] is known as the CKKW scheme and has been implemented in the event generator SHERPA [41] in full generality [43].
In this scheme

- the separation of the matrix-element and parton-shower domains for different multijet processes is achieved through a k_T measure [53, 55, 54], where $k_{T,0}$ denotes the internal separation cut, also called the merging scale;

- the acceptance/rejection of jet configurations proceeds through a reweighting of the matrix elements with analytical Sudakov form factors and factors due to different scales in α_s;

- the starting scale for the parton shower evolution of each parton is given by the scale where it appeared first;

- a vetoed parton-shower algorithm is used to guarantee that no unwanted hard jets are produced during jet evolution.

In the original paper dealing with e^+e^- annihilations into hadrons, [36], it has been shown explicitly that in this approach the dependence on $k_{T,0}$ cancels to NLL accuracy. This can be achieved by combining the Sudakov reweigthed matrix elements with a vetoed parton shower with angular ordering, subjected to appropriate starting conditions. The algorithm for the case of hadron–hadron collisions has been constructed in analogy to the e^+e^- case. However, it should be stressed that it has not been shown that the CKKW algorithm is correct at any logarithmic order in this kind of process.
For hadron–hadron collisions, the internal jet identification of the SHERPA merging approach proceeds through a k_T scheme, which defines two final-state particles to belong to two different jets, if their relative transverse momentum squared

$$k_T^{(ij)\,2} = 2 \min\left\{ p_T^{(i)},\, p_T^{(j)} \right\}^2 \frac{\left[\cosh(\eta^{(i)} - \eta^{(j)}) - \cos(\phi^{(i)} - \phi^{(j)})\right]}{D^2} \qquad (1.1)$$

is larger than the critical value $k_{T,0}^2$. In addition, the transverse momentum of each jet has to be larger than the merging scale $k_{T,0}$. The magnitude D, which is of order 1, is a parameter of the jet algorithm [62]. In order to completely rely on matrix elements for jet production allowed by the external analysis, the internal D should be chosen less than or equal to the D parameter or, in case of a cone jet algorithm, the R parameter employed by the external analysis.
The weight attached to the generated matrix elements consists of two components, a

strong coupling weight and an analytical Sudakov form factor weight. For their determination, a k_T jet clustering algorithm guided by only physically allowed parton combinations is applied on the initial matrix-element configurations. The identified nodal k_T values are taken as scales in the strong coupling constants and replace the predefined choice in the initial generation. The Sudakov weight attached to the matrix elements accounts for having no further radiation resolvable at $k_{T,0}$. The NLL Sudakov form factors employed, cf. [53], are defined by

$$\Delta_q(Q, Q_0) = \exp\left\{-\int_{Q_0}^{Q} dq\,\Gamma_q(Q, q)\right\},$$

$$\Delta_g(Q, Q_0) = \exp\left\{-\int_{Q_0}^{Q} dq\,[\Gamma_g(Q, q) + \Gamma_f(q)]\right\}, \tag{1.2}$$

where $\Gamma_{q,g,f}$ are the integrated splitting functions $q \to qg$, $g \to gg$ and $g \to q\bar{q}$, which are given through

$$\Gamma_q(Q, q) = \frac{2C_F}{\pi}\frac{\alpha_s(q)}{q}\left(\ln\frac{Q}{q} - \frac{3}{4}\right), \tag{1.3}$$

$$\Gamma_g(Q, q) = \frac{2C_A}{\pi}\frac{\alpha_s(q)}{q}\left(\ln\frac{Q}{q} - \frac{11}{12}\right), \tag{1.4}$$

$$\Gamma_f(q) = \frac{N_f}{3\pi}\frac{\alpha_s(q)}{q}. \tag{1.5}$$

They contain the running coupling constant and the two leading, logarithmically enhanced terms in the limit $Q_0 \ll Q$. The single logarithmic terms $-3/4$ and $-11/12$ may spoil an interpretation of the NLL Sudakov form factor as a non-branching probability. Therefore, $\Gamma(Q, q)$ is cut off at zero, such that $\Delta_{q,g}(Q, Q_0)$ retains its property to define the probability for having no emission resolvable at scale Q_0 during the evolution from Q to Q_0. These factors are used to reweight in accordance to the appearance of external parton lines. A ratio of two Sudakov form factors $\Delta(Q, Q_0)/\Delta(q, Q_0)$ accounts for the probability of having no emission resolvable at Q_0 during the evolution from Q to q. Hence, it is employed for the reweighting according to internal parton lines. The lower limit is taken to be $Q_0 = k_{T,0}$ or $Q_0 = D\,k_{T,0}$ for partons that are clustered to a beam or to another final state parton, respectively.

The sequence of clusterings, stopped after the eventual identification of a $2 \to 2$ configuration (the core process), is used to reweight the matrix element. Moreover, this also gives a shower history, whereas the $2 \to 2$ core process defines the starting conditions for the vetoed shower. For the example of an identified pure QCD $2 \to 2$ core process, the four parton lines left as a result of the completed clustering will start their evolution at the corresponding hard scale. Subsequently, additional radiation is emitted from each leg by evolving under the constraint that any emission harder than the separation cut $k_{T,0}$ is vetoed. The starting scale of each leg is given by the invariant mass of the mother parton belonging to the identified QCD splitting, through which the considered parton has been initially formed.

Finally, it should be noted that the algorithm implemented in SHERPA does the merging of the sequence of processes $pp \to X + n$ jets with $n = 0, 1, \ldots, N$ fully automatically – the user is not required to generate the samples separately and mix them by hand.

1.4   Other merging approaches

1.4.1   The dipole cascade and CKKW merging

The merging prescription developed for the dipole cascade in the ARIADNE program [11] is similar to CKKW, but differs in the way the shower history is constructed, and in the way the Sudakov form factors are calculated. Also, since the ARIADNE cascade is ordered in transverse momentum the treatment of starting scales is simplified. Before going into details of the merging prescription, it is useful to describe some details of the dipole cascade, since it is quite different from conventional parton showers.

The dipole model [16, 63] as implemented in the ARIADNE program is based around iterating $2 \to 3$ partonic splittings instead of the usual $1 \to 2$ partonic splittings in a conventional parton shower. Gluon emission is modelled as coherent radiation from colour–anticolour charged parton pairs. This has the advantage of e.g. including first order corrections to the matrix elements for $e^+e^- \to q\bar{q}$ in a natural way and it also automatically includes the coherence effects modelled by angular ordering in conventional showers. The process of quark–antiquark production does not come in as naturally, but can be added [64]. The emissions in the dipole cascade are ordered according to an invariant transverse momentum defined as

$$p_\perp^2 \;=\; \frac{s_{12}\,s_{23}}{s_{123}}\,, \tag{1.6}$$

s_{ij} is the squared invariant mass of parton i and j, with the offspring having index 2.

When applied to hadronic collisions, the dipole model does not separate between initial- and final-state gluon radiation. Instead all gluon emissions are treated as coming from final-state dipoles [65, 66]. To be able to extend the dipole model to hadron collisions, spatially extended coloured objects are introduced to model the hadron remnants. Dipoles involving hadron remnants are treated in a similar manner to the normal final-state dipoles. However, since the hadron remnant is considered to be an extended object, emissions with small wavelength are suppressed. This is modelled by only allowing a fraction of the remnant to take part in the emission. The fraction that is resolved during the emission is given by

$$a(p_\perp) \;=\; \left(\frac{\mu}{p_\perp}\right)^\alpha\,, \tag{1.7}$$

where μ is the inverse size of the remnant and α is the dimensionality. These are semi-classical parameters, which have no correspondence in conventional parton cascades, where instead a suppression is obtained by ratios of quark densities in the backward evolution. The main effect is that the dipole cascade allows for harder gluon emissions in the beam directions, enabling it to describe properly e.g. forward jet rates measured at HERA (see e.g. [67]).

There are two additional forms of emissions, which need to be included in the case of hadronic collisions. One corresponds to an initial state $g \to q\bar{q}$ [68]. This does not come in naturally in the dipole model, but is added by hand in a way similar to that of a conventional initial-state parton showers [68]. The other corresponds to the initial-state $q \to gq$ (with the gluon entering into the hard subprocess), which could be added in a similar way, but this has not yet been implemented in ARIADNE.

When implementing CKKW for the dipole cascade [38, 44], the procedure is slightly different from what has been described above. Rather than using the standard k_T algorithm to cluster the state produced by the matrix-element generator, a complete set of intermediate partonic states, S_i, and the corresponding emission scales, $p_{\perp,i}$ are constructed, which correspond to a complete dipole shower history. Hence, for each state produced by the matrix-element generator, basically the question *how would ARIADNE have generated this state* is answered. Note, however, that this means that only coloured particles are clustered, which differs from e.g. SHERPA, where also the W and its decay products are involved in the clustering.

The Sudakov form factors are then introduced using the Sudakov veto algorithm. The idea is to reproduce the Sudakov form factors used in ARIADNE. This is done by performing a trial emission starting from each intermediate state S_i with $p_{\perp,i}$ as a starting scale. If the emitted parton has a $p_\perp$ higher than $p_{\perp,i+1}$ the state is rejected. This correspond to keeping the state according to the no-emission probability in ARIADNE, which is exactly the Sudakov form factor.

It should be noted that for initial-state showers, there are two alternative ways of defining the Sudakov form factor. The definition in eq. (1.2) is used in e.g. HERWIG [9], while e.g. PYTHIA [6, 8] uses a form, which explicitly includes ratios of parton densities. Although formally equivalent to leading logarithmic accuracy, only the latter corresponds exactly to a no-emission probability, and this is the one generated by the Sudakov veto algorithm. This, however, also means that the constructed emissions in this case need not only be reweighted by the running α_s as in the standard CKKW procedure above, but also with ratios of parton densities, which in the case of gluon emissions correspond to the suppression due to the extended remnants in eq. (1.7) as explained in more detail in [44], where the complete algorithm is presented.

1.4.2   The MLM matching algorithm

1. The first step is the generation of parton-level configurations for all final-state parton multiplicities n up to a given N ($W + N$ partons). They are defined by the following kinematical cuts:

$$p_T^{part} > p_T^{min} , \quad |\eta_{part}| < \eta_{max} , \quad \Delta R_{jj} > R_{min} , \tag{1.8}$$

where p_T^{part} and η_{part} are the transverse momentum and pseudo-rapidity of the final-state partons, and ΔR_{jj} is their minimal separation in the (η, ϕ) plane. The parameters p_T^{min}, η_{max} and R_{min} are called generation parameters, and are the same for all $n = 1, \ldots, N$.

2. The renormalization scale is set according to the CKKW prescription. The necessary tree branching structure is defined for each event, allowing however only for

branchings, which are consistent with the colour structure of the event, which in ALPGEN is extracted from the matrix-element calculation [69]. For a pair of final-state partons i and j, a k_T measure is used defined by

$$k_T = \Delta R_{ij} \min(p_{\mathrm{T}i}, p_{\mathrm{T}j}) \tag{1.9}$$

where $\Delta R = \sqrt{\Delta \eta^2 + \Delta \phi^2}$, while for a pair of initial/final-state partons $k_T^2 = p_{\mathrm{T}}^2$ is taken, i.e. the p_{T} of the final-state one.

3. The k_T value at each vertex is used as a scale for the relative power of α_s. The factorization scale for the parton densities is given by the hard scale of the process, $Q_0^2 = M_W^2 + p_{T,W}^2$. It may happen that the clustering process stops before the lowest-order configuration is reached. This is the case, e.g., for an event like $u\bar{u} \to Wc\bar{s}g$. Flavour conservation allows only the gluon to be clustered, since $u\bar{u} \to Wc\bar{s}$ is a LO process, first appearing at $\mathcal{O}(\alpha_s^2)$. In such cases, the hard scale Q_0 is adopted for all powers of α_s corresponding to the non-merged clusters.

4. Events are then showered, using PYTHIA or HERWIG. The evolution for each parton starts at the scale determined by the default PYTHIA and HERWIG algorithms on the basis of the kinematics and colour connections of the event. The upper veto cutoff to the shower evolution is given by the hard scale of the process, Q_0. After evolution, a jet cone algorithm is applied to the partons produced in the perturbative phase of the shower. Jets are defined by a cone size R_{clus}, a minimum transverse energy $E_{\mathrm{T}}^{\mathrm{clus}}$ and a maximum pseudo-rapidity $\eta_{\max}^{clus}$. These parameters are called matching parameters, and should be kept the same for all samples $n = 0, 1, \ldots, N$. These jets provide the starting point for the matching procedure, described in the next item. In the default implementation, $R_{\mathrm{clus}} = R_{min}$ is taken, $\eta_{\max}^{clus} = \eta_{max}$ and $E_{\mathrm{T}}^{\mathrm{clus}} = p_T^{min} + \max(5 \text{ GeV}, 0.2 \times p_T^{min})$, but these can be varied as part of the systematics assessment. To ensure a complete coverage of phase space, however, it is necessary that $R_{\mathrm{clus}} \geq R_{min}$, $\eta_{\max}^{clus} \leq \eta_{max}$ and $E_{\mathrm{T}}^{\mathrm{clus}} \geq p_T^{min}$.

5. Starting from the hardest parton, the jet, which is closest to it in (η, ϕ) is selected. If the distance between the parton and the jet centroid is smaller than $1.5 \times R_{\mathrm{clus}}$, the parton and the jet *match*. The matched jet is removed from the list of jets, and the matching test for subsequent partons is performed. The event is fully matched if each parton matches to a jet. Events, which do not match, are rejected. A typical example is when two partons are so close that they cannot generate independent jets, and therefore cannot match. Another example is when a parton is too soft to generate its own jet, again failing matching.

6. Events from the parton samples with $n < N$, which survive matching, are then required not to have extra jets. If they do, they are rejected, a suppression, which replaces the Sudakov reweighting used in the CKKW approach. This prevents the double counting of events, which will be present in, and more accurately described by, the $n+1$ sample. In the case of $n = N$, events with extra jets can be kept since they will not be generated by samples with higher n. Nevertheless, to avoid double counting, it is required that their transverse momentum be smaller than that of the softest of the matched jets.

When all the resulting samples from $n = 0, \ldots, N$ are combined, an inclusive W+jets sample is obtained. The harder the threshold for the energy of the jets used in the matching, $E_{\mathrm{T}}^{\mathrm{clus}}$, the fewer the events rejected by the extra-jet veto (i.e. smaller Sudakov suppression), with a bigger rôle given to the shower approximation in the production of jets. Using lower thresholds would instead enhance the rôle of the matrix elements even at lower E_T, and lead to larger Sudakov suppression, reducing the rôle played by the shower in generating jets. The matching/rejection algorithm ensures that these two components balance each other. This algorithm is encoded in the ALPGEN generator [39, 46], where evolution with both HERWIG and PYTHIA are enabled. However, in the framework of this study, the parton-shower evolution has been performed by HERWIG.

1.5 Comparative study of various merging algorithms

In the following a first direct comparison is presented of the three approaches, proposed so far and outlined above. In terms of implementations predictions are compared that have been obtained from five different codes, namely ALPGEN, ARIADNE, HELAC, MADEVENT and SHERPA. Here, the discussion will concentrate on ALPGEN, ARIADNE and SHERPA, all of which representing the unambiguous and direct implementations of the three merging approaches under consideration. The testbed of W+jets production at hadron colliders has been chosen, which is one of the most studied final states because of its important rôle as a background to top quark studies at the Tevatron. At the LHC, W+jets, as well as the similar Z+jets processes, will provide the main irreducible backgrounds to signals such as multijet plus missing transverse energy, typical of Supersymmetry and of other manifestations of new physics. The understanding of W+multijet production is therefore an essential step towards the validation and tuning of the tools discussed here, in particular, prior to their utilization at the LHC.

For each of the codes, a large set of observables has been considered, addressing inclusive properties of the events (transverse-momentum spectrum of the W boson and of leading jets) as well as geometric correlations between the jets. After the specifications of the analysis for the study, the following two subsections will present a subset of the results of the study for the Tevatron ($p\bar{p}$ collisions at 1.96 TeV) and for the LHC (pp at 14.0 TeV). This collection of observables will illustrate the main features of the comparison between the different methods.

Confronting the predictions of different merging schemes with each other provides a great opportunity to critically assess the systematic uncertainties of multijet calculations. As already mentioned such schemes in their character constitute more sophisticated factorization prescriptions of combining calculations related to harder scales with those from softer ones, thereby avoiding the double counting and the dead regions. Although following these principles, the different merging schemes use different ways in finally distributing the calculation between the matrix-element and the shower evolution. As in any factorization scheme, the physics is independent of the separation between phases only if complete control over the perturbative expansion is guaranteed. Otherwise a residual scheme dependence is left. Its impact can be studied for any scheme on its own by varying the parameters specifying the details of the merging algorithms, or, even better, in conjunction with other schemes as it is accomplished here. Therefore, an assessment of the systematic

uncertainties underlying the different methods and, hence, codes has been carried out and will also be presented here. Moreover, the intrinsic merging parameters present an opportunity to tune each code so as to best describe the data. This tuning should be seen as a prerequisite for a quantitative study of the overall theoretical systematics: after the tuning is performed on a given set of final states (e.g. the W+jets considered here), the systematics for other observables or for the extrapolation to the LHC can be obtained by comparing the difference in extrapolation between the various approaches.

1.5.1   Properties of the event generation for the study

The elements of the analysis common to all codes are the following.

- *Event samples.* Tevatron results refer to the combination of W^+ and W^- bosons, while at the LHC only W^+ are considered. All codes have generated parton-level samples according to matrix elements with up to 4 final-state partons. Partons are restricted to the light-flavour sector and are taken to be massless. The Yukawa couplings of the quarks are neglected. The PDF set CTEQ6L has been used with $\alpha_s(M_Z) = 0.118$. Further standard-model parameters used were: $m_W = 80.419$ GeV, $\Gamma_W = 2.048$ GeV, $m_Z = 91.188$ GeV, $\Gamma_Z = 2.446$ GeV, the Fermi constant $G_\mu = 1.16639 \cdot 10^{-2}$ GeV^{-2}, $\sin^2 \theta_W = 0.2222$ and $\alpha_{\mathrm{EM}} = 1/132.51$.

- *Jet definitions.* Jets were defined using Paige's `GETJET` cone clustering algorithm, with a calorimeter segmentation of $(\Delta \eta, \Delta \phi) = (0.1, 6°)$ extended over the range $|\eta| < 2.5$ $(|\eta| < 5)$, and cone size of 0.7 (0.4) for the Tevatron (LHC). At the Tevatron (LHC) jets are required with $E_T > 10$ (20) GeV, and pseudo-rapidity $|\eta| < 2$ (4.5). For the analysis of the differential jet rates denoted as d_i, the Tevatron Run II k_T algorithm [62] was applied to all final-state particles fulfilling $|\eta| < 2.5$ (5).

In all cases, except the d_i plots (see below), the analysis is done at the hadron level, but without including the underlying event. For all codes, the systematic uncertainties are investigated by varying the merging scale and by varying the scale in α_s and, for some codes, in the parton density functions. For ALPGEN, the scale in α_s has been varied only in the α_s-reweighting of the matrix elements, while for the others the scale was also varied in the parton cascade. Note that varying the scale in the final-state parton showers will spoil the tuning done to LEP data for the cascades. A consistent way of testing the scale variations would require retuning of hadronization parameters. However, observables considered here are not expected to feature a strong dependence on the hadronization parameters, hence, no attempt has been made to retune them.

The parameter choices specific to the individual codes are as follows:

- ALPGEN: The parton-level matrix elements were generated with ALPGEN [39, 46] and the subsequent evolution used the HERWIG parton shower according to the MLM procedure. Version 6.510 of HERWIG was used, with its default shower and hadronization parameters. The *default* results for the Tevatron (LHC) were obtained using parton-level cuts, see eq. (1.8), of $p_T^{min} = 8$ (15) GeV, $\eta_{max} = 2.5$ (5), $R_{min} = 0.7$ (0.4) and matching defined by $E_T^{\mathrm{clus}} = 10$ (20) GeV, $\eta_{max}^{clus} = \eta_{max}$ and $R_{\mathrm{clus}} = R_{min}$. The variations used in the assessment of the systematics cover:

– different thresholds for the definition of jets used in the matching: $E_{\mathrm{T}}^{\mathrm{clus}} = 20$ and 30 GeV for the Tevatron, and $E_{\mathrm{T}}^{\mathrm{clus}} = 30$ and 40 GeV for the LHC. These thresholds were applied to the partonic samples produced with the default generation cuts, as well as to partonic samples produced with higher p_T^{min} values. No difference was observed in the results, aside from an obviously better generation efficiency in the latter case. In the following studies of the systematics, the two threshold settings will be referred to as ALPGEN parameter sets ALptX, where X labels the value of the threshold. Studies with different values of R_{clus} and R_{min} were also performed, leading to marginal changes, which will not be documented here.

– different renormalization scales at the vertices of the clustering tree: $\mu = \mu_0/2$ and $\mu = 2\,\mu_0$, where μ_0 is the default k_T value. In the following studies of the systematics, these two settings will be referred to as ALPGEN parameter sets ALscL (for "Low") and ALscH (for "High").

The publicly available version V2.10 of the code was used to generate the ALPGEN results.

- ARIADNE: The parton-level matrix elements were generated with MADEVENT and the subsequent evolution used the dipole shower in ARIADNE according to the procedure outlined in sec. 1.4.1. Hadronization was performed by PYTHIA.
For the *default* results at the Tevatron (LHC), the parton-level cuts were $p_{T\min} = 10$ (20), $R_{jj} < 0.5$ (0.4) and, in addition, a cut on the maximum pseudo-rapidity of jets, $\eta_{j,\max} = 2.5$ (5.0). The variations used in the assessment of the systematics cover:

– different values of the merging scales $p_{\perp,\min} = 20$ and 30 GeV for the Tevatron (30 and 40 GeV for the LHC). In the following studies of the systematics, these two settings will be referred to as ARIADNE parameter sets ARptX.

– a change of the soft suppression parameters in eq. (1.7) from the default values of $\mu = 0.6$ GeV and $\alpha = 1$, to $\mu = 0.6$ GeV and $\alpha = 1.5$ (taken from a tuning to HERA data [70]). This setting will be referred to as ARs.

– different values of the scale in α_s: $\mu = \mu_0/2$ and $\mu = 2\,\mu_0$ were used (ARscL and ARscH).

- SHERPA: The parton-level matrix elements used within SHERPA have been obtained from the internal matrix-element generator AMEGIC++ [56]. Parton showering has been conducted by APACIC++ [71, 57] whereas the combination of the matrix elements with this parton shower has been accomplished according to the CKKW procedure.[2] The hadronization of the shower configurations has been performed by PYTHIA 6.214, which has been made available through an internal interface.
For the *default* Tevatron (LHC) predictions, the value of the merging scale has been chosen to $k_{T,0} = 10$ (20) GeV. All SHERPA predictions for the Tevatron (LHC) have been obtained by setting the internally used parameter D, cf. eq. (1.1) in sec. 1.3,

---

[2]Beyond the comparison presented here, SHERPA predictions for W+multijets have already been validated and studied for Tevatron and LHC energies in [42, 61].

through $D = 0.7$ (0.4). Note that, these two choices directly determine the generation of the matrix elements in SHERPA. The variations used in the assessment of the systematics cover:

- different choices of the merging scale $k_{T,0}$. Values of 20, 30, and 30, 40 GeV have been used for the Tevatron and the LHC case, respectively. In the following studies of the systematics, these settings will be referred to as SHERPA parameter sets SHktX where X labels the value of the internal jet scale.

- different values of the scales used in any evaluation of the α_s *and* the parton distribution functions.[3] Two cases have been considered, $\mu = \mu_0/2$ and $\mu = 2\,\mu_0$. The choice of the merging scale is as in the default run, where μ_0 denotes the corresponding k_T values. In the subsequent studies of the systematics these two cases are referred to as SHERPA parameter sets SHscL and SHscH. It should be stressed that these scale variations have been applied in a very comprehensive manner, i.e. in both the matrix-element and parton-showering phase of the event generation.

All SHERPA results presented in this comparison have been obtained with the publicly available version 1.0.10.

1.5.2   Tevatron studies

1.5.2.1   Event rates

The comparison among inclusive jet rates is presented. These are shown in tab. 1.1. For each code, in addition to the default numbers, the results are stated of the various individual alternative choices used to assess the systematics uncertainty. In tab. 1.2 the "additional jet fractions" are shown, namely the rates $\sigma(W + n + 1 \text{ jets})/\sigma(W + n \text{ jets})$, once again covering all systematic sets of all codes. Fig. 1.3, finally, illustrates graphically the systematic ranges of cross sections: for each multiplicity, the rates are normalized to the average of the default values of all the codes.

It should be noted that the scale changes in all codes lead to the largest rate variations. This is reflected in the growing size of the uncertainty with larger multiplicities, a consequence of the higher powers of α_s. Furthermore, note that the systematic ranges of all codes have regions of overlap.

1.5.2.2   Kinematical distributions

In fig. 1.4 the inclusive $E_\perp$ spectra of the leading four jets are shown. The absolute rate predicted by each code is used, in units of pb/GeV. The relative differences w.r.t. to the ALPGEN results, in this figure and all other figures of this section, are shown in the lower in-sets of each plot, where, for the code X, the quantity $(\sigma(X) - \sigma_0)/\sigma_0$ is plotted, σ_0 being the values of the ALPGEN curves. There is generally good agreement between the codes, except for ARIADNE, which has a harder $E_\perp$ spectra for the leading two jets. SHERPA is found slightly harder than ALPGEN.

---

[3]For example, the analytical Sudakov form factors used in the matrix-element reweighting hence vary owing to their intrinsic α_s coupling dependence.

Code	$\sigma[\text{tot}]$	$\sigma[\geq 1\text{ jet}]$	$\sigma[\geq 2\text{ jet}]$	$\sigma[\geq 3\text{ jet}]$	$\sigma[\geq 4\text{ jet}]$
ALPGEN, def	**1933**	**444**	**97.1**	**18.9**	**3.2**
ALpt20	1988	482	87.2	15.5	2.8
ALpt30	2000	491	82.9	12.8	2.1
ALscL	2035	540	135	29.7	5.5
ALscH	1860	377	72.6	12.7	2.0
ARIADNE, def	**2066**	**477**	**87.3**	**13.9**	**2.0**
ARpt20	2038	459	76.6	12.8	1.9
ARpt30	2023	446	67.9	11.3	1.7
ARscL	2087	553	116	21.2	3.6
ARscH	2051	419	67.8	9.5	1.3
ARs	2073	372	80.6	13.2	2.0
SHERPA, def	**1987**	**494**	**107**	**16.6**	**2.0**
SHkt20	1968	465	85.1	12.4	1.5
SHkt30	1982	461	79.2	10.8	1.3
SHscL	1957	584	146	25.2	3.4
SHscH	2008	422	79.8	11.2	1.3

Table 1.1: Cross sections (in pb) for the inclusive jet rates at the Tevatron, according to the default and alternative settings of the various codes.

Code	$\sigma^{[\geq 1]}/\sigma^{[tot]}$	$\sigma^{[\geq 2]}/\sigma^{[\geq 1]}$	$\sigma^{[\geq 3]}/\sigma^{[\geq 2]}$	$\sigma^{[\geq 4]}/\sigma^{[\geq 3]}$
ALPGEN, def	**0.23**	**0.22**	**0.19**	**0.17**
ALpt20	0.24	0.18	0.18	0.18
ALpt30	0.25	0.17	0.15	0.16
ALscL	0.27	0.25	0.22	0.19
ALscH	0.20	0.19	0.17	0.16
ARIADNE, def	**0.23**	**0.18**	**0.16**	**0.15**
ARpt20	0.23	0.17	0.17	0.15
ARpt30	0.22	0.15	0.16	0.16
ARscL	0.26	0.21	0.18	0.17
ARscH	0.20	0.16	0.14	0.14
ARs	0.18	0.22	0.16	0.15
SHERPA, def	**0.25**	**0.22**	**0.16**	**0.12**
SHkt20	0.24	0.18	0.15	0.12
SHkt30	0.23	0.17	0.14	0.12
SHscL	0.30	0.25	0.17	0.13
SHscH	0.21	0.19	0.14	0.12

Table 1.2: Cross-section ratios for $(n + 1)/n$ inclusive jet rates at the Tevatron, according to the default and alternative settings of the various codes.
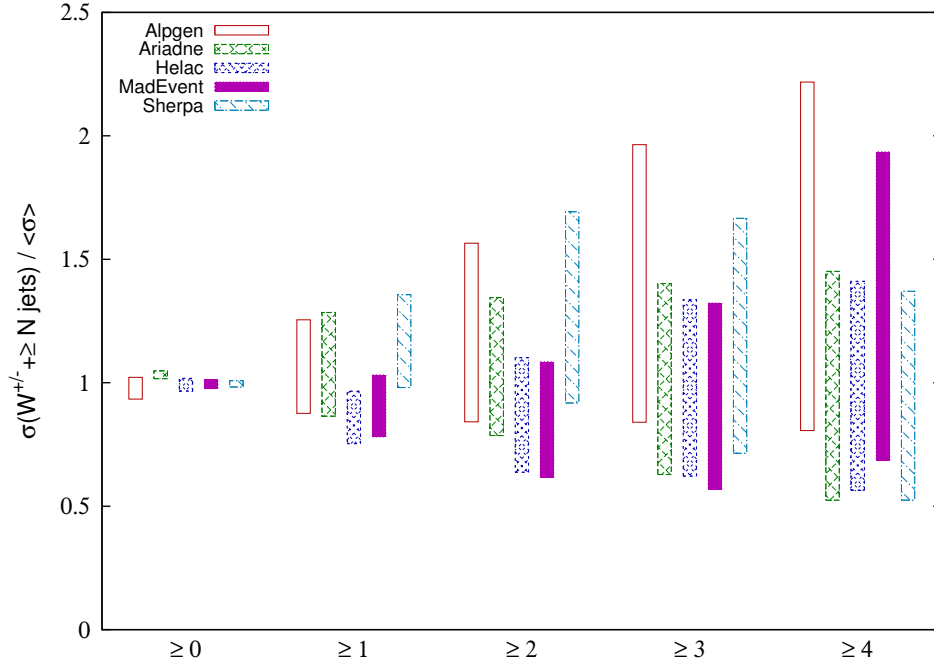
Figure 1.3: Range of variation for the Tevatron cross-section rates of the codes, normalized to the average value of the default settings for all codes in each multiplicity bin.

Fig. 1.5 shows the inclusive η spectra of the leading four jets, all normalized to unit area. ARIADNE and SHERPA spectra appear to be broader than ALPGEN, in particular for the subleading jets. This broadening is expected for ARIADNE since the gluon emissions there are essentially unordered in rapidity, which means that the Sudakov form factors applied to the matrix-element generated states include also a $\ln(1/x)$ resummation absent in the other programs.

Fig. 1.6a shows the inclusive $p_\perp$ distribution of the W boson, with absolute normalization in pb/GeV. This distribution reflects in part the behaviour observed for the spectrum of the leading jet, with ARIADNE harder than SHERPA, which, in turn, is slightly harder than ALPGEN. The region of low momenta, $p_{\perp,W} < 50$ GeV, is expanded in fig. 1.6b. Fig. 1.6c shows the η distribution of the leading jet, when its transverse momentum is larger than 50 GeV. The curves are absolutely normalized, so that the rate can be read off, which is predicted by each code to survive this harder jet cut. The $|\eta|$ separation between the W and the leading jet of the event above 30 GeV is shown in fig. 1.6d, normalized to unit area. ARIADNE has a broader correlation than ALPGEN and SHERPA.

Finally, in fig. 1.7, the merging scales d_i as obtained from the k_T algorithm are depicted, where d_i is the scale in an event where i jets are clustered into $i-1$ jets. Here, parton-level distributions are shown, which are especially sensitive to the behaviour of the merging procedure close to the merging/matching scale. Note that in the plots showing the difference the wiggles stem from both the individual codes and from the ALPGEN reference. Also shown in fig. 1.7 is the separation in $\Delta R = \sqrt{\Delta\eta^2 + \Delta\phi^2}$ between successive jet pairs ordered in hardness. The ΔR_{12} is dominated by the transversal-plane back-to-back
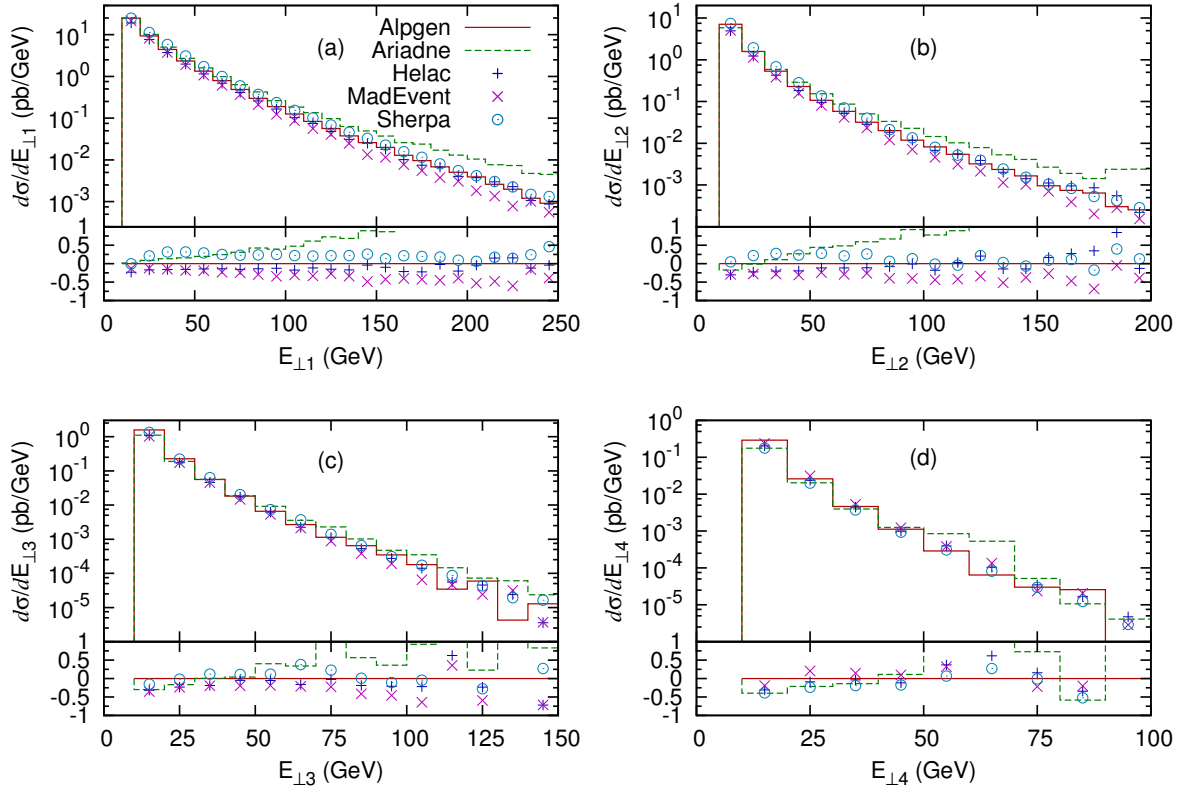
Figure 1.4: Inclusive $E_\perp$ spectra of the leading four jets at the Tevatron (pb/GeV). In all cases the full line gives the ALPGEN results, the dashed line gives the ARIADNE results and the "o" points give the SHERPA results, respectively.

peak at $\Delta R_{12} = \pi$, while for larger ΔR in all cases the behaviour is more dictated by the correlations in pseudo-rapidity. For these larger values, ARIADNE and SHERPA feature a weaker correlation, which can be expected from their broader rapidity distributions displayed in fig. 1.5.
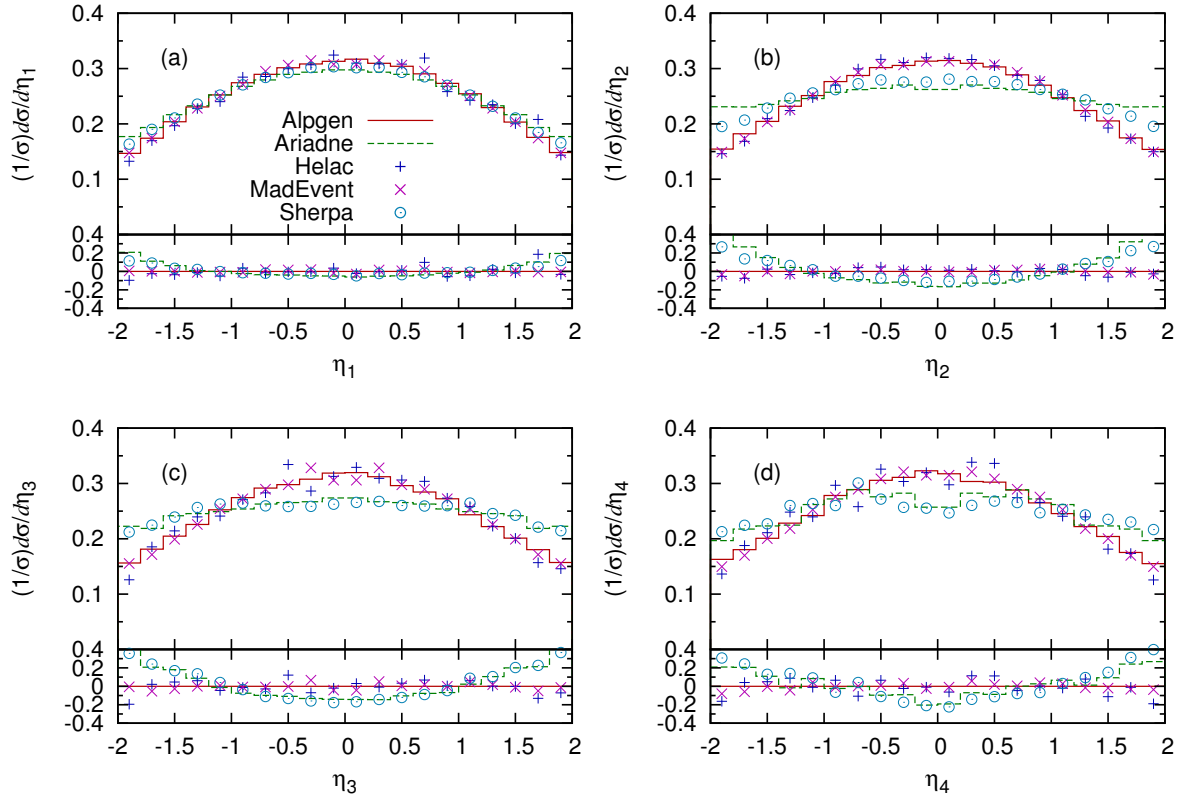
Figure 1.5: Inclusive η spectra of the four leading jets at the Tevatron. All curves are normalized to unit area. Lines and points are as in fig. 1.4.

Figure 1.6: (a) and (b) $p_\perp$ spectrum of $W^\pm$ bosons at the Tevatron (pb/GeV). (c) Inclusive η spectrum of the leading jet, for $p_\perp^{\text{jet}_1} > 50$ GeV; absolute normalization (pb). (d) Pseudo-rapidity separation between the W and the leading jet, $\Delta\eta = |\eta_W - \eta_{\text{jet}_1}|$, for $p_\perp^{\text{jet}_1} > 30$ GeV, normalized to unit area. Lines as well as the points are as in fig. 1.4.
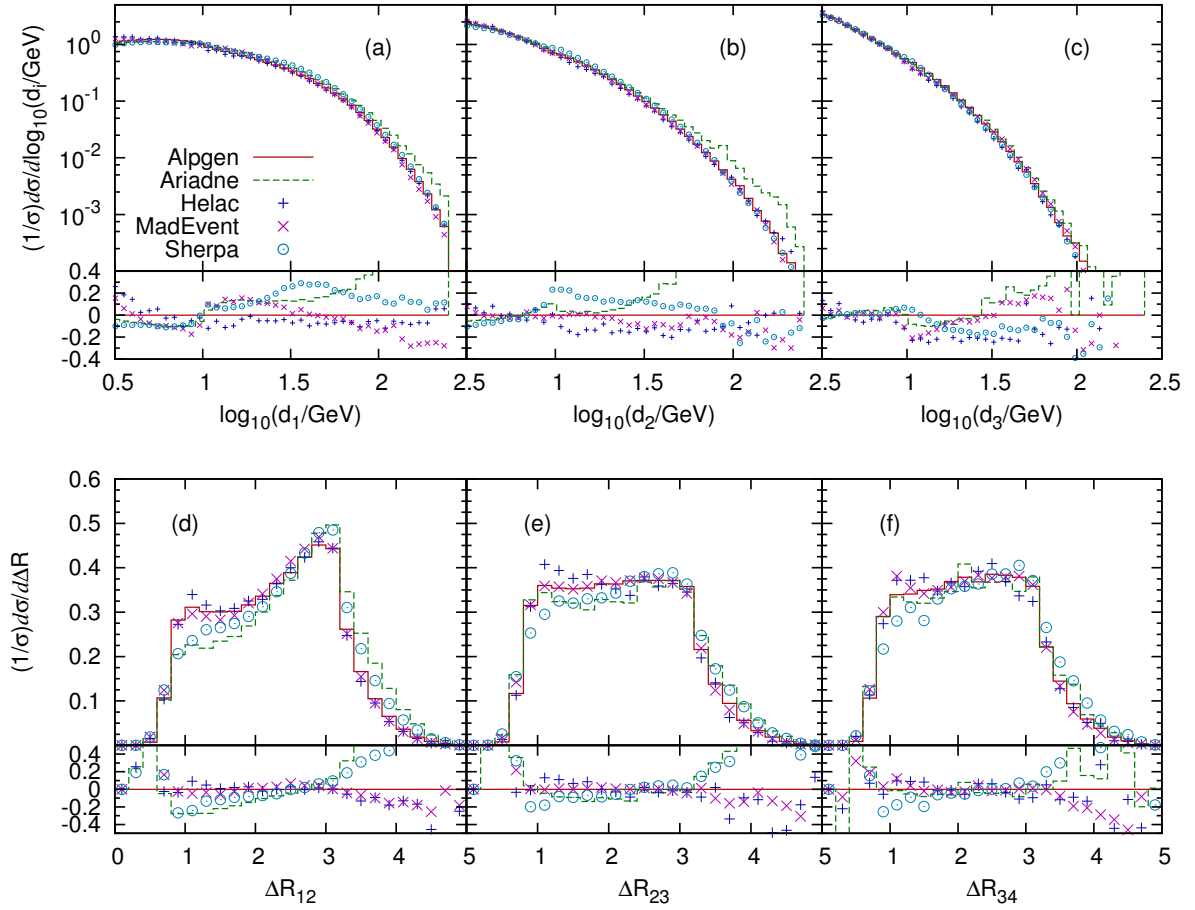
Figure 1.7: (a)–(c) d_i ($i = 1, 2, 3$) spectra, where d_i is the scale in a parton-level event where i jets are clustered into $i - 1$ jets using the k_T algorithm. (d)–(f) ΔR separations at the Tevatron between jet 1 and 2, 2 and 3, and 3 and 4. All curves are normalized to unit area. Lines and points are as in fig. 1.4.
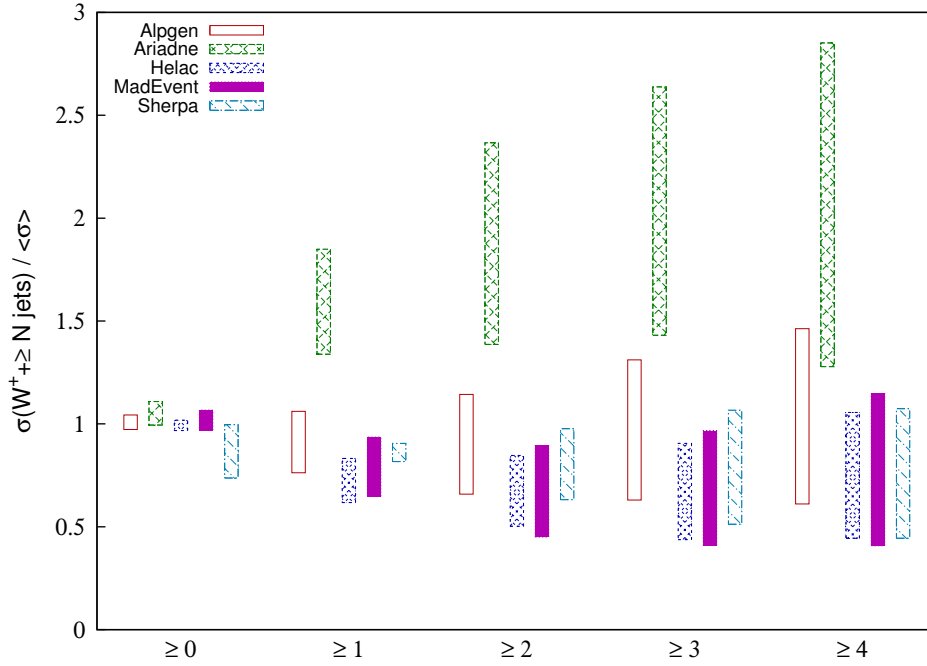
Figure 1.8: Range of variation for the LHC cross-section rates of the codes, normalized to the average value of the default settings for all codes in each multiplicity bin.

1.5.3   LHC studies

1.5.3.1   Event rates

The tables (tab. 1.3 and tab. 1.4) and figure (fig. 1.8) of this section parallel those shown earlier for the Tevatron. The main feature of the LHC results is the significantly larger rates predicted by ARIADNE (see also the discussion of its systematics, sec. 1.5.4.2), which are outside the systematics ranges of the other codes. Aside from this and the fact that SHERPA gives a smaller total cross section (see also the last part of the discussion of the SHERPA systematics in sec. 1.5.4.3), the comparison among the other codes shows an excellent consistency, with a pattern of the details similar to what seen for the Tevatron.

1.5.3.2   Kinematical distributions

Following the same sequence of the Tevatron study, fig. 1.9 shows the inclusive $E_\perp$ spectra of the leading four jets. The absolute rate predicted by each code is used, in units of pb/GeV.

Except for ARIADNE, good agreement is found among the other two codes, with ARIADNE having significantly harder leading jets, wile for subleading jets the increased rates noted in fig. 1.8 mainly come from lower $E_\perp$. Furthermore, SHERPA has consistently somewhat harder jets than ALPGEN.

For the pseudo-rapidity spectra of the jets in fig. 1.10 it is clear that ARIADNE has a much broader distribution in all cases. Also SHERPA has broader distributions, although not as pronounced as ARIADNE.

Code	$\sigma[\text{tot}]$	$\sigma[\geq 1 \text{ jet}]$	$\sigma[\geq 2 \text{ jet}]$	$\sigma[\geq 3 \text{ jet}]$	$\sigma[\geq 4 \text{ jet}]$
ALPGEN, def	**10170**	**2100**	**590**	**171**	**50**
ALpt30	10290	2200	555	155	46
ALpt40	10280	2190	513	136	41
ALscL	10590	2520	790	252	79
ALscH	9870	1810	455	121	33
ARIADNE, def	**10890**	**3840**	**1330**	**384**	**101**
ARpt30	10340	3400	1124	327	88
ARpt40	10090	3180	958	292	83
ARscL	11250	4390	1635	507	154
ARscH	10620	3380	1071	275	69
ARs	11200	3440	1398	438	130
SHERPA, def	**8800**	**2130**	**574**	**151**	**41**
SHkt30	8970	2020	481	120	32
SHkt40	9200	1940	436	98.5	24
SHscL	7480	2150	675	205	58
SHscH	10110	2080	489	118	30

Table 1.3: Cross sections (in pb) for the inclusive jet rates at the LHC, according to the default and alternative settings of the various codes.

Code	$\sigma^{[\geq 1]}/\sigma^{[tot]}$	$\sigma^{[\geq 2]}/\sigma^{[\geq 1]}$	$\sigma^{[\geq 3]}/\sigma^{[\geq 2]}$	$\sigma^{[\geq 4]}/\sigma^{[\geq 3]}$
ALPGEN, def	**0.21**	**0.28**	**0.29**	**0.29**
ALpt30	0.21	0.25	0.28	0.30
ALpt40	0.21	0.23	0.27	0.30
ALscL	0.24	0.31	0.32	0.31
ALscH	0.18	0.25	0.27	0.27
ARIADNE, def	**0.35**	**0.35**	**0.29**	**0.26**
ARpt30	0.33	0.33	0.29	0.27
ARpt40	0.32	0.30	0.30	0.28
ARscL	0.39	0.37	0.31	0.30
ARscH	0.32	0.32	0.26	0.24
ARs	0.31	0.41	0.31	0.30
SHERPA, def	**0.24**	**0.27**	**0.26**	**0.27**
SHkt30	0.23	0.24	0.25	0.27
SHkt40	0.21	0.22	0.23	0.24
SHscL	0.29	0.31	0.30	0.28
SHscH	0.21	0.24	0.24	0.25

Table 1.4: Cross-section ratios for $(n+1)/n$ inclusive jet rates at the LHC, according to the default and alternative settings of the various codes.
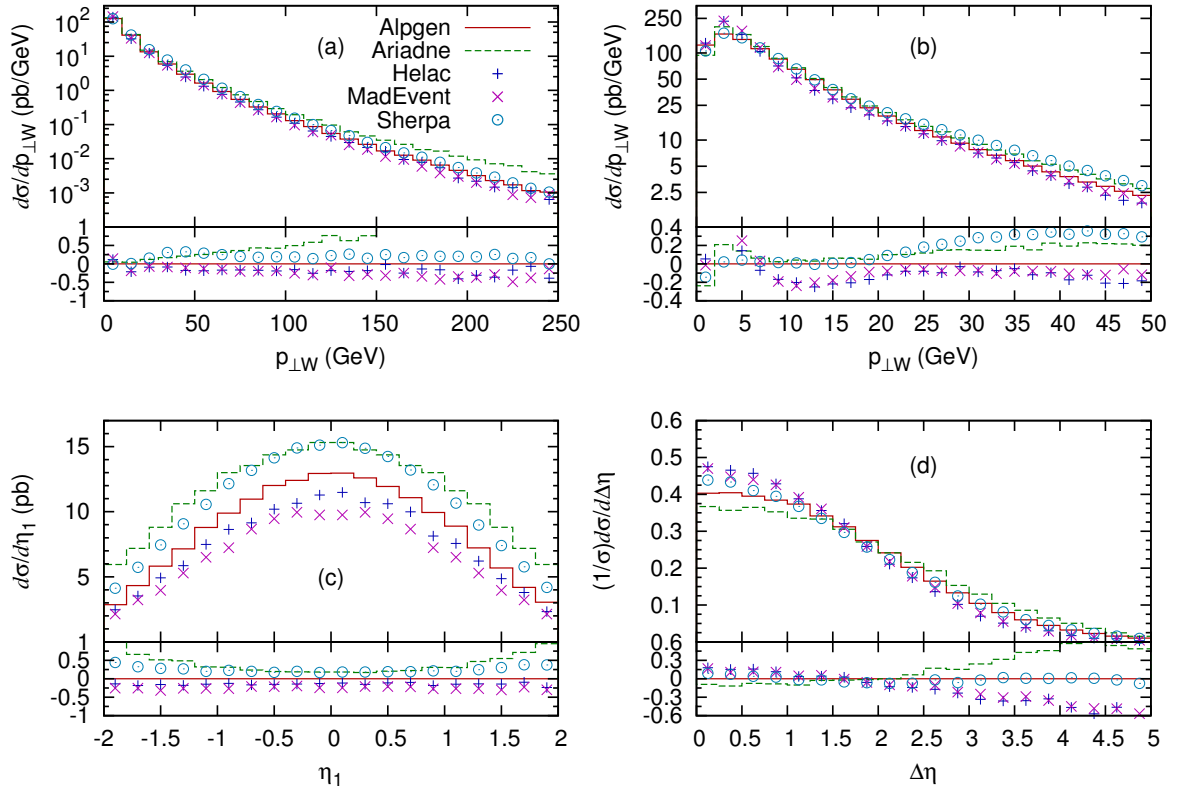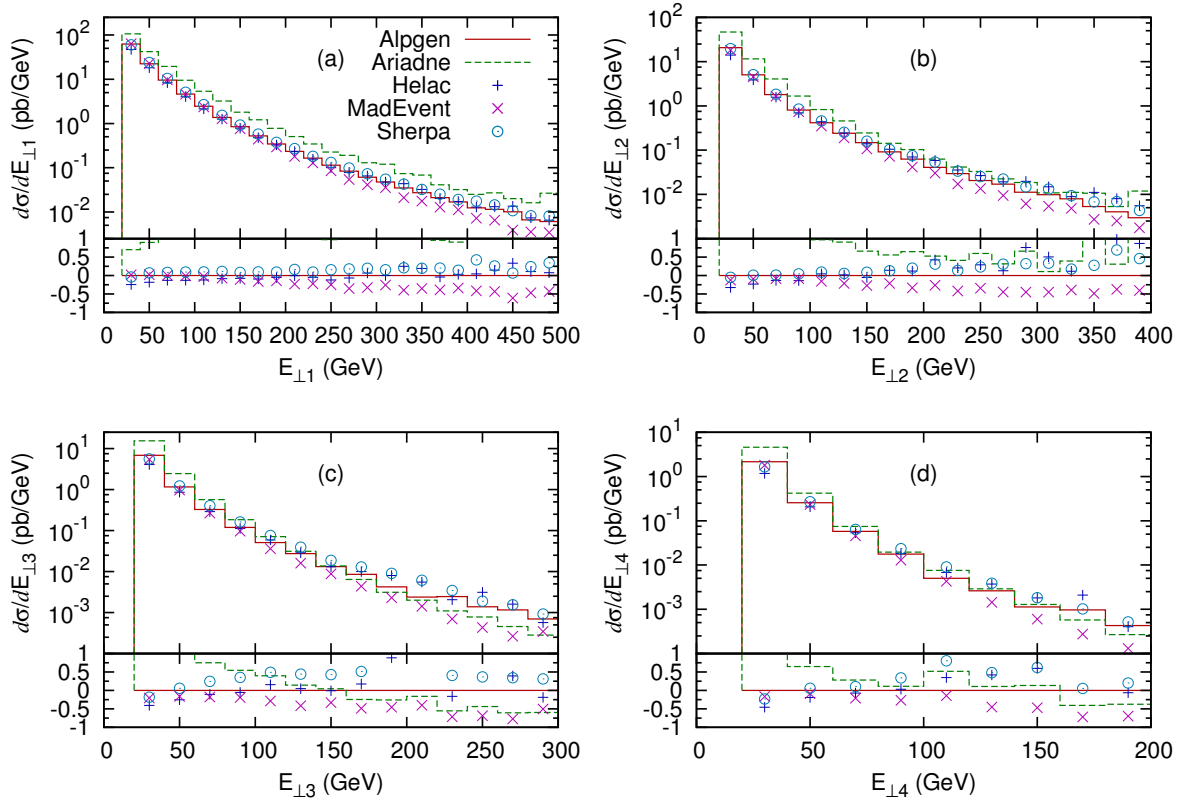
Figure 1.9: Inclusive $E_\perp$ spectra of the leading four jets at the LHC (pb/GeV). In all cases the full line gives the ALPGEN results, the dashed line gives the ARIADNE results and the "o" points give the SHERPA results, respectively.
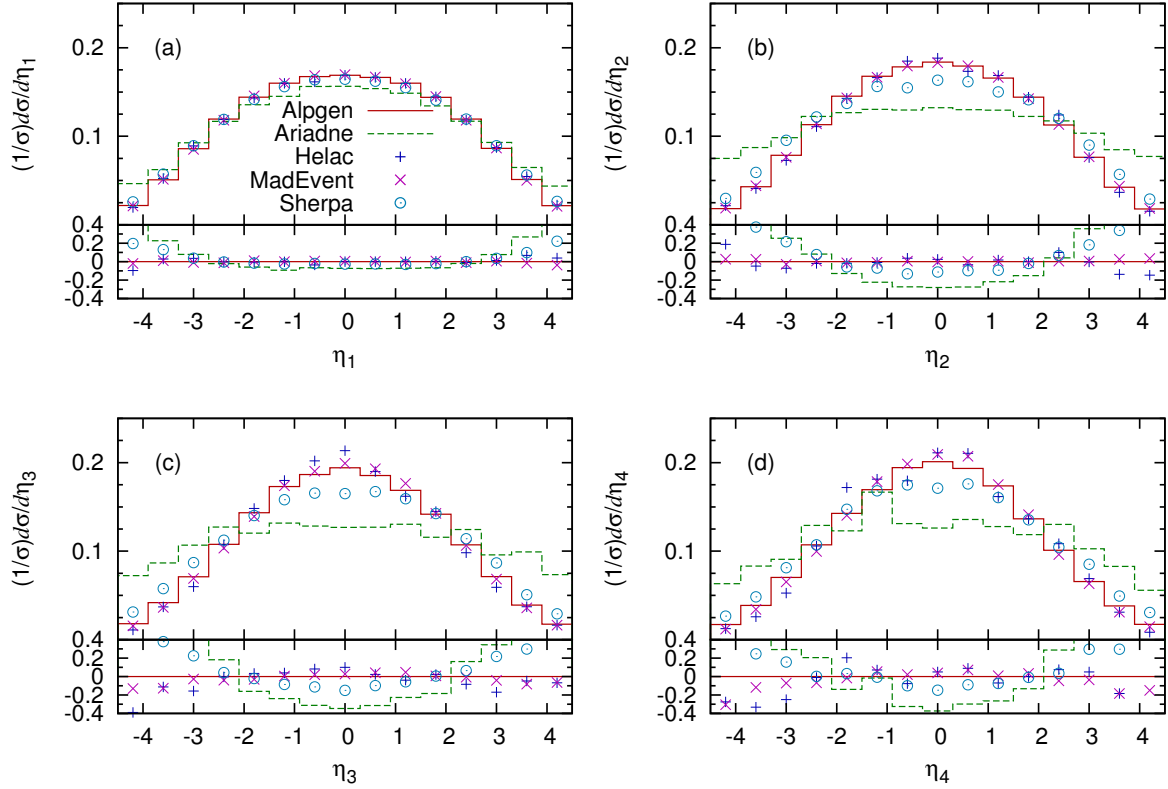
Figure 1.10: Inclusive η spectra of the four leading jets at the LHC. All curves are normalized to unit area. Lines and points are as in fig. 1.9.

The $p_\perp$ distribution of W^+ bosons in fig. 1.11 follows the trend of the leading-jet $E_\perp$ spectra. Increasing the transverse momentum of the leading jet in fig. 1.11a does not much change the conclusion for its pseudo-rapidity distribution. Also the rapidity correlation between the leading jet and the W^+ follows the trend found for the Tevatron, but the differences are larger, with a much weaker correlation for ARIADNE. Also SHERPA shows a somewhat weaker correlation.

For the distribution in clustering scale in fig. 1.12, ARIADNE is by far the hardest. The results given by the other codes are comparable, with the only exception that for the d_1 distribution, SHERPA gives a somewhat harder prediction compared to ALPGEN.

For the ΔR distributions in fig. 1.12, the behaviour for the large values is consistent with the broader rapidity distributions found for SHERPA and, in particular, for ARIADNE in fig. 1.10. For lower values, ARIADNE and SHERPA are below ALPGEN.
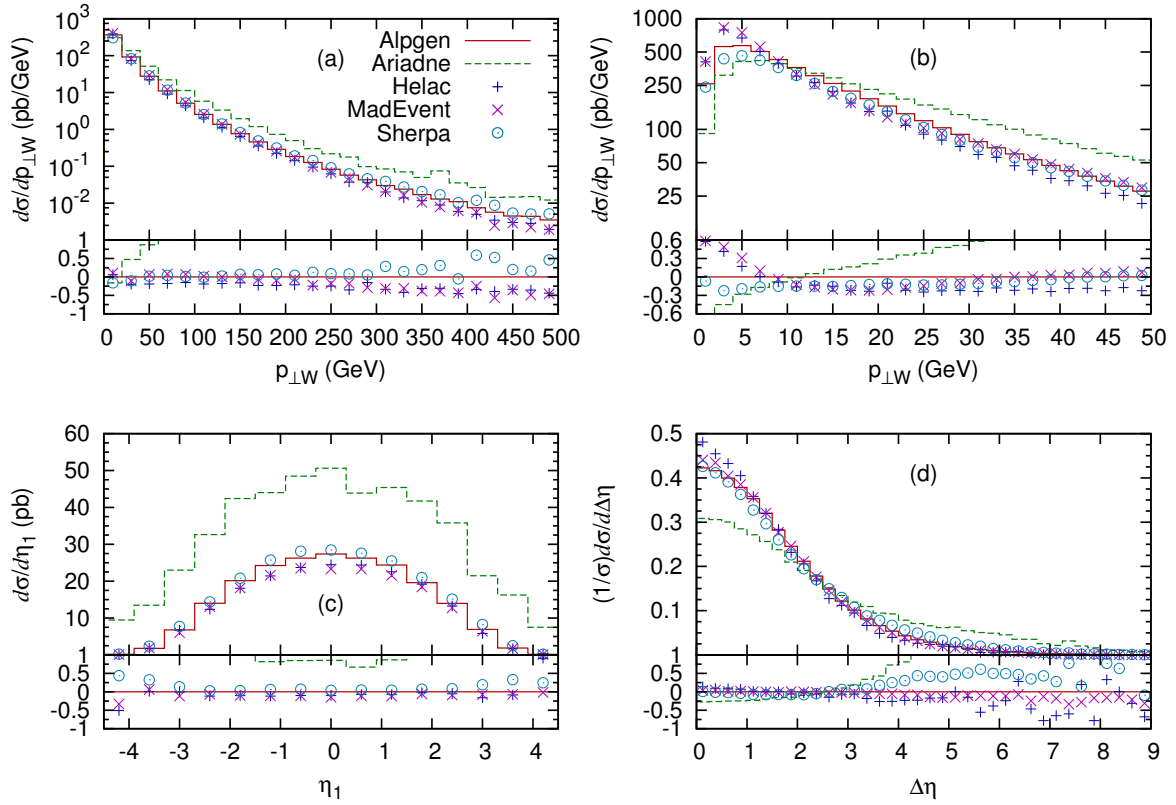
Figure 1.11: (a) and (b) $p_\perp$ spectrum of W^+ bosons at the LHC (pb/GeV). (c) η spectrum of the leading jet, for $p_\perp^{\mathrm{jet}_1} > 100$ GeV; absolute normalization (pb). (d) Pseudo-rapidity separation between the W^+ and the leading jet, $\Delta\eta = |\eta_{W^+} - \eta_{\mathrm{jet}_1}|$, for $p_\perp^{\mathrm{jet}_1} > 40$ GeV, normalized to unit area. Lines and points are as in fig. 1.9.
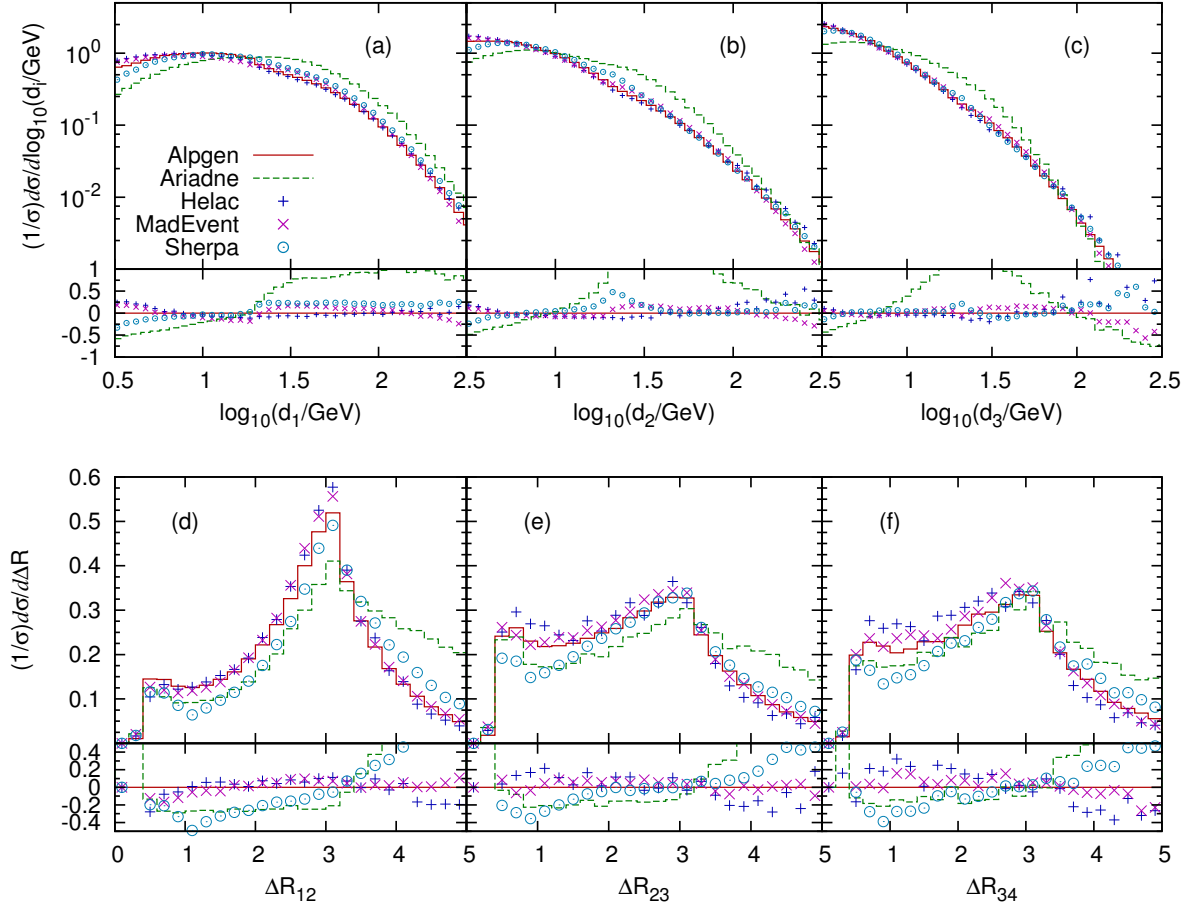
Figure 1.12: (a)–(c) d_i $(i = 1, 2, 3)$ spectra, where d_i is the scale in a parton-level event where i jets are clustered into $i - 1$ jets using the k_T algorithm. (d)–(f) ΔR separations at the LHC between jet 1 and 2, 2 and 3, and 3 and 4. All curves are normalized to unit area. Lines and points are as in fig. 1.9.

1.5.4   Systematic studies

In this section the systematic studies are presented of each of the codes separately for both the Tevatron and the LHC, followed by some general comments on differences and similarities between the codes.

In all a subset of the plots has been chosen shown in the previous sections: the transverse momentum of the W, the pseudo-rapidity of the leading jet, the separation between the leading and the subleading jet, and the d_i logarithmic spectra. As before, all spectra aside from $p_{\perp,W}$ are normalized to unit integral over the displayed range.

1.5.4.1   ALPGEN systematics

The ALPGEN distributions for the Tevatron are shown in fig. 1.13. The pattern of variations is consistent with the expectations. In the case of the $p_{\perp,W}$ spectra, which are plotted in absolute scales, the larger variations are due to the change of scale, with the lower scale leading to a harder spectrum. The $\pm 20\%$ effect is consistent with the scale variation of α_s, which dominates the scale variation of the rate once $p_{\perp,W}$ is larger than the Sudakov region. The change of matching scales only leads to a minor change in the region $0 < p_{\perp,W} < 40$ GeV, confirming the stability of the merging prescription.

In the case of the rapidity spectrum, it is noticed that the scale change leaves the shape of the distribution unaltered, while small changes appear at the edges of the η range. The d_i distributions show agreement among the various options when $d_i < 1$. This is due to the fact that the region $d_i < 1$ is dominated by the initial-state evolution of an $n = i - 1$ parton event, and both the matching and scale sensitivities are reduced. The matching variation affects the region $1 < d_i < \log E_T^{min}$, but is reduced above that. This is because, when the jet transverse energies are above a given matching scale, the sensitivity to lower matching scales is suppressed (the event will *match* in all cases).

For the LHC, the ALPGEN systematics is shown in fig. 1.14. The comparison of the various parameter choices is similar to what we encountered at the Tevatron, with variations in the range of $\pm 20\%$ for the matching-scale systematics, and up to 40% for the scale systematics. The pattern of the glitches in the d_i spectra for the different matching thresholds is also consistent with the explanation provided in the case of the Tevatron.

1.5.4.2   ARIADNE systematics

The ARIADNE systematics for the Tevatron is shown in fig. 1.15. Since the dipole cascade by itself already includes a matrix-element correction for the first emission, no dependence on the merging scale in the $p_{\perp,W}$ is seen, η_{jet_1} and d_1 distributions, which are mainly sensitive to leading-order corrections. For the other distributions, they become sensitive to higher-order corrections, and here the pure dipole cascade underestimates the matrix element and also tends to make the leading jets less back-to-back in azimuth. The first effect is expected for all parton showers, but is somewhat enhanced in ARIADNE due to the missing initial-state $q \to gq$ splitting, and is mostly visible in the d_2 distribution just below the merging scale. The second effect is clearly visible in the ΔR_{12} distribution, which is dominated by low $E_\perp$ jets.

The changing of the soft suppression parameter in ARs has the effect of reducing the available phase space of gluon radiation, especially for large $E_\perp$ and in the beam directions,
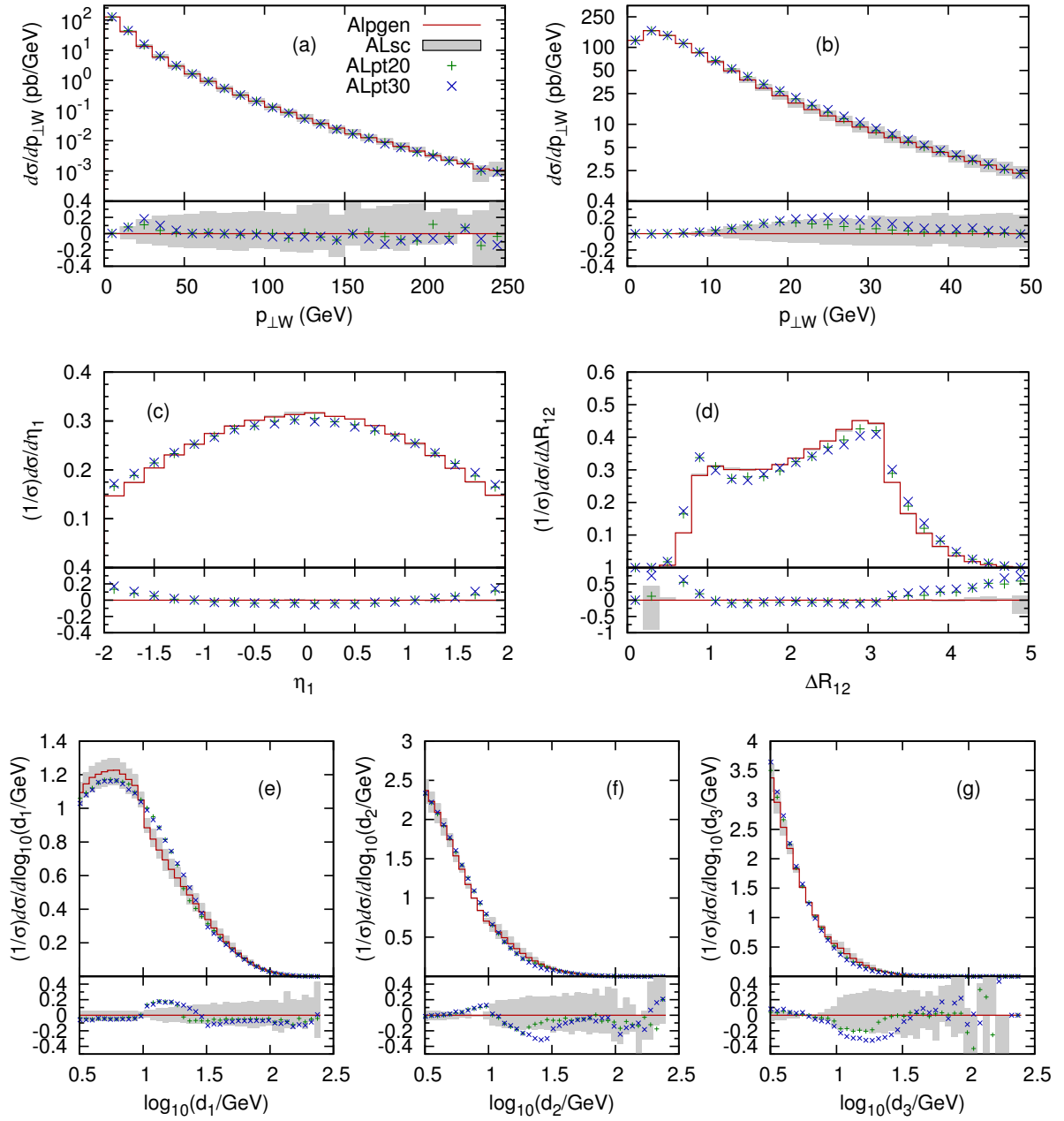
Figure 1.13: ALPGEN systematics at the Tevatron. (a) and (b) $p_\perp$ spectrum of the W boson. (c) Pseudo-rapidity distribution of the leading jet. (d) ΔR separation between the two leading jets. (e)–(g) Distribution in clustering scales as described in fig. 1.7. The full line is the default settings of ALPGEN, the shaded area is the range between ALscL and ALscH, while the points represent ALpt20 and ALpt30 as defined in sec. 1.5.1.
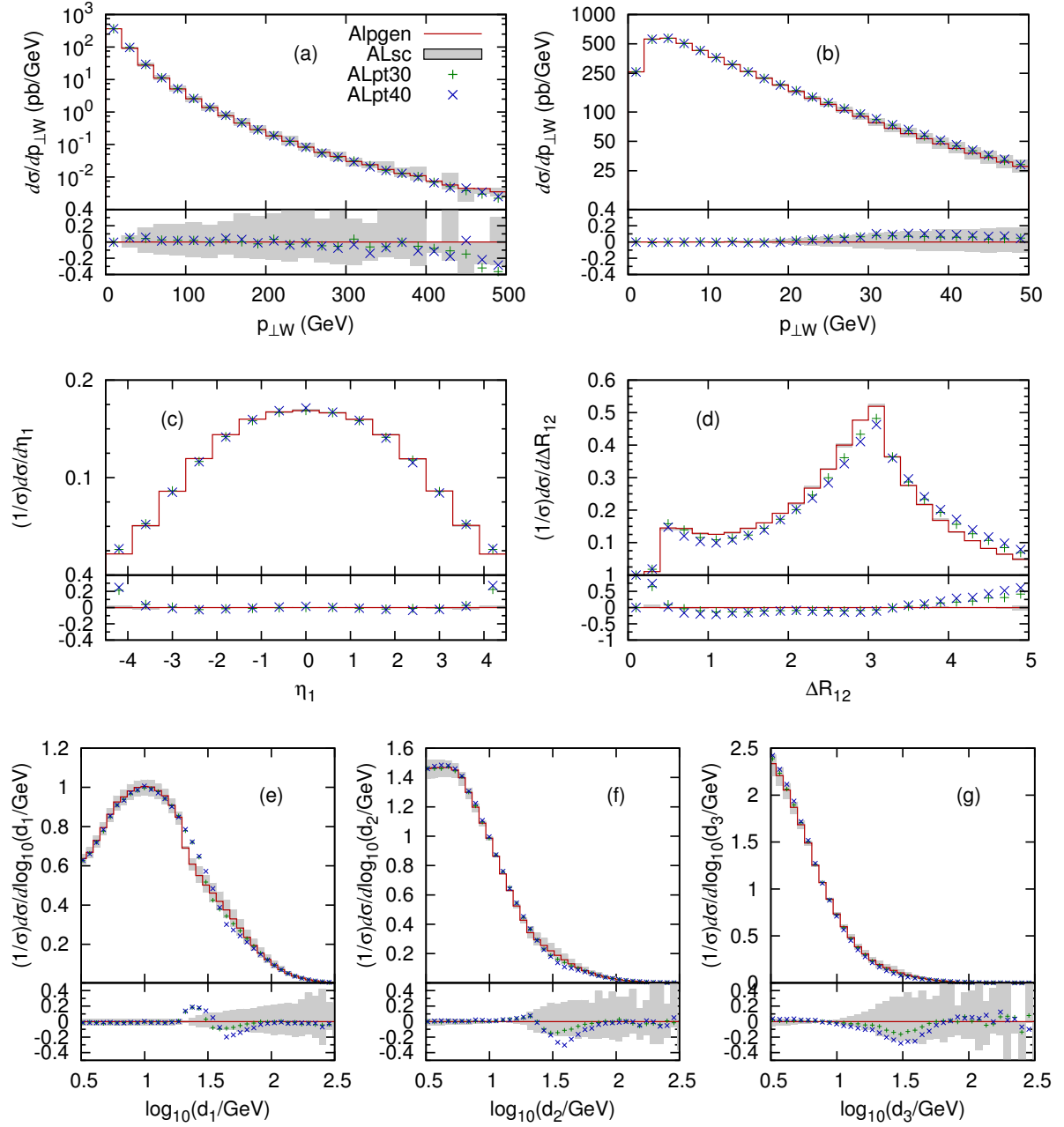
Figure 1.14: ALPGEN systematics at the LHC. (a) and (b) show the $p_\perp$ spectrum of the W, (c) shows the pseudo-rapidity distribution of the leading jet, (d) shows the ΔR separation between the two leading jets, and (e)–(g) show the distribution in clustering scales as described in fig. 1.12. The full line is the default settings of ALPGEN, the shaded area is the range between ALscL and ALscH, while the points represent ALpt20 and ALpt30 as defined in sec. 1.5.1.
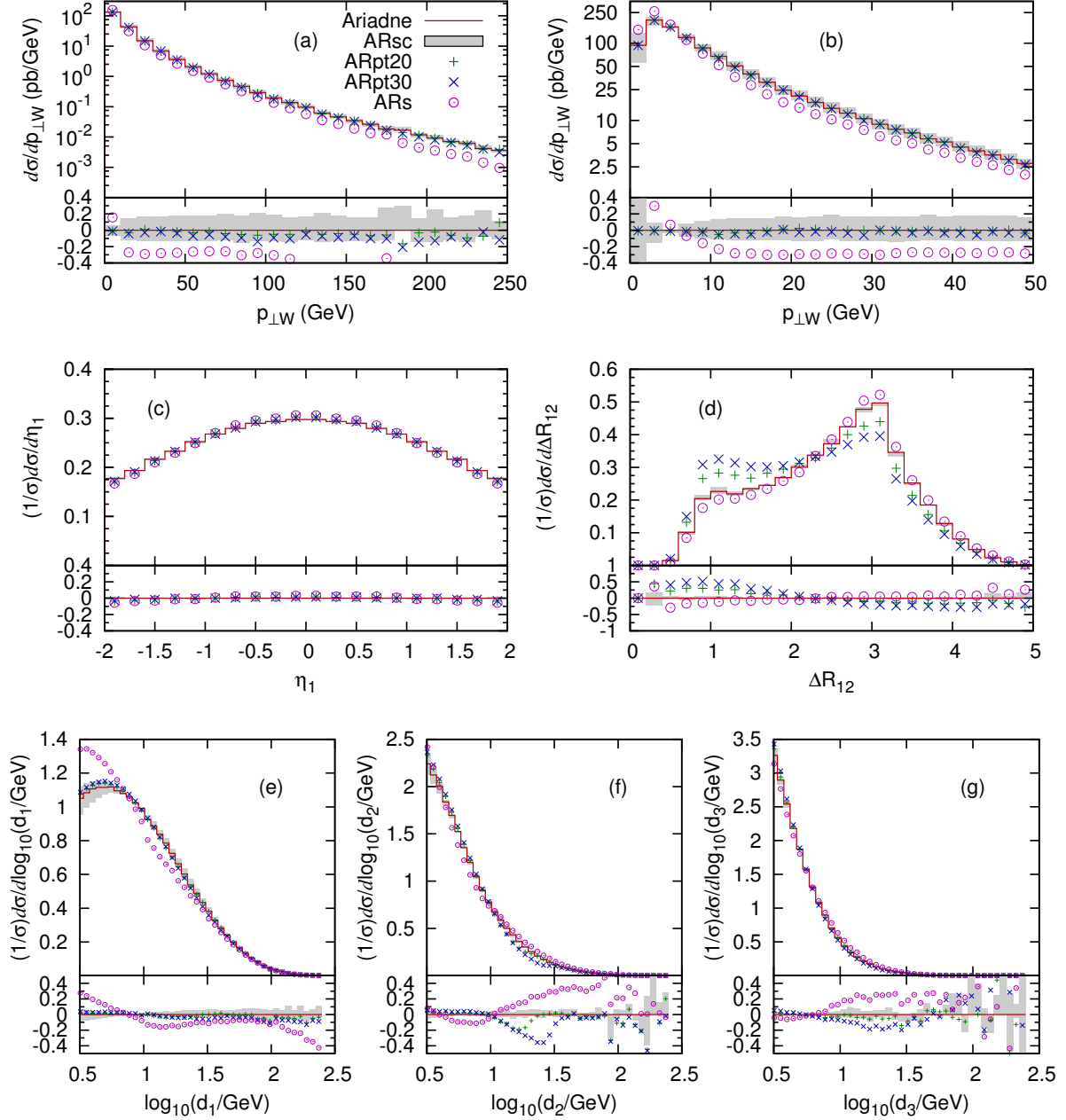
Figure 1.15: ARIADNE systematics at the Tevatron. The plots are the same as in fig. 1.13. The full line is the default settings of ARIADNE, the shaded area is the range between ARscL and ARscH, while the points represent ARpt20, ARpt30 and ARs as defined in sec. 1.5.1.

Figure 1.16: ARIADNE systematics at the LHC. The plots are the same as in fig. 1.14. The full line is the default settings of ARIADNE, the shaded area is the range between ARscL and ARscH, while the points represent ARpt20, ARpt30 and ARs as defined in sec. 1.5.1.

an effect, which is mostly visible for the hardest emission and in the $p_{\perp,W}$ distribution.

As for ALPGEN, and also for the other codes, the change in scale mainly affects the hardness of the jets, but not the η_{jet_1} and the ΔR_{12} distribution.

For the LHC, the ARIADNE systematics is shown in fig. 1.16. Qualitatively, the same effects as in the Tevatron case are found. In particular, the strong dependence on the soft suppression parameters in ARs can be noted, and it is clear that these have to be adjusted to fit Tevatron (and HERA) data before any predictions for the LHC can be made. It should be noted, however, that while e.g. the high $p_{\perp,W}$ tail in fig. 1.16a for ARs is shifted down to be comparable to the other codes (cf. fig. 1.11a), the medium $p_{\perp,W}$ values are less affected and here the differences compared to the other codes can be expected to remain after a retuning.

This difference is mainly due to the fact that the dipole cascade in ARIADNE, contrary to the other parton showers, is not based on standard DGLAP evolution, but also allows for evolution, which is unordered in transverse momentum à la BFKL. [4] This means that in ARIADNE there is also a resummation of logarithms of $1/x$ besides the standard $\ln Q^2$ resummation. This should not be a large effect at the Tevatron, and the differences there can be tuned away by changing the soft suppression parameters in ARIADNE. However, at the LHC there will be quite small x-values, $x \sim m_W/\sqrt{S} < 0.01$, which allow for a much increased phase space for jets as compared to what is allowed by standard DGLAP evolution. As a result one obtains larger inclusive jet rates as documented in tab. 1.3. The same effect is found in DIS at HERA, where x is even smaller as are the typical scales, Q^2. And here, all DGLAP based parton showers fail to reproduce final-state properties, especially forward jet rates, while ARIADNE does a fairly good job.

It would be interesting to compare the merging schemes presented here also to HERA data to see if the DGLAP based showers would better reproduce data when merged with higher-order matrix elements. This would also put the extrapolations to the LHC on safer grounds. However, so far there exists one preliminary such study for the ARIADNE case only [72].

1.5.4.3   SHERPA systematics

The systematics of the CKKW algorithm as implemented in SHERPA is presented in fig. 1.17 for the Tevatron case. The effect of varying the scales in the PDF *and* strong coupling evaluations by a factor of 0.5 (2.0) is that for the lower (higher) scale choice, the W boson's $p_{\perp}$ spectrum becomes harder (softer). For this kind of observables, the uncertainties given by scale variations dominate the ones emerging through variations of the internal separation cut. This is mainly due to a reduced (enhanced) suppression of hard-jet radiation through the α_s rejection weights. The differential jet rates, $d_{1,2,3}$, shown in fig. 1.17e–g, have a more pronounced sensitivity on the choice of the merging scale, leading to variations at the 20% level. In the CKKW approach this dependence can be understood since the k_T measure intrinsically serves as the discriminator to separate the matrix-element and parton-shower regimes. Hence, the largest deviations from the default typically appear at $d_i \approx k_{T,0}$. However, the results are remarkably smooth, which

---

[4]The dipole emission of gluons in ARIADNE are ordered in transverse momentum, but not in rapidity. Translated into a conventional initial-state evolution, this corresponds to emissions ordered in rapidity but unordered in transverse momentum.
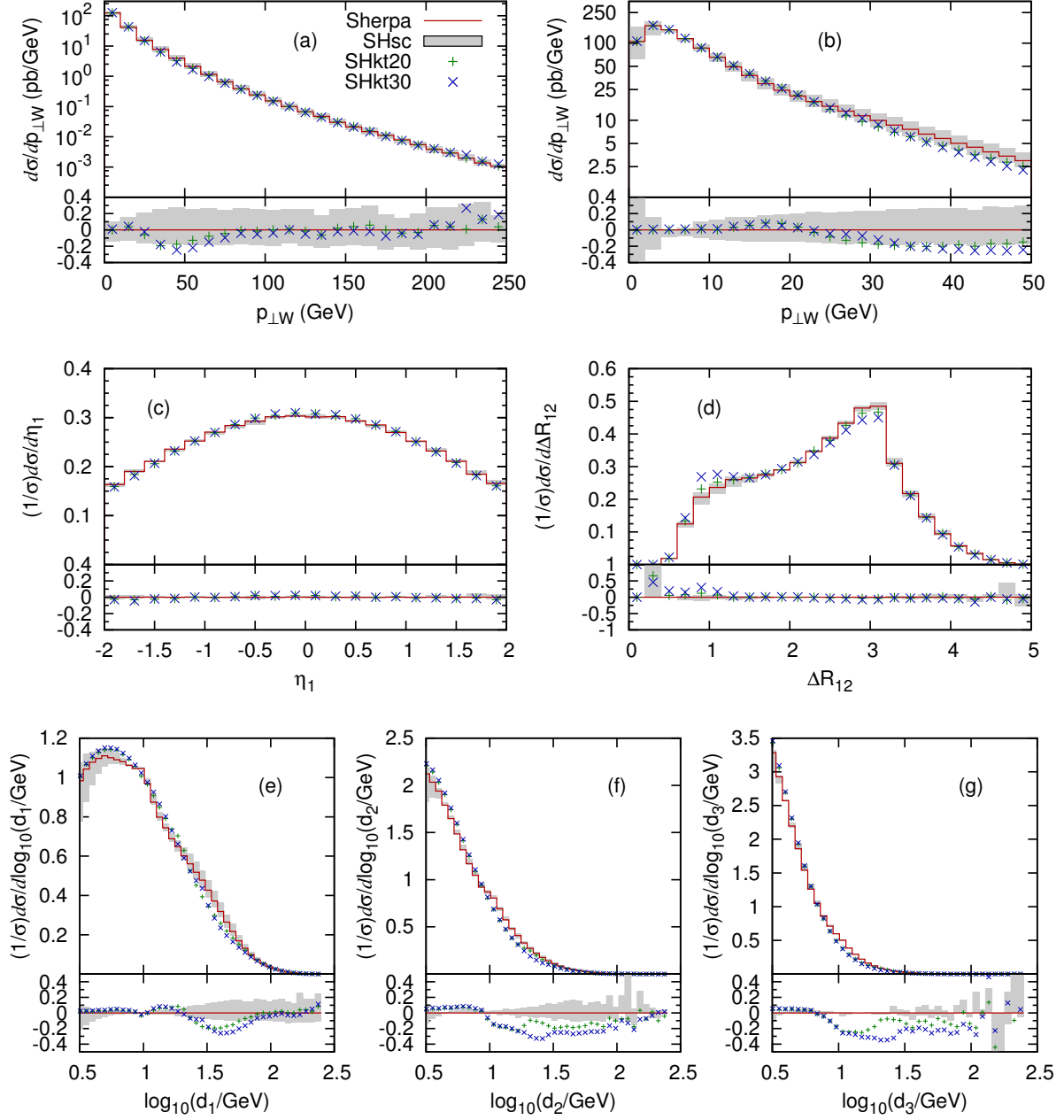
Figure 1.17: SHERPA systematics at the Tevatron. The plots are the same as in fig. 1.13. The full line is the default settings of SHERPA, the shaded area is the range between SHscL and SHscH, while the points represent SHkt20 and SHkt30 as defined in sec. 1.5.1.
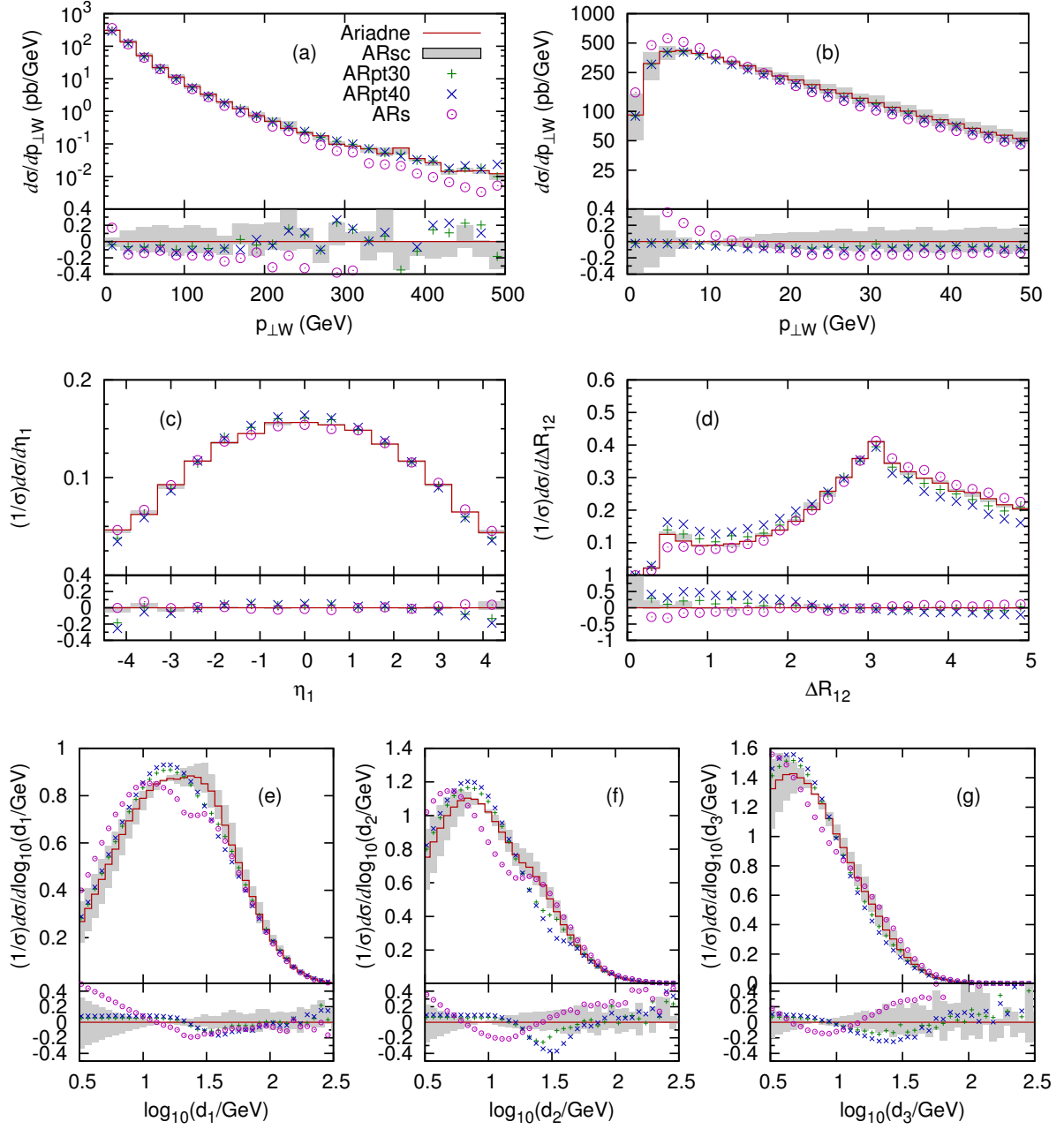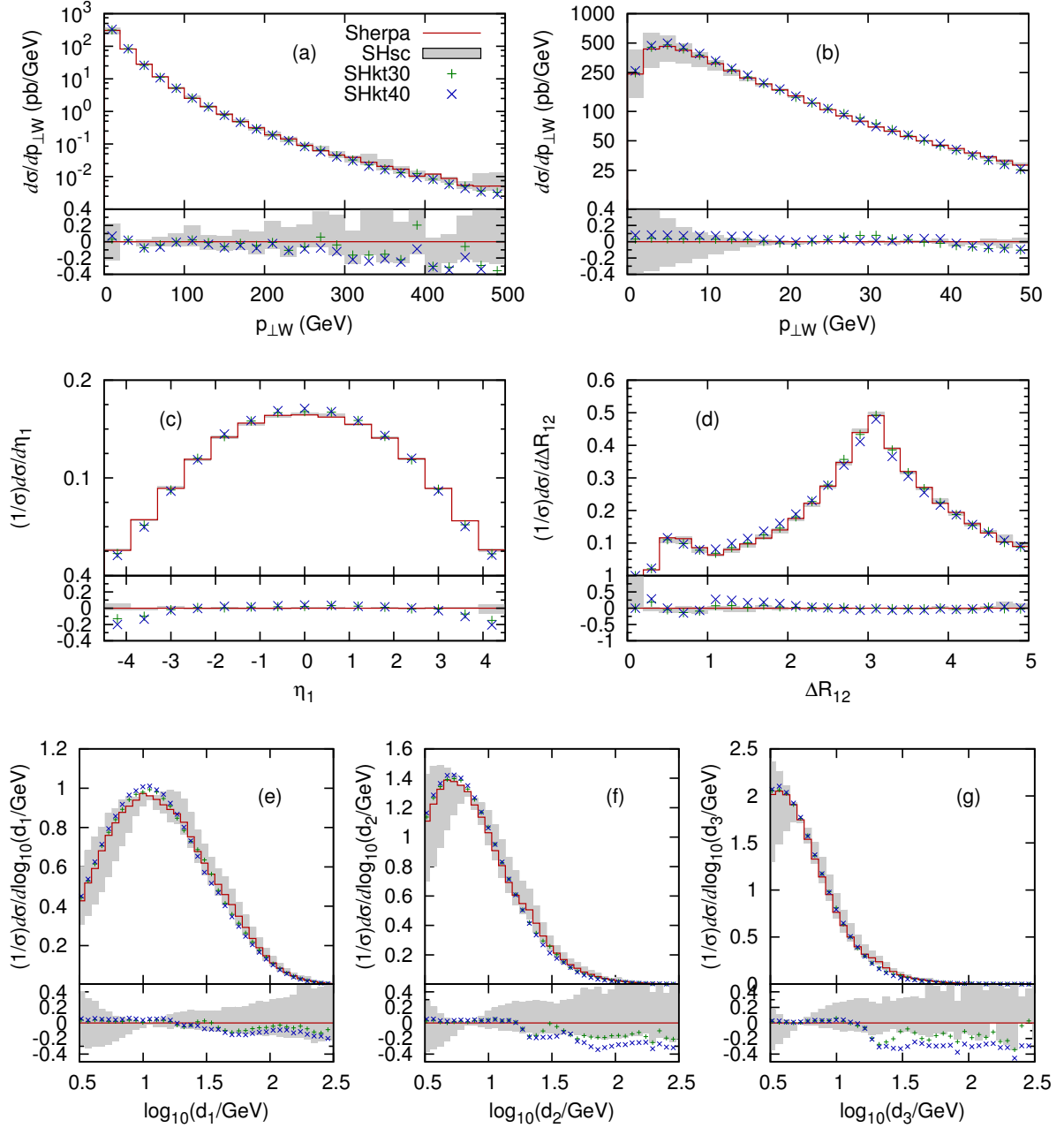
Figure 1.18: SHERPA systematics at the LHC. The plots are the same as in fig. 1.14. The full line is the default settings of SHERPA, the shaded area is the range between SHscL and SHscH, while the points represent SHkt20 and SHkt30 as defined in sec. 1.5.1.

leads to the conclusion that the cancellation of the dominant logarithmic dependence on the merging cut is well achieved. Moreover, considering the pseudo-rapidity of the leading jet and the cone separation of the two hardest jets, these distributions show a very stable behaviour under the studied variations, since they are indirectly influenced by the cut scale only. The somewhat more pronounced deviation at low ΔR_{12} is connected to phase-space regions of jets becoming close together, which is affected by the choice of the merging scale and therefore by its variation. Taken together, SHERPA produces consistent results with relative differences of the order of or less than 20% at Tevatron energies.

The SHERPA studies of systematics for the LHC are displayed in fig. 1.18. Compared to the Tevatron case, a similar pattern of variations is recognized. The $p_\perp$ spectra of the W^+ boson show deviations under cut and scale variations that remain on the same order of magnitude. However, a noticeable difference is an enhancement of uncertainties in the predictions for low $p_\perp$. This phase-space region is clearly dominated by the parton shower evolution, which in the SHERPA treatment of estimating uncertainties undergoes scale variations in the same manner as the matrix-element part. Therefore, the estimated deviations from the default given for low $p_\perp$ are very reasonable and reflect intrinsic uncertainties underlying the parton showering. For the LHC case, the effect is larger, since the evolution is dictated by steeply rising parton densities at x-values that are lower compared to the Tevatron scenario. The pseudo-rapidity of the leading jet and the cone separation of the two hardest jets show again a stable behaviour under the applied variations, the only slight exception is the regions of high $|\eta_{\mathrm{jet}_1}|$ where, using a high k_T cut, the deviations are at the 20% level. The effect of varying the scales in the parton distributions and strong couplings now dominates the uncertainties in the differential jet rates, $d_{1,2,3}$, which are presented in fig. 1.18e–g. This time, owing to the larger phase space, for the low scale choice, $\mu = \mu_0/2$, the spectra become up to 40% harder, whereas, for the high scale choice, the spectra are up to 20% softer. The variation of the internal merging scale does not induce bumps around the cut region, however it has to be noted that for higher choices, e.g. $k_{T,0} = 40$ GeV, there is a tendency to predict softer distributions in the tails compared to the default. To summarize, the extrapolation from Tevatron to LHC energies does not yield significant changes in the predictions of uncertainties under merging-cut and scale variations; for the LHC scenario, they have to be estimated slightly larger, ranging up to 40%. The results are again consistent and exhibit a well controlled behaviour when applying the CKKW approach implemented in SHERPA at LHC energies.

Giving a conservative, more reliable estimate, in SHERPA the strategy of varying the scales in the strong coupling *together with* the scales in the parton densities has been chosen to assess its systematics, for many more details, see app. A. So, to better estimate the impact of the additional scale variation in the parton density functions, renormalization-scale variations on its own have been studied as well. Their results show smaller deviations w.r.t. the default in the observables of this study with the interpretation of potentially underestimating the systematics of the merging approach. Also, then the total cross sections vary less and become 9095 pb and 8597 pb for the low- and high-scale choice, respectively. Note that, owing to the missing simultaneous factorization-scale variation, their order is now reversed compared to SHscL and SHscH, whose values are given in tab. 1.3. Moreover, by referring to tab. 1.4 the cross-section ratios for e.g. $\sigma^{[\geq 1]}/\sigma^{[\mathrm{tot}]}$ now

read 0.26 and 0.22 for the low- and high-scale choice, respectively. This once more emphasizes that the approach's uncertainty may be underestimated when relying on α_s scale variations only. From tab. 1.3 it also can be noted that the total inclusive cross section given by the full high-scale prediction SHscH is – unlike SHERPA's default – close to the ALPGEN default. In contrast to MLM based approaches, which prefer the factorization scale in the matrix-element evaluation set through the transverse mass of the weak boson, the SHERPA approach makes the choice of employing the merging scale $k_{T,0}$ instead. This has been motivated in [37] and further discussed in [42]. Eventually, it is a good result that compatibility is achieved under this additional PDF scale variation for the total inclusive cross sections, however it also clearly stresses that there is a non-negligible residual dependence on the choice of the factorization scale in the merging approaches.

1.5.4.4 Comparison of the systematics

Starting with the $p_{\perp,W}$ spectra, a trivial $20\% - 40\%$ effect of the scale changes is found, with the lower scale leading to a harder spectrum. In the case of ALPGEN, this only affects the spectrum above the matching scale, while for ARIADNE and SHERPA there is also an effect below, as there the scale change is also implemented in the parton shower. For all the codes, the change in merging/matching scale gives effects smaller than or of the order of the change in the α_s scale. For ARIADNE, the change in the soft suppression parameter (ARs) gives a softer spectrum, which is expected as it directly reduces the phase space for emitted gluons.

In the η_1 and ΔR_{12} distributions the effects of changing the scale in α_s are negligible. In all cases, changing the merging/matching scale also has negligible effects on the rapidity spectrum, while ΔR_{12} tends to become more peaked at small values for larger merging/matching scales, and also slightly less peaked at $\Delta R_{12} \approx \pi$. This effect is considerably larger for ARIADNE w.r.t. the other codes.

Finally, for the d_i distributions, wiggles are observed of varying sizes introduced by changing the merging scales.

1.5.5   Summary of the comparative study

In this study, a detailed comparison between three independent approaches to the problem of merging tree-level matrix elements and parton showers has been presented for the "standard-candle" process $W+$jets at Tevatron and future LHC energies. The corresponding codes employed in this comparison, ALPGEN, ARIADNE and SHERPA, differ in which matrix-element generator is used, which merging scheme (MLM or (L)CKKW) is used and the details in the implementation of these schemes, as well as in which parton shower is invoked to handle the intra-jet evolution at lower scales.

The corresponding merging algorithms have been discussed and although the three approaches (MLM, L- and CKKW) aim at a simulation based on the same idea, namely describing jet production and evolution by matrix elements and the parton showers, respectively, they have been found to be quite different. The main differences appear in the way, in which the combination of Sudakov reweighting of the matrix elements interacts with the vetoing of unwanted jet production inside the parton shower. In addition, the lower-scale performance is dictated by different showering schemes, like virtuality order-

ing with explicit angular vetoes as in SHERPA, $p_\perp$ ordering as in ARIADNE, and angular ordering as in ALPGEN (through its interface to HERWIG). Despite these differences, here, in this work, no attempt has been made to compare the three approaches analytically and to formalize the respective level of their logarithmic dependence. However, in consideration of the primary features, all results presented in this study show a reasonably good agreement, which gives rather firm evidence that the sources of the differences are of subleading order only. In particular, it can be concluded that the variety of methods for merging matrix elements and parton showers can be employed with confidence in vector boson plus jet production.

The comparison also points to differences, in absolute rates as well as in the shape of individual distributions, which underscore the existence of an underlying systematic uncertainty. Most of these differences have been found on a level, which can be expected from merging tree-level matrix elements with leading-log parton showers, in the sense that they are smaller than, or of the order of differences found by making a standard change of scale in α_s. In most cases the differences within each code have been as large as the differences between the codes. Importantly, the extrapolation towards LHC energies has been proven to proceed fairly similarly between the three approaches, which yield LHC predictions that feature the same level of deviation compared to those obtained at the Tevatron. Furthermore, as the systematics at the Tevatron resembles that at the LHC, it is conceivable that all the codes can be tuned to Tevatron data to give consistent predictions for the LHC. The latter findings are very encouraging, and, interestingly, also demonstrate a good agreement of complicated and involved numerical calculations. It remains to be seen whether the broadening in the jet pseudo-rapidity and the hardening in the vector-boson transverse-momentum spectra found for ARIADNE at LHC energies will be confirmed by data taken at the LHC.

1.6 CKKW study of diboson production at Tevatron energies

In this study, the validation of the CKKW merging prescription will be continued by investigating a somewhat more complicated scenario w.r.t. the vector boson plus jet studies accomplished so far. Here, it will be applied to W pair production simulated for Tevatron Run II energies, and both W bosons decaying leptonically, i.e. $p\bar{p} \to W^+W^- + X \to e^+\mu^-\nu_e\bar{\nu}_\mu + X$.[5]

The production of W pairs at collider experiments, possibly in association with jets, represents a background to a number of relevant other processes, such as the production of top quarks, the production of a Higgs boson with a mass above roughly 135 GeV, or the production of supersymmetric particles, such as charginos or neutralinos [73, 74]. Furthermore, this process offers a great possibility for tests of the gauge sector of the Standard Model, that has been extensively investigated by the LEP2 collaborations [75, 76, 77, 78, 79]. Tests in this channel are quite sensitive, because there is a destructive interference of two contributions: a t-channel contribution, where both W bosons

---

[5]Singly resonant diagrams contributing to the parton-level processes of $p\bar{p} \to e^+\mu^-\nu_e\bar{\nu}_\mu + X$ have been included.

couple to incoming fermions, and an s-channel contribution, where the W bosons emerge through a triple gauge coupling, either γW^+W^- or ZW^+W^-. New physics beyond the Standard Model could easily manifest itself, either through new particles propagating in the s-channel, like, for instance, a Z' particle in L-R symmetric models [80, 81, 82, 83], or through anomalous triple gauge couplings, which could be loop-induced, mediated by heavy virtual particles running in the loop. In [84, 85, 86] the most general form of an effective Lagrangian for such interactions has been developed and discussed. Such tests of anomalous triple gauge couplings have been performed both at LEP2 [87, 88, 89, 90] and at Tevatron, Run I [91, 92, 93, 94] and at Run II [95]. Both scenarios could clearly modify the total cross section or, at least, lead to different distributions of the final state particles.

Accordingly, there are a number of calculations and programs dealing with this process. At next-to-leading order (NLO) in the strong coupling constant W pair production has been calculated in [96, 97, 98]. In addition, a number of programs have been made available, allowing the user to implement phase-space cuts and to generate single events. First of all, there are fixed order calculations. At leading order (LO), i.e. at tree-level, they are usually performed through automated tools – the matrix-element or parton-level generators. Examples for such programs include `COMPHEP` [99], MADGRAPH/MADEVENT [47, 48], ALPGEN [46], and AMEGIC++ [56]. At NLO, the program `MCFM` [100] provides cross sections and distributions for this process. Moreover, multipurpose event generators such as PYTHIA [6, 7] or HERWIG [9, 10] play a major rôle in the experimental analyses of collider experiments. Also, `MC@NLO` can be used, which has been implemented in conjunction with HERWIG [101] and matches the corresponding NLO calculation with this parton shower, for the process of producing pairs of vector bosons see [31].

The presentation of the study is organized as follows:
After some consistency – including scale variation – checks of the merging algorithm in sec. 1.6.1, the results obtained with SHERPA will be confronted with those from an NLO calculation provided by `MCFM`, cf. sec. 1.6.2. Then, in sec. 1.6.3 some exemplary results of SHERPA are compared with those obtained from other event generators, in particular with those from PYTHIA and `MC@NLO`.
Input parameters used in this analysis and the specifics, how the SHERPA runs have been obtained, are listed in the appendix, see app. B.1 and app. B.3.

1.6.1   Consistency checks

In this section some sanity checks of the merging algorithm for the case of W pair production are presented. For this, first, the dependence of different observables on the key parameters of the merging procedure, namely the internal matrix-element parton-shower separation scale Q_{cut} and the highest multiplicity n_{max} of included tree-level matrix elements, is examined. Secondly, the sensitivity of the results with respect to changes in the renormalization scale μ_{R} and the factorization scale μ_{F} will be discussed.

All distributions shown in this section are inclusive results at the hadron level, where restrictive jet and lepton cuts have been applied, for details on the cuts cf. app. B.3. In all cases, the distributions are normalized to one using the respective total cross section as delivered by the merging algorithm.

1.6.1.1   Impact of the phase-space separation cut

First of all, the impact of varying the jet resolution cut Q_{cut} is studied. SHERPA results have been obtained with an inclusive 2jet production sample, i.e. tree-level matrix elements up to two additional QCD emissions have been combined and merged with the parton shower. In all figures presented here the black solid line shows the total inclusive result as obtained by SHERPA for the respective resolution cut Q_{cut}. The reference curve drawn as a black dashed line has been obtained as the mean of five different runs, where the resolution cut has been gradually increased, $Q_{\mathrm{cut}} = 10, 15, 30, 50$ and 80 GeV. The coloured curves represent the contributions stemming from the different matrix-element final-state multiplicities. Results are shown for three different resolution cuts, namely $Q_{\mathrm{cut}} = 15, 30$ and 80 GeV. It should be noted that the change of the rate predicted by the merging procedure under Q_{cut} variation has been found to be very small, although it is a leading order prediction only. Nevertheless, by varying the separation cut between 10 and 80 GeV, the deviation of the total rate amounts to 2.4% only.

As a first result, consider the p_T distribution of the W^+ boson, presented in fig. 1.19. The distributions become slightly softer for increasing cuts. However, this observable is very stable under variation of Q_{cut} with maximal deviations on the $\pm 5\%$ level only. The shape of the W^+ boson's p_T is already described at LO (using a parton shower only). As it can be seen from the figure, this LO dominance is nicely kept by the SHERPA approach under Q_{cut} variation. There the 1jet (green line) and 2jet (blue line) contributions are reasonably – for the 80 GeV run, even strongly – suppressed with respect to the leading contribution.

In fig. 1.20 the transverse momentum spectrum of the W^+W^- system is depicted. Here, deviations show up, but they do not amount to more than $\pm 20\%$. Thus, the QCD radiation pattern depends only mildly on Q_{cut} (indicated by a vertical dashed-dotted line), which at the same time has been varied by nearly one order of magnitude. For $Q_{\mathrm{cut}} = 15$ GeV the matrix element domain is enhanced with respect to the reference resulting in a harder p_T tail. In contrast by using $Q_{\mathrm{cut}} = 80$ GeV the hard tail of the diboson transverse momentum is underestimated with respect to the reference, since the parton shower attached only to the lowest order matrix element starts to fail in the description of high p_T QCD radiation at $p_T \approx 30$ GeV. At $Q_{\mathrm{cut}} = 80$ GeV a smooth transition is required. The higher order matrix elements then stop the decrease in the p_T prediction.

In previous publications it turned out that differential jet rates most accurately probe the merging algorithm, since they most suitably reflect the interplay of the matrix elements and the parton shower in describing QCD radiation below and above the jet resolution cut. Results obtained with the Run II k_T algorithm using $R = 1$ are shown for the $1 \rightarrow 0$, $2 \rightarrow 1$ and $3 \rightarrow 2$ transition in the left, middle and right panels of fig. 1.21, respectively. The value for the internal cut increases from $Q_{\mathrm{cut}} = 15$ GeV (top) to $Q_{\mathrm{cut}} = 80$ GeV (bottom). Compared with the p_T^{WW} spectra, similar characteristics of deviations from the reference curve appear. However, here, they are moderately larger reaching up to $\pm 30\%$. The dashed dotted vertical line again marks the position of Q_{cut}, which also pictures the separation of the $n$jet from the $n + 1$jet contribution. Small holes visible around the respective separation cuts are due to a mismatch of matrix element and parton shower kinematics. For $Q_{\mathrm{cut}} = 80$ GeV these holes are much more pronounced, reflecting the failure of the parton shower in filling the hard p_T emission phase space appropriately.
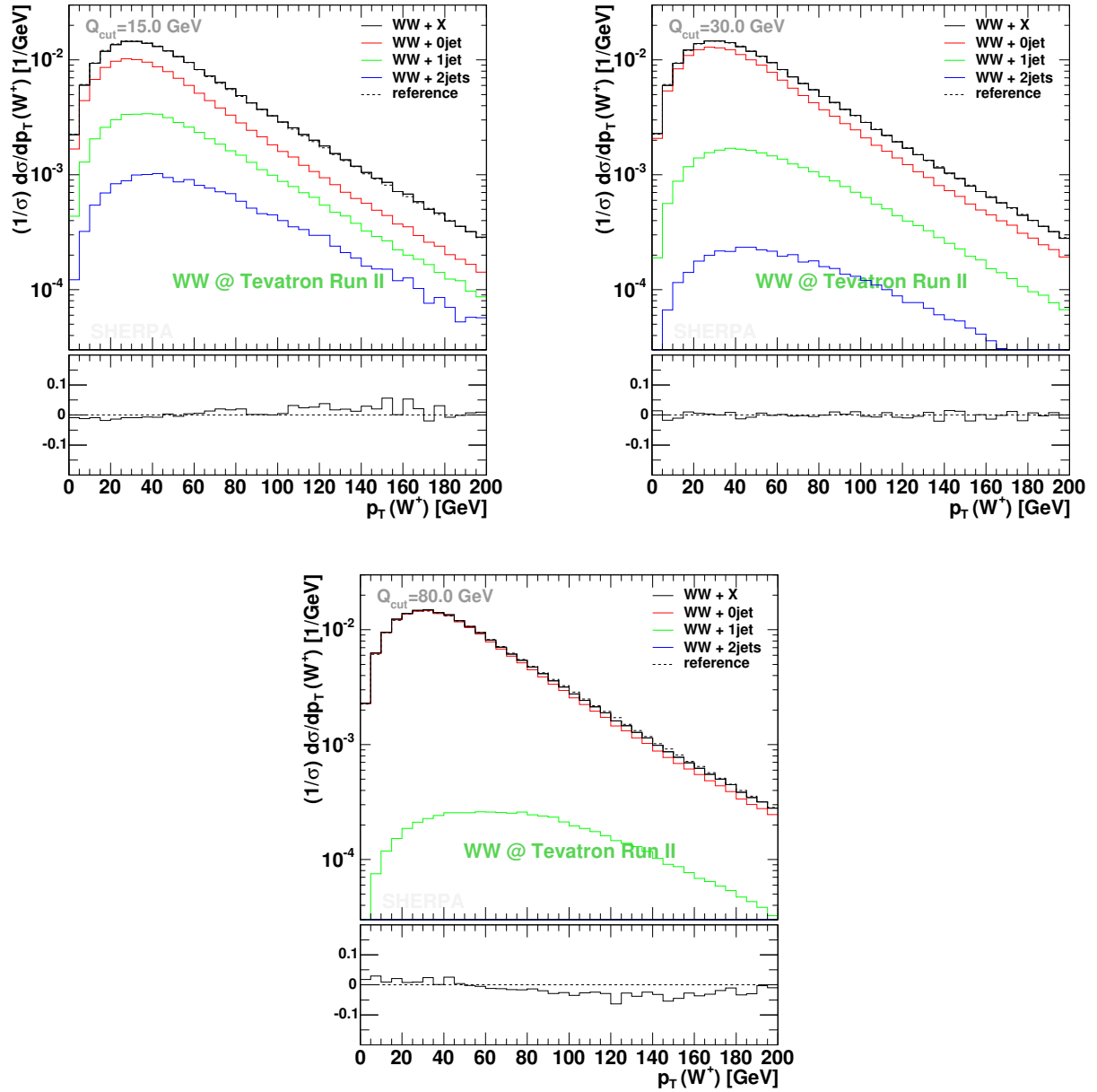
Figure 1.19: The p_T distribution of the W^+ boson and its dependence on Q_{cut}, chosen to be 15, 30 and 80 GeV (from top to bottom). The black solid line shows the SHERPA prediction obtained with $n_{\text{max}} = 2$, the black dashed one is the reference obtained as the mean of different Q_{cut} runs and the coloured lines indicate the different multiplicity contributions. The lower part of the plots exhibits the normalized difference of the prediction with respect to the reference. Cuts and input parameters are specified in the appendices.
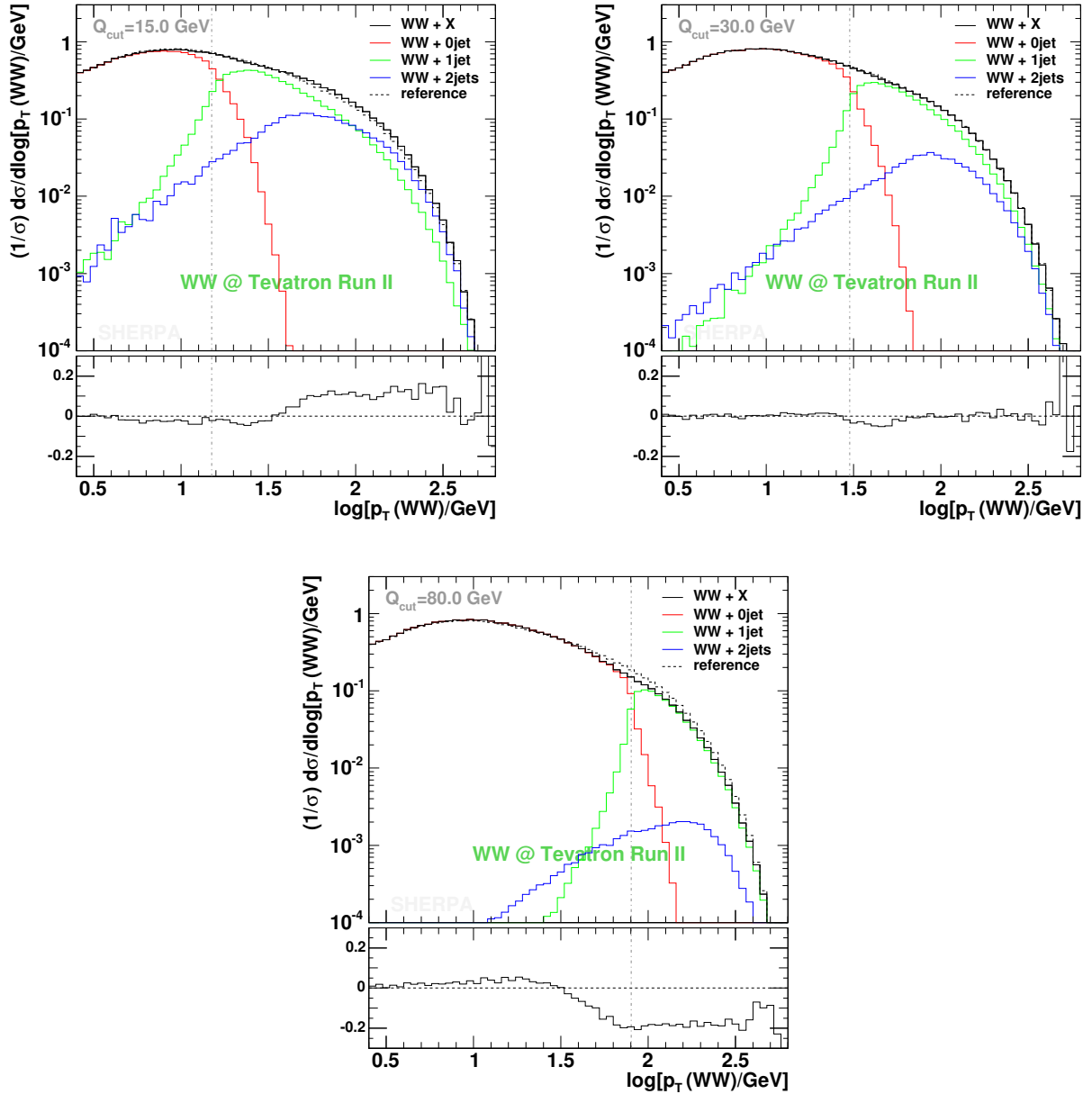
Figure 1.20: The p_T distribution of the W^+W^- system under merging scale variation. The cut indicated through a vertical dashed-dotted line has been chosen as $Q_{\text{cut}} = 15, 30$ and 80 GeV (from top to bottom). The black solid line shows the SHERPA prediction obtained with $n_{\max} = 2$, the black dashed one is the reference obtained as the mean of different Q_{cut} runs and the coloured lines indicate the different multiplicity contributions. The lower part of the plots exhibits the normalized difference of the prediction with respect to the reference. Cuts and input parameters are specified in the appendices.
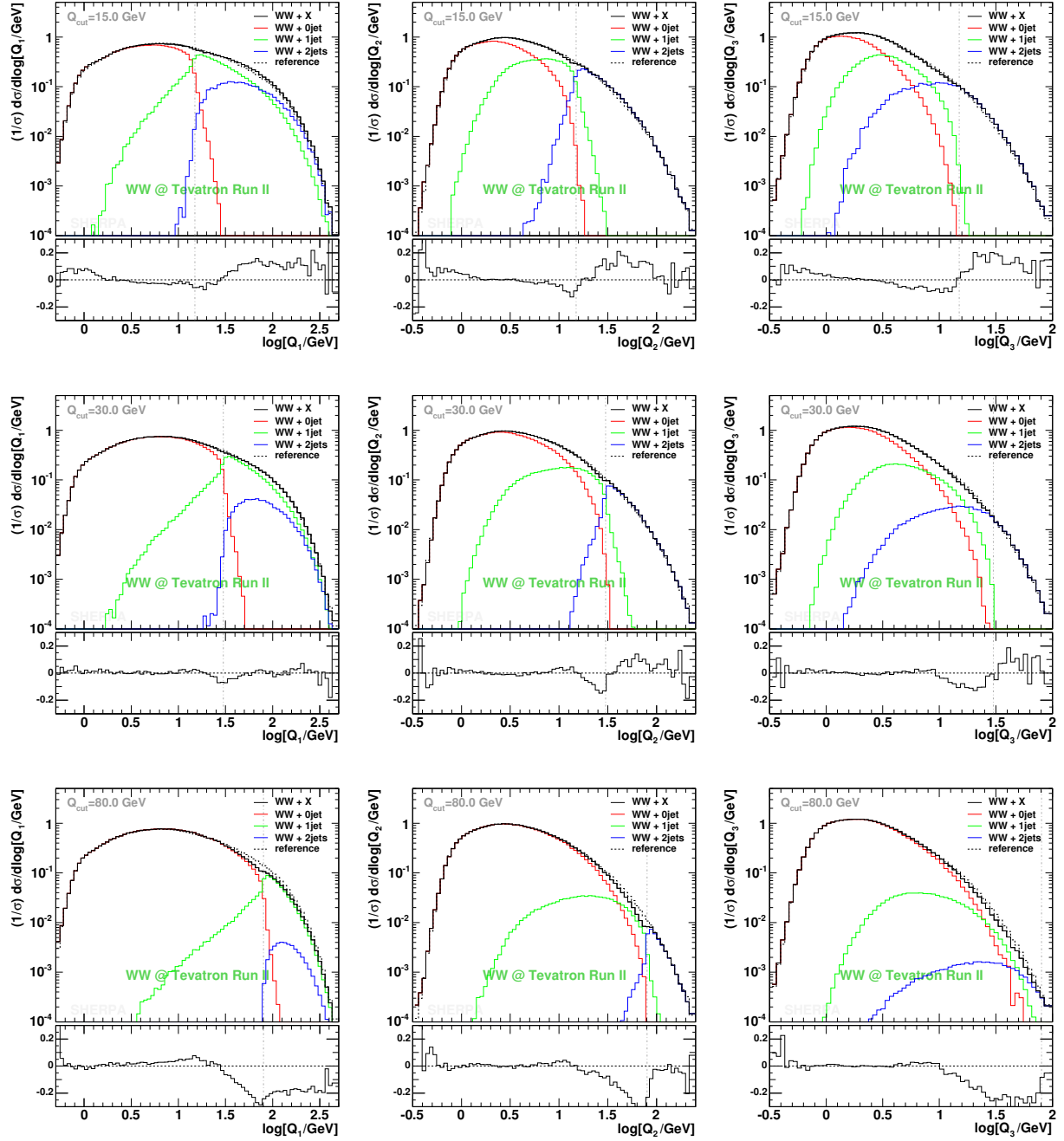
Figure 1.21: Differential $1 \to 0$ jet rate Q_1, $2 \to 1$ jet rate Q_2 and $3 \to 2$ jet rate Q_3 (left to right) for the SHERPA $n_{\mathrm{max}} = 2$ configuration. The cut has been chosen to be 15, 30 and 80 GeV (from top to bottom). The black solid line shows the total result, the black dashed one is the reference obtained as the mean of different Q_{cut} runs and the coloured lines indicate the different multiplicity contributions. The vertical dashed dotted line indicates the separation cut position. The lower part in all plots pictures the normalized difference of the corresponding prediction with respect to the reference. For input parameters and cuts, see apps. B.1 and B.3.
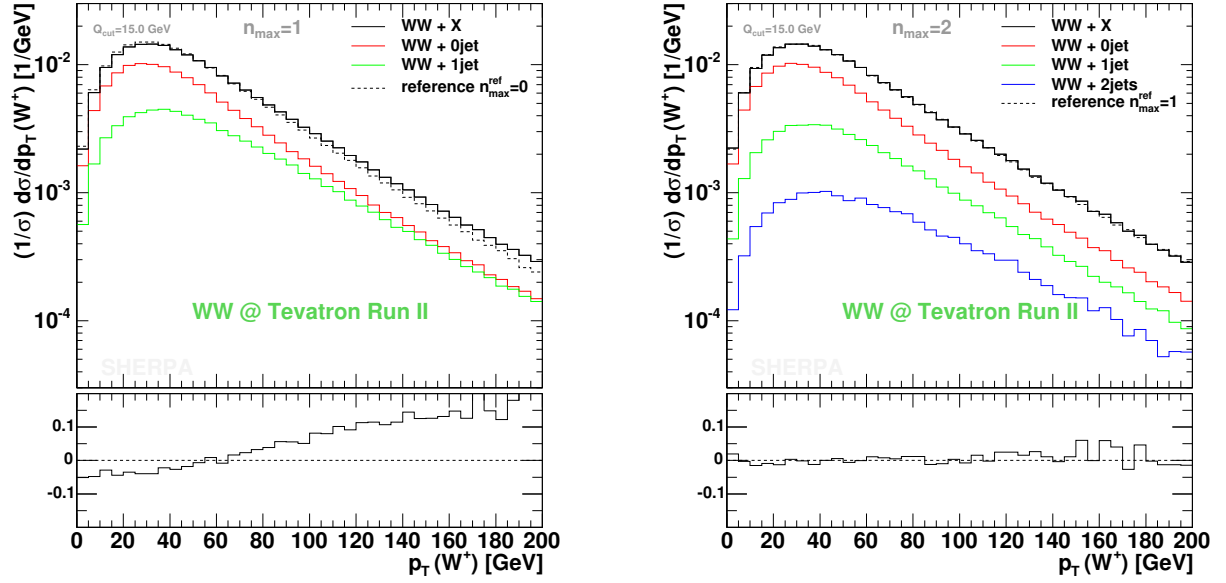
Figure 1.22: The p_T distribution of the W^+ boson in dependence on the variation of the maximal jet number. The comparison is to a (black dashed) reference curve obtained with $n_{max}^{ref} = n_{max} - 1$. The cut has been chosen to be 15 GeV. In both plots the black solid line shows the total result obtained with SHERPA. The coloured lines indicate the different multiplicity contributions. The lower part in both plots visualizes the normalized difference of the corresponding prediction with respect to the reference. For input parameters and cuts, see apps. B.1 and B.3.

Taken together, the deviations found are very moderate; however, in certain phase-space regions they may reach up to 30%. This is satisfactory, since the merging algorithm guarantees Q_{cut} independence on the leading logarithmic accuracy only. The residual dependence of the results on Q_{cut} may be exploited to tune the perturbative part of the Monte Carlo event generator.

1.6.1.2   Impact of the maximal number of included matrix elements

The approach of varying the maximal jet number n_{max} can be exploited to further scrutinize the merging procedure. In all cases considered here, Q_{cut} has been fixed to $Q_{cut} = 15$ GeV. This maximizes the impact of higher order matrix elements. In spite of this, for very inclusive observables, the rates differ very mildly, the change is less than 2%.
In fig. 1.22, once more the transverse momentum distribution of the W^+ gauge boson is presented, illustrating that the treatment of the highest multiplicity matrix elements (for more details cf. [42, 43]) completely compensates for the missing 2jet matrix element in the $n_{max} = 1$ case. The behaviour is almost unaltered when changing from the $n_{max} = 1$ to the $n_{max} = 2$ prediction (cf. the right panel). In contrast, $n_{max} = 0$ yields a considerably softer distribution (cf. the left panel).
Lepton p_T spectra show similar characteristics like the W^+ distribution. However, there are a number of observables, which turned out to be rather stable under the variation of
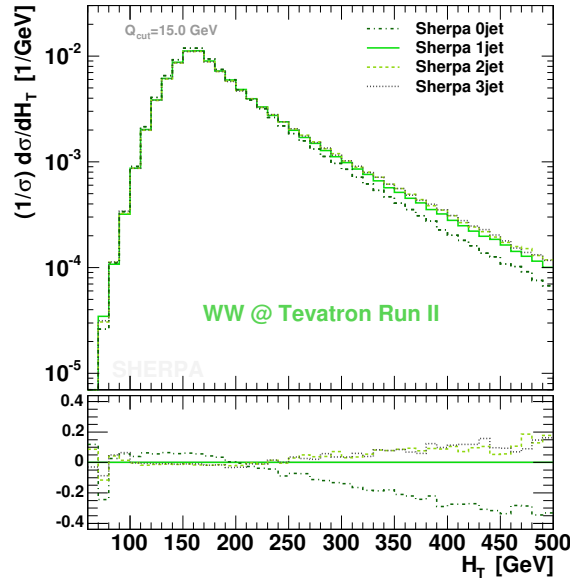
Figure 1.23: The H_T distribution and its dependence on the variation of the maximal jet number. The separation cut has been chosen to be 15 GeV. The green solid line shows the SHERPA prediction obtained with $n_{max} = 1$, the lighter dashed and the grey dotted one stand for the $n_{max} = 2$ and $n_{max} = 3$ prediction, respectively; the darkgreen dashed-dotted curve pictures the pure shower performance of SHERPA starting off with the lowest order matrix element. The lower part of the plot shows the normalized differences with respect to the $n_{max} = 1$ case. For input parameters and cuts, see apps. B.1 and B.3.

n_{max}, such as the pseudo-rapidity spectra of the W^+ boson, the positron and muon or correlations between the leptons, e.g. the $\Delta\phi$ or ΔR distribution. In these cases, deviations turn out to be smaller than $\pm 5\%$ in total, i.e. when considering the change between the pure shower and the inclusive 3jet production performance of SHERPA. Even the pseudo-rapidity spectra of the resolved jets are rather unaffected.

In contrast, three more observables are presented showing a sizeable ($< \pm 30\%$) or even strong ($\approx \pm 100\%$) dependence on the variation of the maximal jet number. The H_T distribution is depicted in fig. 1.23, where throughout this work H_T is defined as the scalar sum of all lepton and jet transverse momenta. The inclusive p_T spectra of associated jets are exhibited in fig. 1.24, where the left and right panel of fig. 1.24 show the spectra of the hardest and the second hardest jet, respectively. Owing to the nature of these three observables to be sensitive on extra jet emissions, predictions – as expected – become harder with the increase of n_{max}. However, a stabilization of the predictions is clearly found with the inclusion of more higher order matrix elements, which describe real QCD emissions.
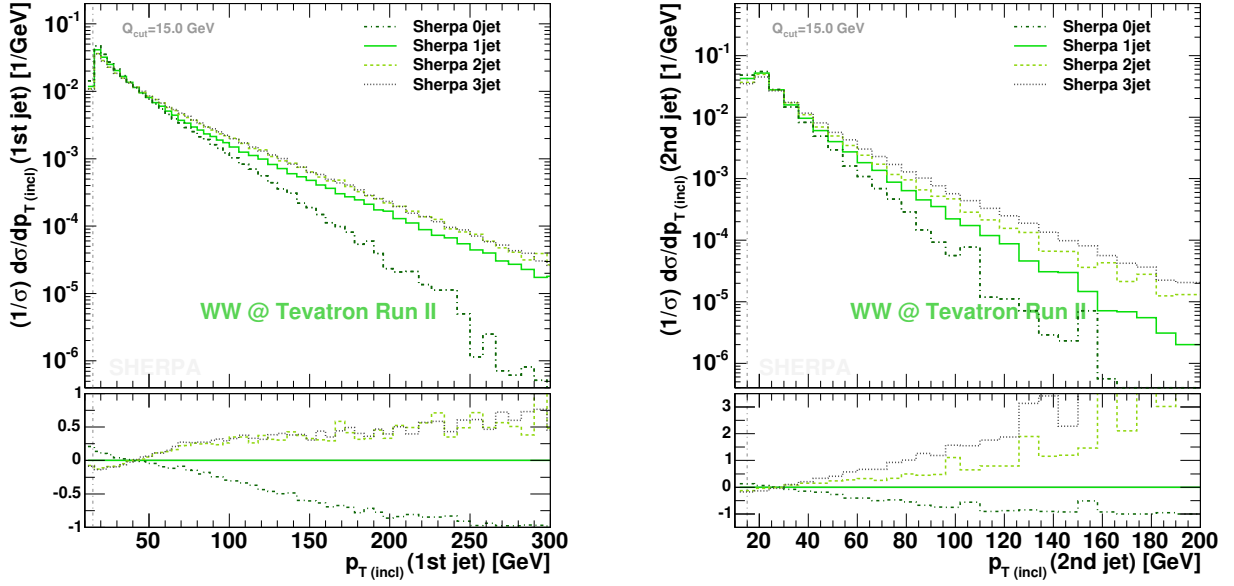
Figure 1.24: SHERPA predictions of the inclusive p_T of the associated jets considered in dependence on the variation of the maximal jet number. The spectra of the hardest and the second hardest jet are depicted in the left and the right panel, respectively. The jet resolution cut has been taken to be 15 GeV. The green solid line shows the result of the $n_{\max} = 1$ sample, the brighter dashed and the grey dotted one stand for the $n_{\max} = 2$ and $n_{\max} = 3$ sample, respectively; the darkgreen dashed-dotted curve depicts the pure shower performance. The lower part of the plot shows the normalized differences with respect to the $n_{\max} = 1$ case. For the jet definition, the Run II k_T algorithm with $R = 0.7$ and $p_T^{\mathrm{jet}} > 15$ GeV has been used. For more details, see apps. B.1 and B.3.

1.6.1.3   Effects of renormalization and factorization scale variations

In the following the impact of renormalization and factorization scale variations is discussed. For the SHERPA merging approach, this variation (also cf. [61]) is performed by multiplying all scales with a constant factor in all coupling constants and PDFs, which are relevant for the matrix element evaluation, the Sudakov weights and for the parton shower evolution.

For this study, the SHERPA samples are produced with $n_{\max} = 1$ and $Q_{\mathrm{cut}} = 15$ GeV. In all figures the green solid line represents SHERPA's default scale choices, whereas the black dashed and the black dotted curve show the outcome for scale multiplications by 0.5 and 2.0, respectively. The total rate as provided by the merging algorithm is again remarkably stable, varying with respect to the default only by $\pm 4.2\%$, thereby increasing for smaller scales.

The transverse momentum distribution of the W^+ boson is investigated in fig. 1.25. Scale variations slightly distort the shape, shifting it towards harder p_T for smaller scales and vice versa. The effect is more pronounced in the H_T distribution, shown in fig. 1.26, and in the transverse momentum distribution of the diboson system, depicted in fig. 1.27.
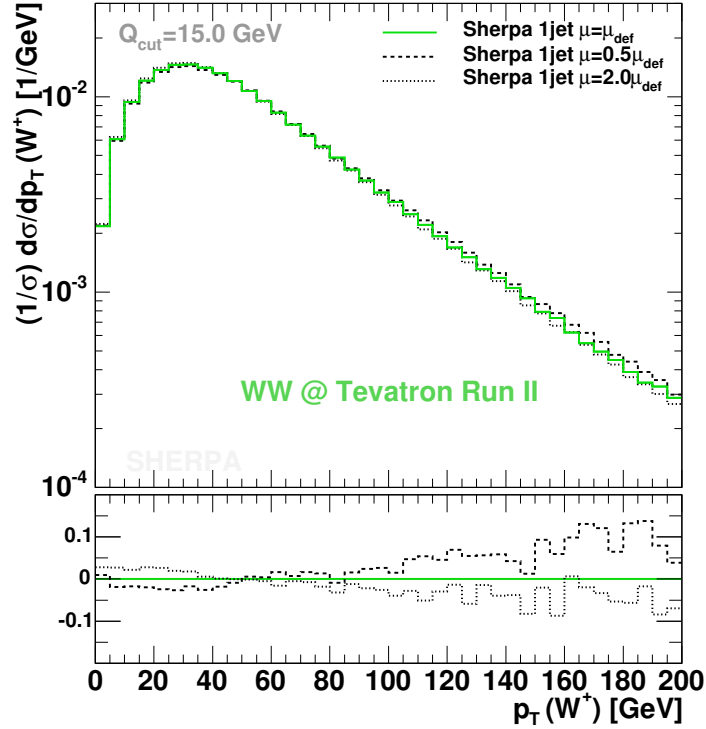
Figure 1.25: The p_T distribution of the W^+ boson under scale variations. All predictions stem from SHERPA with $n_{max} = 1$ and $Q_{cut} = 15$ GeV. The green solid line shows the prediction under default scale choices for the merging procedure. For the black dashed and the black dotted curve, all scales for the coupling constants and PDFs have been multiplied by 0.5 and 2.0, respectively. The lower part of the plot presents the normalized differences with respect to the default choice. Input parameters and cuts are given in apps. B.1 and B.3.

However, the deviations maximally found reach up to ±30%. In contrast to the findings stated so far, jet transverse momentum spectra do not feature shape distortions under scale variations.

The pattern found from these investigations can be explained as follows. The single matrix element contributions – here the 0jet and 1jet contribution – have their own rate and shape dependencies under scale variations. In their interplay these differences transfer to changing the admixture of the single contributions. Hence, shape modifications can appear as soon as different phase-space regions are dominated by a single contribution. This also explains the behaviour found for jet p_Ts. In the case studied here, they are solely described by the 1jet matrix element with the parton shower attached, thus, their different rates cancel out due to normalization and their shapes are not affected.

Taken together, the dependencies found here, together with the ones on Q_{cut} and n_{max}, yield an estimate for the uncertainty related to the SHERPA predictions.
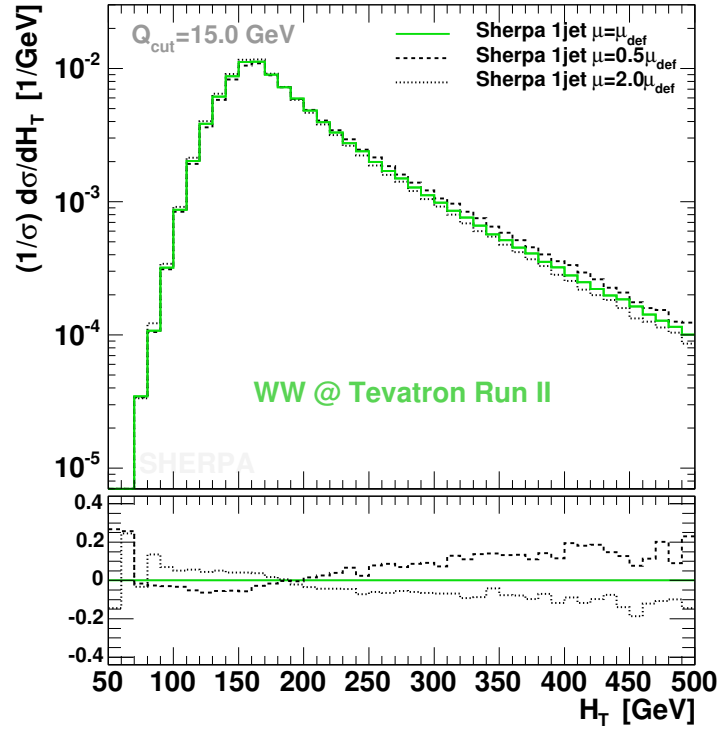
Figure 1.26: The H_T distribution and its dependence on the variation of μ_R and μ_F in the merging prescription. Fixing $n_{max} = 1$ and $Q_{cut} = 15$ GeV, the green solid line shows the prediction under default scale choices. For the black dashed and the black dotted curve, all scales for the coupling constants and PDFs have been multiplied by 0.5 and 2.0, respectively. The lower part of the plot presents the normalized differences with respect to the default choice. Input parameters and analysis cuts are given in apps. B.1 and B.3.

1.6.2   SHERPA comparison with MCFM

In this section, the focus shifts from internal sanity checks to comparisons with a full NLO calculation. For this, the MCFM program [100] has been used. In both, MCFM and SHERPA the CKM matrix has been taken diagonal, and no b quarks are considered in the partonic initial state of the hard process. If not stated otherwise, in MCFM the renormalization and factorization scale have been chosen as $\mu_R = \mu_F = M_W$, according to the choice made in [100]. For more details on the input parameters and setups, see apps. B.1 and B.2. In the following the results of MCFM are confronted with those of SHERPA (using $Q_{cut} = 15$ GeV) obtained at the parton shower level. Furthermore, for this analysis, realistic experimental cuts (cf. app. B.3) have been applied and all distributions have been normalized to one. First the H_T distribution, depicted in fig. 1.28, is considered. Clearly, higher order corrections affect the H_T shape. This is due to two reasons. First of all, the additional QCD radiation may manifest itself as jet(s), which thus contribute to H_T. Otherwise the additional partons still form a system against which the W pair may recoil. Quantitatively,
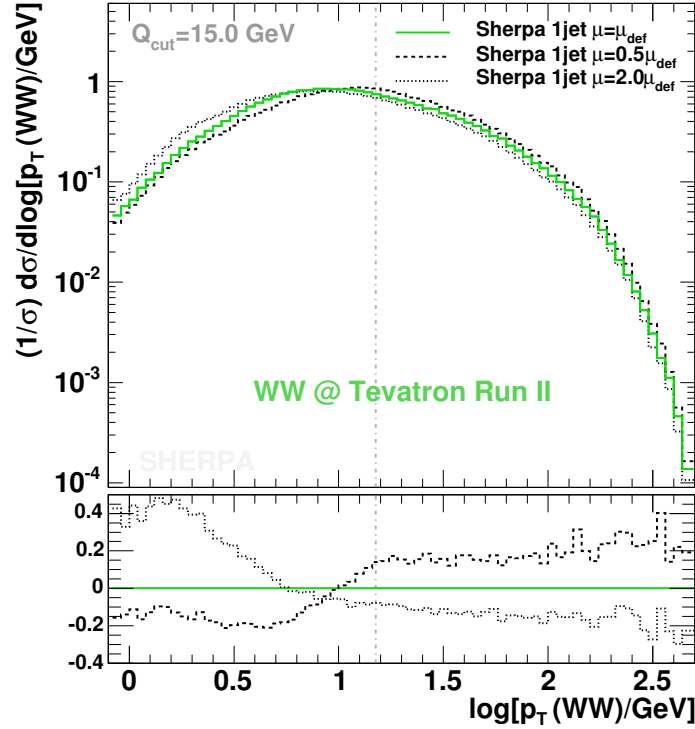
Figure 1.27: The p_T distribution of the W pair under variation of μ_{R} and μ_{F}. Fixing $n_{\max} = 1$ and $Q_{\mathrm{cut}} = 15$ GeV, the green solid line shows the prediction under default scale choices. The black dashed and the black dotted curve is generated when all scales used for the coupling constants and PDFs have been multiplied by 0.5 and 2.0, respectively. The lower part of the plot presents the normalized differences with respect to the default choice. Input parameters (including a primordial k_T smearing) and cuts are given in apps. B.1 and B.3.

the inclusion of NLO results in a shift of the H_T distribution at harder values by up to 20%; in SHERPA this trend is amplified by roughly the same amount. The differences between MCFM and SHERPA, however, are due to the different scale choices in both codes. In MCFM all scales have been fixed to $\mu = M_W$, whereas, forced by the merging procedure, in SHERPA the scales are set dynamically. In view of the scale variation results discussed in the previous section for H_T (cf. fig. 1.26) deviations of this magnitude owing to different scale choices are possible.

The impact of scale variations on the shape of the same observable is quantified in fig. 1.29. This time, however, the SHERPA result with $n_{\max} = 1$ is compared to NLO results obtained from MCFM with scale choices in the range $\mu_{\mathrm{R}} = \mu_{\mathrm{F}} = M_W \ldots 4\, M_W$ and with a LO result taken at $\mu_{\mathrm{R}} = \mu_{\mathrm{F}} = 2M_W$. Obviously, the smaller choice of scale results in the MCFM outcome to be closer to the one of SHERPA. As expected, in comparison to the scale variation results found for SHERPA, the shape uncertainties of the full NLO prediction due to varying the scales are smaller.

In fig. 1.30, H_T is depicted again, this time for the case of exclusive $p\bar{p} \rightarrow e^+\mu^-\nu_e\bar{\nu}_\mu$ production. There, the real part of the NLO correction in MCFM is constrained such that it
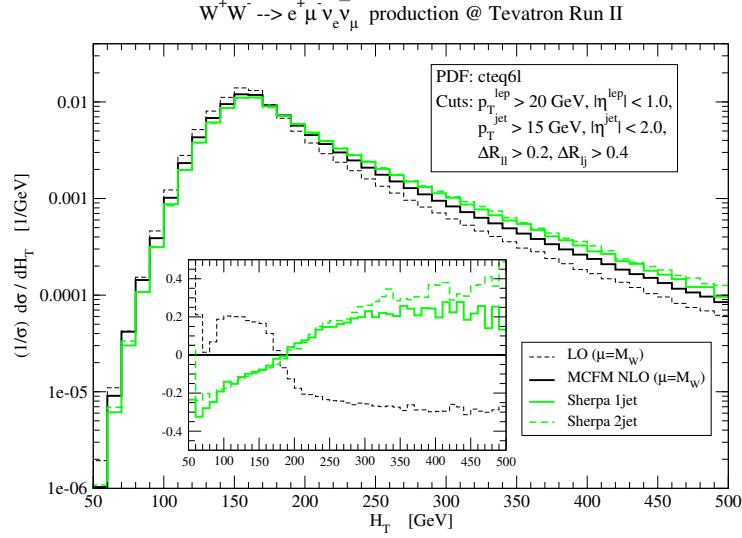
Figure 1.28: Normalized H_T distribution. SHERPA results are shown for $n_{\max} = 1$ (green solid line) and $n_{\max} = 2$ (green dashed line) and compared to the QCD NLO result of MCFM (black solid line). The LO result with the same scale choice is depicted as a thin black dashed line. A difference plot with the MCFM NLO prediction as reference is given within the figure.
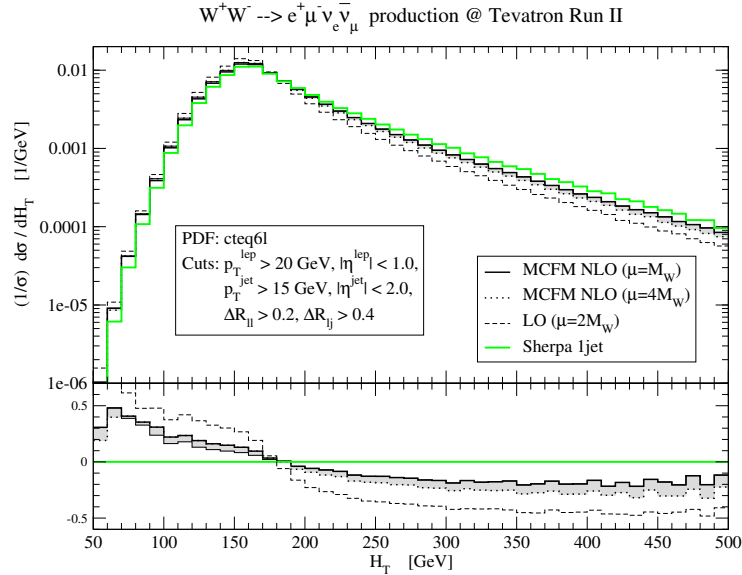
Figure 1.29: Normalized H_T distribution. Here both, the renormalization and factorization scale of the NLO calculation have been varied in the range $\mu_{\mathrm{R}} = \mu_{\mathrm{F}} = M_W \ldots 4\,M_W$, indicated by the shaded area. These MCFM results are compared with the leading order result at $\mu_{\mathrm{R}} = \mu_{\mathrm{F}} = 2\,M_W$ (thin black dashed line) and with the result of SHERPA where $n_{\max} = 1$ (green solid line). The lower part of the plot shows the normalized differences with respect to the SHERPA result.
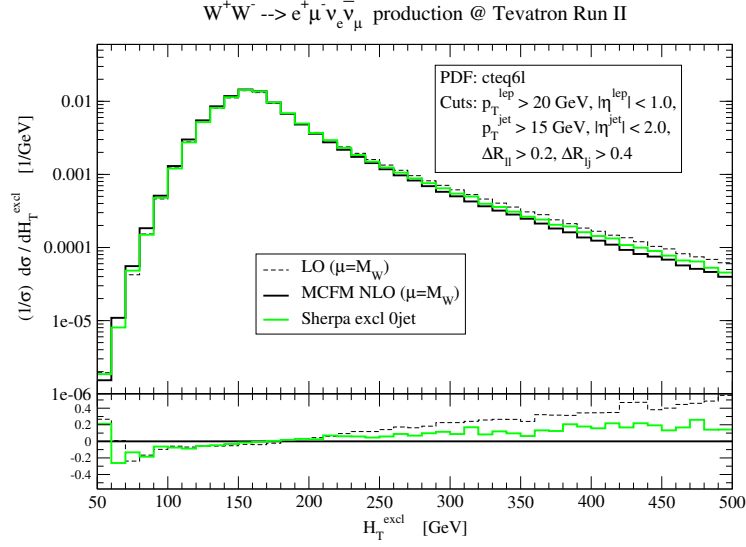
Figure 1.30: Normalized H_T distribution in exclusive $p\bar{p} \to e^+\mu^-\nu_e\bar{\nu}_\mu$ production. The SHERPA result (green solid line) is obtained with $n_{\max} = 0$ and a parton shower constrained not to produce any extra jets. This result is compared with the MCFM result at NLO in α_s (black solid line) and with the LO result (thin black dashed line). The latter two are taken for the default scale choices. The lower part of the plot shows the normalized differences w.r.t. the NLO result obtained from MCFM.
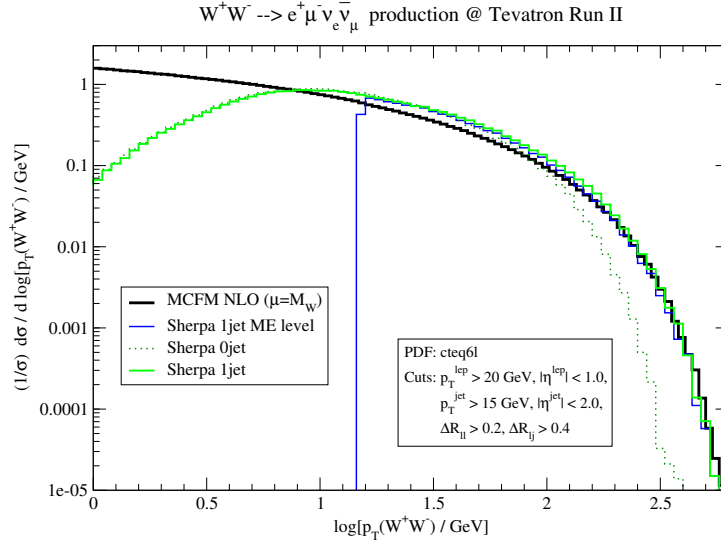
Figure 1.31: Normalized p_T distribution of the W pair. The MCFM result at $\mu_{\mathrm{R}} = \mu_{\mathrm{F}} = M_W$ (black line) is contrasted with the predictions made by SHERPA both at the matrix element level (blue line) and at the parton shower level with $n_{\max} = 0$ (darkgreen dotted line) and $n_{\max} = 1$ (green solid line). A primordial k_T smearing has been used to obtain the SHERPA shower results.
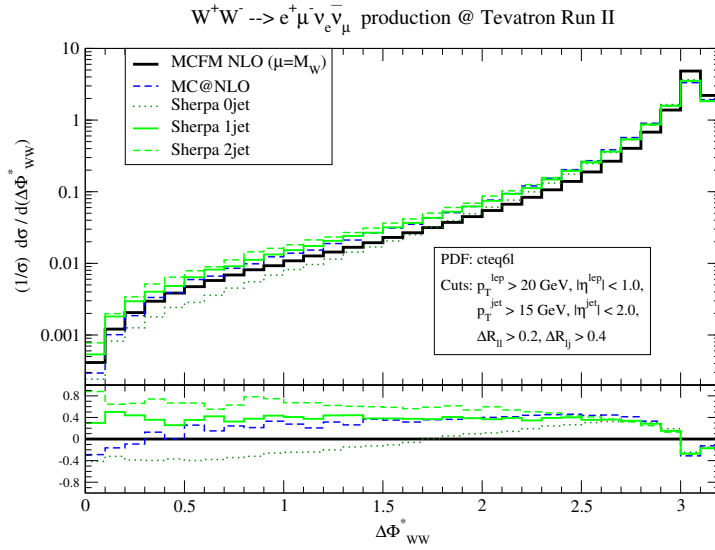
Figure 1.32: Normalized $\Delta\Phi^{\star}_{WW}$ distribution of the W boson system. The `MCFM` result (black line) is contrasted with results from SHERPA at the parton shower level with $n_{\max} = 0$ (darkgreen dotted line), $n_{\max} = 1$ (green solid line) and $n_{\max} = 2$ (green dashed line). Again a primordial k_T smearing has been used. Additionally, the blue dashed curve represents a prediction obtained with `MC@NLO`. The lower part of the plot shows the normalized differences with respect to the result of `MCFM`.

does not produce an extra jet (for jet definition, see app. B.3). In SHERPA the 0jet matrix element with the parton shower attached is considered exclusively, i.e. the parton shower is now forced not to produce any jet at all. In this case, the higher order corrections lead to a softer H_T distribution compared to the leading order prediction, and the results of `MCFM` and SHERPA show the same deviations as before (cf. fig. 1.28).

The effect of QCD radiation is best observed in the p_T distribution of the W pair, depicted in fig. 1.31. Clearly, without any radiation, the p_T of the W pair is exactly zero, and only the emission of partons leads to a recoil of the diboson system. In the NLO calculation of `MCFM`, however, the spectrum is therefore described at lowest order, in this particular case taken at $\mu_{\mathrm{R}} = \mu_{\mathrm{F}} = M_W$. In contrast, in the SHERPA matrix element result, subjected to the explicit jet cut, Sudakov form factors and α_s reweighting are applied with a variable scale choice, explaining the differences between the two matrix-element type results in this figure. Contrasting this with the parton shower approach, it is clear that parton emission through the shower alone is not sufficient to generate sizeable p_T of the W pair in the hard region. For this, the corresponding matrix element has to be employed, leading to a very good agreement with the `MCFM` outcome in the high p_T tail of the distribution. In the soft regime the result of the bare `MCFM` matrix element is unphysical. Due to the cascade emission of soft and collinear partons, SHERPA accounts for resummation effects, which clearly yield the depopulation of the softest p_T region.

Another way to look at the effects of QCD radiation is to consider the relative angle
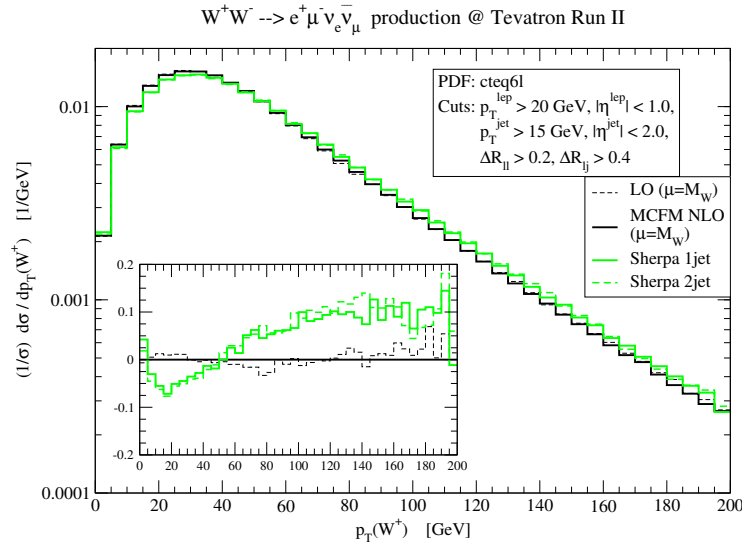
Figure 1.33: Normalized transverse momentum distribution of the W^+ boson. The results of SHERPA for $n_{\max} = 1$ (green solid line) and for $n_{\max} = 2$ (green dashed line) are compared with the QCD NLO result obtained by MCFM (black solid line) and with the LO result (thin black dashed line) for the default scale choices, i.e. $\mu_{\mathrm{R}} = \mu_{\mathrm{F}} = M_W$. Within the plot the normalized differences with respect to the NLO result of MCFM are given.

between the two W bosons, [6] see fig. 1.32. Of course, when they decay into leptons plus neutrinos this is not an experimental observable, on the generator level, however, it is very nice to visualize the effect of QCD radiation in this way. Without any QCD radiation, the two Ws would be oriented back-to-back, at $\Delta\Phi^\star_{WW} = \pi$. Including QCD radiation, this washes out, as depicted in the figure. Again, resummation effects alter the result of the matrix element alone by decreasing the amount of softest radiation, this time corresponding to the back-to-back region around $\Delta\Phi^\star \approx \pi$. The effect of high p_T radiation can be clearly seen for small $\Delta\Phi^\star$ by comparing the different $n_{\max}$ predictions of SHERPA. The larger $n_{\max}$ is chosen, the harder the prediction for small $\Delta\Phi^\star$. On the other hand to better value the influence of the parton shower a prediction made by MC@NLO (see app. B.2) has been included. For a wide region of $\Delta\Phi^\star$, it well agrees with the SHERPA result for $n_{\max} = 1$.

Figs. 1.33 and 1.34 exhibit the transverse momentum distributions of the W^+ and of the e^+ produced in its decay, respectively. Only mild deviations less than 10% between MCFM and SHERPA are found, which again can be traced back to different scale choices in both approaches. These differences recur as and, therefore, explain part of the deviations found in the H_T spectrum, cf. fig. 1.28. As expected, the inclusion of the 2jet contribution in SHERPA gives no further alterations of the $n_{\max} = 1$ result. Of course, the different radiation patterns also have some minor effects on the η distribution of the W^+ depicted in fig. 1.35. In the $\Delta R_{e\mu}$ distribution presented in fig. 1.36, the NLO result of MCFM and the

---

[6]The angle is measured in the frame, where the W^+W^- system rests at the beam axis, i.e. the diboson system is corrected on its initial $\hat{z}$ boost.
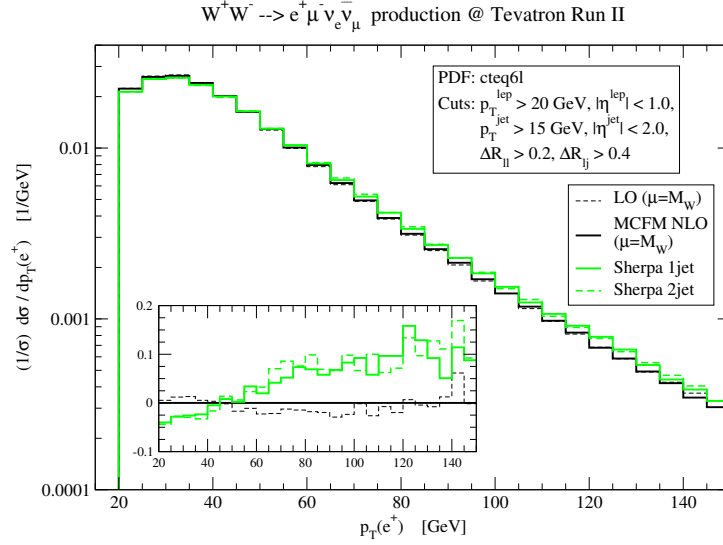
Figure 1.34: Normalized transverse momentum distribution of the e^+ produced in the decay of the W^+. The results of SHERPA for $n_{max} = 1$ (green solid line) and for $n_{max} = 2$ (green dashed line) are confronted with the QCD NLO result obtained by MCFM (black solid line) and with the LO result (thin black dashed line). For the latter two, the scales are again fixed according to the default choices, i.e. $\mu_R = \mu_F = M_W$. Within the plot the normalized differences w.r.t. the NLO result of MCFM are shown.
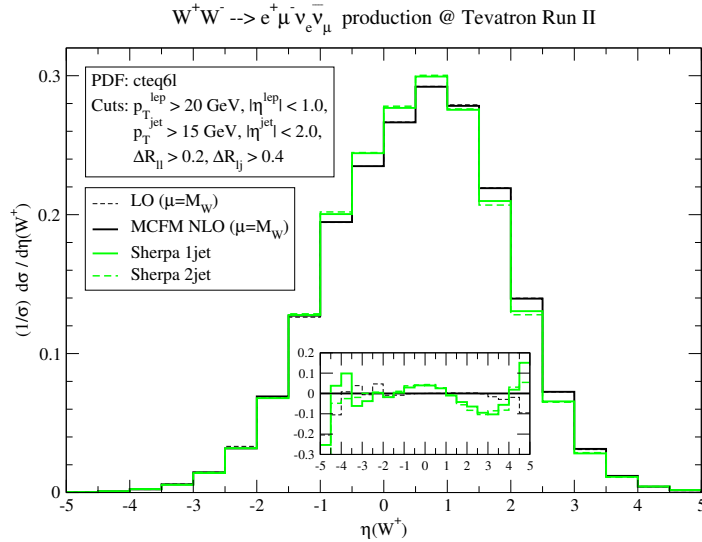
Figure 1.35: Normalized η distribution of the W^+ boson. The SHERPA results for $n_{max} = 1$ (green solid line) and $n_{max} = 2$ (green dashed line) are confronted with those of MCFM (black solid line) and with the LO result (thin black dashed line). Again, in the latter two the scales are chosen as $\mu_R = \mu_F = M_W$. The normalized differences with respect to the NLO result of MCFM are also shown.
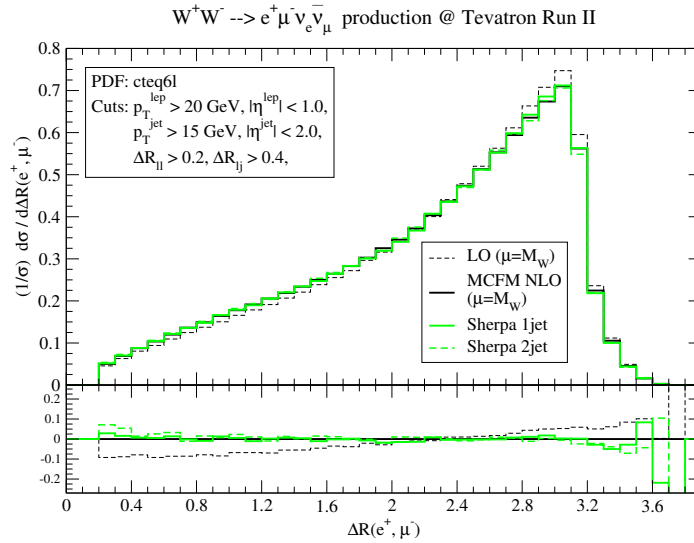
Figure 1.36: Normalized ΔR distribution between the two charged leptons, the positron and the muon, emerging from the W decays. SHERPA results for $n_{\mathrm{max}} = 1$ (green solid line) and $n_{\mathrm{max}} = 2$ (green dashed line) are compared to those predicted by MCFM (black solid line). The LO result with the same scale choice, is shown as a black dashed line. The lower part of the plot shows the normalized differences with respect to the NLO result of MCFM.

parton shower level results of SHERPA are in nearly perfect agreement with each other. Higher order effects tend to change the shape of the LO prediction with respect to the NLO one by roughly 10%. The interesting observation here is that this change is seemingly not related to the transverse hardness of a jet system against which the W pair recoils. This gives rise to the assumption that the change with respect to the LO result is due to some altered spin structure in the $2 \to 5$ matrix element.

1.6.3   Comparison with other event generators

In this section a comparison of SHERPA with other hadron level event generators, in particular PYTHIA and MC@NLO will be discussed. Details on how their respective samples have been produced can be found in the apps. B.1 and B.2. The SHERPA samples have been generated with $n_{\mathrm{max}} = 1$ and $Q_{\mathrm{cut}} = 15$ GeV. The comparison is again on inclusive distributions – normalized to one – under the influence of realistic experimental cuts, for details see app. B.3.

1.6.3.1   Comparison of the QCD activity

As before, the starting point is the discussion of the radiation activity predicted by the various codes. In fig. 1.37, results for the H_T observable obtained from PYTHIA, MC@NLO and SHERPA are displayed. The predictions of the former two codes nicely agree with each other. Similar to the SHERPA MCFM comparison, SHERPA again predicts a slightly harder
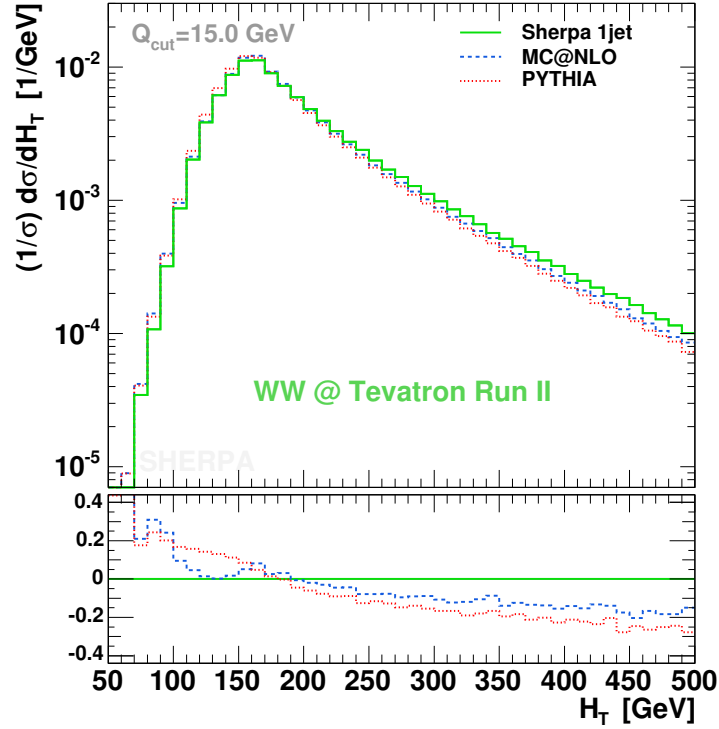
Figure 1.37: Normalized H_T distribution obtained from PYTHIA (red dotted line), MC@NLO (blue dashed line) and SHERPA (green solid line). For the generation of the SHERPA sample, $n_{\max} = 1$ and $Q_{\mathrm{cut}} = 15$ GeV have been chosen. The lower part of the plot exhibits the normalized differences with respect to the SHERPA prediction. Input parameters and the employed cuts are specified in the apps. B.1 and B.3.

spectrum, with relative deviations of up to 20%.

Closer inspection of the reason for the differences in the H_T spectrum reveals that the agreement of PYTHIA and MC@NLO is presumably a little bit accidental. A first hint into that direction can be read off fig. 1.38, where the p_T spectrum of the W pair is displayed. In the region of low p_T (up to 100 GeV), the results of MC@NLO and SHERPA are in fairly good agreement,[7] and sizeable differences larger than 10% appear only for $p_T > 100$ GeV. In contrast, the PYTHIA result for this observable shows a significant enhancement of the low p_T region and stays well below the other predictions for $p_T > 10$ GeV. This comparison of the three differential cross sections clearly underlines that the three codes differ in their description of the QCD emissions.

Fig. 1.39 depicts the norm of the scalar difference of the transverse momenta of the W^+ and W^- gauge boson, $|p_T^{W^+} - p_T^{W^-}|$. This observable is sensitive to higher order effects, since at LO it merely has a delta peak at $p_T = 0$ GeV. Again, the hardest prediction is delivered by SHERPA with $n_{\max} = 1$, results from MC@NLO, PYTHIA, and the pure shower performance of SHERPA are increasingly softer. For $|\Delta p_T| > 60$ GeV, this observable seems to depend more and more on the quality of modelling the hardest emission, which

---

[7]Apart from the very soft region, where the difference is due to parton shower cutoff effects in HERWIG.
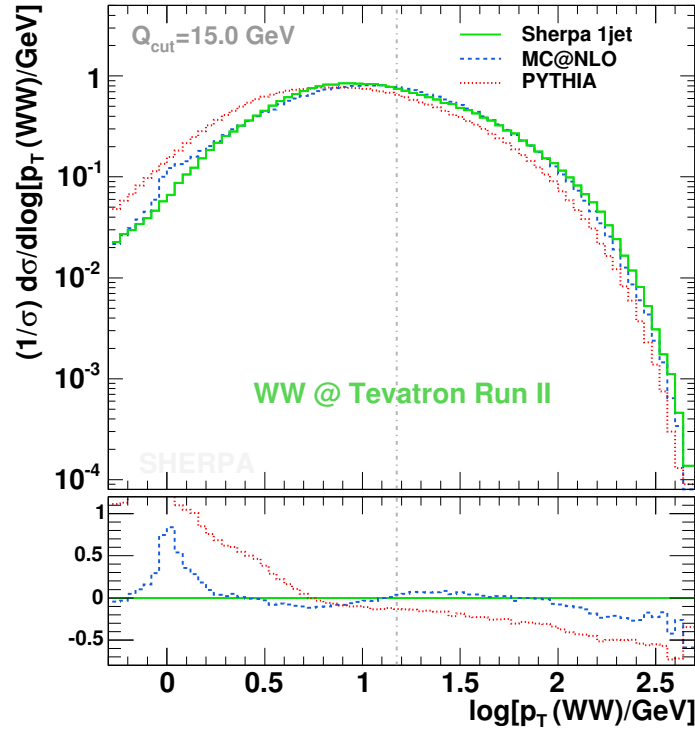
Figure 1.38: Normalized p_T distribution of the W^+W^- system. Results from PYTHIA (red dotted line), MC@NLO (blue dashed line) and SHERPA (green solid line) are compared. For the generation of the latter, $n_{max} = 1$ and $Q_{cut} = 15$ GeV have been chosen. The lower part of the plot presents the normalized differences with respect to the SHERPA prediction. Input parameters (including a primordial k_T smearing) and the employed cuts are specified in the apps. B.1 and B.3.

is intrinsically better described by MC@NLO and by SHERPA with $n_{max} = 1$. The fact that the PYTHIA shower performs better than the pure SHERPA shower for high p_T differences can be traced back to the choice of starting scale for the shower evolution, which is either $s_{p\bar{p}}$ (PYTHIA) or s_{WW} (SHERPA).

In fact, differences appear in the p_T distributions of the hardest two jets, see fig. 1.40. The upper part of this figure depicts the transverse momentum spectrum of the hardest jet. Surprisingly, although MC@NLO contains a matrix element for the emission of an extra jet, its p_T distribution is considerably softer (by up to 40%) than the result of SHERPA generated with $n_{max} = 1$. This trend is greatly amplified when going to the spectrum of the second hardest jet. There, clear shape differences of the order of a factor 2 between the SHERPA 1jet sample and MC@NLO show up for $p_T \approx 180$ GeV. The surprise according to this figure is that PYTHIA and SHERPA using $n_{max} = 1$ almost agree on the p_T distribution of the second jet, although they were different for the hardest jet. At that point it should be noted that the second jet in both cases, PYTHIA and SHERPA with $n_{max} = 1$, is produced by the parton shower only. Given the drastically larger shower start scale of PYTHIA, it seems plausible to achieve to some extent a compensation for the intrinsic
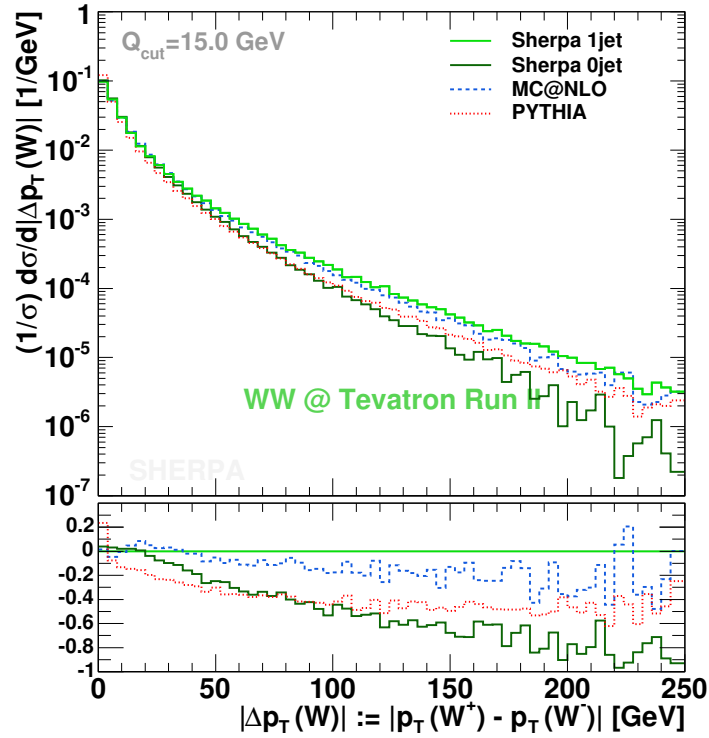
Figure 1.39: Difference of the scalar transverse momenta of the two W bosons, $|p_T^{W^+} - p_T^{W^-}|$. The predictions compared are: PYTHIA given as a red dotted curve, MC@NLO depicted by the blue dashed line and SHERPA in inclusive 1jet production at $Q_{\mathrm{cut}} = 15$ GeV drawn as a green solid line as well as SHERPA in pure shower performance shown as a darkgreen solid line. The lower part of the plot shows the normalized differences with respect to the SHERPA prediction with $n_{\max} = 1$. Input parameters and the employed cuts are summarized in the apps. B.1 and B.3.

parton shower deficiencies in filling the hard emission phase space.[8] However, in the very moment, SHERPA events are generated with appropriate matrix elements, i.e. with $n_{\max} = 2$, this distribution is dramatically different for the three codes with deviations larger than a factor 2 for $p_T \approx 120$ GeV.

Taken together, these findings hint that the three codes differ in their modelling of the QCD activity, especially in those of the hardest QCD emission. For MC@NLO and SHERPA the latter can be traced back to the different ansatz in including the matrix element for this emission, where again different scale choices may trigger effects on the 20% level.

1.6.3.2 Comparison of lepton observables

Finally, the leptons in the final state as described by the three event generators PYTHIA, MC@NLO and SHERPA will be investigated. There, some significant differences appear between SHERPA and PYTHIA on the one hand, and MC@NLO on the other hand. These

---

[8]PYTHIA's ability to account for harder second jets with respect to MC@NLO is a hint for the similarity of their H_T predictions.
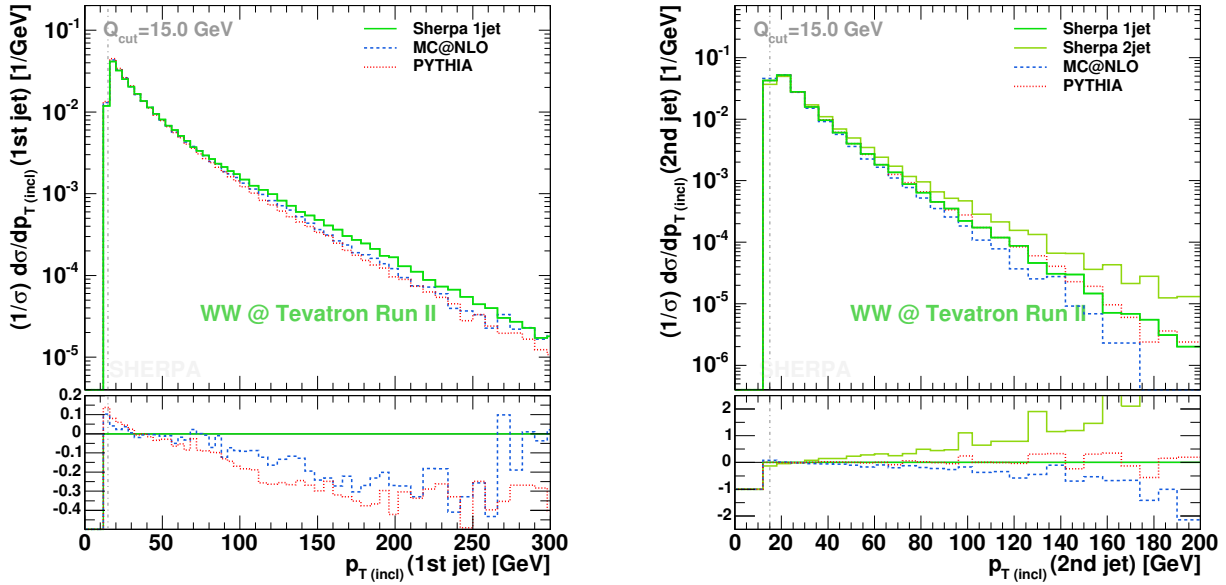
Figure 1.40: Transverse momentum distributions of the associated jets, in the left panel, the inclusive p_T of the hardest jet is depicted, whereas in the right panel that one of the second hardest jet is displayed. Again, results from PYTHIA are given by the red dotted lines, MC@NLO results are represented as blue dashed lines and SHERPA results are the green solid lines. For the generation of the latter, $n_{\max} = 1$ and $Q_{\mathrm{cut}} = 15$ GeV have been used. The lightgreen solid line in the right panel corresponds to the SHERPA result obtained with $n_{\max} = 2$. The lower part of both plots shows the normalized differences with respect to the SHERPA $n_{\max} = 1$ performance. The input parameters and the employed cuts are summarized in the apps. B.1 and B.3.

differences are due to the fact that at the moment spin correlations of the W decay products are not implemented in MC@NLO.[9] To validate that effects are indeed due to the lack of spin correlations, SHERPA samples have been prepared, where these correlations are artificially switched off. Furthermore, in order to quantify these effects without any bias, results have been obtained without the application of any lepton and jet cuts.

The impact of the lack of spin correlations already becomes visible in one-particle observables, such as the p_T or the η spectrum of the positron produced in the W^+ decay. These are shown in figs. 1.41 and 1.42, respectively. Confronting the two methods with each other, which correctly respect spin correlations, for the transverse momentum distribution of the e^+, the following pattern is revealed. Due to the consistent inclusion of higher order tree-level matrix elements, the SHERPA $n_{\max} = 1$ setup produces a considerably harder spectrum than PYTHIA. In contrast, the distributions with no spin correlations both result in an even harder high p_T tail. They agree quite well up to $p_T = 60$ GeV, hence, this coincidence may be assigned to the lack of spin correlations in the gauge boson decays. Above that region, the MC@NLO spectrum again becomes softer with respect to the SHERPA prediction where the spin correlations have been eliminated. The fact that

---

[9]Meanwhile, this weakness has been cured by the authors of MC@NLO who have prepared new versions of their code including spin correlations [35].
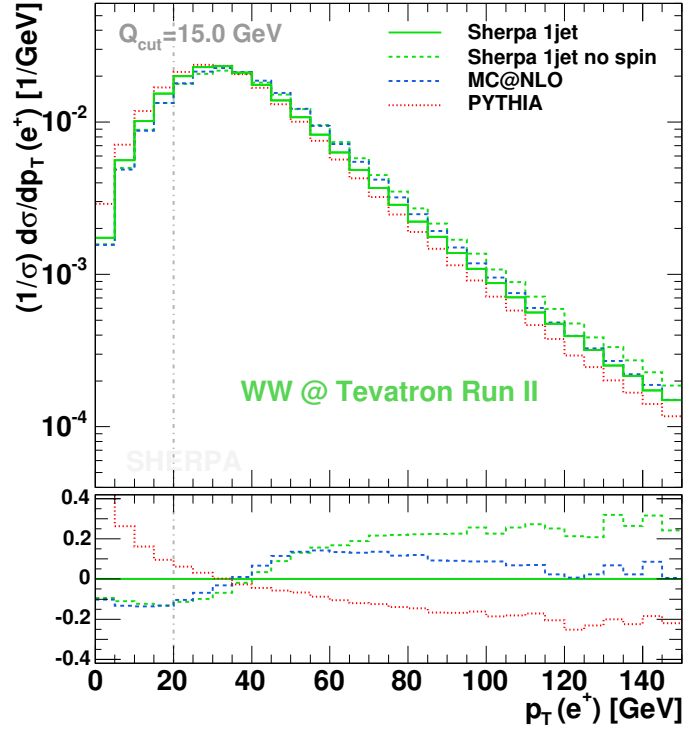
Figure 1.41: Normalized p_T spectrum of the positron. Results of PYTHIA (red dotted line) and SHERPA (green solid line) including spin correlations are confronted with those obtained from MC@NLO (blue dashed line) and with results from SHERPA, where spin correlations have been switched off (green dashed line). All predictions are generated without the use of cuts. The vertical dashed-dotted line is added to indicate the position of the usually employed lepton p_T cut. For input parameters, see app. B.1. The lower part of the plot shows the normalized differences with respect to the SHERPA prediction including spin correlations.

all four predicted distributions alter in their shape is not solely triggered by the different spin correlation treatments, again, the different descriptions of QCD radiation clearly contribute to the deviations found.

In contrast, a simpler pattern is found for the aforementioned η distribution of the e^+. The results of PYTHIA and SHERPA with spin correlations on the one hand and of MC@NLO and SHERPA without spin correlations on the other hand show perfect agreement. Differences between the two spin correlation treatments may, thereby, easily reach up to 40%. The influence of spin correlations can also be seen in observables based on two particle correlations. As two illustrative examples take the $\Delta\phi$ and the ΔR distribution of the e^+ and the μ^- produced in the decay of the two W bosons. Again, the corresponding spectra, which have been exhibited in figs. 1.43 and 1.44, differ significantly in shape depending on whether spin correlations are taken into account or not.

The discussion of the impact of spin correlations is completed by exploring the influence of the application of experimental cuts (cf. app. B.3) on the shape of certain spectra. It is clear that superimposing specific jet and lepton cuts strongly affects the event sample.

Figure 1.42: Normalized η spectrum of the positron. Results of PYTHIA (red dotted line) and SHERPA (green solid line) including spin correlations are compared with those obtained from MC@NLO (blue dashed line) and with results from SHERPA, where spin correlations have been switched off (green dashed line). All predictions are generated without any restriction. The vertical dashed-dotted lines are added to indicate the position of the usually employed lepton η cuts. For input parameters, see app. B.1. The lower part of the plot shows the normalized differences with respect to the SHERPA prediction including spin correlations.

Here, the cuts are mainly on the η and the p_T of the leptons. In turn their distributions alter. The characteristics found for the cutfree case are not substantially changed by the applied cuts and by the renormalization of the spectra according to these given cuts indicated by the vertical lines in the figs. 1.41 and 1.42. More interestingly, however, these distributions drive alterations to secondary observables. In the two-particle correlations mentioned before, the effects already present without applying cuts are enforced. The slopes of the $\Delta\phi$ distributions increase, amplifying the difference between both sets of predictions, the ones with and without spin correlations. The main change in the ΔR spectrum is an additional deviation between 0.2 (the cut) and 2.0, such that now the no-spin-correlation results are roughly 20% above the other ones. The case is different for the pseudo-rapidity distribution of the W^+ boson. Without the application of cuts one starts off distributions that agree on the 10% level. This is severely changed by the introduction of the cuts, see the bottom panel of fig. 1.45. In contrast to the aforementioned two-particle correlations, here the predictions without spin correlations are well separated from the other ones only after the application of the cuts. As a last example, consider the
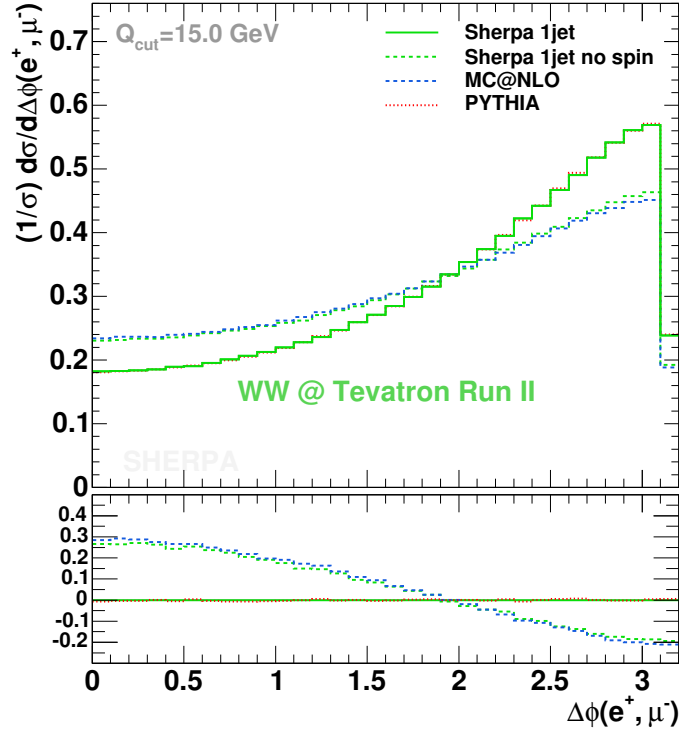
Figure 1.43: Normalized $\Delta\phi_{e\mu}$ distribution. Results of PYTHIA (red dotted line) and SHERPA (green solid line) including spin correlations are compared with those obtained from MC@NLO (blue dashed line) and with results from SHERPA, where spin correlations have been switched off (green dashed line). All predictions are obtained without the use of cuts. For input parameters, see app. B.1. The lower part of the plot shows the normalized differences with respect to the SHERPA prediction including spin correlations.

transverse momentum distribution of the W^+ boson. Both types of predictions stemming from uncutted (top left panel) and from samples analysed with cuts (top right) are pictured in fig. 1.45. The inclusion of cuts apparently brings MC@NLO and SHERPA including the full correlations into good agreement, but this clearly happened accidentally.

To summarize, the examples shown here, clearly hint that the superposition of spin correlations (or their absence) together with cuts triggers sizeable effects in both types of observables, such that have already shown deviations in the absence of cuts and, more crucially, such that have not. In specific cases, such as the p_T spectrum of the W^+, this may possibly lead to misinterpretations of the results.

1.6.4   Summary of the study

In this work, the merging procedure of combining multiparticle tree-level matrix elements with the parton showers as implemented in SHERPA has been further validated; this time, the case of W pair production at Tevatron energies has been considered. First, it has been shown that the results obtained with SHERPA are widely independent of specific
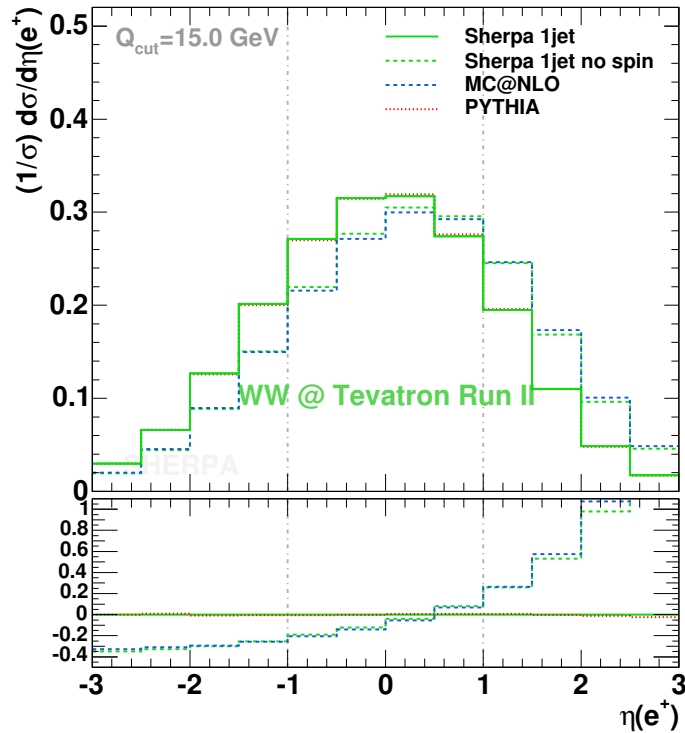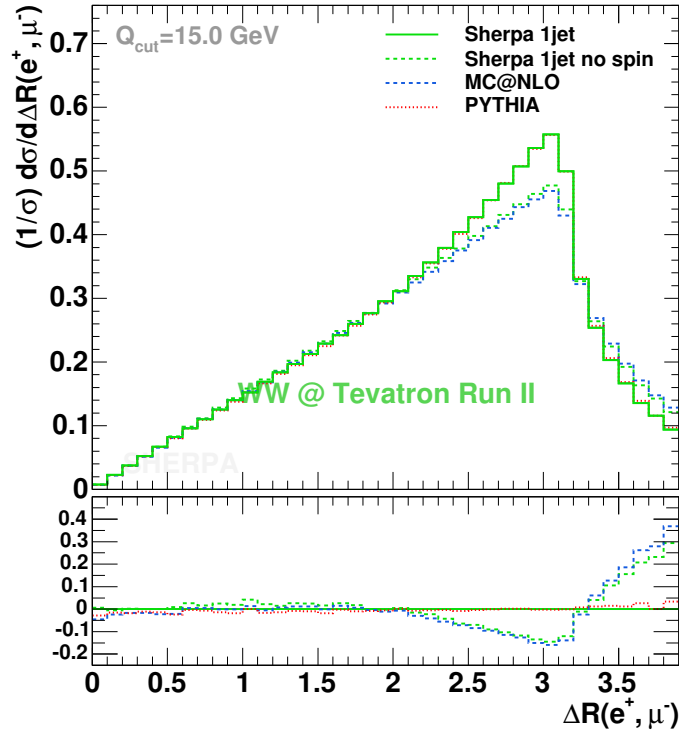
Figure 1.44: Normalized $\Delta R_{e\mu}$ distribution. Results of PYTHIA (red dotted line) and SHERPA (green solid line) including spin correlations are compared with those obtained from MC@NLO (blue dashed line) and with results from SHERPA, where spin correlations have been eliminated (green dashed line). All predictions are obtained without the use of cuts. For input parameters, see app. B.1. The lower part of the plot shows the normalized differences with respect to the SHERPA prediction including spin correlations.

merging-procedure details such as the choice of the merging scale and, for sufficiently inclusive observables, the number of extra jets covered by the tree-level matrix elements. In addition, it has been shown that the specific form of the spectra produced by SHERPA is nearly independent – with deviations less than 20% – of the choice of the factorization and renormalization scale.

Having established the self-consistency of the SHERPA results, they have been compared to those from an NLO calculation provided through MCFM. There, good agreement of the two codes has been found, again on the 20% level. Thus it is fair to state that the SHERPA results for the shapes are within theoretical errors consistent with an NLO calculation. The inclusion of the parton shower connected with specific scale choices in SHERPA, however, produces a surplus of QCD radiation with respect to the single parton emission in the real part of the NLO correction in MCFM.

Finally, the results of SHERPA have been compared with those of other hadron-level event generators, namely with PYTHIA and MC@NLO. There, it turned out that SHERPA predicts a significant increase of QCD radiation with respect to the other two codes. For the p_T spectra of jets accompanying the two W bosons, the differences are dramatic in the
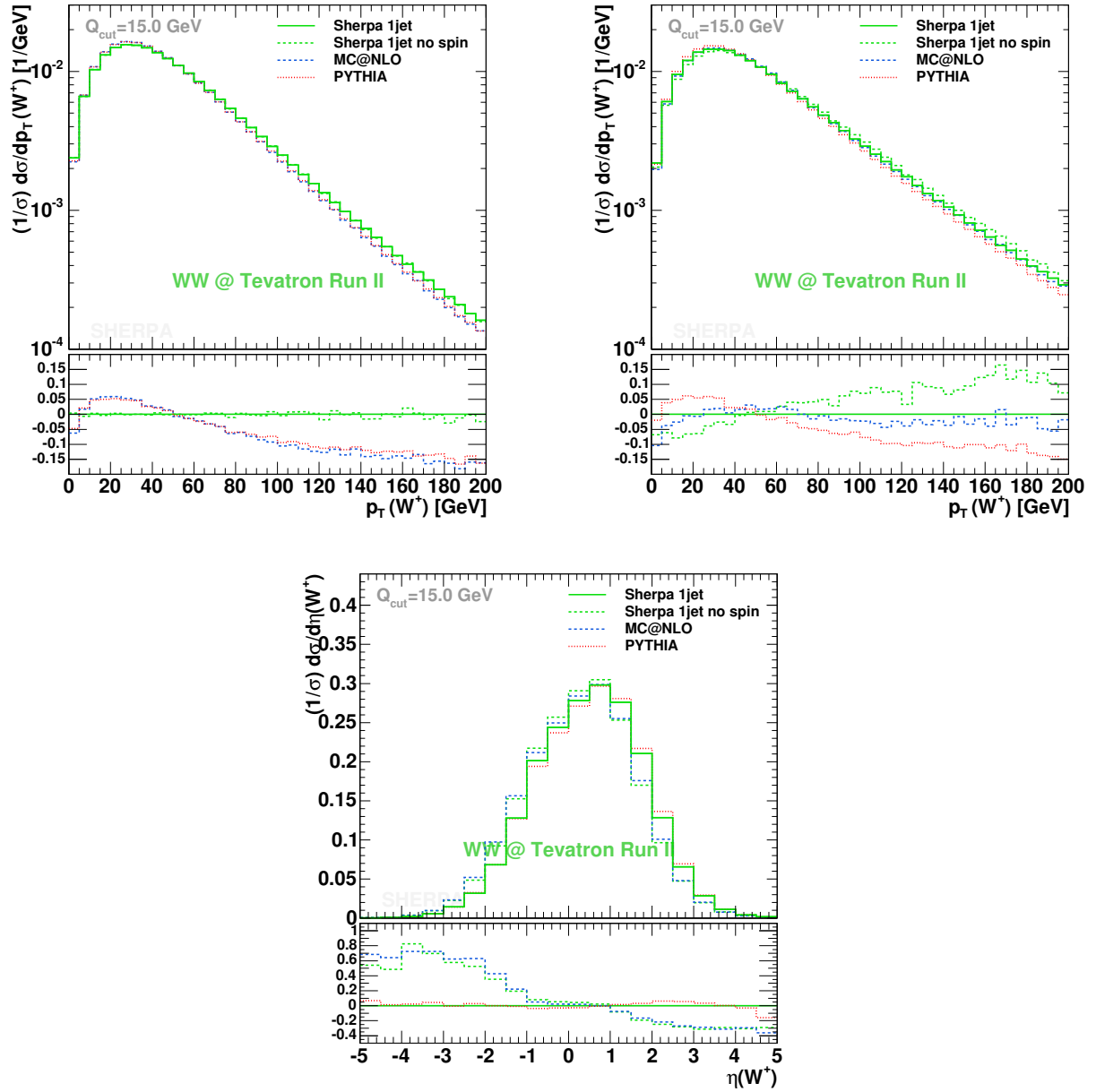
Figure 1.45: In the top left and right panel the p_T spectrum of the W^+ before and after the application of cuts is depicted, respectively. The bottom panel exhibits the η distribution of the W^+ under the influence of these cuts. The predictions compared are: PYTHIA (red dotted line), SHERPA (green solid line), MC@NLO (blue dashed line) and SHERPA without correlations in the boson decays (green dashed line). For input parameters, see app. B.1. The lower part of the plots shows the normalized differences with respect to the SHERPA prediction including spin correlations.

high p_T tails. In addition, the impact of spin correlations has been quantified. In the observables considered here, it reaches $20\% - 50\%$. This may be even larger than the impact of higher order corrections.

1.7 Conclusions

In this chapter two phenomenological studies have been presented with the goal of, first, delivering predictions for realistic hadron-collision scenarios, and, second, further validating Sherpa's CKKW implementation. The first study exhibits the comparison between the Lönnblad, MLM and CKKW schemes, where some emphasis has been put on estimating the underlying systematics of these different procedures and their implementations for combining fixed-order tree-level matrix elements with parton showers. Concerning the second study, the impact of the CKKW prescription on describing the QCD activity accompanying the production of charged dibosons has been investigated in detail, supplemented by a consideration of the effect of spin correlations in the leptonic decays of the W bosons. The more detailed conclusions of the two studies have been already given in their respective summaries, sec. 1.5.5 and sec. 1.6.4. For both cases, however, Sherpa predictions obtained from the consistent merging of parton showers and tree-level matrix elements for the production of multijet final states have been very reasonable. This once more justifies that the CKKW implementation in its present form constitutes a major cornerstone of the event generator Sherpa.

2 QCD dipole shower for hadronic collisions

2.1 Introduction

As outlined in the Introduction of this thesis, conventional parton showers preferably account for the logarithmically enhanced emission of soft and/or collinear QCD particles by an expansion around the collinear limit. In contrast, the shower in ARIADNE [11] is based on the Colour Dipole Model (CDM) [16, 17, 18], which formulates QCD evolution in terms of splitting parton dipoles rather than in terms of parton splittings. This is equivalent to an expansion around the soft limit of the radiation process and realized through an ordering in relative transverse momenta of subsequent splittings. In [16] it has been argued that such a dipole shower then quite naturally fulfils the requirement of quantum coherence, which, for the parton showers, led to the angular ordering. However, in the CDM, initial-state radiation (ISR), i.e. parton emission off incoming partons is not explicitly treated but taken into account by redefining ISR as final-state radiation (FSR) off hadron remnants [65]. To correctly model ISR in this picture, some non-perturbative corrections have to be applied, cf. sec. 2.2. Nevertheless, it has been an interesting feature of ARIADNE that its shower formulation yields results, which show a similar or even better agreement with data from electron–positron annihilations into hadrons [102, 103, 104, 105, 106]. In addition, ARIADNE equipped with this non-perturbative component in its modelling of radiation that is associated with the initial state also succeeded in describing a wealth of DIS data in a very reassuring way [107]. To some extent, the reason for this performance is subject of speculation, including a suspected better treatment of small-x effects, which are assumed to be an issue of greater importance for the forthcoming LHC. Equally well, it could be just the effect of a careful tuning of the additional non-perturbative parameters in the case of DIS, or an improved simulation of single, potentially non-global, potentially large logarithms stemming from the soft corner of the emission phase space. The latter appears as a consequence of the fact that the leading $1/N_{\mathrm{C}}$ terms of such contributions are better accounted for if the description of the radiation is based on the dipole structure in both matrix element and phase space [108]. This blurred picture of on the one hand delivering overwhelming agreement with data of various measurements and on the other hand lacking an unambiguous determination of the source of the success is enough motivation to try out an alternative path in modelling ISR in terms of colour dipoles.

The latest developments in the field of QCD event generators all aim at a systematic and exact inclusion of higher orders in the calculation of jets additionally arising from some leading-order process involving strong particles. As already discussed there have

been two directions of improvements, namely the matching of corresponding NLO QCD matrix elements with the parton shower, such that the total cross section and the first extra QCD emission are correctly described at NLO, see the Introduction of the thesis, and, the other direction, the merging of tree-level multi-leg matrix elements with the parton shower to generate a fully inclusive sample correct at leading logarithmic accuracy, which avoids double-counting phase-space regions covered by both matrix elements and the parton shower, see again the overall Introduction, also cf. ch. 1. Concerning matching, a CDM seems to be the more natural partner to the matrix-element bit of the calculation based on a subtraction method using antenna factorization [29]. Concerning merging, the dipole-shower maxim of leaving all particles involved in the splitting on their mass shells may lead to an alleviation of combining matrix-element and shower kinematics. However concerning both, it can be anticipated that a model relying on some additional non-perturbative input may hinder straightforwardly approaching the task.

In this thesis, therefore, an extension of the "perturbative" dipole shower [17] as implemented in ARIADNE [11] to true initial-state radiation is proposed. This is in striking contrast to the original ISR Lund CDM, where initial-state radiation is modelled as final-state radiation, involving the beam remnant particle [18, 109].

Hence, the goal is to formulate the QCD evolution of a hard process initiated through a hadronic collision as a sequence of colour-dipole emissions in an entirely perturbative description. In particular, emissions associated to the initial state are treated as to directly emerge from colour dipoles spanned by the incoming parton lines. The beam remnants are kept completely outside the perturbative evolution, their connection to the evolved cascade is left to the hadronization to deal with. As a direct consequence three types of dipoles and, hence, of associated radiation contribute to the full development of the final cascade, namely emissions from initial–initial (II), final–initial (FI) and vice versa (IF), and final–final (FF) dipoles. Consequently, the emissions are denoted as initial-, final–initial- and final-state radiation (ISR, FISR, FSR), respectively. Unquestionable, in order to model ISR and FISR in the fully perturbative version of the CDM proposed here, a backward evolution of the initial-state related radiation pattern of the shower becomes mandatory and automatically with it the inclusion of parton distribution functions (PDFs) to the Monte Carlo approach.

Accordingly, the cornerstones of the construction of the "perturbative" dipole shower proposed here can be identified and the shower will be based on:

- the generalization to the case of ISR and FISR of the kinematics setup including the evolution variables used in the original CDM and ARIADNE.

- the backward-evolution description of radiation that is related to incoming partons, consequently, the emergence of PDFs in the shower algorithm similar to conventional parton showers.

- the construction of on-shell kinematics for the new momenta of the splitting on an emission-by-emission basis, which in turn allows just stop and restart the cascading after any emission.

- factorization of the emission phase space and matrix element in the soft limit; the
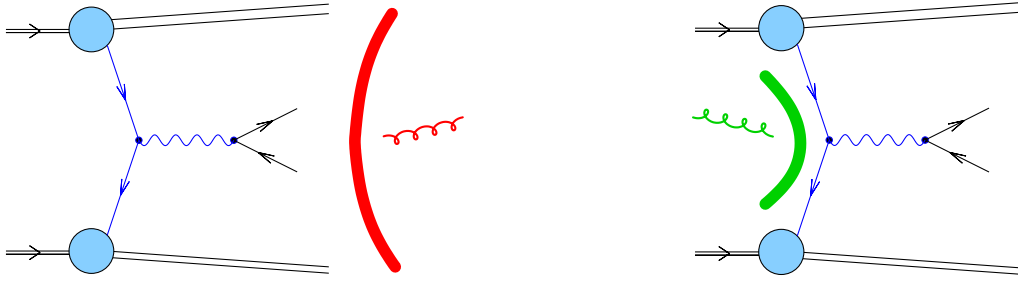
Figure 2.1: The Lund CDM approach to initial-state radiation in Drell–Yan processes (left panel) vs. the direct, perturbative approach as suggested by the new dipole-shower model (right panel). The treatment in modelling a first gluon emission is illustrated.

radiation pattern has to be factorized in terms of $2 \rightarrow 3$ splittings, which have to be derived for II and FI dipoles.

- the large N_C limit of the radiation pattern, considering only the leading terms, i.e. the leading dipoles, of this expansion.

- the probabilistic interpretation of emissions as encoded in the Sudakov form factor, which will be obtained from the exponentiation of minus the single-emission differential cross section.

Issues that are not covered here, instead left for future work, are:

- the potential splitting of gluons present in the final and/or initial state while evolving the dipole cascade, i.e. in this work it is dealt with the generalization of gluon emissions only,

- and, the consideration of finite non-zero quark masses, i.e. currently all quarks are treated as massless.

Consider Drell–Yan processes; in the Lund approach a first gluon emerges from the starting dipole spanned between the two hadron remnants, see fig. 2.1. In ARIADNE the emission is corrected for the exact matrix element for boson plus gluon production, and, the gluon's recoil is transferred to the vector boson, such that it acquires a suitable amount of tranverse momentum [110].

In contrast, in the dipole picture suggested here it is started off a $\bar{q}_i q_i'$ primary dipole, directly formed by the two incoming quarks, and, the emission will be calculated from the competition between gluon (see fig. 2.1), quark and antiquark bremsstrahlung. The real-emission matrix-element information will directly enter, since the corresponding dipole splitting functions can be corrected for it, as in the FF counterpart of emitting a first gluon off the $q\bar{q}$ dipole. Then, no additional correction has to be imposed, the demand to provide for distinct new initial-state momenta oriented along the beam direction will generate the boson's transverse momentum naturally, and, in case of an actual gluon emission, a system of colour-connected successor dipoles emerges, an IF dipole $\bar{q}_i g_f$ and
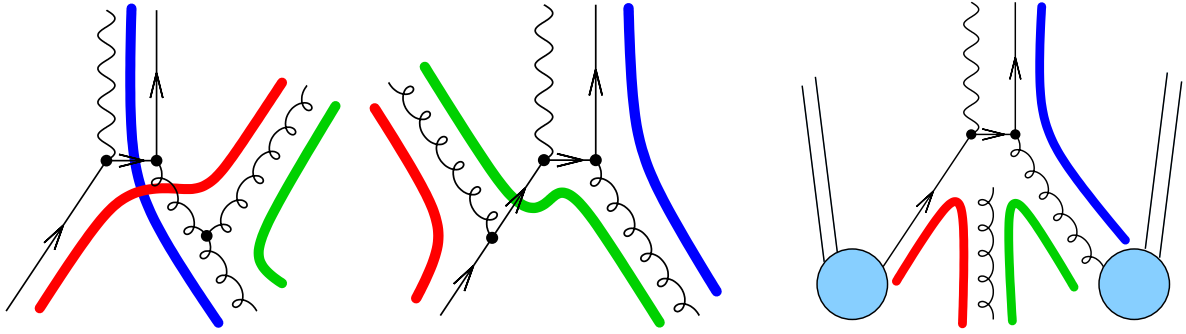
Figure 2.2: Modelling a second emission, emerging off the successor II dipole after a first radiation of a quark. The right panel depicts this gluon emission in a simplified manner, whereas the other two panels show the two contributions to the full description of this gluon emission.

an FI dipole $g_f q_i$. A further gluon radiated into the final state will then create a first FF dipole, hence, the QCD evolution of the LO Drell–Yan pair production process will involve all possible dipole types. In fig. 2.2 a first gluon emission is illustrated in case of the very primary one appeared as a release of a quark into the final state.

Finally, the outline of this chapter is as follows: In sec. 2.2 the basics of the dipole-shower model as implemented in ARIADNE and as employed as a starting point of the new model presented here will briefly be introduced. In addition, the treatment of ISR through final-state dipole splittings involving the beam remnants will be discussed. In the next section, sec. 2.3, the kinematics of all dipole splittings in various configurations of initial- and final-state partons will be presented, starting with the generalization of the kinematical framework and of the evolution variables. Before the new types will be dealt with, this is first applied to the case of dipoles consisting of final-state partons only, the case indeed implemented in ARIADNE. Then, in sec. 2.4 all single-splitting cross sections employed by the new model for the various dipole configurations will be highlighted. The complete shower algorithm will be presented in sec. 2.5 and its performance for various physics processes will be exposed in sec. 2.6. The conclusions will finalize the discussion of the dipole shower.

2.2   The Colour Dipole Model

2.2.1   Physical background of the CDM

The Lund colour dipole model (CDM) has strong connections to the semiclassical method of virtual quanta [111, 112, 113], which equates the electromagnetic energy flux associated with the fields emitted by fast moving charges with an energy flux of equivalent photons. Owing to the large Lorentz boosts of the charged emitter, the corresponding electric and magnetic fields are orthogonal to each other and they populate a plane orthogonal to the direction of motion of the emitter only. This amounts to a pulse of electromagnetic

energy, given by

$$dI(\omega, b) \;\simeq\; \hbar\alpha\, d\omega\, \frac{2\pi\, b\, db}{\pi^2}\,, \tag{2.1}$$

where b denotes the impact parameter, i.e. the distance w.r.t. the emitter and ω is the frequency, which is bound from above such that $\omega < p/mb$, where p and m are the momentum and rest mass of the emitter, respectively. Equating this energy pulse I with a number of equivalent quanta n,

$$dI \;=\; \hbar\omega\, d\omega\,, \tag{2.2}$$

and replacing the impact parameter with transverse momentum yields

$$dn \;\simeq\; \frac{\alpha}{\pi}\, \frac{dk_\perp^2}{k_\perp^2}\, \frac{d\omega}{\omega}\,. \tag{2.3}$$

A similar result emerges when considering bremsstrahlung off a charged particle, changing its otherwise straight direction of motion through a sudden "kick", or connected with the pair production of charged particles. Then, in the Breit-frame of the former process, or in the centre-of-mass frame of the latter, a rapidity y can be defined w.r.t. the axis of motion of the charged particle(s). A short calculation based on a full quantum-mechanical treatment shows that, neglecting spin effects, the number of bremsstrahlung-photons is well approximated by

$$dn \;=\; \frac{2\alpha}{\pi}\, \frac{d\omega}{\omega}\, dy\,, \tag{2.4}$$

cf. [3]. Here, the rapidity must satisfy

$$|y| \;<\; |y_0|\,, \tag{2.5}$$

and y_0 is the rapidity of the emitter(s). Rewriting energy through transverse momentum,

$$k_\perp \;=\; \frac{\omega}{\cosh y}\,, \tag{2.6}$$

then leads to

$$dn \;=\; \frac{\alpha}{\pi}\, \frac{dk_\perp^2}{k_\perp^2}\, dy\,. \tag{2.7}$$

Although this equation is somewhat obscured, it is important to stress that because of its equivalence to eq. (2.4), it exhibits the dominance of soft radiation in the semi-classical limit. In this context it is worth noting that the same limit is used in eikonal-type factorization of matrix elements employed, for instance, in antenna subtraction methods [29, 114] for the calculation of perturbative higher-order corrections to scattering cross sections in QCD.

The simple formula for the semi-classical limit of photon radiation off a charged dipole, eq. (2.7), can be refined through a full quantum-mechanical treatment, including spin

effects, see also sec. 2.4. However, the dominant features of the radiation pattern are already fixed by the simple formula, which in turn denotes the starting point for a shower simulation based on individual dipole emissions. The differential cross section $d\mathcal{P} = d\sigma/d\sigma_0$ for such an emission to occur in an interval $dp_\perp^2$ and dy is given by

$$d\mathcal{P} \simeq \frac{\alpha_s}{\pi} \frac{dp_\perp^2}{p_\perp^2} dy \,. \tag{2.8}$$

Here $p_\perp$ denotes a transverse momentum, which in the CDM is constructed out of Lorentz invariant quantities. Numbering the momenta of the particles after emission such that the newly emitted particle is labelled with "2", and, denoting the momenta before and after the emission with $\tilde{p}_i$ and p_i, respectively, the emission can be symbolized as

$$\tilde{p}_1 + \tilde{p}_3 = p_1 + p_2 + p_3 \,. \tag{2.9}$$

The squared invariant masses of sets of momenta are denoted as

$$s_{ij\ldots} = (p_i + p_j + \ldots)^2 \qquad \text{and} \qquad \tilde{s}_{ij\ldots} = (\tilde{p}_i + \tilde{p}_j + \ldots)^2 \,. \tag{2.10}$$

Then, the Lorentz invariant transverse momentum is defined as

$$p_\perp^2 = \frac{s_{12}\,s_{23}}{s_{123}} = \frac{s_{12}\,s_{23}}{\tilde{s}_{13}} \,, \tag{2.11}$$

in agreement with [17, 3] and the implementation in ARIADNE. The rapidity can then be computed through

$$y = \frac{1}{2} \ln \frac{s_{12}}{s_{23}} \,. \tag{2.12}$$

This Lorentz invariant choice guarantees a frame-independent description of the dipole splitting process. Using $p_\perp$ as the ordering parameter for subsequent emissions, a Sudakov form factor encodes the non-emission probability between two scales $p_{\perp,\text{high}}^2$ and $p_{\perp,\text{low}}^2$ in analogy to conventional parton showers:

$$\Delta(p_{\perp,\text{high}}^2, p_{\perp,\text{low}}^2) = \exp\left\{ -\int_{p_{\perp,\text{low}}^2}^{p_{\perp,\text{high}}^2} dp_\perp^2 \int_{y_-(p_\perp^2)}^{y_+(p_\perp^2)} dy \, \frac{d\mathcal{P}}{dp_\perp^2\,dy} \right\} \,. \tag{2.13}$$

In this form, the leading logarithms are resummed to all orders.

The Sudakov form factor constitutes the basis of the simulation of parton emission also in the framework of the CDM. In contrast to ordinary parton showers, however, here the relevant objects are colour dipoles, which emerge naturally when considering the large N_C limit. In this limit, colour charges in the fundamental representation (quarks and antiquarks) have one colour partner, and colour charges in the adjoint representation (gluons) have two colour partners. The dipoles are built from such colour partners, and the emission of a gluon off such a dipole effectively amounts to splitting the dipole into two. In this way single colour lines are associated to the dipole spanned between colour-connected partons. The gluon then arises from the connecting colour line (acting as a

radiating antenna). In case the dipole contains a gluon leg, the evolution can also proceed through a gluon splitting, which separates the connecting line from one that accompanies it only due to the double-line character of gluons in the limit of large N_C. The emission pattern of accompanied lines is taken care of by the neighbouring dipole(s) carrying it actively. Hence, subsequent radiation is understood to only emerge from the currently present leading N_C dipoles.

This self-similar process of dipole splitting, described in a probabilistic fashion is easily encoded as a Markovian process in form of a computer program. Adding in the leading logarithmic behaviour and colour coherence as a dominant feature of QCD emissions results in a strict ordering of subsequent emissions such that the actual $p_\perp$ of a dipole splitting sets the maximal $p_\perp$ for the splittings of the two resulting dipoles.

2.2.2 Initial-state radiation in the original CDM

In ARIADNE, the so far only CDM implementation, initial state radiation off incoming partons is not explicitly taken into account. Instead, initial-state radiation is *redefined* as final-state radiation, where dipoles are spanned between potential final-state partons and the outgoing hadron remnants [65, 115, 116, 110]. Considering DIS of leptons on hadrons, it can be argued that, as the hadron is in a bound state, all radiation comes from the colour dipole between the struck pointlike quark and the hadron remnant – being an extended object composed of individual valence quarks and sea partons. Thus, an extended "antenna" is formed and from the electro-magnetic (semi-classical) analogy it follows that radiation of wavelengths smaller than the extension of the antenna is suppressed. Therefore, the original CDM was modified such that only a $p_\perp$ dependent fraction $a(p_\perp)$ of the remnant enters the dipole splitting process [65]:

$$a(p_\perp) \;=\; \left(\frac{\mu}{p_\perp}\right)^\alpha , \qquad\qquad\qquad (2.14)$$

where μ parametrizes the inverse size of the remnant and α refers to the dimensionality of the emitter, both being parameters to be tuned to data. In e^+e^- annihilation the ("triangle") phase-space boundaries are approximated by $|y| < \ln(M/p_\perp)$, which now are supplemented by the extra condition $y < \ln(M\mu/p_\perp^2)$. This obviously limits the range of accessible $p_\perp$ values in the splitting of the dipole of mass M. The strategy of sharing the recoil in such cases was inspired by the Lund string model, where an extra kink on the string (hadron) is interpreted as an extra gluon. This led to the introduction of recoil gluons compensating for the recoil dedicated to the part of the hadron partaking in the emission.[1] Moreover, in cases where a sea quark is hit, the picture is slightly modified further. Taken together, through all these assumptions a good fraction of phenomenological, non-perturbative modelling enters the Lund CDM for ISR.

Consider again Drell–Yan processes; as already exemplified in the introduction, sec. 2.1, there, a quark–antiquark pair annihilates to produce a lepton pair. In conventional parton showers, the two incoming quarks would emit secondary partons, typically simulated in a backward evolution algorithm [12, 15]. The recoil of these emissions is transferred

---

[1]For the `C++` rewrite of ARIADNE the possibility of completely discarding recoil gluons is under consideration.

to colour partners and the final-state leptons. In contrast, in Ariadne the incoming quarks do not radiate but rather the two beam remnants, which are the only two coloured final-state objects before radiation. Then, the recoil of the first emission is compensated for by the final-state leptons [110, 44], for all further dipole emissions, additional recoil gluons are added, if the emission occurred significantly away in phase space from the vector boson [110]. A further obvious refinement is the correction of the first emission to the correct matrix-element expression, where available. Then, the sharp phase-space cutoff is replaced by a softer suppression function, in order to describe the high transverse-momentum spectrum of the vector boson. The two way of modelling ISR, in the Lund CDM and in the new proposal, are pictorially represented in fig. 2.1, respectively.

2.3   Dipole single-emission phase space and kinematics

In sec. 2.2 the general form of the dipole splittings has been presented, cf. eq. (2.8), which constitutes the limiting case of soft emissions, i.e. the case, where the energy of the emitted gluon approaches zero. In this section all ingredients are discussed, which are necessary to construct the kinematics of three-parton final states emerging from splitting the original two-parton configurations. The corresponding dipole splitting matrix elements, which depend on the particles involved, will be specified in the next section, sec. 2.4. In both cases, only massless partons are considered, an extension to massive partons is tedious but straightforward and will be left for future consideration.

The derivation of the splitting kinematics for each dipole type (FF, II, and FI/IF) will be pursued in four steps:

- First, the evolution variables $p_\perp$ and y are identified.

- Then, limits of the emission phase space are discussed. They guarantee that the evolution takes place within the physical region of phase space. These limitations are imposed through constraints on the evolution variables and, thus, determine the actual computation of the Sudakov form factor, see eq. (2.13) and sec. 2.5.

- Furthermore, together with the strict limits, approximate ones are stated, which eventually enable the direct evaluation of the Sudakov form factors according to a veto algorithm, see e.g. [7].

- Finally the kinematics of the splittings characterized by $p_\perp$ and y are constructed, i.e. the three new momenta are determined.

To begin with, the kinematic framework for all sorts of dipole splittings is introduced in parallel with the nomenclature employed throughout this paper. This procedure amounts to an universal definition of the evolution variables for all dipole types. After that, as the first specific instance, the traditional FF dipole case originally realized within Ariadne will be briefly reviewed. This is followed by the consideration of the new cases, namely those of II and FI/IF dipoles.

QCD dipoles, $\quad \tilde{k}\,\tilde{\ell}$			
II dipoles $\tilde{i}'\,i$	IF dipoles $\bar{i}\,\bar{f}$	FI dipoles $f\,i$	FF dipoles $f\,\bar{f}'$
$\bar{q}_\mathrm{i}'q_\mathrm{i}$	$\bar{q}_\mathrm{i}'\bar{q}_\mathrm{f}$	$q_\mathrm{f}q_\mathrm{i}'$	$q_\mathrm{f}\bar{q}_\mathrm{f}'$
$g_\mathrm{i}q_\mathrm{i}$	$g_\mathrm{i}\bar{q}_\mathrm{f}$	$q_\mathrm{f}g_\mathrm{i}$	$q_\mathrm{f}g_\mathrm{f}$
$\bar{q}_\mathrm{i}g_\mathrm{i}$	$\bar{q}_\mathrm{i}g_\mathrm{f}$	$g_\mathrm{f}q_\mathrm{i}$	$g_\mathrm{f}\bar{q}_\mathrm{f}$
$g_\mathrm{i}g_\mathrm{i}$	$g_\mathrm{i}g_\mathrm{f}$	$g_\mathrm{f}g_\mathrm{i}$	$g_\mathrm{f}g_\mathrm{f}$

Table 2.1: All dipole types appearing in QCD (the supplemental indices i or f label whether the parton is in the initial or final state, respectively; if clear from the context, the index f will be left out). The primes indicate that different quark flavours may constitute the dipole.

2.3.1 Towards generalized evolution variables

The occurrence of new dipoles and corresponding splittings is an immediate consequence of the suggested new CDM approach. A list summarizing allowed dipoles in QCD is shown in tab. 2.1. The extension of the original perturbative CDM, relying on FF dipoles only, to a framework explicitly including initial-state partons is governed by three principles: the crossing symmetry of the splitting amplitudes of the CDM, the symmetry of Quantum Chromodynamics under charge conjugation and the concept of working in the limit of large N_C. The first arises naturally from the crossing symmetry of the $1 \rightarrow 3$ real-gluon production matrix elements underlying the various $2 \rightarrow 3$ splitting cross sections in the original CDM. Its implications will be discussed in more detail in sec. 2.4. According to the second principle only three dipole types have to be distinguished. They differ in their partons' association to the initial or final state, and thus there are FF, II and FI dipoles. According to the third principle, dipoles consist of two colour-connected partons where one carries a colour (triplet) and the other one the respective anticolour (antitriplet). In this picture, of course, each gluon belongs to two dipoles and hence plays a dual rôle. Dipoles are then labelled by $\tilde{k}\tilde{\ell}$, so that in the most general way a splitting triggered by the emission of a (new) gluon g is expressed as

$$\tilde{k}\,\tilde{\ell} \; \rightarrow \; k\,g\,\ell\,. \tag{2.15}$$

The notation is chosen such that the flavour and colour flow of all particles is outgoing, and is, therefore, independent of the partons being in the initial or final state. Specifically, the generalization of the CDM leads to three types of gluon emission related to each other by crossing symmetry; any such splitting, however, will leave the number of initial-state partons constant:

$$\tilde{k}\,\tilde{\ell} \; \rightarrow \; \begin{cases} \tilde{k}\,g_\mathrm{f}\,\tilde{\ell} & : \quad \text{gluon emission}\,, \\ q\,g_\mathrm{i}\,\tilde{\ell} & : \quad \text{quark emission, provided that } \tilde{k} = \bar{q}_\mathrm{i}\,, \\ \tilde{k}\,g_\mathrm{i}\,\bar{q} & : \quad \text{antiquark emission, provided that } \tilde{\ell} = q_\mathrm{i}\,. \end{cases} \tag{2.16}$$

Here, the subscripts indicate whether the gluon emerges in the initial or final state. In the former case, this hence requires to replace the initial (anti)quark of the original dipole by the initial gluon and emit the corresponding antiquark (quark) in the final state; see the last two splitting types above. However, since the last channel just exhibits the charge-conjugated process of the quark emission, only the first two processes – although linked by crossing – are generic, and, hence, will be dealt with on a case-by-case basis throughout this work.

Having clarified the notations used for the dipoles and their splittings, the kinematic objects will be introduced. First of all, the momenta are defined as incoming/outgoing if they are associated with the physical initial/final state. Those before and after the emission are denoted by $\tilde{p}_{\tilde{m}}$ and p_m, respectively, such that, expressed through the momenta alone the dipole splitting process can be written as

$$\tilde{\varsigma}_{\tilde{k}}\,\tilde{p}_{\tilde{k}} + \tilde{\varsigma}_{\tilde{\ell}}\,\tilde{p}_{\tilde{\ell}} \quad \longrightarrow \quad \varsigma_k\,p_k + \varsigma_g\,p_g + \varsigma_\ell\,p_\ell\,. \tag{2.17}$$

Here and in the following the signature factors $\tilde{\varsigma}_{\tilde{m}} = \pm 1$ and $\varsigma_m = \pm 1$ for partons in the final (+) and initial (−) state. The before- and after-emission total momenta $\tilde{p}_0$ and p_0 then read

$$-\varsigma_0\,\tilde{p}_0 \;=\; \tilde{\varsigma}_{\tilde{k}}\,\tilde{p}_{\tilde{k}} + \tilde{\varsigma}_{\tilde{\ell}}\,\tilde{p}_{\tilde{\ell}}\,, \tag{2.18}$$

$$-\varsigma_0\,p_0 \;=\; \varsigma_k\,p_k + \varsigma_g\,p_g + \varsigma_\ell\,p_\ell\,, \tag{2.19}$$

with the requirement that $\tilde{p}_0^2 = p_0^2$. Furthermore $\tilde{\varsigma}_0 \equiv \varsigma_0$, and the signature factor ς_0, i.e. the assignment of the total momenta to the initial or final state is chosen such that the after-emission constellation exhibits a production ($\varsigma_0 = -1$, FF dipoles), scattering ($\varsigma_0 = -1$, FI dipoles), or annihilation ($\varsigma_0 = 1$, II dipoles) process. Consequently, the four-vector $\tilde{p}_0$ then corresponds to the four-momentum of the decaying parent dipole having mass $|M|$ such that

$$\tilde{p}_0^2 \;=\; M^2 \equiv -Q^2 \;=\; p_0^2\,, \tag{2.20}$$

with Q^2 arranged to be positive definite for FI dipole emissions. Accordingly, Lorentz invariant energy fractions w.r.t. p_0 are defined through [2]

$$x_m \;=\; \frac{2\,p_m p_0}{p_0^2}\,. \tag{2.21}$$

The squared invariant masses of two- and three-parton systems are denoted by

$$s_{mn} \;=\; (\varsigma_m\,p_m + \varsigma_n\,p_n)^2 \qquad \text{and} \qquad s_{mnr} \;=\; (\varsigma_m\,p_m + \varsigma_n\,p_n + \varsigma_r\,p_r)^2 \tag{2.22}$$

where the inclusion of p_0 and the expressions related to the momenta before the emission are understood. Concerning all gluon emissions considered here, the identity

$$M^2 \;=\; s_{kg} + s_{g\ell} + s_{k\ell} \;=\; s_{kg\ell} \;=\; -Q^2\,, \tag{2.23}$$

---

[2] The notion "energy fraction" is clear in the centre-of-mass frame of a parent FF dipole, where $x_m = 2E_m/M$.

generically holds, since the partons are consistently treated as massless.

Next, suitably generalized dipole evolution variables must be found, in order to retrieve an universal and consistent CDM-like evolution treatment that naturally embeds the new dipole types and their emissions on equal level besides those invoked by sole final-state cascading. These variables should have the property of leaving the well-established FSR treatment unchanged and they should satisfy the constraint that all splitting cross sections, i.e. those involving initial-state partons as well, will follow the approximate form given in eq. (2.8). This is just another manifestation of the universal feature of soft QCD radiation reproducing eikonal distributions in emissions off initial and final states. In the soft limit the spin of the emitting (hard) partons is irrelevant and the gluon radiation is described through the eikonal factor

$$-\frac{1}{2}\left(\frac{p_k}{p_k p_g}-\frac{p_\ell}{p_g p_\ell}\right)^2 \; = \; \frac{2\,s_{k\ell}}{s_{kg}\,s_{g\ell}}\,, \tag{2.24}$$

which factorizes off the squared matrix elements. The right-hand-side expression explicitly assumes massless partons. Following eq. (2.11), the factor $2/p_\perp^2$ becomes identical to the eikonal factor in the soft limit, and the collinear limits manifest themselves in the two-parton squared masses appearing in this $p_\perp^2$ definition. Then, a generalization should show the same limiting behaviour and reflect that the kinematic regimes of the different dipole types are linked by crossing. Therefore, a generalized transverse momentum and rapidity are proposed, given by

$$p_\perp^2 \; = \; \left|\frac{s_{kg}\,s_{g\ell}}{s_{kg\ell}}\right|\,, \tag{2.25}$$

and

$$y \; = \; \frac{1}{2}\,\ln\left|\frac{s_{g\ell}}{s_{kg}}\right|\,, \tag{2.26}$$

where the invariant masses $s_{mn(r)}$ are calculated including the signature factors $\varsigma_{m,n,r}$, i.e. through eqs. (2.22). Clearly, for FF dipole cascading, all invariant masses are positive and hence the original CDM evolution variables of eqs. (2.11) and (2.12) are trivially recovered. For the other cases, owing to the crossing symmetry the generalized form suggested here is merely a minimal extension keeping the feature of Lorentz invariance that will assure a frame-independent evolution and setup of the three-parton kinematics similar to the Lund CDM. Moreover, these shower variables enable an overall ordering of all emissions, since defined in this way they arise from the same principle regardless of the considered kinematic regime (FF, II or FI). Given these generalized definitions, the identities

$$|s_{kg}| \; = \; |M|\,p_\perp e^{-y} \qquad \text{and} \qquad |s_{g\ell}| \; = \; |M|\,p_\perp e^{+y} \tag{2.27}$$

are found, indeed showing the similarities to the original Lund CDM. Finally, rescaled $p_\perp$ variables are defined,

$$x_\perp \; = \; \frac{p_\perp}{\sqrt{s}}\,. \tag{2.28}$$

This rescaling is performed w.r.t. a reference invariant-mass quantity s, which has to be specified for every generic dipole splitting, and the findings for the approximate phase-space limits will dictate its choice; but, typically, it will be given as a function of $|M^2|$.

2.3.2 Final–final dipoles

As a first instance, the kinematical details of emissions emerging from FF dipoles are considered. This is the case already dealt with in the original version of the CDM, which is implemented in ARIADNE. The dipole splitting process can be specified by

$$f(\tilde{k})\,\bar{f}'(\tilde{\ell})\;\to\;f(k)\,g\,\bar{f}'(\ell)\,. \tag{2.29}$$

Apart from $\varsigma_0 = -1$, all other signature factors equal one. Moreover, since the recoil of the emission will be completely shared between the three new partons, momentum conservation,

$$\tilde{p}_0 = \tilde{p}_f + \tilde{p}_{\bar{f}'} \;=\; p_f + p_g + p_{\bar{f}'} = p_0\,, \tag{2.30}$$

is realized between the momenta present before and after the emission. Neglecting parton masses, the relations

$$0 \;\leq\; s_{mn} \;=\; s_{0r} \;=\; M^2(1 - x_r) \;\leq\; M^2\,, \qquad m \neq n \neq r \in \{f, g, \bar{f}'\}\,, \tag{2.31}$$

and the identity

$$M^2 \;=\; s_{fg} + s_{g\bar{f}'} + s_{f\bar{f}'}\,, \qquad \text{also expressed by} \qquad 2 \;=\; x_f + x_g + x_{\bar{f}'} \tag{2.32}$$

are obtained. All energy fractions fall into the range $0 \leq x_r \leq 1$, and, hence, the physics constraints imposed on the kinematic invariants s_{mn} are satisfied. Following the steps outlined in the introduction of this section, the $(p_\perp^2, y)$ phase-space parametrization can be specified:

- The two Lorentz invariant dipole evolution variables are $p_\perp^2$, which in this case reads

$$p_\perp^2 \;=\; \frac{s_{fg}\,s_{g\bar{f}'}}{M^2} \;=\; M^2(1 - x_{\bar{f}'})(1 - x_f)\,, \tag{2.33}$$

  cf. eqs. (2.11) and (2.25), and the associated rapidity y, which is given by

$$y \;=\; \frac{1}{2}\,\ln\frac{s_{g\bar{f}'}}{s_{fg}} \;=\; \frac{1}{2}\,\ln\frac{1 - x_f}{1 - x_{\bar{f}'}}\,, \tag{2.34}$$

  cf. eqs. (2.12) and (2.26). Therefore, the invariant masses can be re-expressed through them,

$$\begin{aligned} s_{g\bar{f}'} &= M p_\perp e^{+y}\,, \\ s_{fg} &= M p_\perp e^{-y}\,, \\ s_{f\bar{f}'} &= M^2 - 2 M p_\perp \cosh y\,, \end{aligned} \tag{2.35}$$

  cf. eqs. (2.27). As expected, the dominant phase-space regions are characterized by $p_\perp \to 0$, which fortifies $p_\perp$'s utilization to order and steer the development of the FF colour-dipole part of the cascade.

- The kinematical phase-space boundaries given through the relations in eqs. (2.31) determine the (maximal) integration limits $p_{\perp,\text{high}}^2$ and $y_\pm$ stated in eq. (2.13). For example, simple rapidity bounds are easily obtained from $s_{fg}, s_{g\bar{f}'} \leq M^2$, however, a more precise determination of the boundaries beyond this rough estimate, requires to analyze

$$s_{fg} + s_{g\bar{f}'} = M^2 - s_{f\bar{f}'} \leq M^2. \tag{2.36}$$

This yields symmetric rapidity limits,

$$|y| \leq \operatorname{arcosh}\frac{\sqrt{s}}{2\,p_\perp} = \operatorname{arcosh}\frac{1}{2\,x_\perp} = \ln\left(\frac{M}{2p_\perp} + \sqrt{\frac{M^2}{4p_\perp^2} - 1}\right). \tag{2.37}$$

The largest possible value for $p_\perp^2$ can also be read off these bounds,

$$p_{\perp,\text{max}}^2 = \frac{s}{4}, \qquad \text{where} \qquad s = M^2, \tag{2.38}$$

and the choice of s is clarified in the next item.

- Concerning the approximate limits, as mentioned $s_{fg}, s_{g\bar{f}'} \leq M^2$ has to be interpreted instead of eq. (2.36); this leads to

$$\ln x_\perp = -\ln\frac{M}{p_\perp} \leq y \leq \ln\frac{M}{p_\perp} = -\ln x_\perp, \tag{2.39}$$

which is nothing but the $(y, z = \ln x_\perp)$ "triangle" commonly used to illustrate the dipole emission phase space. Thus, the quantity s that appears in eq. (2.28) is fixed by the squared mass of the parent FF dipole. The effect of the sharper bounds now becomes apparent: they sizeably reduce the "triangle" area particularly in the central rapidity region.

- Splitting kinematics: once the evolution variables have been obtained, they serve as the central variables from which the on-shell three-parton kinematics is generated. Physically motivated recoil strategies and four-momentum conservation fix leftover degrees of freedom. Advantageously, the latter can be accomplished locally among the partons participating in the splitting only.

  In the case considered here the optimal frame to actually set up the new momenta is given through the centre-of-mass system of the parent FF dipole. Light-cone momenta [3] w.r.t. the back-to-back axis of the two partons that constitute the dipole can then be used to express all momenta conveniently:

$$
\begin{aligned}
\tilde{p}_0 &= \left(M,\, M,\, \vec{0}\right) &\rightarrow\quad p_0 &= \left(M,\, M,\, \vec{0}\right), \\
\tilde{p}_f &= \left(M,\, 0,\, \vec{0}\right) &\rightarrow\quad p_f &= \left(f_\perp\, e^{y_f},\, f_\perp\, e^{-y_f},\, \vec{f_\perp}\right), \\
\tilde{p}_{\bar{f}'} &= \left(0,\, M,\, \vec{0}\right) &\rightarrow\quad p_{\bar{f}'} &= \left(f_\perp'\, e^{y_f'},\, f_\perp'\, e^{-y_f'},\, \vec{f_\perp'}\right), \\
& & p_g &= p_0 - p_f - p_{\bar{f}'}.
\end{aligned}
\tag{2.40}
$$

---

[3]In this work, light-cone momenta are defined as follows: $q = (q_+, q_-, \vec{q}_\perp)$ where $q_\pm = E_q \pm q_\parallel$; on-shell conditions can be intrinsically satisfied, if $q = (m_\perp e^z, m_\perp e^{-z}, \vec{q}_\perp)$ is chosen, using $m_\perp^2 = q^2 + q_\perp^2$ and $z = \ln(q_+/q_-)/2$ such that $E_q = m_\perp \cosh z$ and $q_\parallel = m_\perp \sinh z$.

The further specification of the $\vec{f}_\perp^{(')}$ and $y_f^{(')}$ is only achieved under incorporation of the particular recoil strategies. This will not be demonstrated here, however, the implementation used in this model closely follows the suggestions of the Lund CDM, see e.g. [11]. Note that, if the recoil of the emitted gluon is only compensated by one of the dipole partons, then the corresponding $\vec{f}_\perp^{(')} \equiv \vec{0}$ and $y_f^{(')} \equiv \pm\infty$; one of the products $f_\perp^{(')} e^{\pm y_f'}$ however will be finite and the other one be identical to zero. This for example becomes relevant when strategies similar to the Kleiss trick [117] are implemented.

2.3.3 Initial–initial dipoles

The first case, which goes beyond the original CDM, is radiation off an initial-state dipole $\bar{\imath}'i$ of mass M. Two generic splittings based on gluon emission are now available, namely

$$\bar{\imath}'(\tilde{k})\,i(\tilde{\ell}) \;\to\; \bar{\imath}'(k)\,g\,i(\ell) \qquad \text{and} \qquad \bar{q}_\mathrm{i}(\tilde{k})\,i(\tilde{\ell}) \;\to\; q(k)\,g_\mathrm{i}\,i(\ell)\,. \tag{2.41}$$

As discussed in sec. 2.3.1, the case of antiquark emission is closely to that of quark emission. Restating eqs. (2.18) and (2.19) for the II dipole scenario, i.e. setting $\varsigma_0 = \varsigma_{g/q} = 1$ and all other signature factors equal to -1, yields

$$\tilde{p}_{\bar{\imath}'/\bar{q}_\mathrm{i}} + \tilde{p}_i \;=\; \tilde{p}_0 \qquad \text{and} \qquad p_{\bar{\imath}'/g_\mathrm{i}} + p_i \;=\; p_0 + p_{g/q}\,, \qquad \text{with} \qquad p_0^2 = \tilde{p}_0^2 = M^2\,. \tag{2.42}$$

Contrary to the previously presented case, $\tilde{p}_0 \neq p_0$ (unless it is worked in the $\bar{\imath}'i$ dipole's rest frame), since the recoil of the emitted parton $p_{g/q}$ cannot be absorbed by $p_{\bar{\imath}'/g_\mathrm{i}}$ and p_i while keeping them fixed on their respective beam axis. In addition, initial-state radiation typically is related to an increase of the "Bjørken-x" and hence of the energy of at least one of the incoming partons. The kinematics of the emission process here corresponds to that of a $2 \to 2$ scattering process. Therefore, Mandelstam variables are defined, reading

$$\begin{aligned}
\hat{s} &= (p_0 + p_{g/q})^2 = (p_{\bar{\imath}'/g_\mathrm{i}} + p_i)^2 = M^2(1 + x_{g/q}) \;\geq\; M^2 \equiv \hat{s}_0\,, \\
\hat{t} &= (p_0 - p_i)^2 = (p_{\bar{\imath}'/g_\mathrm{i}} - p_{g/q})^2 = M^2(1 - x_i) \;\leq\; 0\,, \\
\hat{u} &= (p_0 - p_{\bar{\imath}'/g_\mathrm{i}})^2 = (p_i - p_{g/q})^2 = M^2(1 - x_{\bar{\imath}'/g_\mathrm{i}}) \;\leq\; 0\,,
\end{aligned} \tag{2.43}$$

where, again for massless partons, the bounds on $\hat{s}$, $\hat{t}$ and $\hat{u}$ together with their parametrizations in terms of energy fractions are simple, and, furthermore,

$$\hat{s} + \hat{t} + \hat{u} \;=\; M^2 \qquad \text{as well as} \qquad x_{\bar{\imath}'/g_\mathrm{i}} + x_i \;=\; 2 + x_{g/q}\,. \tag{2.44}$$

As already indicated, the emission of a parton here requires an increase in $\hat{s}$ against $\hat{s}_0$. This is in contrast to the FF case, where the system's centre-of-mass energy remains constant. In view of further considerations, a generic parametrization is introduced that relates the maximal partonic centre-of-mass squared energy to the squared mass of the parent dipole,

$$\hat{s}_\mathrm{max} \;=\; a\,M^2 \;\geq\; \hat{s}\,, \qquad \text{so that} \qquad 1 \;\leq\; \hat{s}/M^2 \;\leq\; a \;\leq\; S/M^2\,, \tag{2.45}$$

where $\sqrt{S}$ is the centre-of-mass energy of the colliding hadrons. The limits on the invariants, detailed in eqs. (2.43) and (2.45), clearly differ from the ones of the FF scenario, cf. sec. 2.3.2. This implies that the II dipole splittings arise in phase-space regions distinct from the FF case and thus with a different kinematics. Consequently, the energy fractions populate new ranges compared to the FF splittings, namely

$$
\begin{aligned}
0 \ &\leq \ & x_{g/q} \ & \leq \ a-1\,, \\
1 \ &\leq \ & x_{\bar{\imath}'/g_{\mathrm{i}}},\, x_i \ & \leq \ 1+x_{g/q}\,, \\
2 \ &\leq \ & x_{\bar{\imath}'/g_{\mathrm{i}}} + x_i \ & \leq \ 1+a\,.
\end{aligned}
\tag{2.46}
$$

2.3.3.1 Gluon emission phase space of initial–initial dipoles

The phase-space parametrization is better worked out separately for both relevant II dipole splitting channels. First, the case of final-state gluon (g_{f}) emission, i.e. $\bar{\imath}'i \to \bar{\imath}'gi$, is discussed:

- The evolution variables are taken as suggested by the generalization of eqs. (2.25) and (2.26). Recalling eqs. (2.43), for the emission type considered here, the Lorentz invariant $p_\perp^2$ reads

$$
p_\perp^2 \ = \ \left| \frac{s_{\bar{\imath}'g}\, s_{gi}}{s_{\bar{\imath}'gi}} \right| \ = \ \frac{\hat{t}\,\hat{u}}{M^2} \ = \ M^2(1-x_i)(1-x_{\bar{\imath}'})\,,
\tag{2.47}
$$

and the Lorentz invariant y is given by

$$
y \ = \ \frac{1}{2}\,\ln\left|\frac{s_{gi}}{s_{\bar{\imath}'g}}\right| \ = \ \frac{1}{2}\,\ln\frac{\hat{u}}{\hat{t}} \ = \ \frac{1}{2}\,\ln\frac{1-x_{\bar{\imath}'}}{1-x_i}\,,
\tag{2.48}
$$

such that the kinematic invariants can be re-written as

$$
\begin{aligned}
\hat{s} \ &= \ s_{0g} \ = \ s_{\bar{\imath}'i} \ = \ M^2 + 2M\,p_\perp\cosh y \ \geq \ M^2\,, \\
\hat{t} \ &= \ s_{0i} \ = \ s_{\bar{\imath}'g} \ = \ -M\,p_\perp e^{-y} \ \leq \ 0\,, \\
\hat{u} \ &= \ s_{0\bar{\imath}'} \ = \ s_{gi} \ = \ -M\,p_\perp e^{+y} \ \leq \ 0\,.
\end{aligned}
\tag{2.49}
$$

- The bounds on the Mandelstam variables – or equally well – on the invariant energy fractions translate, of course, into bounds on the evolution variables that have to be respected during the emission's computation. As for FF dipoles emitting gluons, the sharp requirement is obtained from

$$
(a-1)\,M^2 \ = \ \hat{s}_{\max} - M^2 \ \geq \ \hat{s} - M^2 \ = \ -\hat{u} - \hat{t} \ = \ 2M\,p_\perp\cosh y\,.
\tag{2.50}
$$

Hence, the allowed phase space is described through

$$
|y| \ \leq \ \mathrm{arcosh}\,\frac{\sqrt{s}}{2\,p_\perp} \ = \ \mathrm{arcosh}\,\frac{1}{2\,x_\perp}\,,
\tag{2.51}
$$

and

$$p_{\perp,\mathrm{max}}^2 \;=\; \frac{(\hat{s}_{\mathrm{max}} - M^2)^2}{4\,M^2} \;=\; \frac{s}{4}\,, \tag{2.52}$$

where this time the quantity s, used to set down the rescaled $p_\perp$, is defined through

$$s \;=\; \left(\frac{\hat{s}_{\mathrm{max}} - M^2}{M}\right)^2 \;=\; (a-1)^2\,M^2\,. \tag{2.53}$$

Again, this setting is justified in the next item discussing the less accurate phase-space bounds. The above statement about $p_{\perp,\mathrm{max}}^2$ is gained from eq. (2.50) with $y = 0$ resulting from $(\cosh y)_{\mathrm{min}} = 1$. On the other hand, the maximal rapidity range, is determined by the overall cut-off on $p_\perp$ and the equation $\hat{s}_{\mathrm{max}} - M^2 = 2M\,p_{\perp,\mathrm{cut}}\cosh|y|_{\mathrm{max}}$.

- Loose constraints are obtained from

$$\hat{s}_{\mathrm{max}} - M^2 \;\geq\; \hat{s} - M^2 \;\geq\; -\hat{u}, -\hat{t} \tag{2.54}$$

and, as in the FF case, they result in symmetric rapidity limits,

$$|y| \;\leq\; \ln\frac{\hat{s}_{\mathrm{max}} - M^2}{M\,p_\perp} \;=\; \ln\frac{\sqrt{s}}{p_\perp} \;=\; -\ln x_\perp\,. \tag{2.55}$$

These estimates lead to the above definition of s, once they ought to be described by minus the logarithm of the rescaled transverse momentum, hence they again are visualized by a "triangle" in the $(y, z = \ln x_\perp)$ plane.

- The splitting kinematics concerning the new momenta will be detailed in sec. 2.3.3.3 together with the quark-emission process.

Taken together, when the results for the strict and loose rapidity bounds are compared to the FF case, they are found to be form-invariant apart from the differences in the definition of the scale s. Moreover, a new issue appears, which is absent for FF splittings, namely that the choice of the maximal partonic centre-of-mass scale regulates the maximal size of the allowed emission phase space. This will be discussed in more detail when presenting the shower algorithm within sec. 2.5.

2.3.3.2   Quark emission phase space of initial–initial dipoles

Along the lines of the previous section, the phase-space parametrization and its consequences are now discussed for gluon emission into the initial state (g_i), or, equivalently, (massless) quark emission into the final state, i.e. $\bar{q}_\mathrm{i}i \to qg_\mathrm{i}i$. Here, the associated (massless) parton can be thought of a spectator, similar to the FF gluon splitting into quarks. The details of the steps outlined in this section's introduction are given below:

- In regard to eqs. (2.43) and according to the comments of sec. 2.3.1, the Lorentz invariant evolution variables expressed through the Mandelstam variables read

$$p_\perp^2 \;=\; \left|\frac{s_{qg_\mathrm{i}}\,s_{g_\mathrm{i}i}}{s_{qg_\mathrm{i}i}}\right| \;=\; -\frac{\hat{t}\,\hat{s}}{M^2} \;=\; M^2(x_i - 1)(1 + x_q) \tag{2.56}$$

for the squared transverse momentum, and

$$y \;=\; \frac{1}{2}\,\ln\left|\frac{s_{g_i i}}{s_{q g_i}}\right| \;=\; \frac{1}{2}\,\ln\frac{\hat{s}}{-\hat{t}} \;=\; \frac{1}{2}\,\ln\frac{1+x_q}{x_i-1} \tag{2.57}$$

for the rapidity. This allows re-writing the kinematic invariants as

$$
\begin{aligned}
\hat{s} &= s_{0q} = s_{g_i i} = +M\,p_\perp e^{+y} \;\geq\; M^2\,, \\
\hat{t} &= s_{0i} = s_{q g_i} = -M\,p_\perp e^{-y} \;\leq\; 0\,, \\
\hat{u} &= s_{0 g_i} = s_{qi} = M^2 - 2M\,p_\perp \sinh y \;\leq\; 0\,,
\end{aligned}
\tag{2.58}
$$

implying, compared to the case of $g_{\rm f}$ emission, a different shape of the valid $(p_\perp, y)$ phase space covered by this type of emission.

- The accessible rapidity range is

$$\ln\left(\frac{M}{2p_\perp} + \sqrt{\frac{M^2}{4p_\perp^2}+1}\,\right) \;=\; \operatorname{arsinh}\frac{M}{2\,p_\perp} \;\leq\; y \;\leq\; \ln\frac{a\,M}{p_\perp}\,, \tag{2.59}$$

where the left and right bounds result from $\hat{u} \leq 0$ and $\hat{s} \leq \hat{s}_{\max}$, cf. eq. (2.45), respectively. This is well visualized in the $(y, z = \ln\frac{p_\perp}{a\,M})$ plane as a "strip" that emerges in the point $(y_{\min}, z_{\max} = -y_{\min})$ and is confined between $z = -y - \ln a$ and $z = -y$. The equations $y_{\min} = \operatorname{arsinh}\frac{M}{2\,p_{\perp,\max}}$ and $\hat{s}_{\max} = M\,p_{\perp,\max}\,e^{y_{\min}}$ yield

$$y_{\min} \;=\; \frac{1}{2}\,\ln\frac{\hat{s}_{\max}}{\hat{s}_{\max}-M^2} \;=\; \frac{1}{2}\,\ln\frac{a}{a-1}\,, \tag{2.60}$$

and

$$p_{\perp,\max}^2 \;=\; (\hat{s}_{\max}-M^2)\,\frac{\hat{s}_{\max}}{M^2} \;=\; a(a-1)\,M^2 \;=\; s\,. \tag{2.61}$$

- The scale s is again taken from a suitable overestimation of the exact rapidity range. In fact, the "strip" is safely covered by a "half-triangle" described through $y_{\min} \leq y \leq -z$. Accordingly, $\Delta y = -z - y_{\min} = \ln(p_{\perp,\max}^2/p_\perp^2)/2$, such that s is read off easily: $s = p_{\perp,\max}^2$, as already indicated in the above item. This s identification is in analogy to the previous cases featuring a full triangle whereas $\Delta y = \ln x_\perp^{-2} = \ln(s/p_\perp^2)$. Finally, notice that, as before, in both cases of strict and approximate limits, the maximally available emission phase space is defined through the value, which $\hat{s}_{\max}$ has been appointed to, see sec. 2.5.

- The splitting kinematics is presented in the next subsection.

2.3.3.3   Construction of the splitting kinematics

Once the evolution variables have been generated for a particular emission, the full kinematics of the splitting can be deduced. Remaining degrees of freedom are fixed with a few additional assumptions, i.e. through a splitting-specific recoil strategy. The Lorentz

invariant definition of the evolution variables guarantees the frame-independence of the actual construction. However, any construction method is unavoidably affected by the constraint that in the lab-frame the momenta of the incoming partons eventually point along the beam axis, which is a consequence of the collinear approximation in the factorization theorem. In the model presented here the initial–initial dipole kinematics qualified below is directly constructed in the lab-frame. Particularly, to handle the recoils for the case of $\bar{q}'_i q_i$ dipoles, the strategy according to Kleiss [117, 118] has been implemented.

Lab-frame kinematics: the preset orientation of the incoming partons simplifies specification of the $2 \to 1$ and $2 \to 2$ like momentum balances of eqs. (2.42). Thus, the emitted parton's recoil will directly be transferred to the entire final-state system, i.e. to all QCD and non-QCD final-state particles that are present before the emission takes place. As an example, consider the first emission in a Drell–Yan process, where the corresponding recoil is compensated for by the lepton pair. This recoil transfer results in $\tilde{p}_0 \neq p_0$, and, therefore, a Lorentz transformation $\mathcal{T}$ is necessary, which is defined through $p_0 = \mathcal{T}\tilde{p}_0$ and will be applied on all particles (whose vectors are summed up in $\tilde{p}_0$). For the construction of the momenta, a light-cone decomposition w.r.t. the beam axis is well suited, such that, for massless partons, the situation without and with the emission is summarized as [4]

$$
\begin{aligned}
\tilde{p}_i &= \left(\tilde{x}_+ \sqrt{S}, 0, \vec{0}\right) &\to& \quad p_i &= \left(x_+ \sqrt{S}, 0, \vec{0}\right), \\
\tilde{p}_{\bar{i}'/\bar{q}_i} &= \left(0, \tilde{x}_- \sqrt{S}, \vec{0}\right) &\to& \quad p_{\bar{i}'/g_i} &= \left(0, x_- \sqrt{S}, \vec{0}\right), \\
\tilde{p}_0 &= \left(M e^{\tilde{y}_0}, M e^{-\tilde{y}_0}, \vec{0}\right) &\to& \quad p_0 &= \left(M_\perp e^{y_0}, M_\perp e^{-y_0}, -\vec{\ell}_\perp\right), \\
& & & \quad p_{g/q} &= \left(\ell_\perp e^{y_e}, \ell_\perp e^{-y_e}, \vec{\ell}_\perp\right).
\end{aligned}
\tag{2.62}
$$

Further definitions are: $\hat{s}_0 = \tilde{x}_+ \tilde{x}_- S = M^2$ and $\tilde{y}_0 = \tilde{y}_{cm} = \ln(\tilde{x}_+/\tilde{x}_-)/2$ with $\tilde{y}_{cm}$ denoting the centre-of-mass rapidity of the collider system. The $\tilde{x}_\pm$, here functions of M, S and $\tilde{y}_{cm}$, parametrize the momentum fractions of the partons w.r.t their respective hadron. Employing $M_\perp^2 = M^2 + \ell_\perp^2$, after the emission they read

$$
x_\pm = \frac{\ell_\perp e^{\pm y_e} + M_\perp e^{\pm y_0}}{\sqrt{S}} \geq \tilde{x}_\pm.
\tag{2.63}
$$

Clearly, emissions leading to $x_\pm > 1$ must be rejected. The vector $\vec{\ell}_\perp = (\ell_\perp \cos\varphi, \ell_\perp \sin\varphi)$ and the quantity y_e denote the transverse momentum and the rapidity of the emitted parton w.r.t. the beam axis, respectively. In terms of the Mandelstam variables, cf. eq. (2.43), they are:

$$
\ell_\perp^2 = \frac{\hat{t}\hat{u}}{\hat{s}} \qquad \text{and} \qquad e^{y_e} = \frac{e^{y_0}}{M_\perp \ell_\perp}(-\hat{t} - \ell_\perp^2).
\tag{2.64}
$$

The azimuthal angle φ can in first approximation be assumed to be uniformly distributed, and unquestionably $\hat{s}$, $\hat{t}$, $\hat{u}$ are determined by the evolution parameters $p_\perp^2$ and y through

---

[4]The $\pm$ labelling is arbitrarily chosen and does not refer to some actual beam assignment of the partons contained by the original dipoles $\bar{i}'i$ or $\bar{q}_i i$.

eqs. (2.49) and eqs. (2.58) for g_f and g_i emissions, respectively. Below the squared lab-frame transverse momenta are exemplified as functions of $p_\perp$ and y. For gluon emission into the final state,

$$\ell_\perp^2 \;=\; \frac{M^2\,p_\perp^2}{\hat{s}} \;=\; \frac{p_\perp^2}{2\,p_\perp M^{-1}\cosh y + 1}\,, \tag{2.65}$$

whereas for quark emission,

$$\ell_\perp^2 \;=\; \frac{M^2\,p_\perp^2}{\hat{s}} - \frac{(M^2 + |\hat{t}|)\,|\hat{t}|}{\hat{s}} \;=\; (Me^{-y})^2\,(2\,p_\perp M^{-1}\sinh y - 1)\,. \tag{2.66}$$

When comparing both equations for the same ratio $p_\perp^2/\hat{s}$, it becomes apparent that in the lab-frame the emissions of quarks yield smaller physical transverse momenta than those of gluons.

To fix the last degree of freedom, an additional assumption is necessary, which is to preserve the rapidity of the system of outgoing particles, $y_0 = \tilde{y}_0 = \tilde{y}_\mathrm{cm}$.[5] Having the complete emission at hand, $\hat{s} = x_+ x_- S$ and $y_\mathrm{cm} = \ln(x_+/x_-)/2 = \ln(\hat{u}/\hat{t})/2 + y_e$.[6] In more detail,

$$y_\mathrm{cm} \;=\; \tilde{y}_\mathrm{cm} + \frac{1}{2}\ln\frac{\hat{u}}{\hat{t}} + \ln\left(\frac{-\hat{t}\,(\hat{s}+\hat{u})}{\sqrt{M^2\,\hat{s}\,\hat{t}\,\hat{u} + (\hat{t}\,\hat{u})^2}}\right) \;=\; \tilde{y}_\mathrm{cm} + \frac{1}{2}\ln\frac{M^2 - \hat{t}}{\hat{s}+\hat{t}}\,, \tag{2.67}$$

which exposes the impact of the $y_0 = \tilde{y}_\mathrm{cm}$ choice and shows that during splitting the system undergoes a rapidity shift. In addition, the new momentum fractions $x_\pm$ can be written down,

$$x_\pm \;=\; e^{\pm y_0}\sqrt{\frac{\hat{s}}{S}\left(\frac{M^2 - \hat{t}}{\hat{s}+\hat{t}}\right)^{\pm 1}}\,. \tag{2.68}$$

Finally the momenta, $\tilde{p}_0^{(j)}$, of all final-state particles, numbered by j, have to be transformed in order to account for the non-trivial change of $\tilde{p}_0 \to p_0$. Here, the Lorentz transformation $\mathcal{T}$ is specified as follows: the particles are boosted into the original dipole's centre-of-mass frame, afterwards the boost that forms p_0 out of $(M,\vec{0})$ is applied on them likewise. Altogether $p_0^{(j)} = \mathcal{B}(-\vec{p_0}/p_0^0)\mathcal{B}(\vec{\tilde{p}_0}/\tilde{p}_0^0)\,\tilde{p}_0^{(j)} = \mathcal{T}\,\tilde{p}_0^{(j)}$ is computed. This finalizes the construction of the on-shell kinematics of an individual emission.

Improved description of lepton–hadron correlations (Kleiss trick):   when analyzing eqs. (2.62) again, it is noticed that, apart from the azimuthal angle φ, which eventually fixes the vector $\vec{\ell}_\perp$, all unknown variables are determined by Lorentz invariants plus the

---

[5]If $y_\mathrm{cm} = \tilde{y}_\mathrm{cm}$ was naively exploited, the ratio of momentum fractions would remain constant, $x_+/x_- = \tilde{x}_+/\tilde{x}_-$, which constitutes a rather strange behaviour, since, for instance, very asymmetric starting configurations would persist to the end of the shower evolution.

[6]Particularly, for gluon emissions into the final state, $y_\mathrm{cm} - y_e = y$. This simply expresses that rapidity differences are invariant under boosts along the beam axis.

additional assumption $y_0 = y_{\mathrm{cm}}$.[7] In a first approximation, the choice is to uniformly distribute in azimuth w.r.t. the lab-frame, but more sophisticated schemes can be introduced correcting this simple ansatz. One such scheme can be derived from the work presented in [117] where it has been shown how to exactly factorize the first order tree-level corrections to the electroweak production of quarks. The corresponding Monte Carlo algorithm in fact is employed within the Lund CDM to arrange the splitting kinematics of $q_{\mathrm{f}}\bar{q}'_{\mathrm{f}}$ dipoles. In [118] this factorization was proven for scattering and annihilation processes involving initial states and corresponding algorithms were developed. Accordingly, for the $\bar{q}'_{\mathrm{i}}q_{\mathrm{i}}$ dipoles of this model, the suggestion of [118] has been employed to improve their splitting kinematics: the new momenta are constructed in the original dipole's rest frame in a distinct way, then they are transformed to the lab-frame such that the 0-particle's rapidity is preserved. The essence is that the primitive φ choice is substituted by a prescription, which e.g. in Drell–Yan processes correctly accounts for correlations between the radiated parton and the leptons. As before, the particles associated to the parent II dipole have to be transformed, however they now undergo a more complicated series of transformations out of the (before-emission) lab-frame, i.e. precisely

$$p_0^{(j)} \;=\; \mathcal{B}_{\parallel}\left(\beta_3 = \left.\frac{p_{0,+} - e^{2y_0}p_{0,-}}{p_{0,+} + e^{2y_0}p_{0,-}}\right|_{\hat{z}\text{-align.f.}}\right) \mathcal{R}_{\hat{z}}\,\mathcal{B}_{\mathrm{align}}\left(\left.\frac{\vec{p}_{\bar{\imath}'/g_{\mathrm{i}}} + \vec{p}_i}{p_{\bar{\imath}'/g_{\mathrm{i}}}^0 + p_i^0}\right|_{\mathrm{dip.rf.}}\right) \mathcal{B}_{\parallel}\left(\frac{\vec{\tilde{p}}_0}{\tilde{p}_0^0}\right)\tilde{p}_0^{(j)},$$

$$(2.69)$$

where starting from the right, one applies to a momentum: the longitudinal boost into the dipole's rest frame, the alignment boost followed by the rotation that brings the newly incoming partons onto the light-cone axis maintaining the initial $\pm$ assignments, and the final longitudinal boost to satisfy that y_0 stays the same as it was before the emission, i.e. $y_0 = \tilde{y}_0$.

2.3.4 Final–initial/initial–final dipoles

Owing to the QCD symmetry under charge conjugation, the discussion here concentrates on FI dipoles and the results can be easily transferred to IF dipoles.[8]

The branching of an FI dipole, fi, caused by a gluon may occur again in two ways, first, by releasing it to the final state, and, second, by putting it to the initial state, releasing an antiquark instead:

$$f(\tilde{k})\,i(\tilde{\ell}) \to f(k)\,g\,i(\ell) \qquad \text{and} \qquad f(\tilde{k})\,q_{\mathrm{i}}(\tilde{\ell}) \to f(k)\,g_{\mathrm{i}}\,\bar{q}(\ell)\,. \qquad (2.70)$$

In deep inelastic scattering, the evolution of the QCD part can be considered completely separated from the leptonic part, therefore, not only the squared momentum transfer $-Q^2$ is a constant while emitting a QCD particle, but also its vector can be assumed fixed. This is used as the paradigm for the construction of the FI dipole kinematics in this model. Hence, as for FF dipoles, the subsystem kinematically fully decouples from

---

[7]Therefore, when neglecting the angle φ, it makes no difference whether the kinematics is arranged in the parent dipole's rest frame or in the lab-frame.

[8]The change is to reverse the colour flow, $\bar{\imath}\bar{f} \mapsto fi$, and simply map the momenta.

the rest of the cascade. This implies that in contrast to the case of II dipoles only the partons directly involved in the splitting process need to be considered. Therefore,

$$\tilde{p}_0 \equiv p_0 \tag{2.71}$$

and

$$\tilde{p}_0 + \tilde{p}_{i/q_i} = \tilde{p}_f, \qquad p_0 + p_{i/g_i} = p_f + p_{g/\bar{q}}, \qquad \text{with} \qquad \tilde{p}_0^2 = M^2 \equiv -Q^2 < 0, \tag{2.72}$$

such that Q may be interpreted as the "mass" of the parent dipole. In correspondence to eqs. (2.18) and (2.19) the signature factors are $\tilde{\varsigma}_f = \varsigma_f = \varsigma_{g/\bar{q}} = 1$, all other ones equal -1. The underlying $2 \to 2$ character of the process then allows to define kinematic invariants for radiating FI dipoles:

$$\begin{aligned}
\hat{s} &= (p_0 + p_{i/g_i})^2 = (p_f + p_{g/\bar{q}})^2 = -Q^2(1 + x_{i/g_i}) \geq 0 \equiv \hat{s}_0, \\
\hat{t} &= (p_0 - p_f)^2 = (p_{g/\bar{q}} - p_{i/g_i})^2 = -Q^2(1 - x_f) \leq 0, \\
\hat{u} &= (p_0 - p_{g/\bar{q}})^2 = (p_f - p_{i/g_i})^2 = -Q^2(1 - x_{g/\bar{q}}) \leq 0, \tag{2.73}
\end{aligned}$$

and the identification of the energy-fraction expressions and the bounds are again for massless partons. The Mandelstam variables then satisfy

$$\hat{s} + \hat{t} + \hat{u} + Q^2 = 0 \qquad \text{such that} \qquad 2 + x_{i/g_i} = x_f + x_{g/\bar{q}}. \tag{2.74}$$

In analogy to the case of II dipoles, the maximal $\hat{s}$ is parametrized in terms of Q^2 as

$$\hat{s}_{\max} = a\,Q^2 \qquad \text{implying that} \qquad 0 \leq \hat{s} \leq \hat{s}_{\max} \leq \mathcal{S}. \tag{2.75}$$

Here, the quantity $\mathcal{S} = (p_0 + P)^2$ plays the rôle, which the squared collider energy S does for II dipoles, namely to function as the strict upper bound. The use of $p_0 = \tilde{p}_0$ and the rigorous definition of the Bjørken-x variable,

$$x_B = \frac{Q^2}{2\,\tilde{p}_0 P}, \tag{2.76}$$

where P labels the momentum of the incoming hadron, lead to

$$\mathcal{S} = Q^2 \left(\frac{1}{x_B} - 1 \right). \tag{2.77}$$

This signifies that the Bjørken-x determines the maximal range for the parameter a, namely $0 \leq a \leq 1/x_B - 1$. Since parton masses are neglected, $\hat{s}_0 = (\tilde{p}_0 + \tilde{p}_{i/q_i})^2 = 0$ and the Bjørken-x is the momentum fraction $\tilde{x}$ of the original incoming parton, $\tilde{p}_{i/q_i} = x_B P$. Employing $p_{i/g_i} = xP$, it is found that $x_B \leq x = -x_{i/g_i} x_B \leq (a+1)\,x_B \leq 1$ and the limits on x_{i/g_i} are clear:

$$\begin{aligned}
-1 - a &\leq & x_{i/g_i} & \leq -1, \\
1 + x_{i/g_i} &\leq & x_f,\, x_{g/\bar{q}} & \leq 1, \\
1 - a &\leq & x_f + x_{g/\bar{q}} & \leq 1. \tag{2.78}
\end{aligned}$$

The various other bounds then follow from eqs. (2.73) and (2.74).

2.3.4.1   Gluon emission phase space of final–initial dipoles

First, FI dipole gluon emissions emerging into the final state, $fi \to fgi$, are discussed in more detail, again, according to the steps outlined in the introduction of this section:

- The evolution variables are identified as before by particularizing eqs. (2.25) and (2.26) for the considered case. They read

$$p_\perp^2 \;=\; \left| \frac{s_{fg}\, s_{gi}}{s_{fgi}} \right| \;=\; \frac{\hat{s}\,\hat{t}}{-Q^2} \;=\; Q^2(|x_i| - 1)(1 - x_f)\,, \tag{2.79}$$

  and

$$y \;=\; \frac{1}{2}\,\ln \left| \frac{s_{gi}}{s_{fg}} \right| \;=\; \frac{1}{2}\,\ln \frac{-\hat{t}}{\hat{s}} \;=\; \frac{1}{2}\,\ln \frac{1 - x_f}{|x_i| - 1}\,, \tag{2.80}$$

  where eqs. (2.73) have been invoked to find the connection to the Mandelstam variables, which, hence, can be re-written as

$$\begin{aligned}
\hat{s} \;&=\; s_{0i} \;=\; s_{fg} \;=\; +Q\,p_\perp e^{-y} \;\geq\; 0\,, \\
\hat{t} \;&=\; s_{0f} \;=\; s_{gi} \;=\; -Q\,p_\perp e^{+y} \;\leq\; 0\,, \\
\hat{u} \;&=\; s_{0g} \;=\; s_{fi} \;=\; -Q^2 + 2Q\,p_\perp \sinh y \;\leq\; 0\,.
\end{aligned} \tag{2.81}$$

  Obviously, the rightmost relations for $\hat{s}$ and $\hat{t}$ are trivially fulfilled.

- The largest available phase space is found from $\hat{s} \leq \hat{s}_{\max}$, cf. eq. (2.75), and $\hat{u} \leq 0$, such that it can be characterized by

$$-\ln \frac{a\,Q}{p_\perp} \;\leq\; y \;\leq\; \operatorname{arsinh} \frac{Q}{2\,p_\perp}\,. \tag{2.82}$$

  In the $(y, z = \ln \frac{p_\perp}{a\,Q})$ plane these bounds manifest themselves in a deformed "triangle", whose right side is curved to the inside diverging for $y \to 0$ while approaching $z = -y - \ln a$ for $y \to \infty$. The left side of the "triangle" is described by $z \leq y$ and the intersection is at $(y = z_{\max}, z_{\max} = \ln \sqrt{1 + 1/a}\,)$, suggesting that

$$p_{\perp,\max}^2 \;=\; a\,(a + 1)\,Q^2 \;=\; (\hat{s}_{\max} + Q^2)\,\frac{\hat{s}_{\max}}{Q^2} \;=\; s\,. \tag{2.83}$$

  This statement is nicely confirmed as follows: for a given $p_\perp$, the $\hat{s}$ expression in eqs. (2.81) becomes smallest by taking the rapidity according to its right bound, i.e. $\hat{s}_{\min}(p_\perp) = Q\,p_\perp \exp(-\operatorname{arsinh} \frac{Q}{2\,p_\perp})$. This function is however monotonically rising with $p_\perp$. Therefore $\hat{s}_{\min}(p_{\perp,\max}) \equiv \hat{s}_{\max}$ must hold true and the analysis of this equation leads to eq. (2.83).

- The exact rapidity interval is overestimated through the "triangle" bounds that read $z \leq y \leq -z + 2\,z_{\max}$, resulting in $\Delta y = \ln(p_{\perp,\max}^2/p_\perp^2)$. Again the scale s is easily discovered applying the reasoning given under the similar item in sec. 2.3.3.2. Note that the final setting for s has been already indicated in eq. (2.83).

- Again, the actual construction of the momenta is separately detailed, see sec. 2.3.4.3.

To round off, the maximum size of the emission phase space is dictated – similar to II dipole splittings – by the choice of $\hat{s}_{\max}$, see eq. (2.75). This dependence is understandable, since, again in contrast to the FF case, the emission involving incoming partons implies a new initial state with a larger momentum fraction taken off the corresponding hadron.

2.3.4.2 Antiquark emission phase space of final–initial dipoles

In this subsection, the details concerning the phase-space parametrization are given for initial-state gluon emission involving massless (anti)quarks, $fq_{\mathrm{i}} \to fg_{\mathrm{i}}\bar{q}$. They are:

- According to eqs. (2.25), (2.26) and (2.73) the assignments that are present in this case imply that

$$
p_\perp^2 \;=\; \left| \frac{s_{fg_{\mathrm{i}}}\, s_{g_{\mathrm{i}}\bar{q}}}{s_{fg_{\mathrm{i}}\bar{q}}} \right| \;=\; \frac{\hat{u}\,\hat{t}}{Q^2} \;=\; Q^2 (1 - x_{\bar{q}})(1 - x_f)\,, \tag{2.84}
$$

and

$$
y \;=\; \frac{1}{2}\,\ln\left| \frac{s_{g_{\mathrm{i}}\bar{q}}}{s_{fg_{\mathrm{i}}}} \right| \;=\; \frac{1}{2}\,\ln\frac{\hat{t}}{\hat{u}} \;=\; \frac{1}{2}\,\ln\frac{1 - x_f}{1 - x_{\bar{q}}}\,, \tag{2.85}
$$

both of which being Lorentz invariants as usual. The Mandelstam variables can then be cast into the form

$$
\begin{aligned}
\hat{s} &\;=\; s_{0g_{\mathrm{i}}} \;=\; s_{f\bar{q}} \;=\; 2Q\,p_\perp \cosh y - Q^2 \;\geq\; 0\,, \\
\hat{t} &\;=\; s_{0f} \;=\; s_{g_{\mathrm{i}}\bar{q}} \;=\; -Q\,p_\perp e^{+y} \;\leq\; 0\,, \\
\hat{u} &\;=\; s_{0\bar{q}} \;=\; s_{fg_{\mathrm{i}}} \;=\; -Q\,p_\perp e^{-y} \;\leq\; 0\,,
\end{aligned} \tag{2.86}
$$

where the inequalities for $\hat{t}$ and $\hat{u}$ are satisfied by construction.

- The requirement $0 \leq \hat{s} \leq \hat{s}_{\max} = a\,Q^2$ in conjunction with eqs. (2.86) leads to

$$
\operatorname{arcosh}\frac{Q}{2\,p_\perp} \;\leq\; |y| \;\leq\; \operatorname{arcosh}\frac{\hat{s}_{\max} + Q^2}{2\,Q\,p_\perp} \;=\; \operatorname{arcosh}\frac{(a+1)\,Q}{2\,p_\perp}\,, \tag{2.87}
$$

where the inner and outer bounds follow from the lower and upper limits of the accessible $\hat{s}$ interval, respectively. Concerning the former the central rapidity region becomes unaccessible for emissions of $p_\perp < Q/2$. In the latter case the similarities to g_{f} emissions off II dipoles, cf. sec. 2.3.3.1, are fairly obvious, such that the definition of the scale s already becomes apparent for the antiquark emissions discussed here:

$$
s \;=\; \left(\frac{\hat{s}_{\max} + Q^2}{Q} \right)^2 \;=\; (a+1)^2\,Q^2\,, \tag{2.88}
$$

and the outer bounds therefore read

$$
|y| \;\leq\; \operatorname{arcosh}\frac{\sqrt{s}}{2\,p_\perp}\,. \tag{2.89}
$$

If the available squared energy $\hat{s}_{\max}$ completely goes into the generation of the transverse momentum then $\cosh y \equiv 1$ and the maximal $p_\perp$ is reached, given by

$$p_{\perp,\max}^2 \;=\; \frac{(\hat{s}_{\max} + Q^2)^2}{4\,Q^2} \;=\; \frac{1}{4}(a+1)^2\,Q^2 \;=\; \frac{s}{4}\,. \tag{2.90}$$

As in all cases involving initial-state partons, the adjustment of the size of the phase space is triggered by the choice of $\hat{s}_{\max}$, which will be discussed within the presentation of the full shower algorithm in sec. 2.5.

- Loose constraints stem from $\hat{s}_{\max} + Q^2 \geq -\hat{t}, -\hat{u}$ and yield an increased phase space w.r.t. the precise one discussed above:

$$|y| \;\leq\; \ln \frac{\hat{s}_{\max} + Q^2}{Q\,p_\perp} \;=\; \ln \frac{(a+1)\,Q}{p_\perp} \;=\; \ln \frac{\sqrt{s}}{p_\perp}\,. \tag{2.91}$$

  This invokes the usual "triangle" interpretation in the $(y, z = \ln x_\perp)$ plane. Moreover, it justifies the anticipated definition of the rescaling quantity s that has been already given under the previous item.

- The splitting kinematics will be discussed in the next subsection.

2.3.4.3   Construction of the emission momenta

The basic construction principles mentioned in secs. 2.3.1 and 2.3.3.3 are, of course, taken over when explicitly establishing the FI splitting kinematics. The kinematical decoupling, $p_0 \equiv \tilde{p}_0$, alleviates the task, since potential Lorentz transformations only touch the local splitting. Thus, including the fact that the squared dipole momentum $\tilde{p}_0^2 = (\tilde{p}_f - \tilde{p}_{i/q_\mathrm{i}})^2 = -Q^2$, the original dipole's Breit-frame constitutes the optimal frame to set up the three new four-momenta. Using light-cone notation again, in this frame the momenta read

$$
\begin{aligned}
\tilde{p}_0 &= \left(-Q,\, Q,\, \vec{0}\right) &\rightarrow\quad p_0 &= \left(-Q,\, Q,\, \vec{0}\right), \\[4pt]
\tilde{p}_{i/q_\mathrm{i}} &= \left(Q,\, 0,\, \vec{0}\right) &\rightarrow\quad p_{i/g_\mathrm{i}} &= \left(-x_{i/g_\mathrm{i}}\,Q,\, 0,\, \vec{0}\right), \\[4pt]
\tilde{p}_f &= \left(0,\, Q,\, \vec{0}\right) &\rightarrow\quad p_f &= \left(\frac{(1-x_f)(-x_{i/g_\mathrm{i}}-1)}{|x_{i/g_\mathrm{i}}|}\,Q,\; \frac{x_f - x_{i/g_\mathrm{i}} - 1}{|x_{i/g_\mathrm{i}}|}\,Q,\, \vec{b}_\perp\right), \\[4pt]
& & p_{g/\bar{q}} &= p_0 + p_{i/g_\mathrm{i}} - p_f\,.
\end{aligned}
\tag{2.92}
$$

The Breit-frame transverse momentum is given through $\vec{b}_\perp = (b_\perp \cos\varphi,\, b_\perp \sin\varphi)$, where

$$b_\perp \;=\; \frac{\sqrt{\hat{s}\,\hat{t}\,\hat{u}}}{\hat{s} + Q^2} \;=\; \sqrt{(1-x_f)(-x_{i/g_\mathrm{i}}-1)(x_f - x_{i/g_\mathrm{i}} - 1)} \;\; \frac{Q}{|x_{i/g_\mathrm{i}}|}\,. \tag{2.93}$$

Note that, e.g. for g_f emissions, it doubtlessly can become zero for $\hat{u} \to 0$ (in this limit the rapidity value associated to this emission then coincides with the y_+ bound, cf. sec. 2.3.4.1). This, however, happens independently of the actual value for the evolution variable $p_\perp$, therefore, ordering the emissions in $p_\perp$ does not impose any ordering in

$b_\perp$. Finally, the new Breit-frame momenta are transformed into the lab-frame. [9]

From eqs. (2.92) the recoil strategy can directly be read off: before and after the splitting the initial-state parton is fixed to the + direction of the light-cone decomposition, therefore to the beam axis [10], leaving the recoil to be completely compensated for by the final-state particle. Of course, more sophisticated recoil strategies following the ones of the Lund model and/or the Kleiss idea are possible. Especially the prescription for quark scattering processes given in [118] seems very attractive, since it includes correlations between leptons and partons associated to the lowest-order DIS process and the first emission. However, in the framework of this thesis, it is refrained from considering such improvements.

2.4 Dipole splitting cross sections for QCD radiation

This section is to display the characteristics of partonic radiation emerging from QCD colour dipoles as employed throughout this model, i.e. the point has come to concretize the approximate form of the splitting cross sections given in eq. (2.8). As the major result all gluon-emission types of $2 \to 3$ splitting functions are compiled. The details are worked out for the new types of I/FI dipoles that may appear in the initial state and their ability to either emit a gluon or a/an quark/antiquark. [11]

First, however, it is worthwhile to briefly review according to the Lund CDM [16, 17, 18, 11] the refinement of the eikonal splitting cross sections, in particular for the gluon arising from a $q_\text{f}\bar{q}'_\text{f}$ dipole. This serves as preparation before those splitting functions are specified that will be taken for dipole configurations that include at least one incoming parton, i.e. for $\bar{\imath}'i$ and $fi/\bar{\imath}\bar{f}$ dipoles, cf. the first three columns in tab. 2.1. Accordingly, the second part of this section is used to explicitly demonstrate the factorization that is applied to separate the emission from the first-order real matrix element. Having revealed the general structure of I/FI dipole branchings, in the third part the exploitation of crossing relations is presented to incorporate corrections, which go beyond the eikonal approximation. In turn things have been prepared to eventually derive the I/FI $2 \to 3$ dipole splitting functions.

2.4.1 Final-state colour dipoles

The $2 \to 3$ splitting $q\bar{q}' \to qg\bar{q}'$ is worked out from the comparison of the real-emission process $V \to q\bar{q}'g$ to the Born contribution for the vector-boson decay $V \to q\bar{q}'$. The lower-order expression in fact can be factored out the real emission, and, for massless partons, one finds the differential dipole splitting cross section,

$$\frac{d\sigma_{q\bar{q}' \to qg\bar{q}'}}{dx_q dx_{\bar{q}'}} = d\sigma_0 \, \frac{C_F \alpha_s}{2\pi} \, \frac{x_q^2 + x_{\bar{q}'}^2}{(1 - x_q)(1 - x_{\bar{q}'})} \,, \tag{2.94}$$

---

[9]This is done by inverting the transformations that (1) align the lab-frame momenta $\tilde{p}_{i/q_\text{i}}$ and $\tilde{p}_f$ and (2) rotate them afterwards onto the $\hat{z}$ axis.

[10]The choice $p_{i/g_\text{i}} = -x_{i/g_\text{i}} \tilde{p}_{i/q_\text{i}} = (-x_{i/g_\text{i}} x_B \sqrt{S}, 0, \vec{0}) \big|_\text{lab-f.}$ constitutes a Lorentz invariant choice.

[11]The splitting of gluons potentially contained by the I/FI dipole has not yet been considered in full detail, this is left for future consideration.

in terms of the Lorentz invariant energy fractions defined in eq. (2.21). C_F is the colour factor of this emission. Re-expressed through the corresponding dipole evolution variables invoking the Jacobian read off $M^2 dx_q dx_{\bar{q}'} = dp_\perp^2 dy$, the exact differential splitting cross section and its eikonal (soft-gluon/no-spin-correlation [12]) approximation become

$$
\begin{aligned}
\frac{d\sigma_{q\bar{q}' \to qg\bar{q}'}}{dp_\perp^2 dy} &= d\sigma_0 \, \frac{C_F \alpha_s}{2\pi} \, \frac{(1 - \frac{p_\perp}{M} e^{+y})^2 + (1 - \frac{p_\perp}{M} e^{-y})^2}{p_\perp^2} = d\sigma_0 \, \frac{C_F \alpha_s}{2\pi} \, \frac{x_1^2 + x_3^2}{p_\perp^2} \\
&= d\sigma_0 \, \frac{C_F \alpha_s}{2\pi} \, \frac{x_q^2(p_\perp, y) + x_{\bar{q}'}^2(p_\perp, y)}{p_\perp^2}
\end{aligned}
\tag{2.95}
$$

and

$$
\frac{d\sigma_{q\bar{q}' \to qg\bar{q}'}^{\text{approx}}}{dp_\perp^2 dy} = d\sigma_0 \, \frac{C_F \alpha_s}{2\pi} \, \frac{2}{p_\perp^2} \,,
\tag{2.96}
$$

respectively. In regard of $x_{q,\bar{q}'} \leq 1$, the latter expression can be easily revealed from the former. Because of their positive definiteness, they can be folded into Sudakov exponentials that yield the all-orders expressions of emitting no parton between two evolution scales. Its probabilistic interpretation forms the basis of determining the cascading, i.e. the set of evolution variables that characterizes the next emission. The phase-space limits discussed in sec. 2.3.2 qualify the Sudakov computation of these variables.

Similar reasoning yields the splitting cross sections for quark–gluon and gluon–gluon dipoles [119] and the results read

$$
\begin{aligned}
\frac{d\sigma_{qg \to qgg}}{dp_\perp^2 dy} &= d\sigma_0 \, \frac{C_A \alpha_s}{4\pi} \, \frac{(1 - \frac{p_\perp}{M} e^{+y})^2 + (1 - \frac{p_\perp}{M} e^{-y})^3}{p_\perp^2} = d\sigma_0 \, \frac{C_A \alpha_s}{4\pi} \, \frac{x_1^2 + x_3^3}{p_\perp^2} \,, \\
\frac{d\sigma_{gg \to ggg}}{dp_\perp^2 dy} &= d\sigma_0 \, \frac{C_A \alpha_s}{4\pi} \, \frac{(1 - \frac{p_\perp}{M} e^{+y})^3 + (1 - \frac{p_\perp}{M} e^{-y})^3}{p_\perp^2} = d\sigma_0 \, \frac{C_A \alpha_s}{4\pi} \, \frac{x_1^3 + x_3^3}{p_\perp^2} \,.
\end{aligned}
\tag{2.97}
$$

Note that a factor of $\frac{1}{2}$ has entered these differential cross sections, since gluons are always shared among two dipoles. Introducing an additional factor, ξ, for the Lund FF dipoles that contain a gluon, it is specified by $\xi = \frac{1}{2}$, otherwise by $\xi = 1$. The eikonal approximations or, equally well, overestimated cross sections are then given as

$$
\frac{d\sigma_{qg \to qgg}^{\text{approx}}}{dp_\perp^2 dy} = \frac{d\sigma_{gg \to ggg}^{\text{approx}}}{dp_\perp^2 dy} = d\sigma_0 \, \frac{C_A \alpha_s}{4\pi} \, \frac{2}{p_\perp^2} \,.
\tag{2.98}
$$

Kinematic structure of the single emission

Making use of the factorization, the information of the kinematic structure of the singled-out emission can be solely associated with a function $\mathcal{K}$ universally defined through

$$
\mathcal{K}_{\tilde{k}\tilde{\ell} \to kg\ell}(s_{kg\ell}, s_{kg}, s_{g\ell}) = \frac{1}{8\pi \, C\alpha_s} \, \frac{|\mathcal{M}_{0 \to kg\ell}|^2}{|\mathcal{M}_{0 \to \tilde{k}\tilde{\ell}}|^2} \,,
\tag{2.99}
$$

where owing to energy-momentum conservation and zero parton masses, cf. eq. (2.23), the set of two-parton scalars, which the function depends on, is arbitrarily interchangeable

---

[12]The overestimated cross section just corresponds to the soft-gluon/no-spin-correlation approximation.

between s_{kg}, $s_{g\ell}$ and s_{kg}, $s_{k\ell}$ and $s_{k\ell}$, $s_{g\ell}$. The colour factor labelled C has been introduced explicitly and can be one of the following, $C = C_F = \frac{4}{3}$ for gluons emitted off quarks, $C = C_A = 3$ for gluons emitted off gluons, or $C = T_R = \frac{1}{2}$ for gluon splittings, assuming $N_C = 3$ for the number of colours.

If applied to gluon emission off a $q_f\bar{q}_f$ dipole ($C = C_F$, $s_{kg\ell} = s_{qg\bar{q}} = M^2$), one may use the colour-summed, spin-averaged matrix element squared for the process $\gamma^* \to q\bar{q}g$ [120], which is written as

$$\overline{|\mathcal{M}_{\gamma^* \to q\bar{q}g}|^2} = 32e^2 e_q^2 \, 4\pi\alpha_s \, \frac{x_q^2 + x_{\bar{q}}^2}{(1 - x_q)(1 - x_{\bar{q}})} \tag{2.100}$$

and, for the before-emission state $\gamma^* \to q\bar{q}$, one may utilize

$$\overline{|\mathcal{M}_{\gamma^* \to q\bar{q}}|^2} = 24e^2 e_q^2 \, \tilde{p}_q\tilde{p}_{\bar{q}} = 12e^2 e_q^2 \, M^2 \,. \tag{2.101}$$

Accordingly, eq. (2.94) can be re-written for equal quark flavours using the kinematic function $\overline{\mathcal{K}}_{q\bar{q} \to qg\bar{q}}(M^2, s_{qg} \to x_{\bar{q}}, s_{g\bar{q}} \to x_q)$, where the notation for colour-summing spin-averaging has been adopted,

$$\frac{d\sigma_{q\bar{q} \to qg\bar{q}}}{dx_q dx_{\bar{q}}} = d\sigma_0 \, \frac{C_F \alpha_s}{2\pi} \, M^2 \, \overline{\mathcal{K}}_{q\bar{q} \to qg\bar{q}}(M^2, s_{qg}, s_{g\bar{q}}) \,. \tag{2.102}$$

Similar equations hold for the other FF kinematic functions connecting them to the respective differential dipole splitting cross sections, see eqs. (2.97). Importantly, the kinematic functions obey crossing symmetry. Hence, later on this fact can be exploited: the kinematic structure of, e.g. the $2 \to 3$ splitting $\bar{q}_i q_i \to \bar{q}_i g q_i$ can be straightly related to that of the FF splitting $q\bar{q} \to qg\bar{q}$.

2.4.2 Identifying the generic structure of $2 \to 3$ dipole splittings involving initial states

In the dipole picture one is interested in a description of the emission as coherently shared between the two partons that establish the dipole. Therefore, as a basis in finding $2 \to 3$ splitting cross sections, it is advantageous to use tree-level matrix elements that exhibit the real-emission process and to relate them to the Born level ones, which correspond to the before-emission state represented by the parent dipole. It is to explore under which approximations the desired factorization of the emission off the Born process can be achieved. In this way, the final-state partons radiated off the I/FI dipoles potentially inherit the characteristics one obtains from calculating real-gluon/(anti)quark emission on the partonic level. Accordingly, first-order real corrections may already be encoded in the splitting formulae, automatically finding their way into the calculation of the emission.

Initial–initial dipole splittings

For the class of dipoles exclusively made up of colour-connected incoming partons, cf. first column in tab. 2.1, the extraction of dipole splitting cross sections has to be done on the level of hadronic cross sections to correctly account for PDF effects and possible phase-space (suppression) factors. The $\bar{\imath}'i$ dipole's situation before the emission (indexed
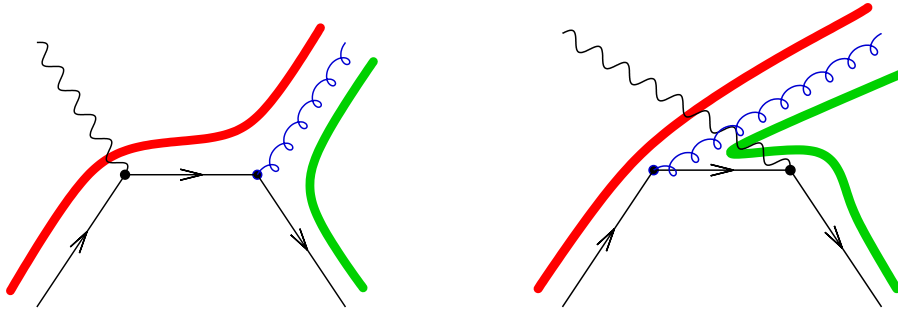
Figure 2.3: Relevant Feynman diagrams contributing to vector boson production in association with a gluon, the $\hat{t}$ and $\hat{u}$ channel contributions are shown on the left and right part of the figure, respectively. The modification of the colour flow due to the emission is illustrated by the thick lines accompanying the particle ones.

by 0) can be expressed by the $2 \to 1$ Born term of creating a gauge boson V (if considering a $\bar{q}_i q_i'$ dipole) or off-shell parton of mass M through the matrix element $\mathcal{M}_0$, where the momentum balance is given in eq. (2.42). According to the factorization theorem, the hadronic Born differential cross section is

$$d\sigma_0 \;=\; f_{\bar{i}'}(\tilde{x}_\pm, \tilde{\mu}_\mathrm{F})\, f_i(\tilde{x}_\mp, \tilde{\mu}_\mathrm{F}) \, \frac{\pi}{S} \, \frac{|\mathcal{M}_0|^2}{M^2} \, d\tilde{y}_\mathrm{cm}\,, \tag{2.103}$$

and the definitions are as introduced in sec. 2.3.3.3. At leading order the $f_k(\tilde{x}_\pm, \tilde{\mu}_\mathrm{F})$ are the PDFs describing how likely parton k escapes from the nucleon moving along the beam direction; $\tilde{\mu}_\mathrm{F}$ names the factorization scale (here defined in squared energy units).
Re-doing the exercise for the radiative correction, which is described through a $2 \to 2$ matrix element and corresponds to the after-emission state (indexed by 1), one obtains

$$d\sigma_1 \;=\; f_{\bar{i}'(g)}(x_\pm, \mu_\mathrm{F})\, f_i(x_\mp, \mu_\mathrm{F}) \, \frac{1}{S} \, \frac{|\mathcal{M}_1|^2}{16\pi \hat{s}_1^2} \, d\hat{s}_1 \, d\hat{t}_1 \, dy_\mathrm{cm}\,, \tag{2.104}$$

where for the partonic differential cross section $d\hat{\sigma}_1/d\hat{t}_1 = |\mathcal{M}_1|^2/(64\pi \hat{s}_1 p_\mathrm{cm}^2)$ has been employed, with the incoming partons taken on their mass shell, $p_\mathrm{cm}^2 = \hat{s}_1/4$. The Mandelstam variables here carrying the additional index 1 are taken according to eqs. (2.43).

Specifically, if one considers the first QCD-type emission in vector boson production (real-gluon bremsstrahlung or QCD Compton), this corresponds to the coherent emission of a gluon or a(n) (anti)quark off the primary $\bar{q}_i q_i'$ dipole or, correspondingly, off its associated colour line (cf. fig. 2.1). For gluon bremsstrahlung $\bar{q}q' \to Vg$ (index g_f), the amplitude can be obtained from the Feynman diagrams depicted in fig. 2.3. The partonic squared matrix element $\overline{|\mathcal{M}_1|^2}$, whose colour and spin indices are averaged (summed) over initial (final) states, can then be expressed in terms of the Born amplitude squared,

$$\overline{|\mathcal{M}_1^{g_\mathrm{f}}|^2} \;=\; 4\,\frac{8}{3}\, \pi \alpha_s \, \frac{\overline{|\mathcal{M}_0|^2}}{M^2} \, \frac{M^4 + \hat{s}_1^2 - 2\hat{u}_1 \hat{t}_1}{\hat{u}_1 \hat{t}_1}\,, \tag{2.105}$$

such that, exploiting eqs. (2.103) and (2.104), it yields the differential hadronic cross section

$$d\sigma_1^{g_f} = \left(d\sigma_0 \frac{dy_{\text{cm}}}{d\tilde{y}_{\text{cm}}} \right) \frac{f_{\bar{q}}(x_{\pm}, \mu_{\text{F}}) \, f_{q'}(x_{\mp}, \mu_{\text{F}})}{f_{\bar{q}}(\tilde{x}_{\pm}, \tilde{\mu}_{\text{F}}) \, f_{q'}(\tilde{x}_{\mp}, \tilde{\mu}_{\text{F}})} \frac{M^4}{\hat{s}_1^2} \frac{2\alpha_s}{3\pi} \frac{M^4 + \hat{s}_1^2 - 2\hat{u}_1\hat{t}_1}{M^4 \, \hat{u}_1\hat{t}_1} \, d\hat{s}_1 \, d\hat{t}_1 \,. \tag{2.106}$$

Clearly, the factorization $d\sigma_1 = d\sigma_0 \, d\mathcal{F}_{\bar{q}_i q'_i \to \bar{q}_i g q'_i} \frac{dy_{\text{cm}}}{d\tilde{y}_{\text{cm}}}$ is unambiguous, if, by imposing a suitable recoil strategy, the rapidity derivative becomes identical to 1. The best instance is to introduce a shift on $\tilde{y}_{\text{cm}}$ through some function $\hat{y}$ that exclusively depends on the variables associated to the emission,

$$y_{\text{cm}} = \tilde{y}_{\text{cm}} + \hat{y}(M^2, \hat{s}_1, \hat{t}_1) \,. \tag{2.107}$$

This is in fact the case for the recoil strategies presented in sec. 2.3.3.3, where eq. (2.67) is exactly of the suggested form. Assuming, for the moment, that recoil strategies of that kind can be found generally, then, for the desired splitting $\bar{q}_i q'_i \to \bar{q}_i g q'_i$, one hence arrives at the differential splitting cross section

$$\frac{1}{d\sigma_0} \frac{d\sigma_{\bar{q}_i q'_i \to \bar{q}_i g q'_i}}{d\hat{s} d\hat{t}} = \left[\frac{f_{\bar{q}}(x_{\pm}, \mu_{\text{F}}) \, f_{q'}(x_{\mp}, \mu_{\text{F}})}{f_{\bar{q}}(\tilde{x}_{\pm}, \tilde{\mu}_{\text{F}}) \, f_{q'}(\tilde{x}_{\mp}, \tilde{\mu}_{\text{F}})} \right] \left[\frac{M^4}{\hat{s}^2} \right] \frac{C_F \alpha_s}{2\pi} \frac{f(M^2, \hat{u}, \hat{t})}{M^4 \, \hat{u}\hat{t}} \,, \tag{2.108}$$

where the function f can be written as

$$f(M^2, \hat{u}, \hat{t}) = M^4 + \hat{s}^2 - 2\hat{u}\hat{t} = \hat{u}^2 + \hat{t}^2 + 2\hat{s}M^2 = (M^2 - \hat{u})^2 + (M^2 - \hat{t})^2 \,. \tag{2.109}$$

and the subscript labelling the after-emission state is now omitted. If compared to the g_f emission process of FF dipoles, cf. eq. (2.94), which – using $M^4 \, dx_q dx_{\bar{q}'} = ds_{qg} ds_{g\bar{q}'}$ – is re-expressed by

$$\frac{1}{d\sigma_0} \frac{d\sigma_{q\bar{q}' \to q g \bar{q}'}}{ds_{qg} ds_{g\bar{q}'}} = \frac{C_F \alpha_s}{2\pi} \frac{(M^2 - s_{qg})^2 + (M^2 - s_{g\bar{q}'})^2}{M^4 \, s_{qg} s_{g\bar{q}'}} \leq \frac{C_F \alpha_s}{2\pi} \frac{2}{s_{qg} s_{g\bar{q}'}} \,, \tag{2.110}$$

additional factors are recognized for the II scenario, namely a ratio of PDFs or a PDF weight, $\mathcal{W}_{\text{PDF}}$ (first term in squared brackets), and a phase-space weight, $\mathcal{W}_{\text{PSP}}$ (second term in squared brackets). As in the FF case, full first-order real corrections will be present in the emission's computation, since the parton-level matrix-element structure appears in the last part of eq. (2.108). The maximum of the function f is $M^4 + \hat{s}^2$, which, if divided by $\hat{s}^2$, can be safely overestimated by a factor of 2. Thus, the approximate differential cross section can be noted down,

$$\frac{1}{d\sigma_0} \frac{d\sigma_{\bar{q}_i q'_i \to \bar{q}_i g q'_i}^{\text{approx}}}{d\hat{s} d\hat{t}} = \mathcal{N}_{\text{PDF}} \frac{C_F \alpha_s}{2\pi} \frac{2}{\hat{u}\hat{t}} \,, \tag{2.111}$$

where the constant $\mathcal{N}_{\text{PDF}}$ is used to estimate the upper bound of the PDF weight.

For quark [13] emission $gq' \to Vq$ (index g_i), the amplitude can be worked out using the Feynman diagrams illustrated in fig. 2.4. In the dipole-shower picture this process alternatively can be viewed as an initial-gluon emission off a $\bar{q}_i q'_i$ dipole, while turning the
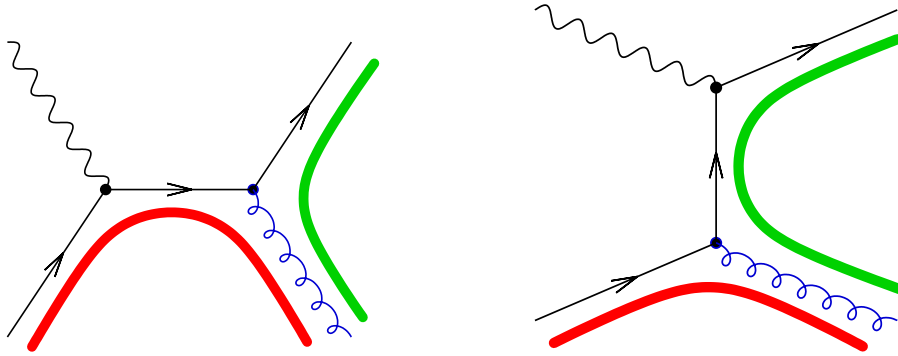
Figure 2.4: Relevant Feynman diagrams contributing to vector boson production in association with a quark, the $\hat{t}$ and $\hat{s}$ channel contributions are shown on the left and right side of the figure, respectively. The modification of the colour flow due to the emission again is illustrated by the thick lines. Consider e.g. $gq' \to Wq$ production; starting from the $\bar{q}_{\mathrm{i}} q'_{\mathrm{i}}$ dipole, an FI dipole $q_{\mathrm{f}} g_{\mathrm{i}}$ and a successor II dipole $g_{\mathrm{i}} q'_{\mathrm{i}}$ will be generated with a dual rôle played by the gluon g_{i}.

previously incoming antiquark into a final-state offspring. The partonic squared matrix element can again be written in terms of the Born amplitude squared,

$$\overline{|\mathcal{M}_1^{g_{\mathrm{i}}}|^2} \;=\; 4\,\pi\alpha_s\,\frac{\overline{|\mathcal{M}_0|^2}}{M^2}\,\frac{M^4 + \hat{u}_1^2 - 2\hat{s}_1\hat{t}_1}{-\hat{s}_1\hat{t}_1}\,. \tag{2.112}$$

One then proceeds along the same lines to derive the differential branching cross section, which for quark emission eventually reads (omitting the index 1 again)

$$\frac{1}{d\sigma_0}\,\frac{d\sigma_{\bar{q}_{\mathrm{i}} q'_{\mathrm{i}} \to q g_{\mathrm{i}} q'_{\mathrm{i}}}}{d\hat{s}d\hat{t}} \;=\; \left[\frac{f_g(x_\pm, \mu_{\mathrm{F}})\,f_{q'}(x_\mp, \mu_{\mathrm{F}})}{f_{\bar{q}}(\tilde{x}_\pm, \tilde{\mu}_{\mathrm{F}})\,f_{q'}(\tilde{x}_\mp, \tilde{\mu}_{\mathrm{F}})}\right]\left[\frac{M^4}{\hat{s}^2}\right]\frac{T_R\alpha_s}{2\pi}\,\frac{f(M^2, \hat{s}, \hat{t})}{-M^4\,\hat{s}\hat{t}}\,, \tag{2.113}$$

with the function f this time defined as

$$f(M^2, \hat{s}, \hat{t}) \;=\; M^4 + \hat{u}^2 - 2\hat{s}\hat{t} \;=\; \hat{s}^2 + \hat{t}^2 + 2\hat{u}M^2 \;=\; (M^2 - \hat{s})^2 + (M^2 - \hat{t})^2\,. \tag{2.114}$$

Certainly, since $\hat{s} - M^2 \le \hat{s}$ and $M^2 - \hat{t} = \hat{s} + \hat{u} \le \hat{s}$, the maximum of the function f is given by $2\hat{s}^2$. Using again $\mathcal{N}_{\mathrm{PDF}}$ to denote an estimate for the upper limit of the PDF weight, the approximation of the differential cross section hence is

$$\frac{1}{d\sigma_0}\,\frac{d\sigma_{\bar{q}_{\mathrm{i}} q'_{\mathrm{i}} \to q g_{\mathrm{i}} q'_{\mathrm{i}}}^{\mathrm{approx}}}{d\hat{s}d\hat{t}} \;=\; \mathcal{N}_{\mathrm{PDF}}\,\frac{T_R\alpha_s}{2\pi}\,\frac{2}{-\hat{s}\hat{t}}\,. \tag{2.115}$$

In fact, the details of the factorization only have been demonstrated for gluon and (anti)quark emission off a $\bar{q}_{\mathrm{i}} q'_{\mathrm{i}}$ dipole by means of the factorization properties of the underlying $2 \to 2$ annihilation-plus-gluon, $\bar{q}q' \to Vg$, and QCD Compton processes,

---

[13]Antiquark emission is straightforwardly deduced from the symmetry.

$gq'(\bar{q}g) \to Vq(V\bar{q}')$, respectively. It can be assumed that for all other II dipoles the factorization can be shown similarly, so that initial–initial dipole splitting cross sections may in general be written as

$$
d\sigma_{\bar{\imath}'i(\bar{q}_\mathrm{i}i)\to\bar{\imath}'gi(qg_\mathrm{i}i)} \;=\; \left[d\sigma_0 \frac{dy_\mathrm{cm}}{d\tilde{y}_\mathrm{cm}} \right] \frac{f_{\bar{\imath}'(g)}(x_\pm,\mu_\mathrm{F})\, f_i(x_\mp,\mu_\mathrm{F})}{f_{\bar{\imath}'(\bar{q})}(\tilde{x}_\pm,\tilde{\mu}_\mathrm{F})\, f_i(\tilde{x}_\mp,\tilde{\mu}_\mathrm{F})} \frac{M^2}{s^2_{\bar{\imath}'i(g_\mathrm{i}i)}}\, \xi\, \frac{C\alpha_s}{2\pi}
$$
$$
\times\; \mathcal{K}_{\bar{\imath}'i(\bar{q}_\mathrm{i}i)\to\bar{\imath}'gi(qg_\mathrm{i}i)}(M^2, s_{\bar{\imath}'i(g_\mathrm{i}i)}, s_{\bar{\imath}'g(qg_\mathrm{i})})\, ds_{\bar{\imath}'i(g_\mathrm{i}i)}\, ds_{\bar{\imath}'g(qg_\mathrm{i})}
\tag{2.116}
$$

where in the parentheses the case of quark emission is signified. Furthermore, the function $\mathcal{K}_{\bar{\imath}'i(\bar{q}_\mathrm{i}i)\to\bar{\imath}'gi(qg_\mathrm{i}i)}$ is revealed, which on more general grounds has been already introduced in sec. 2.4.1, see eq. (2.99).

$$
\mathcal{K}_{\bar{\imath}'i(\bar{q}_\mathrm{i}i)\to\bar{\imath}'gi(qg_\mathrm{i}i)}(M^2, s_{\bar{\imath}'i(g_\mathrm{i}i)}, s_{\bar{\imath}'g(qg_\mathrm{i})}) \;=\; \frac{1}{8\pi\, C\alpha_s} \frac{|\mathcal{M}_{\bar{\imath}'i(gi)\to 0g(0q)}|^2}{|\mathcal{M}_{\bar{\imath}'i(\bar{q}i)\to 0}|^2}\,,
\tag{2.117}
$$

and carries as before the sole kinematic information of the emission. In the next section its connection to the FF kinematic functions is clarified. In the discussed examples the colour factor is $C = C_F$ and $C = T_R$ for final- and initial-gluon emissions, respectively. Note that also the gluon-sharing factor ξ has been introduced in the general formula, respecting a potential sharing of gluons with other dipoles.

Final–initial dipole splittings

The generic structure of final–initial dipole splitting cross sections for gluon (antiquark) emissions into the final state is written [14] (in the limit of zero quark masses)

$$
\frac{d\sigma_{fi(fq_\mathrm{i})\to fgi(fg_\mathrm{i}\bar{q})}}{d\sigma_0} \;=\; \frac{f_{i(g)}(-x_{i/g_\mathrm{i}}x_B,\mu_\mathrm{F})}{f_{i(q)}(x_B,\tilde{\mu}_\mathrm{F})} \frac{Q^2}{(s_{fg(f\bar{q})}+Q^2)^2}\, \xi\, \frac{C\alpha_s}{2\pi}
$$
$$
\times\; \mathcal{K}_{fi(fq_\mathrm{i})\to fgi(fg_\mathrm{i}\bar{q})}(-Q^2, s_{fg(f\bar{q})}, s_{gi(g_\mathrm{i}\bar{q})})\, ds_{fg(f\bar{q})}\, ds_{gi(g_\mathrm{i}\bar{q})}\,,
\tag{2.118}
$$

where the appearing two-parton squared masses are related to the Mandelstam variables stated in eqs. (2.73), $s_{fg(f\bar{q})} = \hat{s}$ and $s_{gi(g_\mathrm{i}\bar{q})} = \hat{t}$, see also sec. 2.3.4. The kinematic function $\mathcal{K}_{fi(fq_\mathrm{i})\to fgi(fg_\mathrm{i}\bar{q})}$ is defined according to eq. (2.99) as

$$
\mathcal{K}_{fi(fq_\mathrm{i})\to fgi(fg_\mathrm{i}\bar{q})}(-Q^2, s_{fg(f\bar{q})}, s_{gi(g_\mathrm{i}\bar{q})}) \;=\; \frac{1}{8\pi\, C\alpha_s} \frac{|\mathcal{M}_{0i(0g)\to fg(f\bar{q})}|^2}{|\mathcal{M}_{0i(0q)\to f}|^2}\,.
\tag{2.119}
$$

These formulae have been acquired in the same manner as those of II dipoles, namely by comparing the (differential) hadronic cross sections before and after the emission. They again rest upon a factorization theorem, which this time is appropriate to cope with scattering scenarios. Note that the first two terms on the right-hand side of eq. (2.118) show, as for emissions off II dipoles, the additional PDF and phase-space weights, respectively, which enter the calculation here but are absent in the generation of FF dipole radiation, cf. e.g. eq. (2.102).

---

[14] The cross sections of initial–final dipoles are understood using the mapping outlined in sec. 2.3.4.

The remaining task is the calculation of the associated kinematic functions to eventually achieve explicit factorized splitting cross sections. Hereby it is essential that a matrix-element factorization be available, which can be resorted to. For qq'_i dipoles emitting gluons, the ratios between the first and zeroth order QCD matrix elements [15] can be formed by starting off the two typical real-correction processes to leading order DIS, namely the QCD Compton and the boson–gluon fusion process. Those are compared to the sole scattering of a quark caused by a space-like vector boson. In this way the dipole's gluon emission will again be treated as coherently arising from the colour line that couples the incoming and the outgoing quark. Utilizing the corresponding colour-summed, spin-averaged matrix elements given e.g. in [120], factorization is indeed achieved rendering

$$\overline{\mathcal{K}}_{qq'_\mathrm{i}\to qgq'_\mathrm{i}}(-Q^2,\hat{s},\hat{t}) = \frac{1}{Q^2}\frac{\hat{s}^2 + \hat{t}^2 - 2\hat{u}Q^2}{-\hat{s}\hat{t}} = -\frac{x^2_{q'_\mathrm{i}} + x^2_q}{Q^2(1 + x_{q'_\mathrm{i}})(1 - x_q)} \tag{2.120}$$

for g_f radiation off an qq'_i dipole using $C = C_F$, and

$$\overline{\mathcal{K}}_{qq'_\mathrm{i}\to qg_\mathrm{i}\bar{q}'}(-Q^2,\hat{s},\hat{t}) = \frac{1}{Q^2}\frac{\hat{u}^2 + \hat{t}^2 - 2\hat{s}Q^2}{\hat{u}\hat{t}} = \frac{x^2_{\bar{q}'} + x^2_q}{Q^2(1 - x_{\bar{q}'})(1 - x_q)} \tag{2.121}$$

for g_i radiation off an qq'_i dipole where $C = T_R$. For the definitions of the Mandelstam variables and their total sum, see eqs. (2.73) and eq. (2.74), respectively. The latter instance determines the production of an FI–IF dipole (sub)system, qg_i–$g_\mathrm{i}\bar{q}'$, whereas the former to finish up with the configuration qg_f–$g_\mathrm{f}q'_\mathrm{i}$, which constitutes a local FF–FI system. Finally, the generic structure from above has to be combined with these specific results of the matrix-element factorization to yield the differential FI dipole splitting cross sections. In sec. 2.4.5 they will be transformed to readily exhibit their dependence on the evolution variables.

2.4.3 $2 \to 3$ colour-dipole splittings from crossing relations

Given the general structure of initial–initial and final–initial dipole splitting cross sections through eqs. (2.116) and (2.118), for those containing a gluon leg, it only remains to identify their kinematic functions $\mathcal{K}$ and to appropriately adapt their colour factors. The first can be achieved exploiting the crossing symmetry of invariant squared amplitudes, which allows to transform the kinematic structure of an interaction process to hold under a different constellation involving the same particles. [16] In this way cross-section results for I/FI dipoles can be derived from the FF dipole ones given through and utilized in the Lund colour-dipole model.

Schematically, it is summarized as follows,

- extract the kinematic function from the corresponding Lund FF dipole splitting cross section according to eq. (2.102);

---

[15]To which extent correlations are included depends on the matrix elements selected to characterize the emission process. In principle, it is possible to go beyond the simple choice made here and additionally take the leptons into account that constitute the scattering boson, as it has been done in [118].

[16]In other words, the crossing symmetry relates different analytic regions of the S matrix to each other in a non-trivial way.

- employ the crossing symmetry to relate $\mathcal{K}^{\mathrm{FF}} \leftrightarrow \mathcal{K}^{\mathrm{I/FI}}$;

- fix the colour factor C according to the generic (large N_{C}) colour structure of the emission.

Importantly, in a first step, the kinematic structures of the fully derived splitting cross sections of the previous section have to be cross-checked whether they are identical to those provided by the scheme. This is outlined below already in the manner of (re-)deriving the I/FI expressions from the FF ones, i.e. $\mathcal{K}^{\mathrm{I/FI}} = \mathrm{cross}\,\mathcal{K}^{\mathrm{FF}}$, as it will be applied in the next two sections.

II antiquark–quark dipoles: the three ways of appropriately crossing the final–final process $q(\tilde{k})\bar{q}'(\tilde{\ell}) \to q(k)g\bar{q}'(\ell)$ yield the eligible processes relevant for emissions off $\bar{q}_{\mathrm{i}}q'_{\mathrm{i}}$ dipoles, namely the quark-induced process $\bar{q}(k)q'(\ell) \to \bar{q}(\tilde{k})q'(\tilde{\ell})g$, and the two gluon-induced processes, which are, first, $gq'(\ell) \to \bar{q}(\tilde{k})q'(\tilde{\ell})q(k)$ and, second, $\bar{q}(k)g \to \bar{q}(\tilde{k})q'(\tilde{\ell})\bar{q}'(\ell)$. The latter is not generic, in fact just the charge-conjugated process of the former eventually handled by a trivial interchange $\tilde{k}, k \leftrightarrow \tilde{\ell}, \ell$. The kinematic structure of all these processes is gained by applying the crossing symmetry transformation onto

$$\overline{\mathcal{K}}_{q\bar{q}'\to qg\bar{q}'} = \frac{x_q^2 + x_{\bar{q}'}^2}{s_{qg\bar{q}'}(1 - x_q)(1 - x_{\bar{q}'})} \tag{2.122}$$

(cf. eq. (2.102) of sec. 2.4.1) delivering the following results:

$$\overline{\mathcal{K}}_{\bar{q}_{\mathrm{i}}q'_{\mathrm{i}}\to\bar{q}_{\mathrm{i}}gq'_{\mathrm{i}}} = \frac{x_{\bar{q}_{\mathrm{i}}}^2 + x_{q'_{\mathrm{i}}}^2}{M^2(1 - x_{\bar{q}_{\mathrm{i}}})(1 - x_{q'_{\mathrm{i}}})} = \frac{(M^2 - \hat{u})^2 + (M^2 - \hat{t})^2}{M^2\,\hat{u}\hat{t}}, \tag{2.123}$$

$$\overline{\mathcal{K}}_{\bar{q}_{\mathrm{i}}q'_{\mathrm{i}}\to qg_{\mathrm{i}}q'_{\mathrm{i}}} = -\frac{x_q^2 + x_{q'_{\mathrm{i}}}^2}{M^2(1 + x_q)(1 - x_{q'_{\mathrm{i}}})} = \frac{(M^2 - \hat{s})^2 + (M^2 - \hat{t})^2}{-M^2\,\hat{s}\hat{t}}, \tag{2.124}$$

where the x_m are now understood according to II kinematics, see sec. 2.3.3, the Mandelstam variables are taken according to eqs. (2.43) and in both cases $s_{kg\ell}$ has been replaced using $s_{kg\ell} = (\mp p_k \pm p_g - p_\ell)^2 = (-p_0)^2 = \tilde{p}_0^2 = M^2$.

FI quark–quark dipoles: starting again from the FF expression, for the desired final-state gluon emission off a qq'_{i} dipole, the antiquarks labelled $\tilde{\ell}$ and ℓ have to be crossed with each other, resulting in $q(\tilde{k})q'(\ell) \to q'(\tilde{\ell})q(k)g$; whereas for initial-state gluon emissions, crossing is applied on the g instead of the $\bar{q}'(\ell)$, leaving $q(\tilde{k})g \to q'(\tilde{\ell})q(k)\bar{q}'(\ell)$. This corresponds to QCD Compton $V(0)q'(\ell) \to q(k)g$ and boson–gluon fusion $V(0)g \to q(k)\bar{q}'(\ell)$, respectively. Without surprise, when the symmetry transformations on eq. (2.122) are carried out accordingly (including $s_{kgl} = p_0^2 = -Q^2$), it precisely unfolds the energy-fraction results stated in eqs. (2.120) and (2.121).

Clearly, for both dipole types $\bar{q}_{\mathrm{i}}q'_{\mathrm{i}}$ and qq'_{i}, the colour factor for the g_{f} emissions is C_F; however, if the radiated gluon is assigned to the initial state, it actually is incoming and splits into a $q\bar{q}$ pair with one of the quarks entering the hard process. Therefore, it has to be T_R for both.

Thus, as expected, all findings and allocations confirm those of the previous section. For qq'_{i} dipoles the same kinematic functions are recovered. For $\bar{q}_{\mathrm{i}}q'_{\mathrm{i}}$ dipoles, the cross sections given in eqs. (2.108) and (2.113) for quark- and gluon-induced radiation, respectively, are regained in regard of eq. (2.116) using the actual kinematic functions stated in this section.

2.4.4   Initial-state colour dipoles

The proposed crossing-relation approach is used to reveal the missing structures of the splitting cross sections for initial–initial dipoles containing gluons. They are inferred according to $\mathcal{K}^{\mathrm{II}} = \mathrm{cross}\,\mathcal{K}^{\mathrm{FF}}$ from the Lund splitting cross sections of the corresponding final–final dipoles, cf. eqs. (2.97). This is briefly discussed.

For $\bar{q}_{\mathrm{i}}g_{\mathrm{i}}$ dipoles, the kinematic functions for the two gluon-emission processes are achieved by crossing the associated FF function $\overline{\mathcal{K}}_{qg\to qgg}$ for $q(\tilde{k})g(\tilde{\ell}) \to q^*(0) \to q(k)gg(\ell)$. The processes then read $\bar{q}(k)g(\ell) \to \bar{q}(\tilde{k})g(\tilde{\ell})g$ (g_{f} emission) and $gg(\ell) \to \bar{q}(\tilde{k})g(\tilde{\ell})q(k)$ (g_{i} emission). The $\overline{\mathcal{K}}_{qg\to qgg}$ function differs from that in eq. (2.122) only in the numerator, which now reads $x_k^2 + x_\ell^3$. The case of $g_{\mathrm{i}}q_{\mathrm{i}}$ dipoles can be referred to that of $\bar{q}_{\mathrm{i}}g_{\mathrm{i}}$ dipoles. Gluon dipoles $g_{\mathrm{i}}g_{\mathrm{i}}$ only emit final-state gluons because of the indistinguishability of identical particles. Crossing symmetry of $\overline{\mathcal{K}}_{gg\to ggg}$, its numerator reading $x_k^3 + x_\ell^3$, is deployed to describe $g(k)g(\ell) \to g(\tilde{k})g(\tilde{\ell})g$.

The colour-factor issue is unproblematic for the latter dipole type, here $C = C_A$ unambiguously, however problematic for the ones that consist of a(n) (anti)quark and a gluon. This (known) problem is already present at the FF dipole level. If the gluon is considered emitted while approaching a collinear limit either with the parent quark or with the parent gluon, where the radiation is governed by C_F or C_A, respectively, then, literally taken, the different colour-factor regimes have to be respected. Currently, however, the following choices are made for II dipoles with a single gluon leg: final-state gluons are emitted adopting the Lund CDM choice of $C = C_A$ (and $\xi = 0.5$); for initial-state ones, $C = T_R$ (and hence $\xi = 1$) is selected adopting the result from the calculation for $\bar{q}_{\mathrm{i}}q'_{\mathrm{i}}$ dipoles. The g_{i} emission cross section is based on the coherent superposition of the $\hat{t}$ channel and $\hat{s}$ channel diagrams, see fig. 2.5, however, since $\hat{s} \geq M^2 > 0$, the latter is non-singular. [17] Therefore, the selection $C = T_R$ at least ensures the correct behaviour in the singular limit $\hat{t} \to 0$ of g_{i} emissions.

Taken it all together, thereby making use of eq. (2.116) under the assumption that the extra Jacobian of $\frac{dy_{\mathrm{cm}}}{d\tilde{y}_{\mathrm{cm}}}$ is trivial, all differential II dipole splitting cross sections can now be formulated in terms of the evolution variables. The coordinate transformation from the $(s_{\bar{\imath}'i(g_{\mathrm{i}}i)}, s_{\bar{\imath}'g(qg_{\mathrm{i}})})$ set to the $(p_\perp^2, y)$ set requires the evaluation of a Jacobian. In all cases $ds_{\bar{\imath}'i(g_{\mathrm{i}}i)}ds_{\bar{\imath}'g(qg_{\mathrm{i}})} = M^2\,dp_\perp^2\,dy$, and it can be straightly concluded that the exact differential splitting cross sections for g_{f} emission read

$$\frac{d\sigma_{\bar{\imath}'i\to\bar{\imath}'gi}}{d\sigma_0\,dp_\perp^2\,dy} = \frac{f_{\bar{\imath}'}(x_\pm,\mu_{\mathrm{F}})\,f_i(x_\mp,\mu_{\mathrm{F}})}{f_{\bar{\imath}'}(\tilde{x}_\pm,\tilde{\mu}_{\mathrm{F}})\,f_i(\tilde{x}_\mp,\tilde{\mu}_{\mathrm{F}})}\,\frac{M^4}{\hat{s}^2(p_\perp,y)}\,\xi_{\{{}^F_A\}}\,\frac{C_{\{{}^F_A\}}\alpha_s}{2\pi}\,\frac{x_{\bar{\imath}'}^{n_{\bar{\imath}'}}(p_\perp,y) + x_i^{n_i}(p_\perp,y)}{p_\perp^2},$$

$$(2.125)$$

---

[17] Parton showers relying on $1 \to 2$ branchings do not account for a configuration as given through the $\hat{s}$ channel.
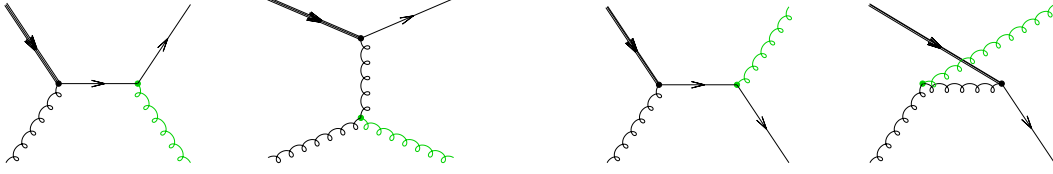
Figure 2.5: Left panel: contributing diagrams ($\hat{t}$ and $\hat{s}$ channel) for initial-state gluon emission originating from a $\bar{q}_i g_i$ dipole. Right panel: Feynman diagrams for final-state gluon; only the $\hat{t}$ and $\hat{u}$ channels contribute, the $\hat{s}$ channel describes an emission, which is associated with the accompanying colour flow, an emission, thus, taken care of by the neighbouring dipole, i.e. the IF dipole $g_i \bar{f}$. The FF-domain equivalent is an emission that escapes from the incoming off-shell quark ready to decay, i.e. also from an accompanied colour line. Therefore it is not considered too.

where $\hat{s}(p_\perp, y) = M^2 + 2M p_\perp \cosh y$, as given in sec. 2.3.3.1,

$$x_{\bar{i}',i}(p_\perp, y) \;=\; 1 + \frac{p_\perp}{M} e^{\pm y} \tag{2.126}$$

and $n_q = n_{\bar{q}} = 2$ and $n_g = 3$. Furthermore $\xi_F = 1$ and $\xi_A = 0.5$ since a gluon links two dipoles. The curly bracket encodes that $\left\{ \begin{smallmatrix} \cdots & \text{for } \bar{q}'_i q_i \\ \cdots & \text{else} \end{smallmatrix} \right\}$; note that the partonic momentum fractions in the PDFs are then given as functions depending on $p_\perp$, y and $\tilde{y}_{\text{cm}}$. The singularity structure is entirely contained in the $p_\perp^{-2}$ term, which becomes infinite in either of the collinear limits that the gluon can have with the parent partons, i.e. the $\hat{t}$ or $\hat{u}$ variables turn separately to zero, or in the soft limit where $x_g \to 0$ and therefore $\hat{t}$ and $\hat{u}$ collectively approach the limit at zero.

Similarly, the differential splitting cross sections for gluons radiated into the initial state can be summarized,

$$\frac{d\sigma_{\bar{q}_i i \to q g_i i}}{d\sigma_0 \, dp_\perp^2 dy} \;=\; \frac{f_g(x_\pm, \mu_F) \, f_i(x_\mp, \mu_F)}{f_{\bar{q}}(\tilde{x}_\pm, \tilde{\mu}_F) \, f_i(\tilde{x}_\mp, \tilde{\mu}_F)} \; \frac{M^4}{\hat{s}^2(p_\perp, y)} \; \frac{T_R \alpha_s}{2\pi} \; \frac{x_q^2(p_\perp, y) + x_i^{n_i}(p_\perp, y)}{p_\perp^2} \,, \tag{2.127}$$

where $\hat{s}(p_\perp, y) = M p_\perp e^y$, as stated in sec. 2.3.3.2, and

$$x_{q,i}(p_\perp, y) \;=\; \mp 1 + \frac{p_\perp}{M} e^{\pm y} \,. \tag{2.128}$$

The singularities again will be entirely mapped out by the transverse momentum tending to zero. For g_i emissions, their structure is however not as rich as for g_f emissions off II dipoles, since $\hat{s}$ is bounded to stay well above zero due to the parent dipole's mass. So, it only is critical if the emitted quark becomes soft or collinear with the incoming splitting gluon g_i. No other radiating dipole contributes to this singularity, therefore $\xi \equiv 1$, consequently being omitted in the formula above.

For the proposed model, the $2 \to 3$ splitting cross sections given in eqs. (2.125) and (2.127) constitute the building blocks out of which the full radiation pattern in II configurations will be generated. In regard of the kinematic phase-space bounds discussed throughout

sec. 2.3.3, the overestimations – finally constituting an eikonal approximation – for the cross sections of eqs. (2.125) and (2.127) can be stated by

$$\frac{d\sigma^{\text{approx}}_{\bar{\imath}'i \to \bar{\imath}'gi}}{d\sigma_0 \; dp_\perp^2 \, dy} \;\; = \;\; \mathcal{N}_{\text{PDF}} \; \xi_{\left\{ {F \atop A} \right\}} \frac{C_{\left\{ {F \atop A} \right\}} \alpha_s}{2\pi} \; \frac{\left\{ {2 \atop a+1} \right\}}{p_\perp^2} \, , \tag{2.129}$$

and

$$\frac{d\sigma^{\text{approx}}_{\bar{q}_{\text{i}}i \to qg_{\text{i}}i}}{d\sigma_0 \; dp_\perp^2 \, dy} \;\; = \;\; \mathcal{N}_{\text{PDF}} \; \frac{T_R \alpha_s}{2\pi} \; \frac{\left\{ {2 \atop a+1} \right\}}{p_\perp^2} \, . \tag{2.130}$$

They exactly hold the same singularity structure as the exact cross sections do, thus, they are ready to be utilized in the Sudakov veto algorithm, see sec. 2.5.2. The meaning of the curly bracket is as before. The quantity a has been introduced in sec. 2.3.3.

2.4.5   Dipoles from final–initial colour flows

All missing kinematic functions are calculated as before under exploitation of the crossing symmetry of the appropriate FF dipole kinematic function taken from the Lund CDM. In the cases where there are different particles in the final state, there are more than one possible crossing and, therefore, more than one corresponding kinematic function. For example, taking $q(\tilde{k})g(\tilde{\ell}) \to q(k)gg(\ell)$, the quark or one of the gluons can be crossed into the initial state. However, there is freedom, which of the initial partons, either $q(\tilde{k})$ or $g(\tilde{\ell})$, can be transferred. Finally the chosen partition is $q(\tilde{k})g(\ell) \to g(\tilde{\ell})q(k)g$ describing g_{f} emission off a qg_{i} dipole, $g(\tilde{\ell})\bar{q}(k) \to \bar{q}(\tilde{k})gg(\ell)$ and $g(\tilde{\ell})g \to \bar{q}(\tilde{k})q(k)g(\ell)$ describing g_{f} and g_{i} emission off a $\bar{q}_{\text{i}}g$ dipole, respectively. It reflects that FI/IF dipoles already containing an initial gluon do not contribute to (anti)quark emissions. For the other dipole types, it is proceeded analogously and the kinematic functions that are obtained by crossing resemble the ones given in eqs. (2.120) and (2.121) for g_{f} and g_{i} radiation, respectively, up to differences in the numerator.

The reasoning concerning the choice of colour factors applies here on equal footing. There are the same ambiguities for final-state gluon emission arising from a quark–gluon dipole. This has been already discussed in the previous section. Finally, the choices made are as for II dipoles. For antiquark radiation, the same problem appears, this time in full analogy to the former case, since the splitting is now singular when both the emitted antiquark ($\hat{t} \to 0$) or the other parton ($\hat{u} \to 0$) in the final state become collinear with the initial-state gluon, cf. eqs. (2.73). This is in contrast to the situation of II dipoles where a collinear divergence cannot emerge between the incoming gluon and the other initial-state parton. The ambiguity occurs when the mentioned "other" final-state parton corresponds to a gluon, apparently resulting in a collinear splitting governed by C_A rather than T_R, which despite of this circumstance is picked throughout to describe the extra occurrence of antiquarks or – for IF dipoles – quarks in the final state.

If all findings are assembled, eq. (2.118) can be re-formulated in detail for the accessible emission channels of all types of FI dipoles (and hence IF dipoles) that are made up of massless partons. Using the evolution variables introduced in the corresponding subsections of sec. 2.3.4, the common Jacobian required to calculate is given through

$d\hat{s}d\hat{t} = Q^2\,dp_\perp^2\,dy$. Then the final result of the differential FI dipole splitting cross section controlling g_f emissions is

$$\frac{d\sigma_{fi \to fgi}}{d\sigma_0\,dp_\perp^2\,dy} = \frac{f_i(-x_i x_B, \mu_{\mathrm{F}})}{f_i(x_B, \tilde{\mu}_{\mathrm{F}})}\,\frac{\xi_{\{{}^F_A\}}}{x_i^2(p_\perp, y)}\,\frac{C_{\{{}^F_A\}}\alpha_s}{2\pi}\,\frac{|x_f(p_\perp, y)|^{n_f} + |x_i(p_\perp, y)|^{n_i}}{p_\perp^2},$$

(2.131)

where the modulus is used to keep the terms in the rightmost numerator positive definite. All quantities denoted by x have been introduced in sec. 2.3.4 with x_B being the Bjørken-x variable and the energy fractions as functions of $p_\perp$ and y read

$$x_{f,i}(p_\perp, y) = \pm 1 - \frac{p_\perp}{Q}\,e^{\pm y}.$$

(2.132)

The meanings of n, ξ and the curly brackets are as in the previous section, $\tilde{\mu}_{\mathrm{F}}$ and μ_{F} are the factorization scales before and after the emission, respectively, their choices will be discussed in sec. 2.5.3. Concerning the divergencies it is as before, they are accumulated in the $p_\perp^{-2}$ term, so that the singular regions are approached while the invariant transverse momentum is vanishing. This fact once more renders its usage as the ordering variable steering dipole splittings. Collinear/soft limits ($\hat{t} \to 0$ or/and $\hat{s} \to 0$) appear [18] in the same manner compared to the II dipole g_f emissions, see previous section.

Applying the same manipulations in the instance of antiquark emissions, they are eventually described by

$$\frac{d\sigma_{fq_i \to fg_i\bar{q}}}{d\sigma_0\,dp_\perp^2\,dy} = \frac{f_{g_i}(-x_{g_i} x_B, \mu_{\mathrm{F}})}{f_{q_i}(x_B, \tilde{\mu}_{\mathrm{F}})}\,\frac{1}{x_{g_i}^2(p_\perp, y)}\,\frac{T_R\alpha_s}{2\pi}\,\frac{|x_f(p_\perp, y)|^{n_f} + x_{\bar{q}}^2(p_\perp, y)}{p_\perp^2},$$

(2.133)

and the employed invariant energy fractions in terms of the evolution variables are

$$x_{f,\bar{q}}(p_\perp, y) = 1 - \frac{p_\perp}{Q}\,e^{\pm y}, \qquad \text{such that} \qquad x_{g_i}(p_\perp, y) = -\frac{2\,p_\perp}{Q}\cosh y.$$

(2.134)

As already mentioned in the discussion of the choice of the colour factor for this type of radiation, the incoming gluon may split collinearly and, therefore, in singular domains w.r.t. both the antiquark and the second final-state parton associated to the emission. The gluon g_i cannot become soft, since it is coupled to the initial state, therefore, the soft limit only comes about when the antiquark is emitted accordingly, with the singular effect only entering through $\hat{t} \to 0$ (the disappearance of $\hat{s}$ is non-singular). Generally $\hat{t}$ and $\hat{u}$ cannot vanish at the same time, which is clear from eqs. (2.78).

Next the overestimated splitting cross sections are displayed. They are deduced under incorporation of the kinematic phase-space limits presented in sec. 2.3.4, and, again form eikonal approximations of the exact cross sections. Thus, eq. (2.131) is constrained from above through

$$\frac{d\sigma_{fi \to fgi}^{\mathrm{approx}}}{d\sigma_0\,dp_\perp^2\,dy} = \mathcal{N}_{\mathrm{PDF}}\,\xi_{\{{}^F_A\}}\frac{C_{\{{}^F_A\}}\alpha_s}{2\pi}\frac{\left\{{}^2_{2(a+1)}\right\}}{p_\perp^2},$$

(2.135)

---

[18] Note that the collinear singularities for gluons only fully appear when including the contributions of the neighbouring dipoles.

and the expression given in eq. (2.133) is overestimated through

$$\frac{d\sigma^{\text{approx}}_{fq_i \to fg_i \bar{q}}}{d\sigma_0 \, dp_\perp^2 dy} \;\; = \;\; \mathcal{N}_{\text{PDF}} \; \frac{T_R \alpha_s}{2\pi} \; \frac{\left\{ \begin{smallmatrix} 1 \\ \max\{2,\, a+1\} \end{smallmatrix} \right\}}{p_\perp^2} \,. \tag{2.136}$$

Again, the PDF ratio has to be under control requiring $\mathcal{N}_{\text{PDF}}$ to be a reasonable over-estimation of the true ratio. Only if guaranteed, the expressions are at hand that will enter the Sudakov veto algorithm as the crude (primary) splitting cross sections allowing hit-or-miss techniques to be applied.

2.4.6   Dipole splitting functions

In analogy to conventional parton showers the notion of splitting function is introduced for the dipole shower. These functions will be employed in the definitions of the Sudakov form factor(s), in sec. 2.5, hence they are stated here.
The differential decay cross section for a $\tilde{k}\tilde{\ell}$ dipole to develop into a $kg\ell$ colour-connected state can be denoted as

$$d\mathcal{P}_{\tilde{k}\tilde{\ell} \to kg\ell} \;\; \equiv \;\; \frac{d\sigma_{\tilde{k}\tilde{\ell} \to kg\ell}}{d\sigma_0} \;\; = \;\; \frac{\alpha_s}{2\pi} \; D_{\tilde{k}\tilde{\ell} \to kg\ell}(p_\perp, y) \, \frac{dp_\perp^2}{p_\perp^2} dy \,, \tag{2.137}$$

which, hence, defines the *dipole splitting function* $D_{\tilde{k}\tilde{\ell} \to kg\ell}$ for a $\tilde{k}\tilde{\ell} \to kg\ell$ transition.
This is applied to *all* cases discussed throughout this work, where the definitions $n_q = n_{\bar{q}} = 2$ and $n_g = 3$, $\xi_F = 1$ and $\xi_A = 0.5$, and $\left\{ \begin{smallmatrix} \cdots & \text{for quark dipoles} \\ \cdots & \text{else} \end{smallmatrix} \right\}$ are generic to all dipole splitting functions detailed below; they are:

- **Final–final dipoles:**
  According to the Lund CDM [16, 17, 18, 11] they are found as

  $$\begin{aligned} D_{f\bar{f}' \to fg\bar{f}'}(p_\perp, y) \;\; &= \;\; \xi_{\{{}^F_A\}} C_{\{{}^F_A\}} \left[x_f^{n_f}(p_\perp, y) + x_{\bar{f}'}^{n_{\bar{f}'}}(p_\perp, y) \right] \\ &\leq \;\; 2\, \xi_{\{{}^F_A\}} C_{\{{}^F_A\}} \,, \end{aligned} \tag{2.138}$$

  with the invariant energy fractions given through

  $$x_{f,\bar{f}'} \;\; = \;\; 1 - \frac{p_\perp}{M} \, e^{\pm y} \,. \tag{2.139}$$

  As indicated, all those dipole splitting functions can be easily approximated, and these $D^{\text{approx}}_{f\bar{f}' \to fg\bar{f}'}$ give upper bounds to any of the splitting functions noted above.

- **Initial–initial dipoles:**
  Here the definition yields, for gluons that are radiated into the final state,

  $$D_{\bar{i}'i \to \bar{i}'gi}(p_\perp, y) \;\; = \;\; \frac{f_{\bar{i}'}(x_\pm, \mu_{\text{F}}) \, f_i(x_\mp, \mu_{\text{F}})}{f_{\bar{i}'}(\tilde{x}_\pm, \tilde{\mu}_{\text{F}}) \, f_i(\tilde{x}_\mp, \tilde{\mu}_{\text{F}})} \, \xi_{\{{}^F_A\}} C_{\{{}^F_A\}} \, \frac{x_{\bar{i}'}^{n_{\bar{i}'}}(p_\perp, y) + x_i^{n_i}(p_\perp, y)}{\left[x_{\bar{i}'}(p_\perp, y) + x_i(p_\perp, y) - 1 \right]^2} \,, \tag{2.140}$$

with the energy fractions given in eq. (2.126), and, for those that are radiated into the initial state

$$D_{\bar{q}_i i \to q g_i i}(p_\perp, y) \;=\; \frac{f_g(x_\pm, \mu_{\mathrm{F}}) \, f_i(x_\mp, \mu_{\mathrm{F}})}{f_{\bar{q}}(\tilde{x}_\pm, \tilde{\mu}_{\mathrm{F}}) \, f_i(\tilde{x}_\mp, \tilde{\mu}_{\mathrm{F}})} \; T_R \; \frac{x_q^2(p_\perp, y) + x_i^{n_i}(p_\perp, y)}{[1 + x_q(p_\perp, y)]^2} \,, \qquad (2.141)$$

with the energy fractions of eq. (2.128). With the above definition the PDF ratios have been formally included into the splitting functions, hence, a redefinition of the Sudakov form factor (cf. sec. 2.5.1) later on will not be required.

- **Final–initial dipoles:**
  Their splitting functions are written

$$D_{fi \to fgi}(p_\perp, y) \;=\; \frac{f_i(-x_i x_B, \mu_{\mathrm{F}})}{f_i(x_B, \tilde{\mu}_{\mathrm{F}})} \; \xi_{\{{}^F_A\}} C_{\{{}^F_A\}} \; \frac{|x_f(p_\perp, y)|^{n_f} + |x_i(p_\perp, y)|^{n_i}}{x_i^2(p_\perp, y)} \,,$$

$$\qquad (2.142)$$

whereas the corresponding energy fractions are stated in eq. (2.132), and

$$D_{fq_i \to f g_i \bar{q}}(p_\perp, y) \;=\; \frac{f_{g_i}(-x_{g_i} x_B, \mu_{\mathrm{F}})}{f_{q_i}(x_B, \tilde{\mu}_{\mathrm{F}})} \; T_R \; \frac{|x_f(p_\perp, y)|^{n_f} + x_{\bar{q}}^2(p_\perp, y)}{x_{g_i}^2(p_\perp, y)} \,, \qquad (2.143)$$

with the energy fractions here taken from eqs. (2.134). As before, the PDF term is included per definition and will therefore directly occur in the Sudakov form factor.

2.4.7 Remarks

Some comments are in order here:

- All results in this work are for massless quarks only.

- In [17, 119] the Lund differential cross sections have been shown to obey the correct QCD behaviour in the soft and/or collinear (Altarelli–Parisi) limit. Strictly, this has been demonstrated without considering the colour factor, therefore, in the strict sense, the reasoning rather applies to the kinematic functions. Moreover, since crossing symmetry has been invoked to obtain the kinematic functions of the new cases, these can be assumed with some confidence to work correctly in the singular domains of QCD too.

- As discussed, the ambiguity in the assignment of the colour factors for quark–gluon dipoles does not allow pinpoint the order of logarithms taken into account. There is no proof of the resummation to be correct at a well-defined order and the Sudakov exponentiation only proceeds upon analogy to existing parton-shower models, following the rule of the thumb that one obtains the all-orders expression by exponentiating the single-emission cross section. A proof cannot be provided at this stage of the project, however evidence can be given, as will be done in sec. 2.6, by presenting detailed results and predictions of observables that are known to be discriminatory for certain issues, e.g. the correct modelling of colour coherence.

- It should also be kept in mind that the splitting functions for quark dipoles were obtained from the consideration of vector boson decays, therefore intrinsically carry their spin structure. It needs to be investigated whether this has consequences for the description of e.g. *b*-quark associated Higgs production owing to the scalar spin structure of the Higgs.

- The kinematic functions of this approach allow direct comparison with the tree-level antenna functions of [30, 121]. Thus, the use of antenna functions, instead of the Lund kinematic functions, constitutes a very attractive alternative, with the clear advantage of constructing a dipole shower, based upon a subtraction method – the antenna subtraction method. Furthermore, antenna functions seem to be better suited to enable a decomposition into subantennæ, such that singularities falling under different colour factor regimes can be separated and individually treated. Using partitioning, the colour-factor ambiguity might be resolved.

2.5   The complete shower algorithm

The dipole-shower algorithm is presented handling QCD radiation of initial-, final–initial and final-state colour-dipoles in equal measure. The construction of the radiation pattern occurs through a Markovian process, which effectively is invoked to resum LL effects by generating exclusive final states of partons. In analogy to conventional parton showers the Sudakov form factor is introduced constituting the central probabilistic quantity that regulates the full development of the cascade. The concept of "time" is realized through the leading evolution variable $p_\perp$ and an imposed ordering of the emissions according to its magnitude. The evaluation of a set of evolution variables $(p_\perp, y)$ qualifying a single emission is briefly demonstrated before the complete algorithm is fixed by specifying the iteration loop that produces the emissions and necessary scales occurring during the evolution.

2.5.1   The Sudakov form factor

As discussed at various places throughout this write-up the evolution variables are given as an invariant transverse momentum $p_\perp$ and an invariant rapidity y playing the rôle of the associated variable. It has been shown that the divergent behaviour of each emission cross section can be always fully folded into a $p_\perp^{-2}$ term in a consistent manner. This earmarks the usage of $p_\perp$ w.r.t. y to operate as the leading variable responsible for the ordering of the emissions. Contrary it tells that the dipole splitting functions $D(p_\perp, y)$ do not at all contribute to the singular structure of the emissions. So, in conclusion, all $2 \rightarrow 3$ dipole splitting cross sections independent of their assignment to a certain kinematic region follow the generic pattern primarily triggered by an accentuation of the soft limit of QCD radiation. This nice feature supplemented by the fact that without exception the definition of the evolution variables consistently succeeds as anticipated through eqs. (2.25) and (2.26) allows to treat all emissions on equal footing enabling a simultaneous competition between them. Hence, the differential decay cross section of a

certain dipole $\tilde{k}\tilde{\ell}$ to branch can be universally given by

$$dP_{\tilde{k}\tilde{\ell}} \equiv \frac{d\sigma_{\tilde{k}\tilde{\ell}}}{d\sigma_0} = \frac{\alpha_s}{2\pi} \sum_{\{kg\ell\}} D_{\tilde{k}\tilde{\ell}\to kg\ell}(p_\perp, y)\, \frac{dp_\perp^2}{p_\perp^2} dy\,, \tag{2.144}$$

where the sum runs over the set of channels available for this dipole to split. The all-orders expression is gained from the exponentiation of minus the corresponding differential single-emission cross section $\frac{d\sigma/d\sigma_0}{dp_\perp^2\,dy}$. Following the general understanding, it is interpreted as the no-branching probability through which the two divergent contributions of virtual and unresolvable real emission are summed up to give a finite result. Consequently, for the dipole splittings employed by this model, the Sudakov form factor is just defined according to this "rule":

$$\Delta(p_{\perp,\mathrm{stt}}^2, p_\perp^2) = \exp\left\{ -\int_{p_\perp^2}^{p_{\perp,\mathrm{stt}}^2} \frac{d\tilde{p}_\perp^2}{\tilde{p}_\perp^2}\, \mathcal{I}(\tilde{p}_\perp^2) \right\}, \tag{2.145}$$

which becomes equivalent to eq. (2.13) of the Lund CDM if reduced to describe FF dipole evolution solely. As given in the equation above it quantifies how likely a state consisting of a number of dipoles will not emit any further resolvable parton between the start scale $p_{\perp,\mathrm{stt}}^2$ and a lower scale $p_\perp^2$. Accordingly, the function $\mathcal{I}(p_\perp^2)$ names the sum of the rapidity integrals of the splitting functions over all contributing dipole-emission channels denoted by $\{\tilde{k}\tilde{\ell}\to kg\ell\}$,

$$\mathcal{I}(p_\perp^2) = \frac{\alpha_s(\mu_\mathrm{R})}{2\pi} \sum_{\{\tilde{k}\tilde{\ell}\to kg\ell\}} \int_{y_-(p_\perp, a)}^{y_+(p_\perp, a)} dy\; D_{\tilde{k}\tilde{\ell}\to kg\ell}(p_\perp, y)\,. \tag{2.146}$$

The fact to pick the sum of real-emission cross sections as the kernel of the all-orders expression has the direct consequence that the PDF ratios present in the I/FI splitting functions emerge in the Sudakov computation. To this extent the ansatz followed here resembles that one of PYTHIA, where the splitting kernels feature a ratio of parton densities ensuring that the parton composition of the hadron is properly reflected [12]. Moreover, μ_R denotes the renormalization scale in squared energy units for the evaluation of the strong coupling, which better be running to enable the inclusion of higher-order virtual contributions beyond the LL approximation. Note that the rapidity limits $y_\pm$ in its functional form also depend on the certain selection of emission channel. This is omitted in the notation of the limits, but it is clear in view of eq. (2.37), eqs. (2.51), (2.59) and (2.82), (2.87), and requires to sum up the rapidity integrals and not vice versa, in order to respect the most general case. Moreover, common to these bounds is their dependence in y_+ and/or y_- on the choice of the maximal available phase space most easily expressed through the scaling quantity a relating the phase-space choice to the actual squared mass of the dipole, cf. eqs. (2.45) and (2.75). As mentioned in sec. 2.3, this is in contrast to the case of FF dipoles, which is unaffected by this choice, cf. eq. (2.37). The implications in opening/restricting the phase space to the emissions will be further discussed in sec. 2.5.3. Hence, the actual probability that some branching occurs at $p_\perp^2$ then manifests itself by

$$\frac{d\Delta(p_{\perp,\mathrm{stt}}^2, p_\perp^2)}{dp_\perp^2} = \frac{\mathcal{I}(p_\perp^2)}{p_\perp^2} \Delta(p_{\perp,\mathrm{stt}}^2, p_\perp^2)\,, \tag{2.147}$$

and subsequent emissions are ordered in $p_\perp$ to generate a Markov chain. Accordingly the
start scale $p_{\perp,\text{stt}}^2$ has to be chosen, however concerning the very first emission an initializing
scale $p_{\perp,\text{ini}}^2$ has to be carefully selected that then specifies the value taken for the starting
scale of the Sudakov computation. This is detailed in sec. 2.5.3.

2.5.2   Generation of the emission's Sudakov variables

The techniques are briefly documented, which are employed to generate a valid set of
evolution variables characterizing an emission.
First, strict $p_\perp$ ordering makes it possible to analyze any dipole individually per emission
channel. Therefore the answer obtained through eq. (2.147) can be equally achieved by
picking the emission of highest $p_\perp$ from the ensemble of trial emissions each of it generated
according to its associated probability density reading

$$
\begin{aligned}
\frac{dF}{dp_\perp^2} &= \frac{\alpha_s(\mu_\mathrm{R}(p_\perp))}{2\pi\,p_\perp^2} \int\limits_{y_-(p_\perp,a)}^{y_+(p_\perp,a)} dy\, D_{\tilde{k}\tilde{\ell}\to kg\ell}(p_\perp,y) \\[2ex]
&\times\ \exp\left\{ -\int\limits_{p_\perp^2}^{p_{\perp,\text{stt}}^2} \frac{d\tilde{p}_\perp^2}{\tilde{p}_\perp^2}\frac{\alpha_s(\mu_\mathrm{R}(\tilde{p}_\perp))}{2\pi} \int\limits_{y_-(\tilde{p}_\perp,a)}^{y_+(\tilde{p}_\perp,a)} dy\, D_{\tilde{k}\tilde{\ell}\to kg\ell}(\tilde{p}_\perp,y) \right\}\ .
\end{aligned}
\tag{2.148}
$$

Notice that μ_R denotes the renormalization scale as some function of $p_\perp^2(\tilde{p}_\perp^2)$.
Second, the standard Monte Carlo technique of the veto algorithm [7] is used to select a
valid trial set $(p_\perp,y)$ from a single-channel distribution. According to the method the set is
actually computed from a sufficiently simpler density with its kernel overshooting the exact
one everywhere and for which the equation $\mathcal{R} = \Delta(p_{\perp,\text{stt}}^2, p_\perp^2)$ can be inverted analytically
invoking a random number $\mathcal{R} \in [0,1]$. The approximate splitting cross sections gathered
throughout sec. 2.4 fulfil these requirements implying that

$$
\frac{dF^\text{approx}}{dp_\perp^2} = \int\limits_{Y_-(p_\perp,a)}^{Y_+(p_\perp,a)} dy\, \frac{d\sigma_{\tilde{k}\tilde{\ell}\to kg\ell}^\text{approx}}{d\sigma_0\,dp_\perp^2\,dy}\ \exp\left\{ -\int\limits_{p_\perp^2}^{p_{\perp,\text{stt}}^2} d\tilde{p}_\perp^2 \int\limits_{Y_-(\tilde{p}_\perp,a)}^{Y_+(\tilde{p}_\perp,a)} dy\, \frac{d\sigma_{\tilde{k}\tilde{\ell}\to kg\ell}^\text{approx}}{d\sigma_0\,d\tilde{p}_\perp^2\,dy} \right\},
\tag{2.149}
$$

where $Y_\pm$ are the loose rapidity bounds, overestimating the sharp ones. The trial $p_\perp$
generation can be analytically solved for this distribution and the associated rapidity
is randomly taken from the exact interval $[y_-, y_+]$. Then, the correction for the actual
distribution basically is accomplished by only accepting the suggested branching, if the
ratio of exact vs. approximate Sudakov kernel is larger than a second random number.
Otherwise, as long as the cut-off scale has not been reached, it is tested for a new branching
with $p_{\perp,\text{stt}}^2$ set by the rejected scale.
The full procedure generates correction weights of the form

$$
\mathcal{W} = \frac{\mathcal{W}_\text{PDF}}{\mathcal{N}_\text{PDF}}\frac{\alpha_s(\mu_\mathrm{R})}{\alpha_s^\text{max}}\frac{\mathcal{W}_\text{PSP}\mathcal{W}_\text{ME}}{\mathcal{N}_\text{PSP+ME}}\frac{\Delta y(p_\perp,a)}{\Delta Y(p_\perp,a)}.
\tag{2.150}
$$

The individual $\mathcal{W}_{...}$ and $\mathcal{N}_{...}$ factors can be easily identified by inspecting the exact and approximate differential splitting cross sections presented throughout sec. 2.4. For instance, the numerators of the $p_\perp^{-2}$ terms of the overestimated cross sections constitute the $\mathcal{N}_{\mathrm{PSP+ME}}$ factors. Apart from the trivial FF dipole PDF factors, the $\mathcal{N}_{\mathrm{PDF}}$, approximating the exact ratio(s) in $\mathcal{W}_{\mathrm{PDF}}$, are taken from a dynamical self-adapting tabulation to improve the efficiency in generating a valid branching. The last term of above equation exhibits the correction for the exact rapidity interval, where $\Delta y = y_+ - y_-$ and $\Delta Y = Y_+ - Y_-$. Note that violated kinematical constraints, such as the demand for valid momentum fractions $x'_\pm \leq 1$ in II dipole evolution, see sec. 2.3.3.3, also force the rejection of a trial emission with the implication to start over again from the rejected scale.

2.5.3 Scale choices, starting conditions and iteration principles

All necessary ingredients are at hand to compute a particular emission. Thus, it remains to specify the cascade-generating algorithm dealing with the multitude of emissions, i.e. various decisions have to be drawn that concern the preparation of the next step and the interplay with the hard process and the hadronization. This is tightly connected with the task of carefully choosing and processing the scales before and while the shower evolves. All of which is commented below with focus on the choices used for the production of the results presented in the next section.

Renormalization scale: various choices have been tried out, finally the results have been obtained employing the $p_\perp^2$ of the emission:

$$\mu_\mathrm{R}\Big|_\mathrm{FF} = \frac{p_\perp^2}{2} \qquad \text{and} \qquad \mu_\mathrm{R}\Big|_\mathrm{I/FI} = 2\,z\,(1-z)\,p_\perp^2 = \frac{p_\perp^2}{1+\cosh(2y)} \leq \frac{p_\perp^2}{2} \quad (2.151)$$

are used for the argument of the running strong coupling. The z variable defined by

$$z = \frac{|s_{kg}|}{|s_{kg}| + |s_{g\ell}|} = \frac{1}{1+e^{2y}} \tag{2.152}$$

is introduced as a fraction of squared two-particle masses of the partons partaking in the emission. An offset of the order of 1 GeV is added ensuring the evolution to proceed well above the Landau pole Λ_QCD.

Factorization scale: the evolution variable $p_\perp^2$ apparently increases faster with the hardness of an emission than its true squared transverse momentum in the lab-frame. Recalling that $M^2/\hat{s} \leq 1$, this fact is evident from e.g. eq. (2.65), which is valid for g_f emissions off II dipoles. Therefore, based on eq. (2.65) the scale $k_\perp^2$ is defined invariantly,

$$k_\perp^2 = \frac{|s_{kg}\,s_{g\ell}|}{|s_{kg\ell}| + |s_{kg}| + |s_{g\ell}|} = \frac{|M|\,p_\perp^2}{|M| + 2\,p_\perp\cosh y}, \tag{2.153}$$

intended to function as a more natural scale for the argument of the parton densities, since it better compares to the lab-frame squared transverse momentum. However, this is done at the prize of violating strict ordering from time to time, which particularly may

happen if an emission of large rapidity is followed by one of rather small rapidity.

Secondly, in the case of II dipoles μ_{F} has to be set in both PDFs at the same time. In first line this can be done as in a cross-section calculation assigning the new $k_\perp^2$ to both PDF scales, however it is found that better performances are achieved by using

$$\mu_{\mathrm{F}} \;=\; (4\,k_\perp^2)^{d/2}\,\tilde{\mu}_{\mathrm{F}}^{\,1-d/2} \tag{2.154}$$

with $d = 1$ and $d = 2$ for II and FI/IF dipoles, respectively. This choice particularly has been found by analyzing the frequency to have at least one parton emission in the inclusive production of Drell–Yan lepton pairs. If, in contrast to the proposed choice, $d = 2$ is used throughout, the non-emission probability, i.e. the rate of longitudinal lepton pairs, becomes somewhat large, easily seen in a reduction of the peaks of the corresponding pseudo-rapidity distribution.

The μ_{F} scales are eventually calculated from the new (trial) emission using its $k_\perp^2$, whereas the respective values present before the emission are kept in the $\tilde{\mu}_{\mathrm{F}}$ scales.

Initializing scales: first, in a hadronic environment, the primary factorization scales $\tilde{\mu}_{\mathrm{F,ini}}$ have to be adopted from the hard process.

Second, it has to be clarified which $p_\perp^2$ scale should initialize the showering off the lowest-order process. In the general case the scale related to this process has to be used to set the hardest scale of the subsequent cascade, since the shower description is valid strictly for soft and collinear emission only. As argued in the last item, the $p_\perp^2$ variable is not a direct transverse-momentum scale in the usual sense, and, therefore, the initializing scale $p_{\perp,\mathrm{ini}}^2$ has to be identified carefully. For the considerations here, three scenarios are distinguished, namely starting from a single $q\bar{q}$ dipole as in e^+e^- collisions, from a single $\bar{q}_{\mathrm{i}}q_{\mathrm{i}}'$ dipole as in Drell–Yan processes, and, from a multi-dipole state as in pure QCD jet production. For the first, a good choice is the squared mass of the parent dipole, $p_{\perp,\mathrm{ini}}^2 = \hat{s}_0 = M^2$. In the Drell–Yan case, in principle, it can be done similarly, however, taking $p_\perp$ ordering into account and referring to eq. (2.153), which corresponds to the true squared transverse momentum $\ell_\perp$ of the final-state gluon emitted from the $\bar{q}_{\mathrm{i}}q_{\mathrm{i}}'$ dipole, the maximum $\ell_\perp$ can never exceed $\ell_\perp = M/\sqrt{3}$, which is somewhat low. So, a better $p_{\perp,\mathrm{ini}}$ estimate is gained by inverting eq. (2.153) for $y = 0$, which yields

$$\left. p_{\perp,\mathrm{ini}} \right|_{\mathrm{DY}} \;=\; k_{\perp,\mathrm{max}} \left(\frac{k_{\perp,\mathrm{max}}}{M} + \sqrt{\frac{k_{\perp,\mathrm{max}}^2}{M^2} + 1} \right) , \tag{2.155}$$

and gives $\left. p_{\perp,\mathrm{ini}} \right|_{\mathrm{DY}} = (1 + \sqrt{2})M$, provided that $k_{\perp,\mathrm{max}}^2 = \ell_{\perp,\mathrm{max}}^2 = \hat{s}_0 = M^2$. However, seriously taking into account that in this model the first emission off a $\bar{q}_{\mathrm{i}}q_{\mathrm{i}}'$ dipole is matrix-element corrected per construction, it is possible to discard the restricted scale, instead allow the shower to evolve freely. In this case the initializing scale can be chosen as large as the kinematically allowed scale, i.e. $\left. p_{\perp,\mathrm{ini}} \right|_{\mathrm{DY}} = p_{\perp,\mathrm{max}}$, see next item.

The multi-dipole start configurations of the shower actually signal the need for a backward-clustering procedure, basically answering the question what was the last emission coupled to which $p_\perp^2$ that produced the present multi-dipole state. Without such an algorithm one can however try to emulate it by simply calculating all possible combinations for the fraction $|s_{kg}\,s_{g\ell}|/|s_{kg\ell}|$ using the strong particles provided by the hard process; choosing

the lowest scale out of those combinations should be sufficient to have a good estimate in hand for the initializing scale. Applied to QCD jet production, the minimal numerator of the fraction mentioned above is given by $\min\{\hat{u}\hat{t}, \hat{s}\hat{t}, \hat{s}\hat{u}\}$ employing the Mandelstam variables of the initiating $2 \to 2$ QCD process. There is also a problem, namely that the denominators are all identical to zero if quarks are considered to be massless. So, instead a squared mass $|s_{kg\ell}|$ has to be "invented", and some simple mean-value choice e.g. reads $(\hat{s} + |\hat{t}| + |\hat{u}|)/3$. Taken together,

$$p^2_{\perp,\text{ini}}\Big|_{\text{Jets}} = \frac{3\,\min\{\hat{u}\hat{t},\,\hat{s}\hat{t},\,\hat{s}\hat{u}\}}{\hat{s} + |\hat{t}| + |\hat{u}|}\,. \tag{2.156}$$

Alternatively, a scale often used in conjunction with $2 \to 2$ QCD scattering processes could be consulted,

$$p^2_{\perp,\text{ini}}\Big|_{\text{Jets}} = \mu_{\text{QCD}} = \frac{2\,\hat{s}\hat{t}\hat{u}}{\hat{s}^2 + \hat{t}^2 + \hat{u}^2}\,. \tag{2.157}$$

A third idea follows from considerations similar to the Drell–Yan case, i.e. the case of a primary II dipole, and leads to

$$p^2_{\perp,\text{ini}}\Big|_{\text{Jets}} = (1 + \sqrt{2})^2\,\ell^2_{\perp,\text{max}} \equiv (1 + \sqrt{2})^2\,\frac{\hat{u}\hat{t}}{\hat{s}}\,. \tag{2.158}$$

This scale is enhanced w.r.t. the other suggestions, since already the sole ratio term is of the order of magnitude of the other scales.

Related to multi-dipole initial states, there is a second issue of assigning large N_C colour flows to the set of dipoles. This is accomplished by analyzing the present $2 \to 2$ QCD subprocess together with its actual intrinsic kinematic configuration.

Maximal phase space: in sec. 2.3 it has been argued that for II and FI dipole regimes the size of the available phase space for a single emission is adjusted through the choices of the $\hat{s}_{\text{max}}$ parameters, cf. eqs. (2.45) and (2.75). Accordingly the limits on the evolution variables vary with these choices restricting the phase space for decreasing $\hat{s}_{\text{max}}$ values. This in turn has two effects, firstly, the kinematic upper bound $p^2_{\perp,\text{max}}$ prohibits start scales $p^2_{\perp,\text{stt}}$, in particular initializing scales $p^2_{\perp,\text{ini}}$, that exceed this bound. Therefore, if sufficiently small, $p^2_{\perp,\text{max}}$ acts as a restricting scale. However, as discussed above, the initializing scales are carefully chosen, and hence, does not need further reduction.

Secondly, it has to be noticed that the valid range for the rapidities Δy increases, see eqs. (2.51), (2.59) and (2.82), (2.87), if the reverse scenario is discussed of assigning more and more phase space to the emission. This permits the generation of either very large or very small y values for a single emission, such that in particular the two-parton invariant masses taken between the incoming and the offspring particle are affected. Hence, extreme sets of $|s_{kg}| = |M|\,p_\perp e^{-y}$ and $|s_{g\ell}| = |M|\,p_\perp e^{+y}$ (cf. sec. 2.3.1) may arise more frequently even though $p_\perp$ and $|M|$ is bounded (e.g. for II dipoles, $M^2 \simeq \hat{s}_0 \ll \hat{s} \simeq \hat{s}_{\text{max}}$). This should lead to an increase in the appearance of very (potentially hard) collinear emissions, which will populate the forward region of the detector. Thus, the enhancement of the single-emission phase space while keeping the same initializing scale should manifest itself in an enhanced production of forward and larger separated emissions (jets).

Concerning the actual choice of the $\hat{s}_{\max}$ values, the default predictions of this work are obtained by allowing the full collision phase space to be available, i.e. $\hat{s}_{\max}\big|_{\mathrm{II}} = S$ (see sec. 2.3.3) and $\hat{s}_{\max}\big|_{\mathrm{FI}} = \mathcal{S}$ (see sec. 2.3.4). [19] By all means, this is consistent with a Markovian ansatz, since no further assumptions are required except for the sensible selection of the initializing scale $p_{\perp,\mathrm{ini}}^2$. The impact of reducing the default $\hat{s}_{\max}$ values will be discussed in the next section.

Cascading: each chain (colour-singlet), once appeared, is independently evolved. The only disturbance that may occur being the recoil transfer in the case of II dipole radiation. It, however, does not spoil the further evolution of the corrected chain owing to the Lorentz invariance of the applied correction and of the shower formulation. Starting off $p_{\perp,\mathrm{ini}}^2$ consecutive emissions are decreasingly ordered in $p_\perp^2$ within a chain. This is achieved by iterating over all dipoles comparing their trial-emission $p_\perp$'s allowing that one to be finalized in its kinematics that gave the largest transverse momentum. For the next evolution step, it is used as the new start scale in the Sudakov form factors responsible for the next round of trial emissions. The procedure continues that way as long as the corresponding cut-off has not been reached, see next item.

Cut-off and hadronization aspects: under all circumstances owing to the ordering in $p_\perp^2$ the cut-off is always taken on $p_\perp^2$, hence denoted by $p_{\perp,\mathrm{cut}}^2$. It can, in principle, be chosen as small as possible, since the setting of the renormalization scale is safe and the Sudakov suppression quenches the appearing soft and collinear divergencies. Furthermore, different cut-offs related to the three dipole regimes are provided all of the order of 1 GeV. After the finalization of the cascade triggered by the certain cut-off(s), the interface to the hadronization, currently describable through phenomenological models only, does not require any special treatment apart from the usual one that also appears for conventional parton cascades. The shower's final state consists of a number of colour-singlet subsets of colour-ordered partons in the limit of large N_{C}. The assignment of an intrinsic transverse momentum to the hard process can be viewed as a hadronization correction, which is applied after the showering phase, and, therefore, irrelevant for the shower kinematics.

2.6 First results

Unquestionably, the newly developed dipole shower has to be validated in its capability of describing QCD dynamics. Therefore, a number of comparisons to data and other calculations has been carried out for various physics processes, namely

- the electroweak production of vector bosons and their subsequent hadronic decays at LEP1 energies,

- the inclusive production of Drell–Yan electron–positron pairs at Tevatron and future LHC energies,

- and, the inclusive production of QCD jets at Tevatron energies.

---

[19]Owing to hadronization issues, it can be argued that they should be taken such that the two-parton squared masses cannot fall below magnitudes of the order of 1 GeV.

All of which is highlighted in the next three subsections. Note that, for the first case only of dealing with a pure final-state cascade, the splitting of gluons into quark–antiquark pairs has been included, and occurs almost along the lines of the treatment proposed in the Lund CDM.

## 2.6.1 Hadron production in electron–positron collisions

A very suitable testbed to exclusively validate the performance of the sole final-state piece of the dipole-shower model is provided by the process $e^+e^- \to Z^0/\gamma^* \to$ hadrons, where the $q\bar{q}$ pair produced in the hard process will initiate the cascade. It allows comparison of the QCD Monte Carlo predictions with large sets of data, which, for example, are available from the LEP1 measurements of hadronic final states produced at the Z^0 pole and precisely tested the QCD dynamics of these final states. However, although given at scales of the order of 1 GeV, the shower predictions cannot be used directly, since they lack non-perturbative corrections appearing through the inevitable confinement of partons into hadrons. Therefore, the final states generated by the dipole shower need to be hadronized, which currently can be achieved through phenomenological models only, since QCD confinement is not yet solved rigorously. For more details concerning hadronization and their modelling, cf. ch. 3.

The shower model presented here has been implemented into the event generator SHERPA, and supplemented by an interface to the Lund string fragmentation routines of PYTHIA 6.2 [7], which are provided by the SHERPA framework. Similarly, the evaluation of the hard process is accomplished within SHERPA and used to initiate the dipole-shower evolution. The comparison to the experimental Z^0 pole data can then be pursued together with a tuning by hand of the parameters of the shower and the hadronization model. In detail this means to specify the value taken for the strong coupling at M_Z, adjust the FF cut-off $p_{\perp,\text{cut}}^2\big|_{\text{FF}}$ of the dipole shower and find suitable values for the Lund string model parameters a (`PARP(41)`), b (`PARP(42)`) and σ_q (`PARP(21)`). This approach is very simple and does not allow comparison to the effort of delicate Monte Carlo tuning procedures as presented in [123] and foreseen in [124] in order to automatize the procedure. However this minimalist method is sufficient to yield first significant results, which are presented in the following.

The tuned parameters read:

$$
\begin{aligned}
\alpha_s(M_Z) &= 0.1254\,, \\
p_{\perp,\text{cut}}^2\Big|_{\text{FF}} &= 0.54 \text{ GeV}^2\,, \\
a &= 0.29\,, \\
b &= 0.76 \text{ GeV}^{-2}\,, \\
\sigma_q &= 0.36 \text{ GeV}\,,
\end{aligned}
\tag{2.159}
$$

and by running the dipole shower at $S = M_Z^2$ a mean parton multiplicity of $\langle \mathcal{N}_{\text{parton}} \rangle = 9.24$ and a mean charged-particle multiplicity of $\langle \mathcal{N}_{\text{ch}} \rangle = 20.47$ are found, where the latter is somewhat below the experimentally detected value of $\langle \mathcal{N}_{\text{ch}} \rangle = 20.92 \pm 0.24$ [105]. Note that, since massless quarks are not handled yet, the dipole shower entirely has been
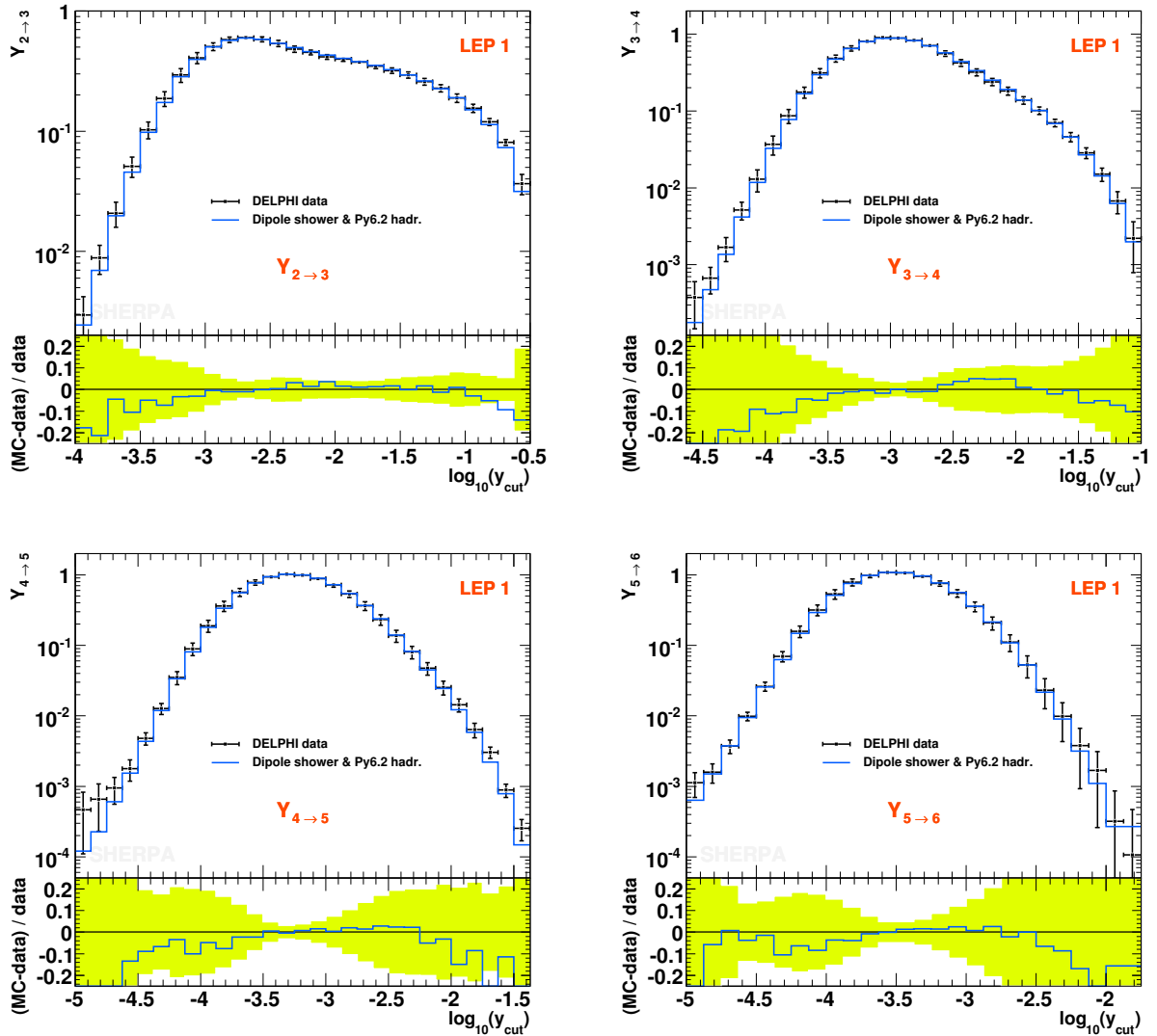
Figure 2.6: Durham differential jet rates as a function of the jet-resolution parameter y_{cut}, dipole-shower prediction vs. DELPHI data taken from [122].

started off massless $q\bar{q}$ pairs.

Figs. 2.6–2.8 show a selection of distributions, which have been obtained with the dipole shower and are compared to DELPHI data taken at $\sqrt{S} = 91.2$ GeV during the LEP1 run. The lower part in all plots visualizes the difference per bin normalized to data between the Monte Carlo prediction and the data. The light-coloured band represents the sum of the statistical and systematic error of the respective measurement.

First, in fig. 2.6 Durham differential jet rates, $Y_{n\to n+1}$, are presented up to $Y_{5\to 6}$. They characterize at which y_{cut} values an $n+1$ jet event is merged into an n jet event according to the Durham jet clustering scheme [53]. The agreement with the data taken by the DELPHI experiment [122] is very good, there is the tendency in all predictions to be below the bin means for low and high values of the jet-resolution parameter y_{cut}, but very rarely
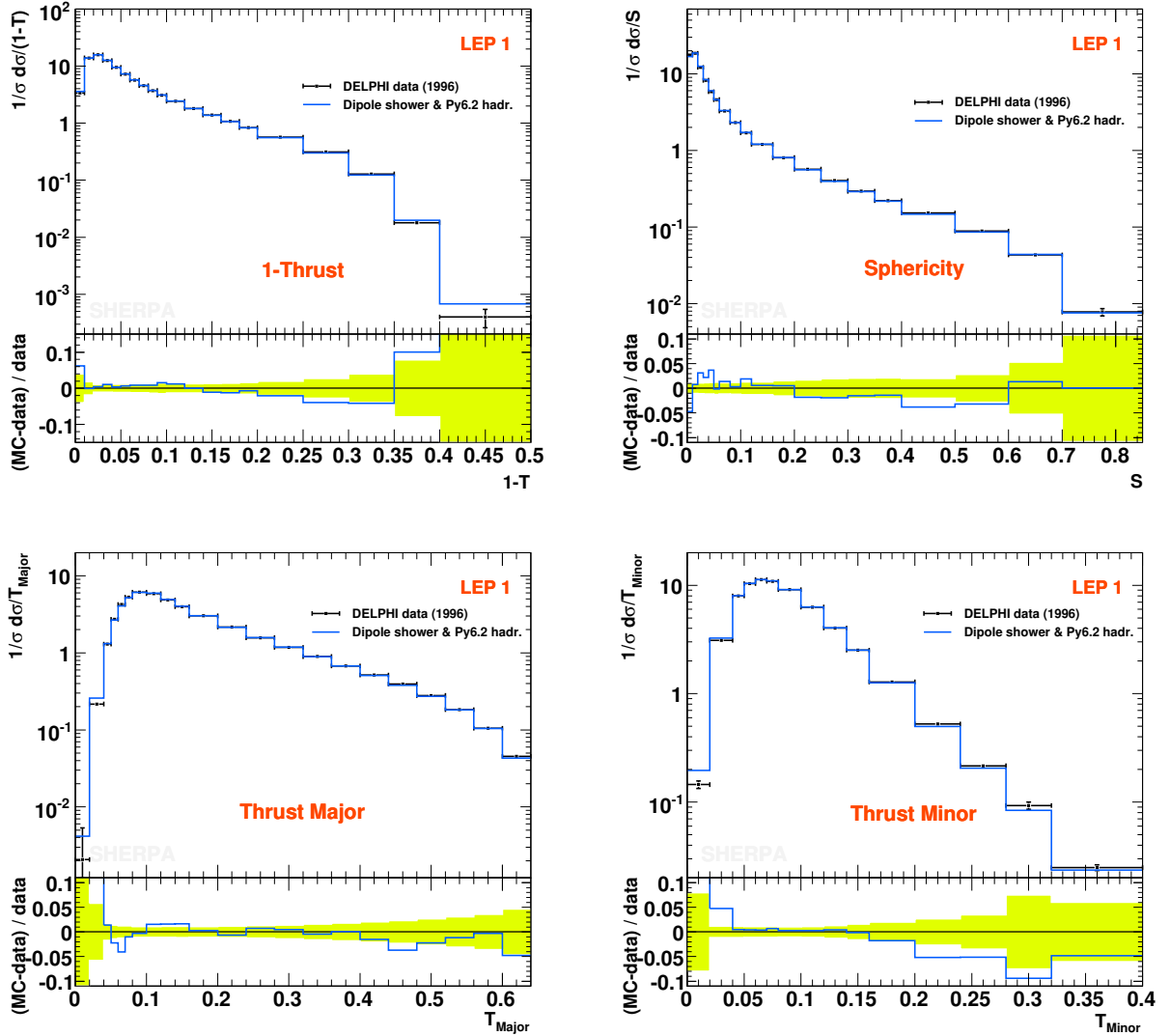
Figure 2.7: The dipole-shower predictions for the event shapes 1−thrust, sphericity, thrust major and thrust minor vs. DELPHI data [105].

the prediction is outside the uncertainty band, see e.g. $Y_{2\to 3}$. The peak positions are however very well described in all distributions.

Second, event shape variables are considered, which probe the pattern of QCD radiation for both soft and hard emissions arising from the primary $q\bar{q}$ dipole. In fig. 2.7 the distributions of 1−thrust, $1 - T$, thrust major, T_{major}, and thrust minor, T_{minor} are displayed together with the sphericity, S, placed in the top right corner of the figure. The former are all obtained from a linear momentum tensor, whereas the latter, as well as the planarity depicted in fig. 2.8, stems from a quadratic one, therefore, puts more emphasis on high momenta. All dipole-shower results are compared, once again, to DELPHI data [105]. It is noticed that the low-value parts, which are sensitive to soft emissions, are all quite well described, except for larger deviations in thrust major and minor, which, for instance, also
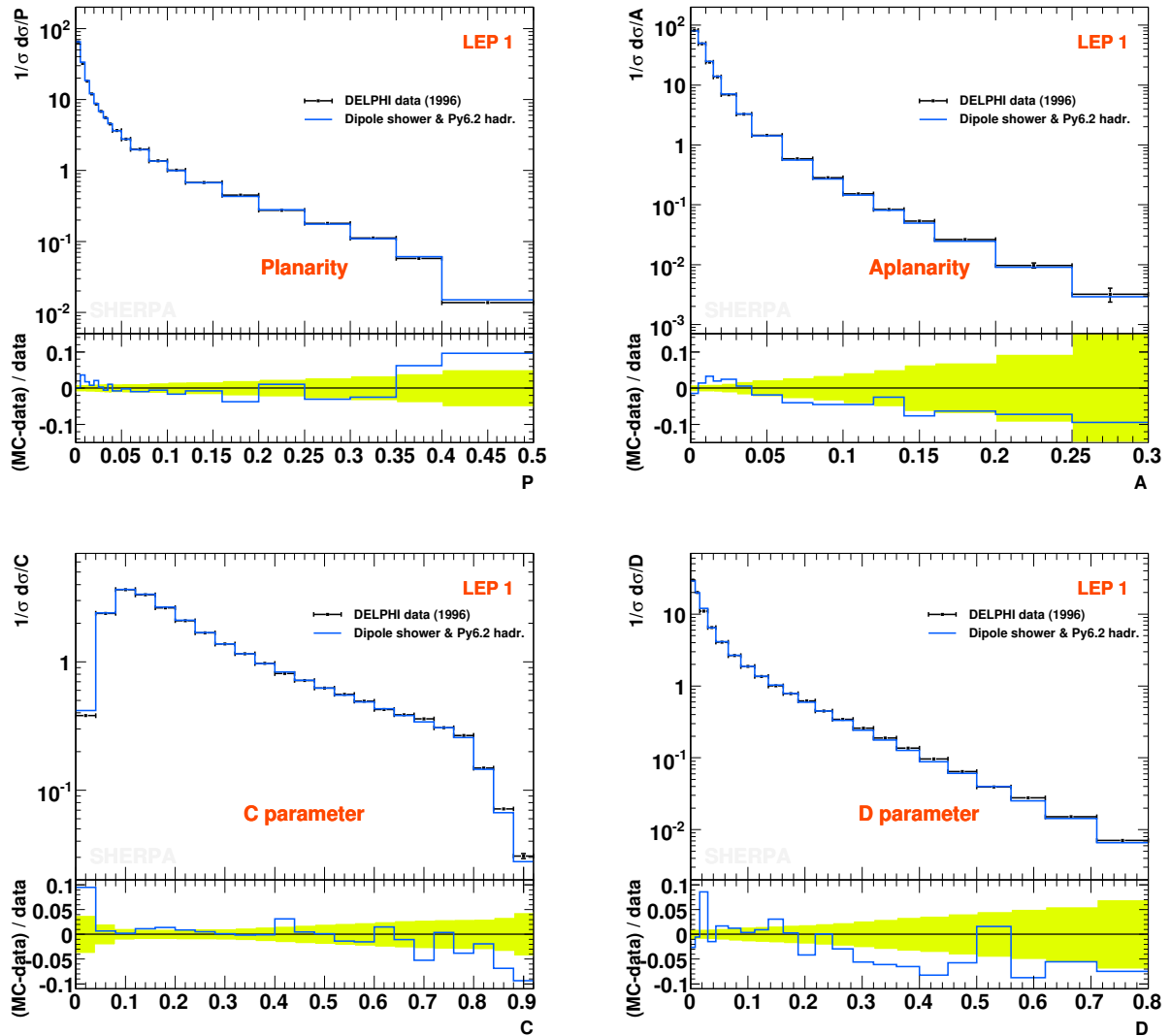
Figure 2.8: Dipole-shower predictions vs. DELPHI data [105] for the planarity and aplanarity distributions and for the C and D parameter.

appear, even somewhat larger, for the new shower of HERWIG++ [19] and the new shower presented in [27] based on Catani–Seymour dipole factorization. Although the soft parts of these distributions are all affected by hadronization corrections and the careful tuning of their underlying model, the good behaviour of the dipole shower in describing soft emissions can be understood as a consequence of exponentiating the eikonal rather than the collinear limit of QCD radiation. The predictions for hard emissions agree somewhat worse with the data. The last two bins of the $1-$thrust distribution are overestimated signalling a slight excess of spherical events, whereas thrust minor is underestimated for high values. Switching to fig. 2.8, which depicts the planarity, P, the aplanarity, A, the C and D parameter, the trend spotted above is preserved. The latter two observables are sensitive to three- and four-jet-like events. Considering the whole set of event shape vari-

ables given here, it becomes apparent that thrust minor, aplanarity and the D parameter are worse described compared to the other distributions.[20] This to some extent reflects that the gluon emergence from the $q\bar{q}$ pair is handled as in a corresponding matrix-element calculation owing to the improvement of the dipole splitting function beyond the eikonal approximation. There is however no such correction related to the description of a fourth jet, which could be the source for undershooting the data in the tails of the T_{minor}, P and D distributions.

Taken together, the agreement with data is satisfactory in all observables, hence, it can be concluded that the final-state piece of the dipole shower sufficiently is under control and continued to tackle the more complicated cases appearing in the scope of hadron colliders.

2.6.2   Inclusive production of Drell–Yan lepton pairs at hadron colliders

Naturally in a next step the performance of the dipole shower should be tested for deep inelastic scattering as measured at HERA. This would allow more exclusive verification whether the final–initial dipole evolution proceeds reasonably. This however is not considered here. For further validation of the dipole shower, its capability of simulating additional QCD radiation is scrutinized for the Drell–Yan production of lepton pairs, specifically, for the processes $pp(p\bar{p}) \to Z^0/\gamma^* \to e^+e^-$. In the scope of hadronic collisions they constitute the most simple and clean cases and form the initial–initial dipole counterpart of the $q\bar{q}$ evolution discussed above.

All predictions that will be presented in the following have been obtained by using the CTEQ6L set of PDFs [125]. In accordance with the choice in the PDF, the strong coupling constant has been fixed through $\alpha_s(M_Z) = 0.118$ and its running is taken at the two-loop level. Only light-quark flavours are considered and the quarks are considered as massless. Furthermore the dipole-shower cut-offs related to FI and II dipole evolution are both set to 1 GeV, i.e. $p_{\perp,\mathrm{cut}}^2\big|_{\mathrm{FI}} = p_{\perp,\mathrm{cut}}^2\big|_{\mathrm{II}} = 1$ GeV^2, in contrast to $p_{\perp,\mathrm{cut}}^2\big|_{\mathrm{FF}} = 0.54$ GeV^2. The hard processes are again provided by the internal matrix-element generation of SHERPA. In cases where hadron-level results are referred to, hadronization has been accomplished, as before, through an interface to the Lund string routines of PYTHIA. The Lund parameter settings found in the previous section are, of course, kept.

The discussion of the dipole-shower predictions starts with the consideration of the transverse-momentum distribution of the bosons (decaying into e^+e^- pairs) in comparison to data taken during Run I at the Fermilab Tevatron. Then various predictions at Run II energies of $\sqrt{S} = 1.96$ TeV will be exposed followed by those obtained at LHC energies of $\sqrt{S} = 14.0$ TeV. In cases where data are not available, the comparison occurs to various SHERPA predictions that have been validated in many other comparative studies [42, 61, 126, 52] or even to data [127]. Thus, both the APACIC++ parton shower of SHERPA will be used and SHERPA's CKKW method will be invoked of merging tree-level matrix elements and parton showers. To this end, inclusive samples combining matrix elements

---

[20]There is also a difference in quality of describing the p_T^{in} and p_T^{out} spectra – with better performances found for the first – present in the larger set of observables prepared for this study. They are calculated w.r.t. the plane defined by the T and T_{major} axes, and, they are related to the planar and non-planar structure of the event, respectively.
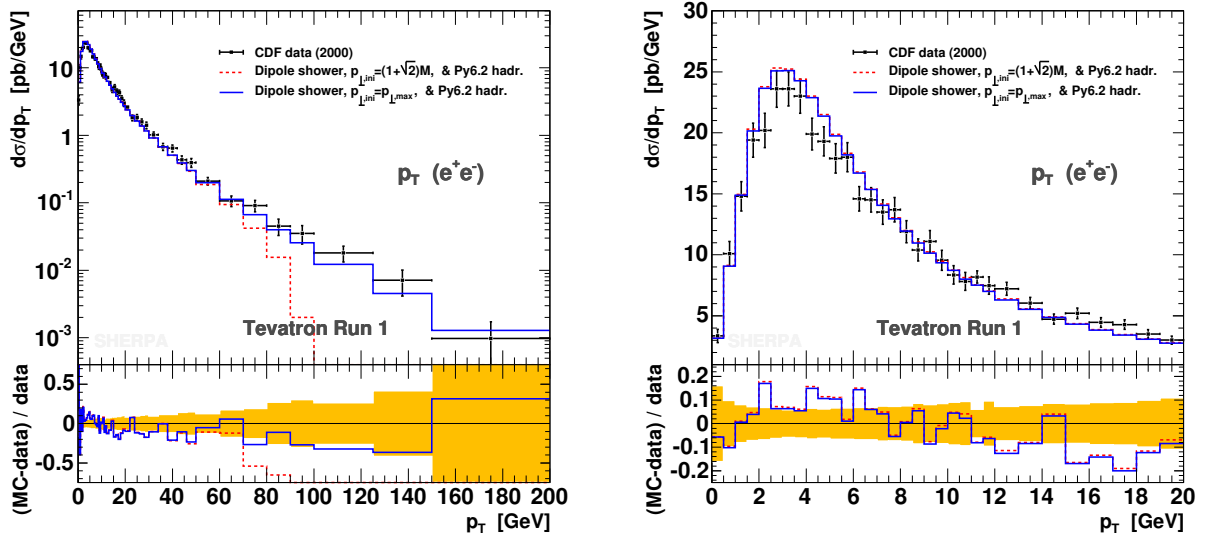
Figure 2.9: Boson transverse-momentum distribution in $e^+e^- + X$ as predicted by the dipole shower for two different choices concerning the initializing scale. The Monte Carlo calculations are compared with CDF data [128] taken during Run I. The right panel depicts the very soft region of the distribution only.

for no extra and extra emissions of final-state partons have been generated using SHERPA version 1.0.10, the variable n_{ME} thereby denotes the maximal number of QCD particles in the final state that have been obtained through a matrix-element description.

Tevatron Run I predictions

In fig. 2.9 the transverse-momentum distribution of the lepton pair is shown, where its mass is constrained to fall into the range of 66 GeV $< M_{ee} < 116$ GeV. The spectrum is heavily influenced by additional QCD radiation arising in both soft and hard phase-space domains and has been measured with high precision by the Tevatron experiments. The hadron-level predictions acquired with the dipole shower and normalized to the inclusive cross section found by the experiment are presented in fig. 2.9. They are confronted with data from a CDF measurement [128]. The right part of the figure contains a closer view of the peak region on a linear scale; as before the lower panel in each plot shows the ratio (MC−data)/data and the bright band illustrates the uncertainty of the measurement. The turn on of the distribution is well described by the dipole shower. Around the peak, which appears to be narrower in data, a slight excess is found, which is followed by an underestimation compared to data for the region above 12 GeV. For very low p_T, an intrinsic transverse-momentum smearing according to a Gaussian having mean of 0.3 GeV and width of 0.4 GeV has been additionally employed. This slightly has improved the shower outcome, since it led to a small shift to the right of the peak of the untouched prediction. Moreover, having used the low p_T data for tuning these parameters, again by hand only, they will be kept fixed for the upcoming investigations. The two dipole-shower

predictions differ in their choice of the initializing scale, using, first, $p_{\perp,\text{ini}} = (1 + \sqrt{2})M_{ee}$ and, second, $p_{\perp,\text{ini}} = p_{\perp,\text{max}}$; the $\hat{s}_{\text{max}}$ values however have been chosen as large as possible, i.e. $\hat{s}_{\text{max}}\big|_{\text{II}} = 1.8$ TeV and $\hat{s}_{\text{max}}\big|_{\text{FI}} = \mathcal{S}$, cf. the discussion in sec. 2.5.3. Hence, in the latter case the shower runs totally unconstrained, which as argued before, can be allowed, since the first emission is matrix-element corrected by construction, and, therefore in principle may appear at a scale exceeding M_{ee}^2. This in turn will set the highest scale for all subsequent emissions. As a result of this treatment, the prediction for large p_T is in good agreement with the data. In contrast, the dipole shower for the case of the restricted initializing scale starts gradually losing hardness above 60 GeV before it dies off rapidly above 80 GeV. Both of which is a consequence of adjusting the scale according to the lab-frame transverse-momentum characteristics of gluon rather than quark emissions, which generate less transverse $\ell_\perp$ in the lab-frame for the same invariant evolution $p_\perp$. Coming back to the soft part of the distribution, this is however almost identically described by both dipole-shower predictions.

Tevatron Run II predictions

Having passed the first crucial test, a more extensive study has been carried out using a large set of observables and their predictions, which on the one hand have been obtained from different SHERPA CKKW samples, namely for $n_{\text{ME}} = 1$ and $n_{\text{ME}} = 2$, and on the other hand from the unconstrained as well as the $p_{\perp,\text{ini}}$ restricted dipole shower. In the plots the former dipole-shower case will be denoted by "Dipole shower, max"; the latter case however is actually considered as the default, since the reasoning concerning matrix-element corrected first emissions does not apply beyond Drell–Yan processes. In the general case such higher-order corrections can only be included by matrix-element parton-shower merging techniques or a matching with NLO calculations.

Some of the observables presented here directly probe the jet structure of the events, so, a jet definition is required, and has been attained according to the Run II k_T algorithm [54, 62] using the parameter $D = 1$. The jet p_T threshold is set to 15 GeV, i.e. $p_{T,\text{jet}} > 15$ GeV, the jet η range is however not constrained to allow better validation of the predictions at large rapidities. In addition, the Drell–Yan lepton-pair mass has been narrowed down w.r.t. the previous study, 71 GeV $< M_{ee} <$ 111 GeV.

Since the comparison is not to data anymore, here and in the following the respective lower panels depict the ratio (MC−ref)/ref, where the reference prediction (ref) is indicated in the plots. Secondly, all distributions are normalized to unit area, allowing for a direct comparison of the shapes of the distributions. Owing to the intrinsic first-order matrix-element correction present in the dipole shower, the performance of the unconstrained shower can be directly compared with that of CKKW for $n_{\text{ME}} = 1$, and, therefore, critically tested against a well validated inclusive vector boson plus one-jet description. To estimate the impact of also describing the second extra parton emission by matrix elements, all plots are supplemented by the respective CKKW prediction for $n_{\text{ME}} = 2$.

In fig. 2.10 two η_{ee} spectra and the $p_{T,ee}$ distribution are shown, the latter this time on a double-logarithmic scale to provide good insight to both soft and hard p_T domains. Concerning the two dipole-shower predictions the findings are as above. In the hard tail the shower result is 20% below the CKKW reference, the difference in the low p_T part amounts up to 40% and the region of 1 GeV $< p_T <$ 10 GeV is preferred by the shower
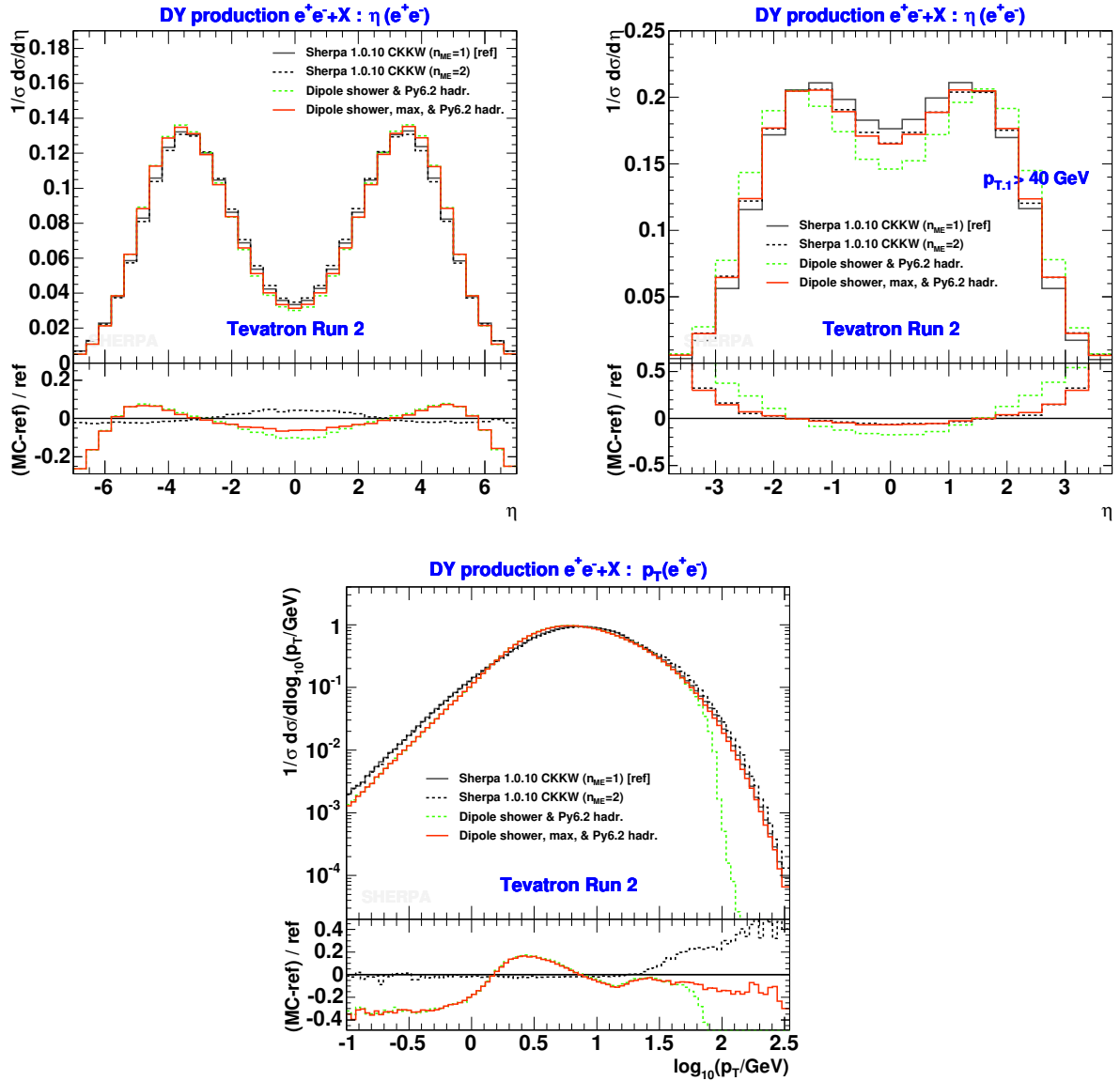
Figure 2.10: SHERPA and dipole-shower predictions for pseudo-rapidity spectra and the transverse-momentum distribution (bottom panel) of the lepton pair in inclusive gauge boson production. For the η_{ee} distribution in the top right panel, the p_T of the leading jet was required to be larger than 40 GeV. The grey solid, the black dashed, the green dashed and the red solid lines give the SHERPA CKKW $n_{ME} = 1$, CKKW $n_{ME} = 2$, the default and unconstrained dipole-shower predictions, respectively.

w.r.t. the CKKW merging. The peak positions are slightly differently predicted with the lower value given by the dipole shower. In first place, these deviations can be traced back, for the very soft part, to different choices in the parameter settings for the fragmentation of the partons (including the intrinsic k_T smearing), for the range 1 GeV $< p_T <$ 15 GeV, to different radiation patterns generated by the dipole shower and the shower used by the CKKW merging, APACIC++, and, for the high p_T tail, to differences in choosing and processing the scales in both approaches, which in the case of CKKW is a tricky and
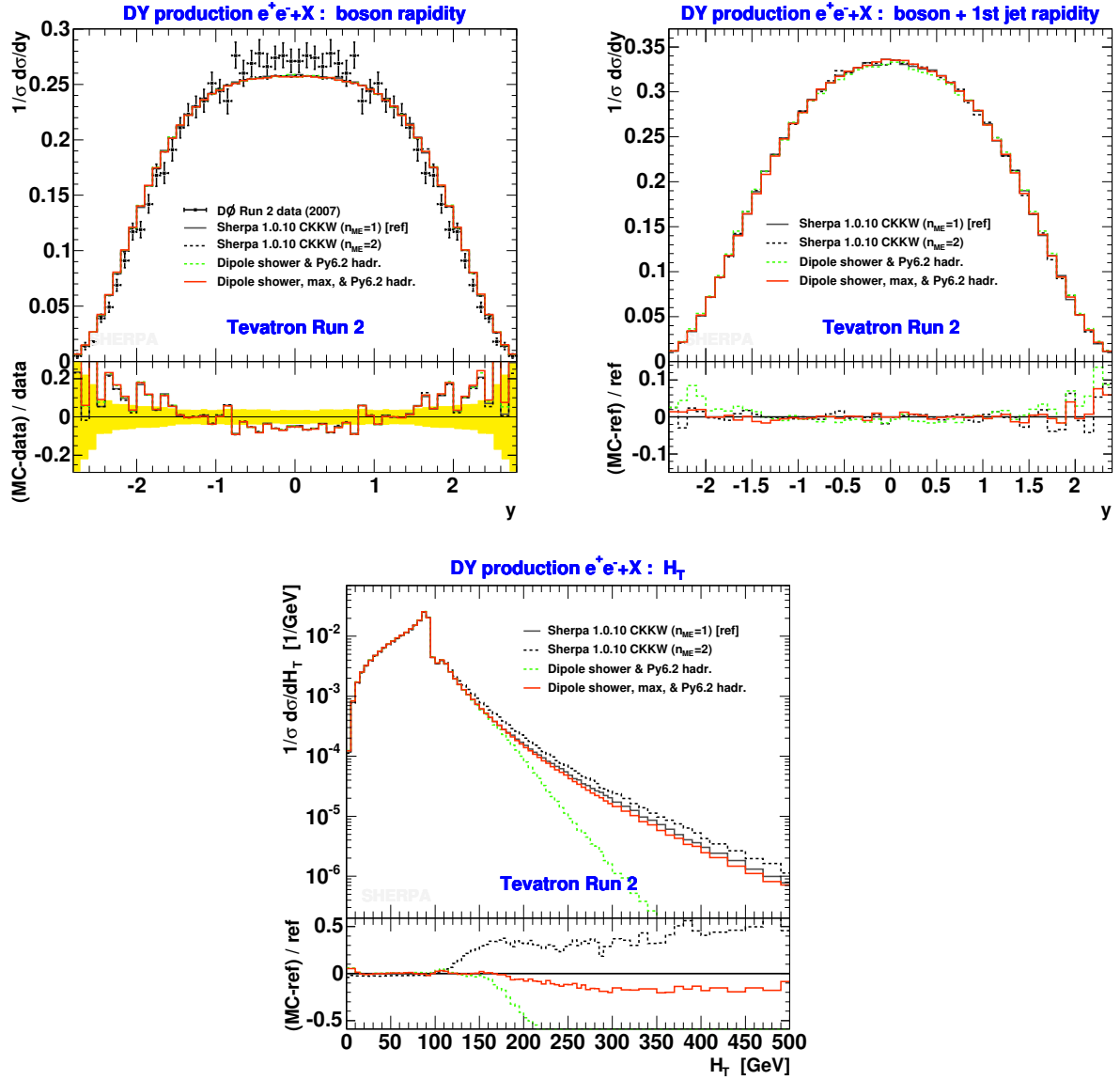
Figure 2.11: Rapidity spectrum of the vector boson (top left panel) as predicted by SHERPA and the dipole shower in comparison to recent DØ data [129], SHERPA and dipole-shower predictions for the rapidity spectrum of the boson plus hardest-jet system (top right panel) and for the scalar sum of lepton and jet transverse momenta, H_T, (bottom panel); all of which shown for the inclusive production of Z^0/γ^* bosons at $\sqrt{S} = 1.96$ TeV. Labelling is as in fig. 2.10.

to some extent the heart of the business. Concerning the second point, APACIC++ is a virtuality-ordered parton shower in the traditional sense resumming large logarithms in the collinear rather than the soft limit of QCD radiation, thus, varying results can be expected. However, taking all these differences into account, deviations at the 40% level are not unusual, on the contrary they are typical, and, hence, the agreement can be judged to be satisfactory. Inspecting the CKKW prediction for $n_{ME} = 2$, a further enhancement of the high p_T tail of up to 40% is found.

Turning to the pseudo-rapidity distributions of fig. 2.10, these leptonic observables are largely determined by the additional QCD emissions, especially by the hardest one. They reflect the way the Drell–Yan lepton pair recoils against all other final-state particles. As for the transverse-momentum distribution they are first defined beyond the leading order Drell–Yan process. The figure's top left panel shows η_{ee} where no further constraints have been applied. All predictions are in rather good agreement, the maxima and the central rapidity region of the distribution are slightly more and less pronounced by the dipole shower, respectively. Furthermore, as it can be read off the plot, an extended capability in describing hard emissions results in an enhanced vector boson appearance in the central η range. This becomes even more apparent in the second pseudo-rapidity distribution, where the additional requirement of the hardest jet having $p_{T,1} > 40$ GeV has been imposed. As expected the default dipole-shower prediction shows the largest deviations w.r.t. that of CKKW $n_{\mathrm{ME}} = 1$, surprisingly the unconstrained result matches well with that of CKKW $n_{\mathrm{ME}} = 2$.

Before the focus of the discussion turns to jet observables, a second set of inclusive observables is presented in fig. 2.11, displaying the rapidity distribution of the vector boson and vector boson plus hardest-jet system, as well as the H_T distribution, where H_T is the scalar sum of the transverse momenta of all leptons and jets in the event. The Monte Carlo predictions are very different in their description of the tail of this distribution, but eventually they are as expected and again the unconstrained dipole shower is only 20% below the CKKW reference. The rapid fall at $H_T \approx 90$ GeV and the little bump at $H_T \approx 110$ GeV emerge due to the small width of the Z^0 boson allowing a maximal leptonic p_T sum of about 90 GeV and the requirement on the p_T of a jet to be above 15 GeV. Switching to the left panel, there is hardly any shape difference visible for the boson rapidity between the various Monte Carlo predictions. Concerning dipole-shower validation, this nicely confirms the good choice made in II dipole kinematics of preserving the rapidity of the final-state particles, cf. sec. 2.3.3.3. Further support is given through the excellent agreement found for the y_{ee1} predictions shown in the top right part of the figure. However, when confronted with data from a recent DØ boson-rapidity measurement [129], the Monte Carlo shapes are somewhat wider with an excess of up to 20% for large rapidities; a better agreement over the full rapidity range is only achieved by the NNLO QCD predictions of [130].

Fig. 2.12 contains the jet pseudo-rapidity, η_i, and transverse-momentum, $p_{T,i}$, distributions of the first three jets. For the former, the dipole-shower predictions are quite similar and in all cases narrower w.r.t. the CKKW SHERPA predictions. For the latter the pattern found is as expected, the default shower is not capable of filling the high p_T phase space. The predictions of the unconstrained dipole evolution agree quite well with the respective ones of SHERPA CKKW $n_{\mathrm{ME}} = 1$, again on a 20%–40% level. It tells that the cascade also reasonably evolves after the hardest emission and the scale setting by the first (unconstrained) emission is meaningful. The hardness of the predictions of the inclusive two-jet sample are of course out of reach for the dipole shower, signalling that for the description of high p_T jets, matrix-element parton-shower merging strategies are indispensable.

The same reasoning holds for jet–jet correlations, which are correctly included in the respective matrix elements only. Therefore, the dipole shower cannot be expected to be capable of their description. However, an estimate of the level of deviation can be gained. As an example the $\Delta R_{ij} = \sqrt{(\eta_i - \eta_j)^2 + (\phi_i - \phi_j)^2}$ separations of jets are shown in the
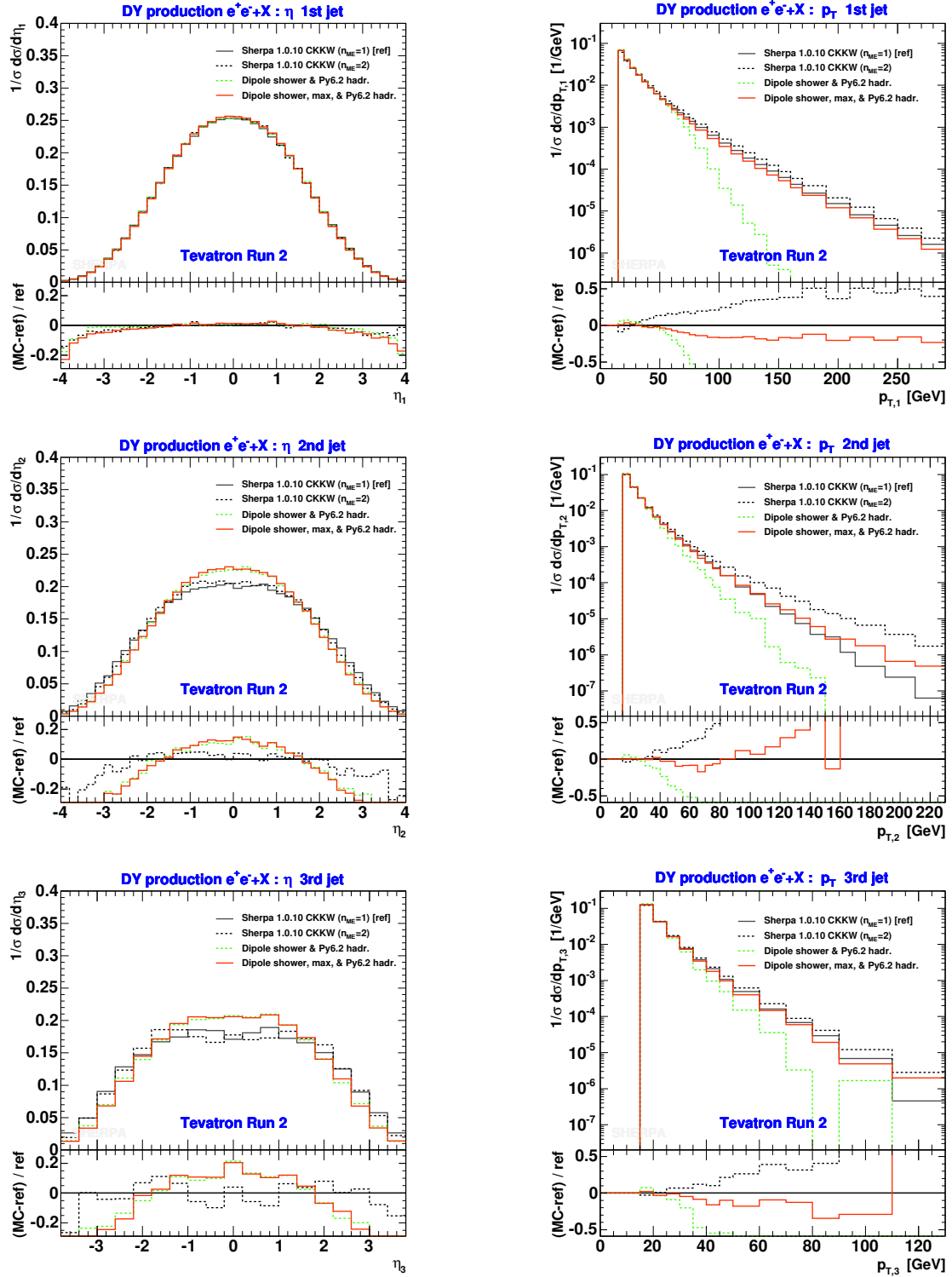
Figure 2.12: Pseudo-rapidity (left column) and transverse-momentum (right column) distributions of the first three jets in inclusive lepton-pair production. Dipole-shower results are shown in comparison to those obtained by the CKKW method of SHERPA. Labelling is as in fig. 2.10.

right column of fig. 2.13. In all plots the differences amount to $\pm 20\%$ at most, and the shower predictions, insignificantly deviating from each other, have the tendency to be distorted towards smaller ΔR values w.r.t. the SHERPA CKKW predictions. For the case of ΔR_{12}, the shower can be validated against the CKKW $n_{\mathrm{ME}} = 2$ calculation, which has the full correlation, with the result that the shower underestimates the peak around $\Delta R = \pi$, and overshoots for small separations. Also shown in fig. 2.13, in its left column there are the k_T differential jet rates, which give good insight to the details of the full radiation pattern in both soft and hard emission phase-space domains. Thereby the cluster scale d_i denotes the k_T value at which the i-th additional parton gets resolved as a jet from the respective $i - 1$ jet configuration. Concerning the comparison, for large values, they mostly reflect the behaviour already found in the p_T spectra of the jets, but they also allow better judgement of the bulk-of-radiation part and there the agreement is remarkably similar between the Monte Carlo predictions. Of course, the region and the differences below 1 GeV are determined by the hadronization procedure.

In addition to the comprehensive comparison, three special cases have been considered, dealing with shower-specific issues. For these considerations, the unconstrained dipole shower has been used and all predictions are obtained without hadronizing the partons. The details are below:

- **All dipole vs. II dipole evolution:**

  This is briefly exemplified in fig. 2.14, showing the p_T distribution of the hardest and the jet in inclusive and exclusive $Z^0/\gamma^* +$jet production, respectively. The II dipole evolution preferably stops after one emission, since the more probable gluon emission leaves two final–initial dipoles. Considering the inclusive case, both dipole-shower predictions agree, simply showing the dominance of the first emission in describing the inclusive spectrum. This also applies to the p_T of the vector boson. Referring to the exclusive case, the two shower setups of course perform very differently, the enhancement of the distribution for II dipole evolution is just a consequence of the artificial stop of the full evolution.

- **Impact of scale variations in the dipole shower:**

  A rough estimate for the uncertainty of the shower predictions can be gained from varying the values taken for the μ_{F} and μ_{R} scales within the shower algorithm. To do so, they are multiplied/divided by 4. The μ_{F} scale enters through the PDF weight, and μ_{R} as the scale of the running strong coupling in the splitting cross sections, cf. sec. 2.5.2. The outcome of this study is exemplified in fig. 2.15, presenting the uncertainties for a few distributions, namely H_T, η_2, η_{ee} and $p_{T,e}$. The SHERPA reference ($n_{\mathrm{ME}} = 1$) is kept in the plots to indicate whether it is contained in the shower's uncertainty band, which is not the case for η_2 that shows the least dependence on the $\mu_{\mathrm{F}}, \mu_{\mathrm{R}}$ manipulation. In contrast the uncertainty is largest for H_T varying on the level of $\pm 40\%$ in the tail of the distribution.

- **Impact of the improved recoil strategy for II antiquark–quark dipoles:**

  Lastly, validating the impact of the Kleiss trick for $\bar{q}'_{\mathrm{i}} q_{\mathrm{i}}$ dipoles, single-lepton spectra, correlations between the leptons of the Drell–Yan pair, and between the lepton and the first jet are considered. First, the performance of the shower stopped after the
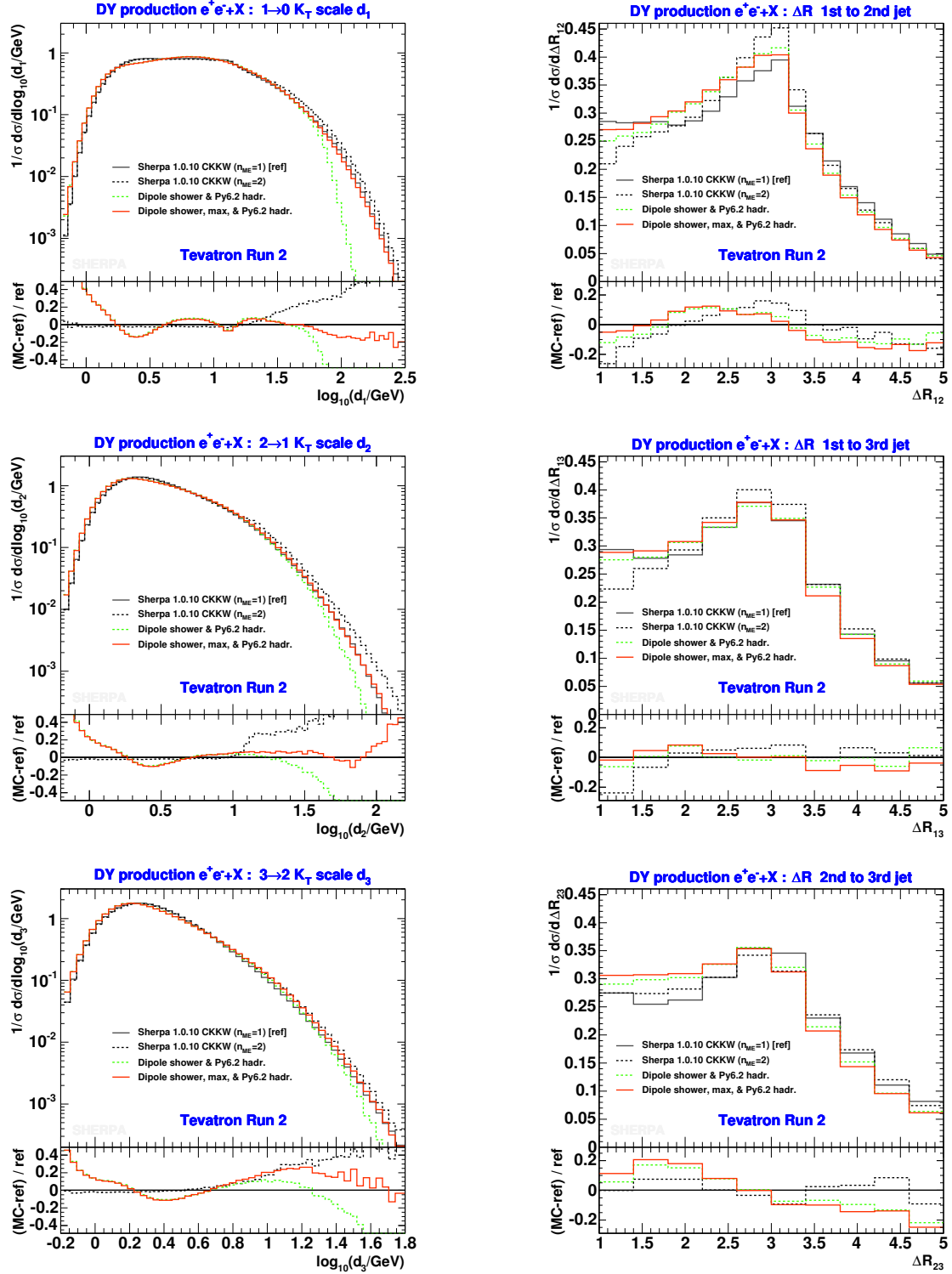
Figure 2.13: The k_T differential jet rates $d_{1,2,3}$ (left column) and ΔR_{ij} separations between the first three jets (right column) in inclusive Drell–Yan e^+e^- production at Tevatron Run II. Results obtained with SHERPA CKKW and the dipole shower are confronted with each other. Labelling is as before, see fig. 2.10.
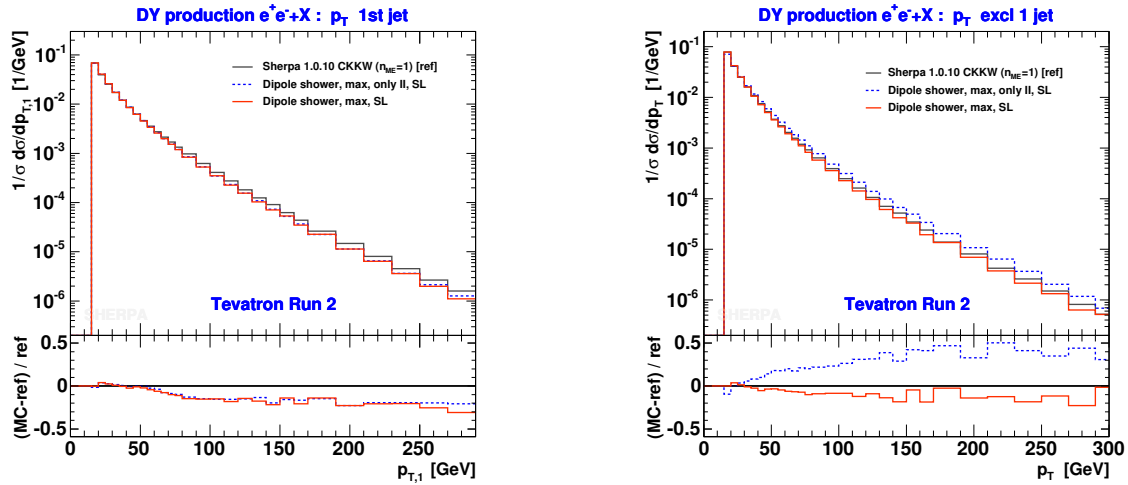
Figure 2.14: Fully evolved cascade vs. pure II dipole cascade: the transverse momentum of the hardest jet in inclusive gauge boson production and of the single jet in exclusive gauge boson plus jet production. The dashed blue line represents the result from the exclusive II dipole evolution, the other lines are as before. Shown are shower-level predictions, denoted by SL.

first emission can be checked against a fixed-order calculation for the production of a jet (extra parton) accompanying the Drell–Yan pair. For this comparison, the strong coupling is kept fixed and a cut on the p_T of the jet of the order of 40 GeV is employed, in order to avoid large Sudakov suppression. Under these circumstances, perfect agreement is found between the fixed-order and the shower result; clear differences arise in the observables outlined above in the very moment the Kleiss improvement will be switched off.

Second, under full Monte Carlo simulation, there are deviations between SHERPA CKKW $n_{ME} = 1$, which accounts for the full correlation via the employed matrix element, and the dipole shower of the order of the already discussed scale uncertainties. It just reflects that the treatment of subsequent emissions after the accomplishment of the first differs in both approaches. However, the differences sizeably increase (get doubled), once the Kleiss corrections are not considered within the dipole showering. All of the second comparison is shown in fig. 2.16, where the plots in the right column are obtained under the additional requirement of $p_{T,1} > 40$ GeV, in order to project out the deviations more clearly. The effects are exemplified by means of the distributions of $p_{T,e}$, $\Delta\eta_{e,e} = \eta_{e^-} - \eta_{e^+}$, $p_{T,e1}$ (the p_T of the electron-hardest-jet system) and $\Delta R_{e,1}$.

LHC predictions

Having studied the performance of the dipole shower for Tevatron energies, it will be verified for increased energies. Therefore, the analysis used in the latter case will be applied to LHC energies, giving a good testbed to check whether the energy extrapolation yields
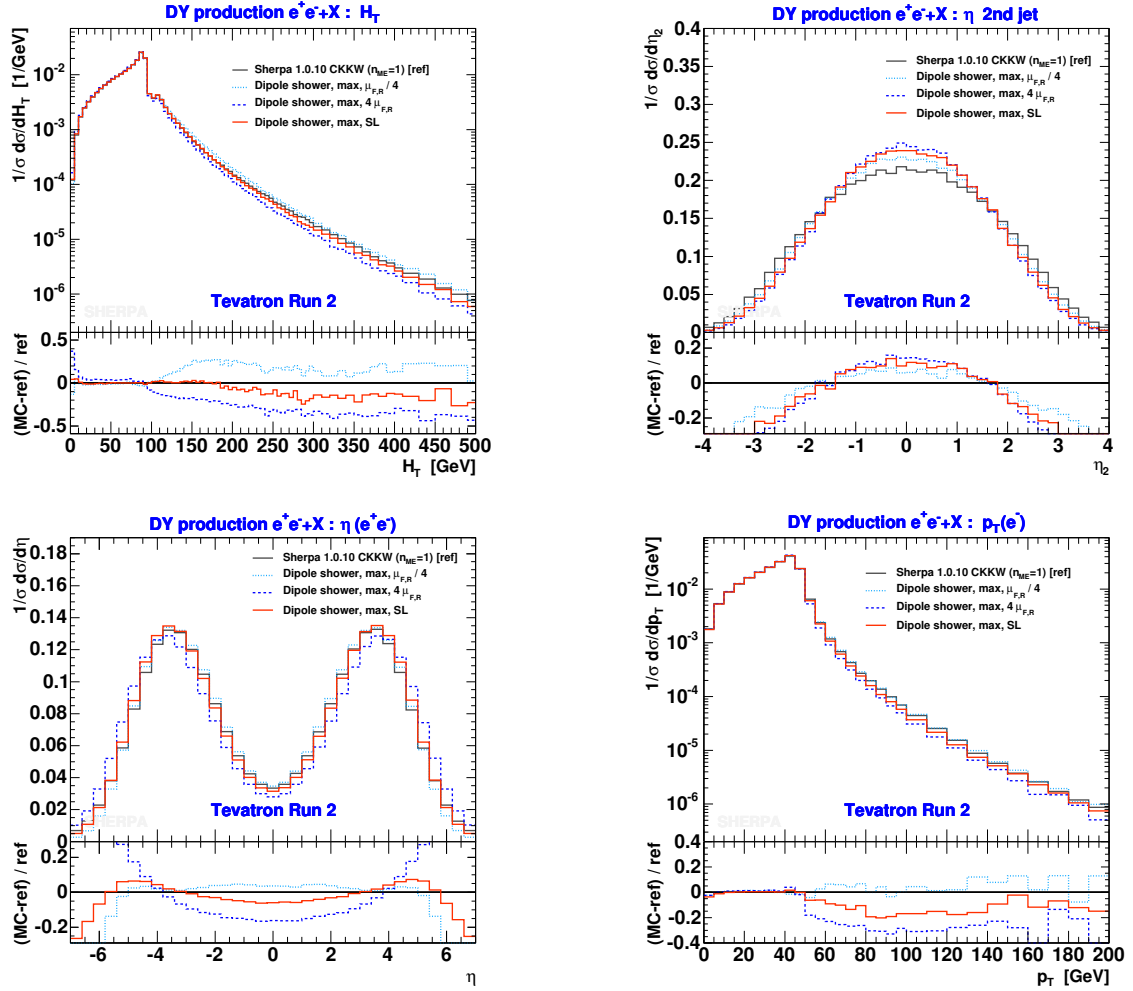
Figure 2.15: Impact of scale variations on the shower evolution exemplified by means of the H_T, η_2, η_{ee} and $p_{T,e}$ distribution. The blue lines give the uncertainty of the default prediction for the unconstrained shower.

reasonable results for the dipole shower. Thus it is concentrated on studying the performance of the unconstrained dipole shower as before w.r.t. SHERPA CKKW predictions, this time for $n_{ME} = 1, 2, 3$ and, additionally, the prediction of the pure SHERPA intrinsic shower, namely APACIC++. The only change in the setup of the analysis is to use a higher jet p_T threshold, namely $p_{T,jet} > 20$ GeV. Moreover, the under LHC conditions considerably larger phase space, which is available for additional QCD radiation leading to the copious production of jets, provides an excellent means to cross-check the $\hat{s}_{max}$ settings used so far and study the effect of changing their defaults.

Figs. 2.17–2.19 show the results of the hadron-level comparison. The trend found in the Tevatron study is followed, which is a very satisfactory result, since it proves reasonable extrapolation towards higher energies. In fig. 2.17, instead of the SHERPA CKKW $n_{ME} = 3$, the APACIC++ result is presented for η_{ee}, featuring a considerably larger dip
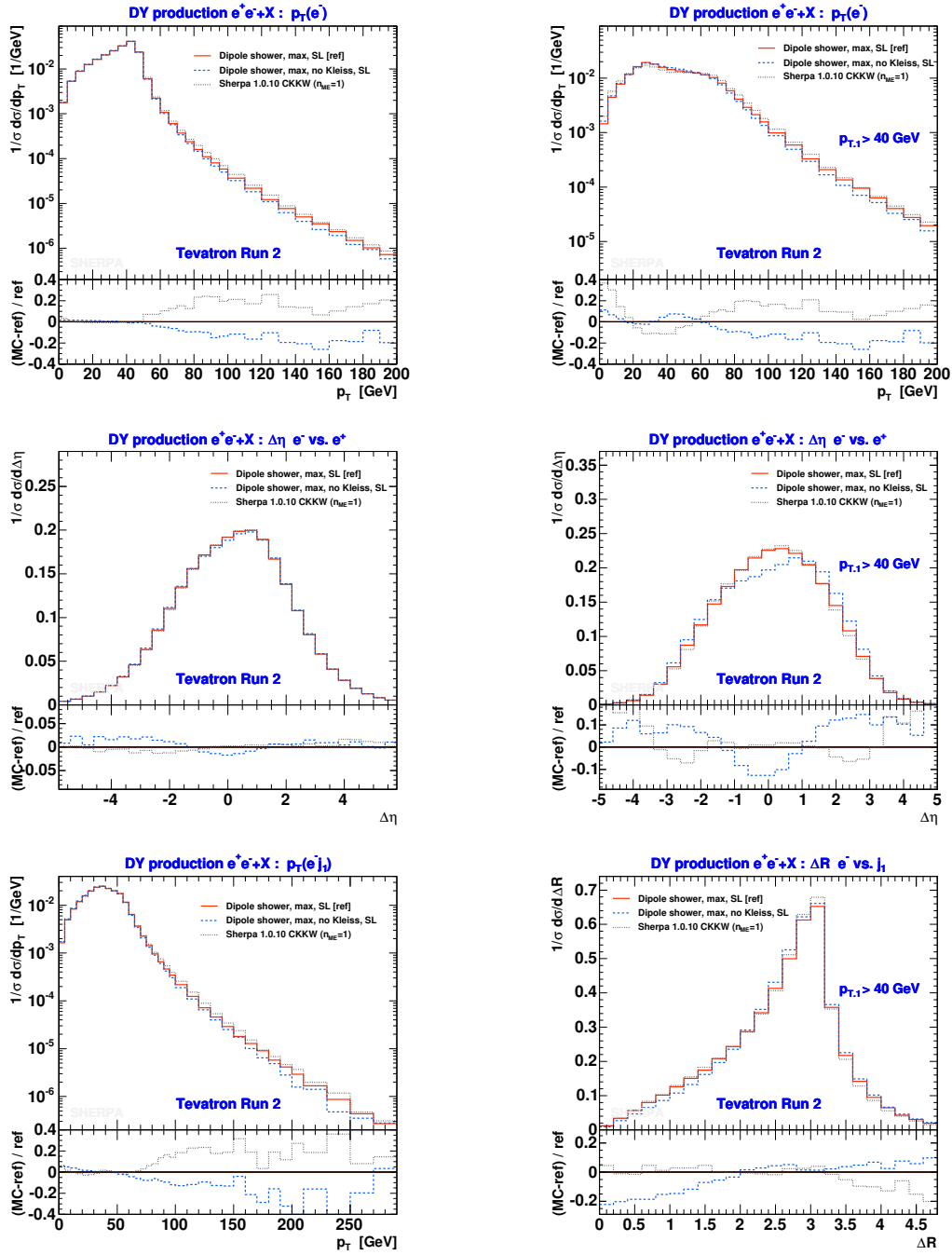
Figure 2.16: Impact of Kleiss trick: first row, transverse-momentum distributions of the electron, second row, pseudo-rapidity differences between the electron and positron $\Delta\eta_{e,e}$, third row, p_T distribution of the electron-hardest-jet system and ΔR separation between the electron and the leading jet, $\Delta R_{e,1}$. The plots of the right column are obtained under the requirement that the hardest-jet p_T exceeded 40 GeV. The red solid, the blue dashed and the grey dotted lines denote the shower-level predictions of the unconstrained dipole shower with and without Kleiss corrections and the SHERPA CKKW $n_{\mathrm{ME}} = 1$ merging, respectively.

in the central pseudo-rapidity region than the other predictions. This is a consequence of lacking sufficiently hard emissions, since this shower cannot be trustworthy applied beyond the collinear and soft phase-space regions, therefore being constrained from above through the invariant mass of the Drell–Yan lepton pair. To the dipole shower this means, that it has improved capability in predicting this distribution w.r.t. APACIC++. An prediction of APACIC++ is also shown for the vector boson rapidity spectrum, which has been obtained under the additional requirement that the first and the second jet appear well separated in rapidity, namely according to $y_1 y_2 < -2$. There APACIC++ predicts – very differently compared to the other codes – a much higher tendency of the boson to accompany one of the jets. On the contrary, the other codes give flat spectra for central rapidities and very nicely the dipole-shower prediction agrees remarkably well with that of SHERPA CKKW $n_{\mathrm{ME}} = 2$.

Three more observables are added to the discussion: they are displayed in fig. 2.20. The p_T distribution of the electron-hardest-jet system is shown in the top left panel of the figure. It documents a nice agreement between the dipole shower and the $n_{\mathrm{ME}} = 1$ SHERPA CKKW results. The other CKKW samples being of higher order predict a rise of the p_T tail of about 50%, which comes about their improved qualification in describing the hard emission domain. The top right plot depicts the $|\Delta\eta_{ee,1}| = |\eta_{ee} - \eta_1|$ distribution. APACIC++ describes a suppression of the region of low values, which is in contrast to the answers of the other methods. The dipole shower almost follows the CKKW curves, which are more reliable in describing this observable due to their higher-order contributions. This tellingly signifies that the improvements of the dipole splitting functions beyond eikonal approximation are very significant. Accordingly, the radiation pattern has been further investigated by looking at the angle θ_{13} between the first and third jet, whereas this angle is measured in the rest frame of the first and second jet. Interestingly, the tendency of the dipole shower is to rather agree with the beyond-first-order CKKW predictions than with that of $n_{\mathrm{ME}} = 1$, as read off the bottom plot of fig. 2.20.

So far all comparisons centered around discussing the shape of distributions. Therefore, tab. 2.2 provides some insight to the predictions concerning the total rate, inclusive and exclusive jet rates. Remarkably, the results given by the unconstrained dipole shower lie between those of SHERPA CKKW $n_{\mathrm{ME}} = 1$ and $n_{\mathrm{ME}} = 2$, which is further verification that the shower evolution proceeds sensibly after the first – the matrix-element-like emission. [21]

A last issue again closely related to shower internals concerns the study of the effects of the $\hat{s}_{\max}$ reduction. The findings are summarized under the item below.

- **Impact of maximal phase space:**
  This is best discussed by means of tab. 2.2 and fig. 2.21, which confront with each other the predictions of the unconstrained, the default and the dipole shower where the $\hat{s}_{\max}$ have been given through $p_{\perp,\max}^2 = p_{\perp,\mathrm{ini}}^2 = (1 + \sqrt{2})^2 M_{ee}^2$ (cf. e.g. eq. (2.52) in sec. 2.3.3.1), which constitutes a dynamic choice, and is therefore denoted by "dyn". As mentioned before, the former two have the full phase space available with

---

[21] It is more meaningful to compare according to values normalized to the total cross; for the inclusive $1, 2, 3$-jet rate, they read $0.30, 0.08, 0.017$ for CKKW $n_{\mathrm{ME}} = 1$; $0.34, 0.11, 0.025$ for CKKW $n_{\mathrm{ME}} = 2$; and $0.29, 0.08, 0.023$ for the unconstrained dipole shower, respectively.
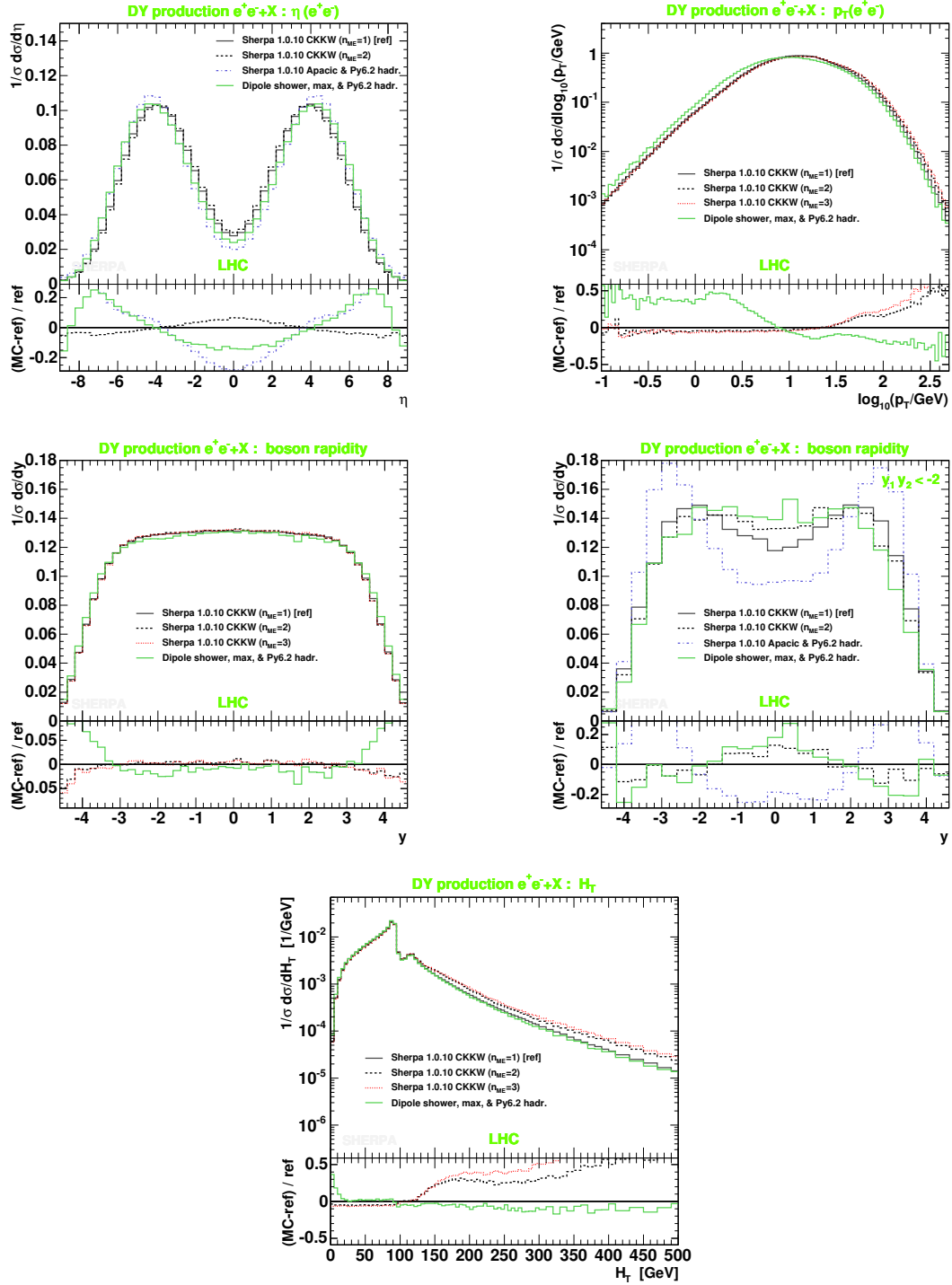
Figure 2.17: Pseudo-rapidity spectrum (top left), p_T distribution (top right), rapidity (left middle) and rapidity for $y_1 y_2 < -2$ (right middle) of the lepton pair in Z^0/γ^*+jets production at the LHC. The H_T distribution is shown at the bottom. The comparison is done at the hadron level between the unconstrained dipole shower (green solid lines) and various SHERPA results, namely CKKW $n_{\mathrm{ME}} = 1$ (grey solid lines), taken as the reference curve, CKKW $n_{\mathrm{ME}} = 2$ (black dashed lines), CKKW $n_{\mathrm{ME}} = 3$ (red dotted lines) and APACIC++ (blue dot-dashed lines).
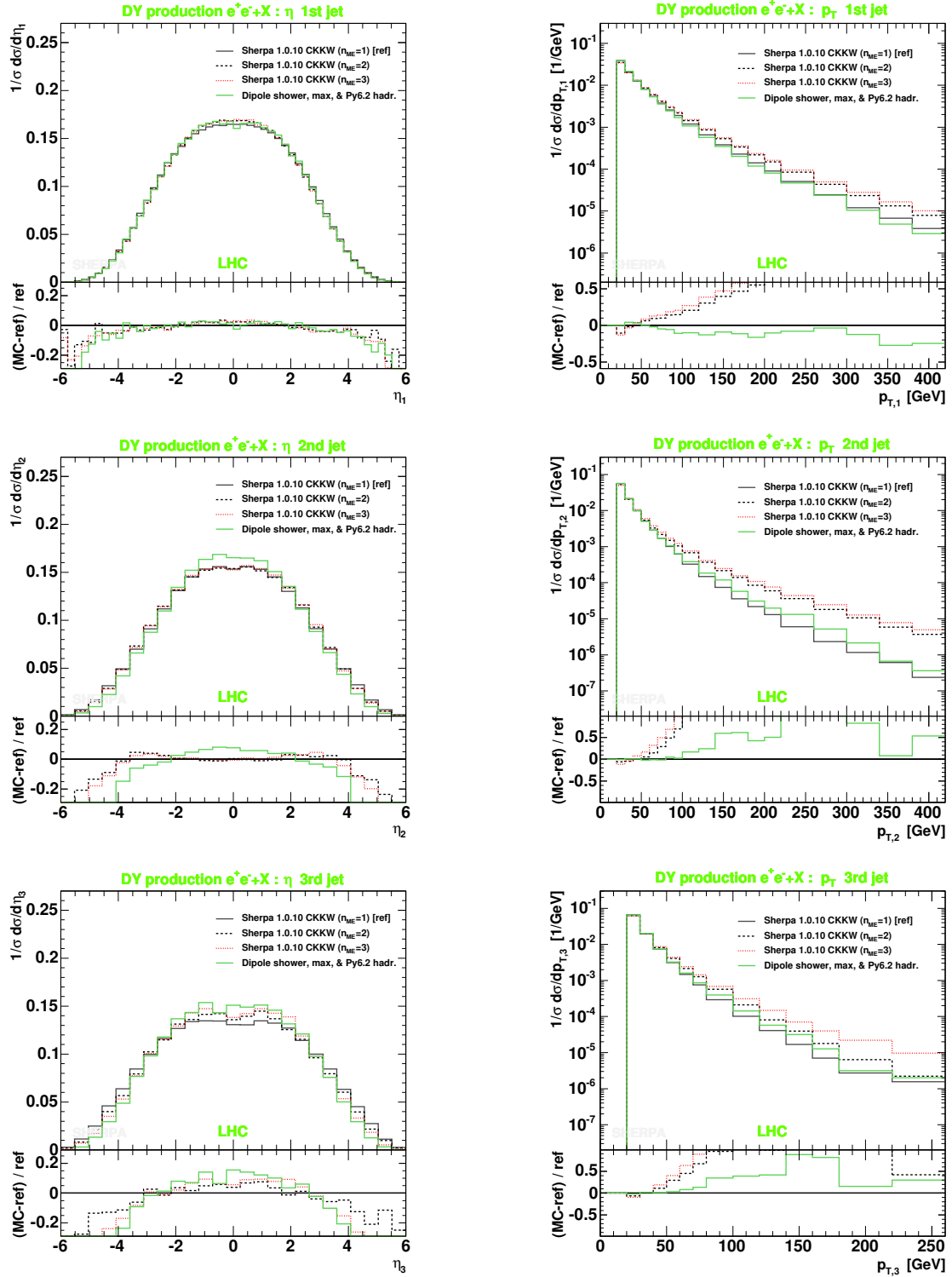
Figure 2.18: Pseudo-rapidity (left column) and transverse-momentum (right column) distributions of the first three jets in inclusive lepton-pair production simulated for LHC energies. Dipole-shower results are shown in comparison to those obtained by the CKKW method of SHERPA. Labelling is as in fig. 2.17.
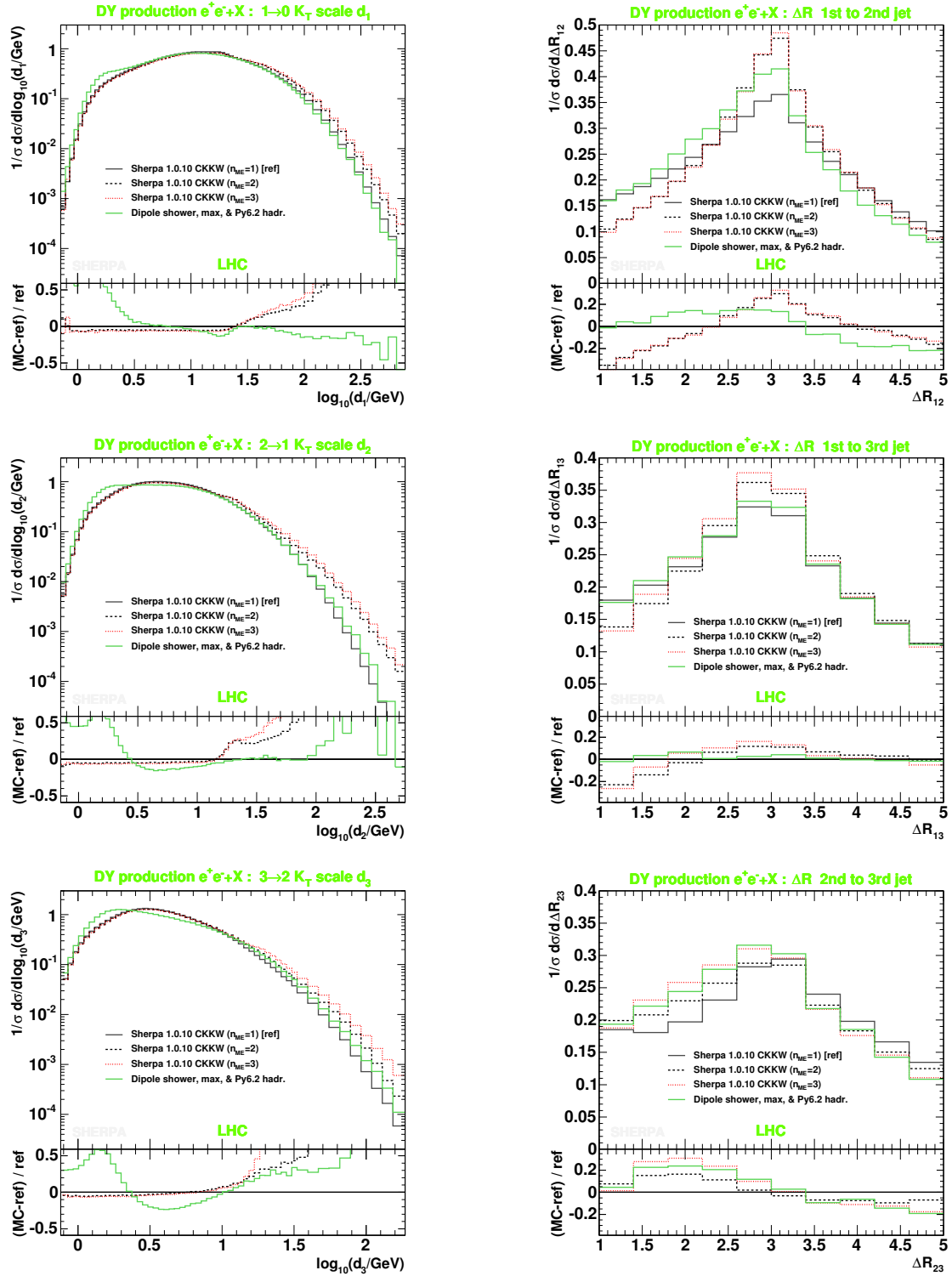
Figure 2.19: The k_T differential jet rates $d_{1,2,3}$ (left column) and ΔR_{ij} separations between the first three jets (right column) in inclusive Drell–Yan e^+e^- production at the LHC. Shown are results obtained with SHERPA CKKW and the dipole shower. Labelling is as in fig. 2.17.

Figure 2.20: The transverse momentum of the electron-hardest-jet system (top left), modulus of the pseudo-rapidity difference between the vector boson and the leading jet (top right) and (bottom) cosine of the angle between the first and the third jet determined in the rest system of the first and second jet. All of which is simulated for inclusive Drell–Yan e^+e^- production at the LHC. The dipole-shower outcome is compared to those received from various SHERPA runs. Labelling is as introduced in fig. 2.17.

the constraint imposed on the default shower to start from $p_{\perp,\text{ini}}^2 = (1 + \sqrt{2})^2 M_{ee}^2$. Between these two variants the differences are as expected in both the table and the figure. The default shower does not account for hard emissions, hence, the rates of tab. 2.2 are somewhat smaller w.r.t. those of the unconstrained shower. In the figure larger deviations appear only for the dijet mass m_{12} of the first and second jet. More importantly, the default shower has to be compared to the "dyn" variant, in order to quantify the impact of maximal phase space. The rates get further decreased and except for the case of rapidity-separated first two jets they resemble those of APACIC++. However, the dramatic fall of σ for $y_1 y_2 < -2$ confirms what has been

| Monte Carlo	σ_{tot}	$\sigma_{\geq 1\text{jet}}$	$\sigma_{\geq 2\text{jet}}$	$\sigma_{\geq 3\text{jet}}$	$\sigma_{=1\text{jet}}$	$\sigma\big|_{y_1 y_2 < -2}$
CKKW $n_{\text{ME}} = 1$	1281	389	105	21.9	284	20.3
CKKW $n_{\text{ME}} = 2$	1349	459	146	34.1	312	22.3
CKKW $n_{\text{ME}} = 3$	1366	476	163	46.0	313	25.2
APACIC++	1484	345	71	9.8	233	15.1
Dipole shower, max	1484	431	124	33.7	307	18.1
Dipole shower, max (SL)	1484	440	129	35.9	311	19.2
Dipole shower (SL)	1485	396	101	23.3	295	15.7
Dipole shower, dyn (SL)	1485	362	77	12.8	286	4.2

Table 2.2: Cross sections (in pb) as obtained from the various Monte Carlo approaches for inclusive and exclusive (hadron- and shower-level "SL") jet rates at LHC energies. Jets are defined according to the Run II k_T algorithm [54, 62] and required to have $p_{T,\text{jet}} > 20$ GeV.

anticipated in sec. 2.5.3, namely that the production of forward jets will decrease once $\hat{s}_{\text{max}}$ is reduced. As a consequence the y_{ee} spectrum under rapidity separation for the first two jets emerges very differently for the "dyn" shower. Also, jets are described less separated, shown through the distortion towards smaller values of the ΔR_{12} distribution plotted in fig. 2.21. Furthermore large dijet masses are considerably suppressed and the third jet appears significantly less collinear w.r.t. the first and second jet, as it can be read off the $\cos\theta_{13}$ distribution in fig. 2.21.

Thus, recalling the good comparisons to the CKKW results, it can be concluded that apart from the unconstrained shower the default shower constitutes the better variant in describing inclusive Drell–Yan lepton pair production, i.e. evidently taking $\hat{s}_{\text{max}}\big|_{\text{II}} = S$ and $\hat{s}_{\text{max}}\big|_{\text{FI}} = \mathcal{S}$ is a good choice. The testbed of inclusive QCD jet production will definitely probe whether this clear choice is the most reliable one. Notice that it can be also read off tab. 2.2 that the default dipole shower predicts much more soft jets compared to APACIC++, the default shower of SHERPA.

2.6.3   Inclusive jet production at hadron colliders

The QCD production of jets at hadron colliders is for sure the most obvious scenario, however, from a theoretical point of view, the task of calculating and/or simulating these processes at higher order in the strong coupling is more complicated and rather involved. Also, for the dipole shower, the further evolution of jet-production processes down to the hadronization scale clearly constitutes a challenge that goes beyond the tasks handled
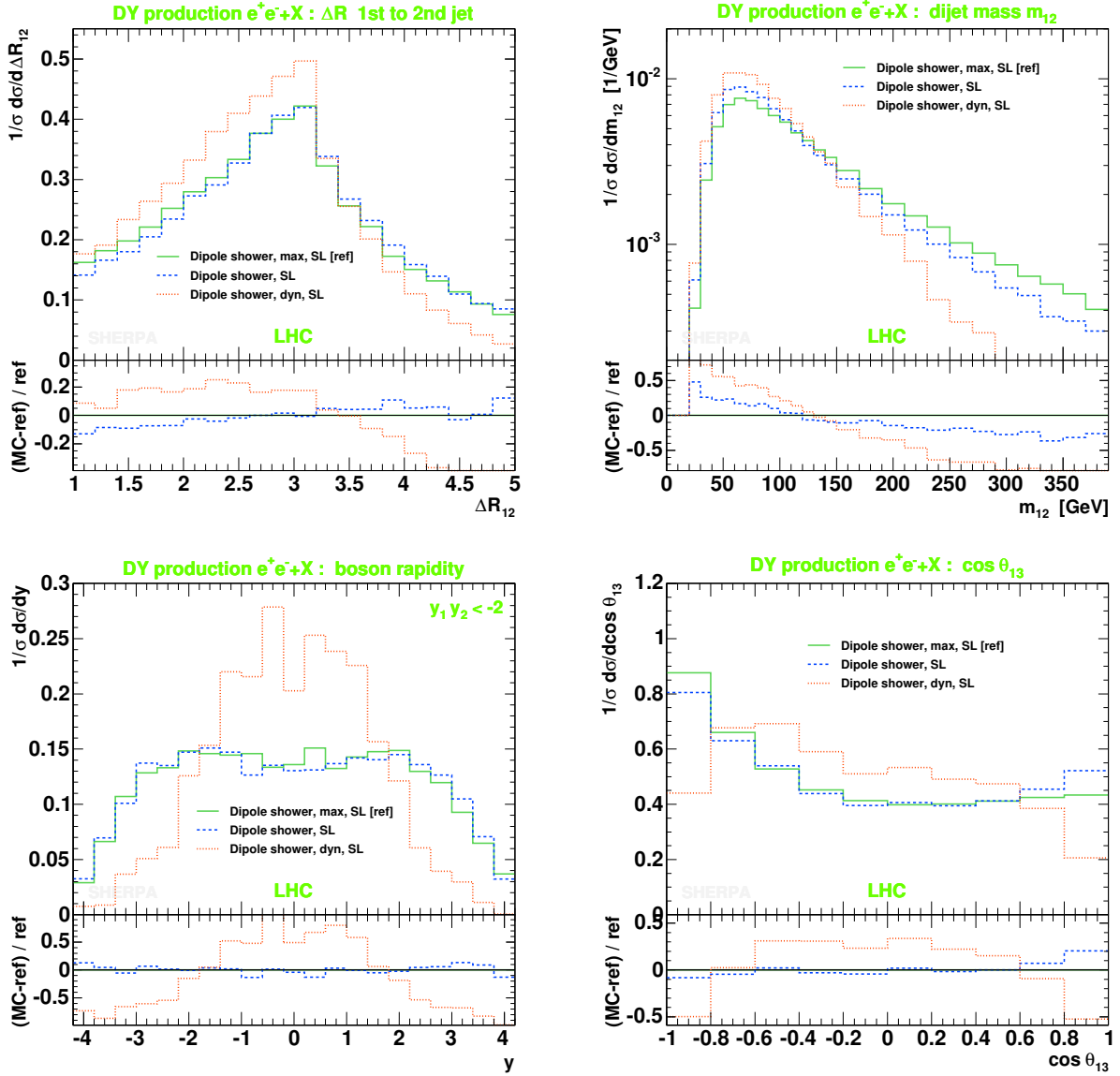
Figure 2.21: Impact of the choice of $\hat{s}_{\mathrm{max}}$ on the ΔR_{12}, dijet mass m_{12}, y_{ee} for $y_1 y_2 < -2$ and $\cos\theta_{13}$ distributions as predicted by the unconstrained (solid green curves), the default (dashed blue curves) and the dipole shower where $\hat{s}_{\mathrm{max}}$ is set dynamically (dotted red curves).

so far. There are several reasons for this. In contrast to the previously discussed cases, the primary state is given through a multi-dipole configuration formed by $2 \to 2$ hard QCD processes and their (large N_{C}) colour connections, which now are also possible between initial- and final-state partons right from the beginning. In addition, these dipoles may all be linked to form only one colour singlet or even a gluonic ring. This in turn requires a careful choice of the initializing scale, as it has been argued in sec. 2.5.3, and clearly forbids an unconstrained setting of it, since reliable intrinsic matrix-element corrections for the first emission in jet production are not present in the dipole splitting

functions. Hence, QCD jet production severely tests the entire shower algorithm, and in a first item the issue of finding a suitable initializing scale will be discussed. For convenience, all jet-production simulations have been accomplished on the shower level only, but hadronization corrections can be expected to be fairly small.

Dijet azimuthal decorrelations at Tevatron Run II energies

The dijet-decorrelation observable measured in the transverse plane between the two hardest jets, $\Delta\phi_{\mathrm{dijet}} = |\phi_1 - \phi_2|$, provides good insight when validating the occurrence of additional soft and hard radiation. Advantageously, there is no necessity to reconstruct further jets, and, furthermore, fully correlated this observable is pinned down through $\Delta\phi_{\mathrm{dijet}} = \pi$, which signifies the initial presence of two "jet candidates" in the hard process, which are oriented back-to-back. The strength of the decorrelation rises in dependence on the hardness of the emissions. Clearly, the validity of the shower description is given in the soft and collinear limits of QCD emission only and has to be guaranteed through the correct choice of the initializing scale. Therefore, the dijet decorrelation can be used to verify any choice taken, culminating in finding the most suitable one.

The observable was subject of a recent measurement by DØ at Tevatron Run II with the data taken in different $p_{T,1} = p_{T,\mathrm{max}}$ windows of the leading jet [131]. The details of the analysis are:

- Reconstruct cone jets for $R = 0.7$,

- require $p_{T,2} > 40$ GeV,

- and, require central jet rapidities, $|y_{1,2}| < 0.5$.

Fig. 2.22 shows the data overlaid with different predictions obtained from the default dipole shower but varied in its choice of the initializing scale: the scale denoted by "II sc." is taken according to eq. (2.158), this one denoted by "QCD sc." corresponds to $p_{\perp,\mathrm{ini}}^2 = 3\mu_{\mathrm{QCD}}$, cf. eq. (2.157), and those of the default follow from eq. (2.156), the low one directly and the plain one from the multiplication of the low one with a factor of three. Obviously the dipole shower initiated through the low default scale does not account for enough hard emissions. The other predictions are quite similar, with the "II sc." and "QCD sc." variants giving slightly harder and softer results w.r.t. the default case, respectively. The default performs best, and, therefore, will be employed in all what follows, hence, it can be fixed:

$$p_{\perp,\mathrm{ini}}^2 \Big|_{\mathrm{Jets}} = \frac{9\,\min\{\hat{u}\,\hat{t},\ \hat{s}\,\hat{t},\ \hat{s}\,\hat{u}\}}{\hat{s} + |\hat{t}| + |\hat{u}|}, \tag{2.160}$$

using the Mandelstam variables of the core process. Still, the default predictions show the tendency to undershoot the data around $\Delta\phi_{\mathrm{dijet}} = 2.8$ in all $p_{T,\mathrm{max}}$ windows of the leading jet, however, keeping in mind that gluon splitting processes have not been taken into account yet, the agreement is satisfactory and gives evidence that, besides the initializing scale, other model-intrinsic scales, such as $\tilde{\mu}_{\mathrm{F}}$, μ_{F} and μ_{R}, have been chosen reasonably.
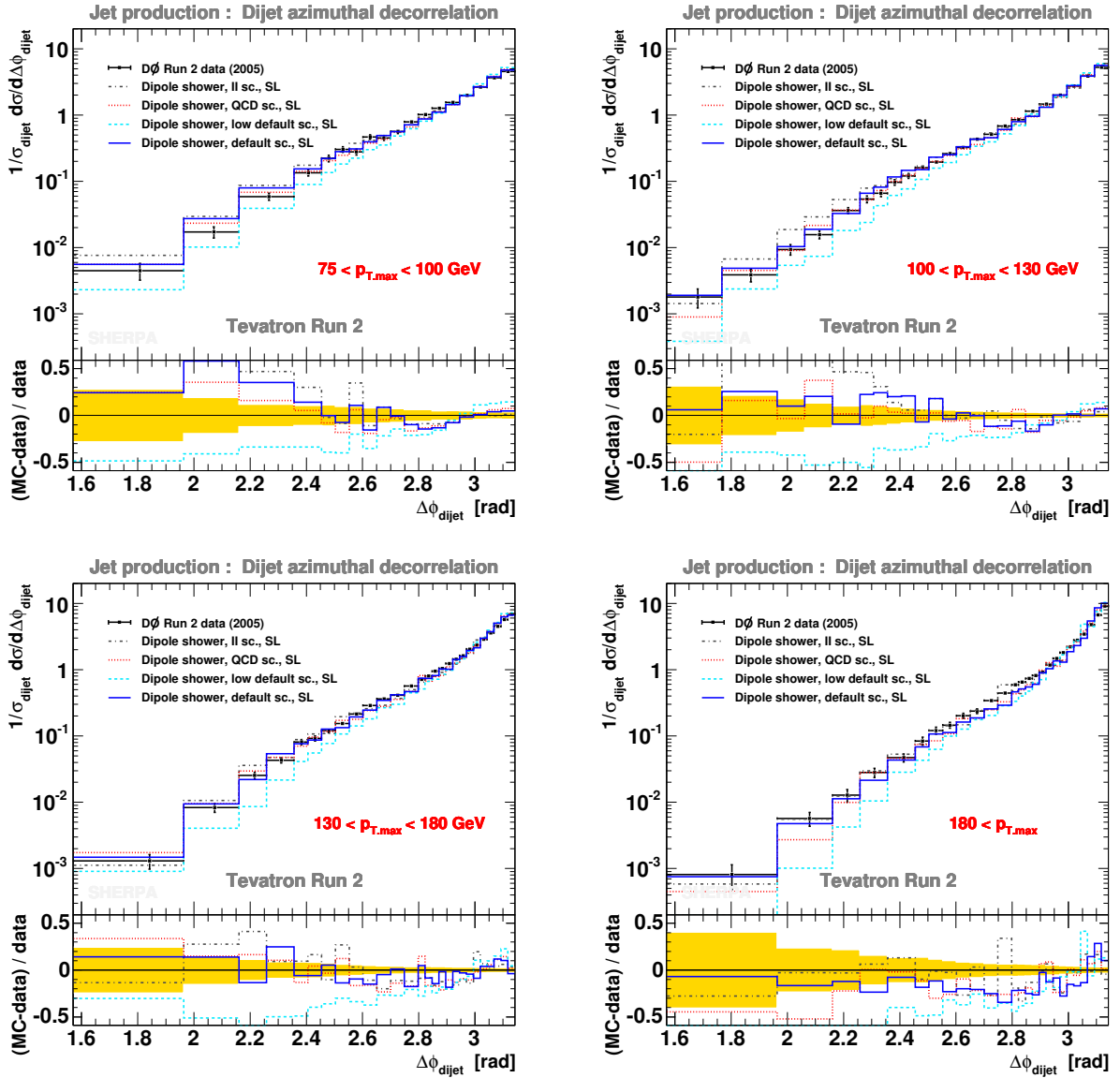
Figure 2.22: The dijet azimuthal decorrelations in different $p_{T,\max}$ ranges. Dipole-shower results for different choices of the initializing scale are overlaid on the data taken by DØ during Tevatron Run II [131].

Dijet mass spectrum at Tevatron Run II energies

With the $p_{\perp,\text{ini}}$ finding in hand, a first further check is to confront the dipole-shower prediction for the dijet mass spectrum with data measured during Run I by the DØ collaboration [132]. The analysis requires:

- reconstruction of jets by using a cone algorithm with $R = 0.7$,

- jet transverse energies above 30 GeV,

- and, the dijet candidates to satisfy $|\eta_{1,2}| < 1.0$.

The result of the dipole shower (normalized to the cross section observed in the experiment) versus data can be seen in the top left corner of fig. 2.23 and the agreement is very encouraging.

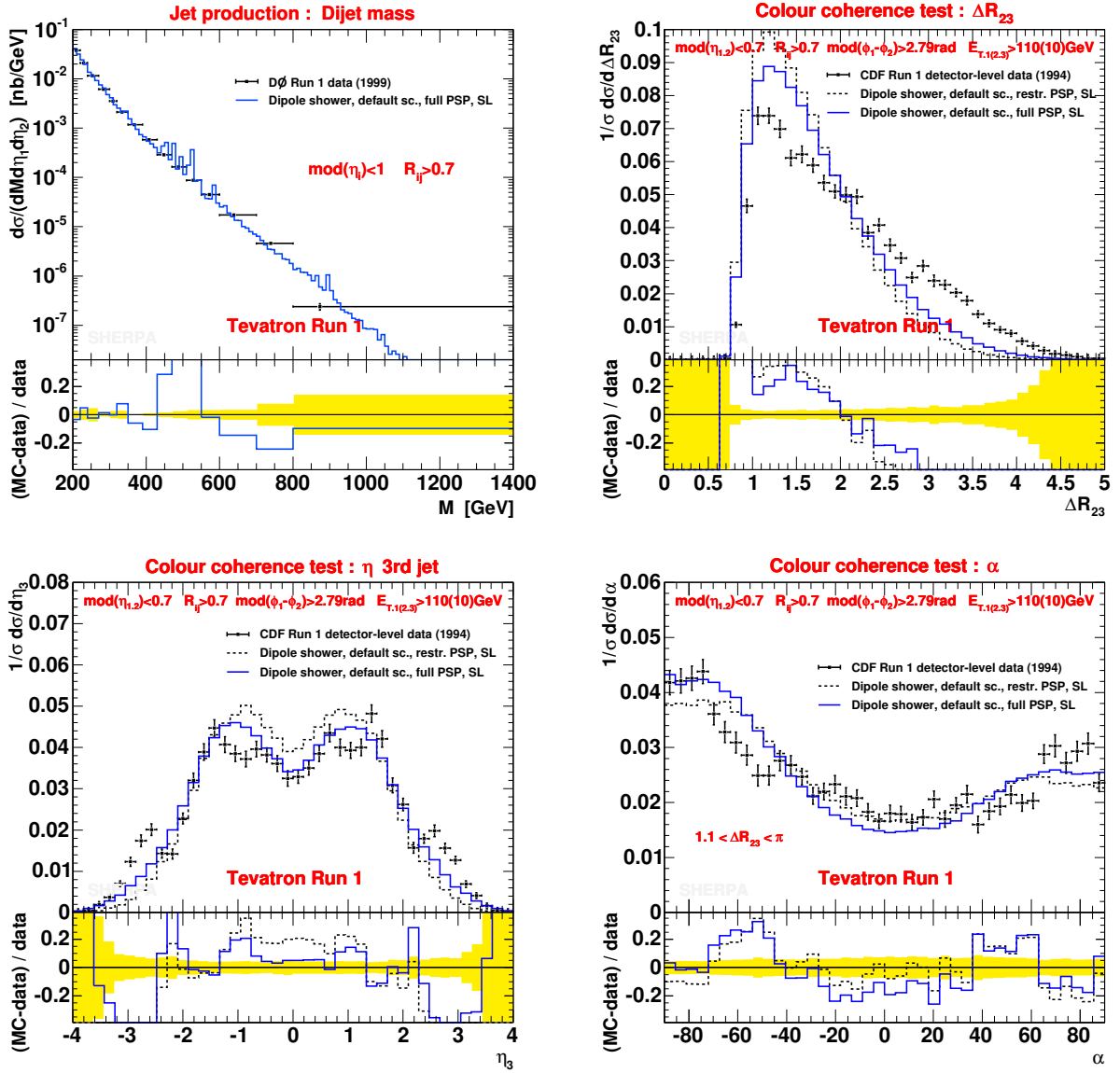## Test of colour coherence at Tevatron Run I energies

An interesting measurement and analysis was carried out by the CDF collaboration during Tevatron Run I, searching for evidence for colour coherence in $p\bar{p}$ collisions at $\sqrt{S} = 1.8$ TeV [133]. Discriminatory observables have been found for three-jet events featuring a hard leading jet and a rather soft third jet. They have been shown to be sensitive to the correct treatment of QCD colour coherence in parton shower simulations, where indeed the models taking into account these effects properly, as for example the HERWIG Monte Carlo does, have the agreement with data. Here, this testbed will be used to verify whether the proposed dipole shower is capable of describing the characteristics found in the data. Often, it is just said that evolving in terms of colour dipoles – as done in ARIADNE – automatically accounts for soft colour coherence, which on the one hand can be expected owing to the eikonal structure of the dipole splitting cross sections, however on the other hand the colour factor mismatch for quark–gluon dipoles (discussed in sec. 2.4) requires more serious investigation in this direction. The comparison with the CDF data, therefore, constitutes a good opportunity of doing a first step.
The requirements of the CDF study are:

- Jets are defined through a cone algorithm, using $R = 0.7$,

- the two leading jets are constrained to $|\eta_{1,2}| < 0.7$,

- they have to be oriented back-to-back within 20 degrees, i.e. $|\phi_1 - \phi_2| > 2.79$,

- jet E_T thresholds have to be respected for the 1st jet and the jets beyond the 1st one of 110 and 10 GeV, respectively,

- and, for the α angle only, a cut on $\Delta R_{23} = \sqrt{(\eta_2 - \eta_3)^2 + (\phi_2 - \phi_3)^2}$ has to be imposed, namely $1.1 < \Delta R_{23} < \pi$.

- The angle α is defined through

$$\tan \alpha = \frac{\text{sign}(\eta_2)(\eta_3 - \eta_2)}{|\phi_3 - \phi_2|}. \tag{2.161}$$

Apart from the top-left-corner plot, in fig. 2.23 the comparison between detector-level data and dipole-shower predictions obtained at the shower level is shown by means of the ΔR_{23}, η_3 and angle α distributions. If colour-coherence effects are modelled correctly, ΔR_{23} should appear sufficiently broader, η_3 should be broadened too and feature the significant dip for central values, and, the α spectrum should be minimal for small $|\alpha|$ followed by a clear rise towards larger positive angles. The dipole shower predicts the significant features for the latter two observables, yet fails in describing the spectrum of ΔR_{23}, since its prediction is too steep. However, first, recall that the data are uncorrected for detector effects, and, second, as pointed out in [133], the ΔR_{23} observable is known to receive the

Figure 2.23: The dijet mass spectrum (top left panel) as measured by DØ during Tevatron Run I [132] compared with the prediction of the dipole shower. Colour-coherence tests in inclusive three-jet production at Tevatron Run I energies according to a CDF study presented in [133]: (top right panel) spatial separation in (η, ϕ) space of the second and third jet, (bottom left panel) pseudo-rapidity distribution of the third jet and (bottom right panel) the angle α (definition is in the text). Experimental errors are statistical only, histograms are normalized to their respective binwidth. For the latter three observables, dipole-shower (shower-level) predictions under full (blue solid lines) and restricted (black dashed lines) emission phase space are shown in comparison with the (detector-level) data of the CDF measurement [133].

largest uncertainties concerning this issue, whereas the other two are quite unaffected. In regard of these uncertainties it hence can be concluded that there is fairly good evidence that the dipole shower reasonably models colour-coherence effects. Notice that, together with the default, a prediction has been added to the figure, where the available emission phase space has been considerably reduced. Then, obviously, the agreement with data starts to deteriorate. This again is evidence that assigning the full phase space is not only the natural but also more correct choice.

Dipole shower vs. SHERPA predictions: shape comparisons

These comparisons have been done closely to those in the Drell–Yan case. Tevatron Run II energies are used for all simulations. Again, the dipole-shower performance will be confronted with predictions obtained from SHERPA version 1.0.10, more exactly, a CKKW $n_{\mathrm{ME}} = 3$ merging sample [22] and APACIC++ on its own (in CKKW scale-scheme mode) have been employed. Jets are defined as before according to the k_T algorithm with the jet threshold $p_{T,\mathrm{jet}} > 20$ GeV and the parameter $D = 1$.

Fig. 2.24 exemplifies jet pseudo-rapidity and transverse-momentum spectra for the first two additional jets, the third and the fourth jet, together with k_T differential jet rates. Again, the jet η_i spectra predicted by the dipole shower are steeper w.r.t. those of SHERPA. Furthermore, they seem fairly independent of the choice of the initializing scale. The $p_{T,i}$ spectra strongly resemble each other for all predictions, whereas the differential jet rates show sizeably larger differences, in particular the default choice for the initializing scale triggers much more radiation above 10 GeV. Hence, the differential jet rates feature a relatively strong sensitivity under variation of the initializing scale.

In fig. 2.25 the $|\Delta\eta_{12,3}|$ spectrum is shown and appears much more flat w.r.t. that of the LHC Drell–Yan case depicted in fig. 2.20. The dipole shower predicts smaller pseudo-rapidity separations compared to the SHERPA predictions, nevertheless it is closer to SHERPA CKKW than APACIC++. The shape of the $\cos\theta_{13}$ distribution arises fairly differently in comparison to both the Drell–Yan case, see again fig. 2.20, and between SHERPA/APACIC++ and the dipole shower. The former signals a less surprising process dependence, which can be expected, whereas the latter indicates that for the dipole shower the third jet is much more often associated to the second jet in the rest frame of the two hardest jets. This clearly points at differences in the details of the radiation pattern between SHERPA and the dipole shower. The last distribution shown in this figure is a histogram of the eikonal factor for the three hardest jets defined as

$$\mathrm{Eik}_{132} \;=\; -\frac{1}{2}\left(\frac{p_1}{p_1 p_3} - \frac{p_2}{p_3 p_2}\right)^2 . \tag{2.162}$$

Interestingly, the dipole-shower predictions show an enhancement for the large values of the eikonal factor, which mainly corresponds to approaching the soft limit. This nicely reflects the dominance of this limit in dipole evolution.

Finally, fig. 2.26 illustrates the impact of the $\hat{s}_{\max}$ restriction, this time for QCD jet production. The effects are less discriminatory compared to the LHC Drell–Yan case. However, for example, in the trijet mass distribution for the three hardest jets the emphasis of

---

[22]For this, matrix elements of the QCD $2 \rightarrow 2$ core (lowest-order) processes have been combined according to CKKW merging with those accounting for the emission of one extra parton.
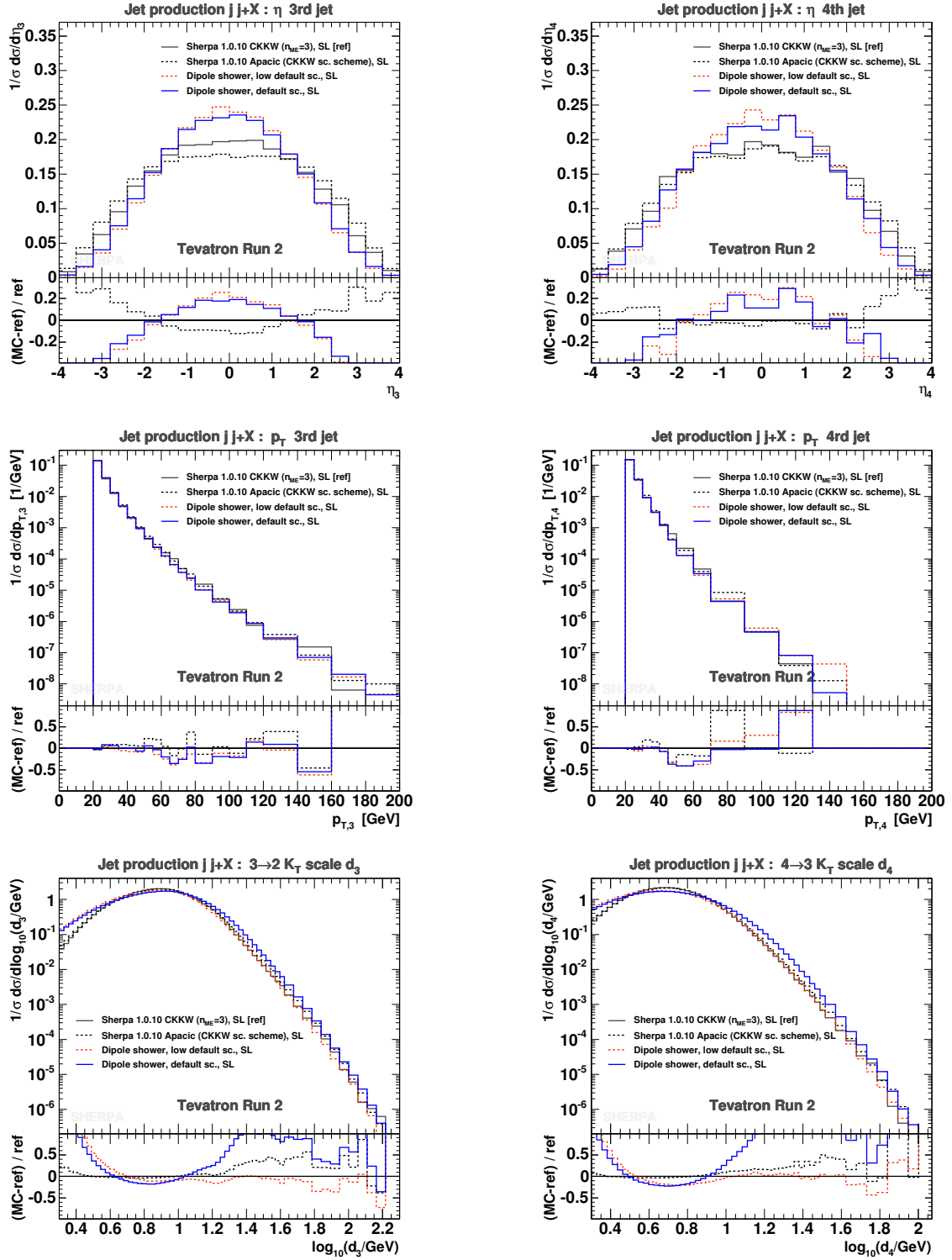
Figure 2.24: Jet pseudo-rapidity (top) and transverse-momentum (middle) spectra, and k_T differential jet rates (bottom) in inclusive jet production simulated for Tevatron Run II energies. Predictions of SHERPA CKKW $n_{ME} = 3$ (grey solid lines), APACIC++ (black dashed lines), and the dipole shower for default (blue solid lines) and lowered initializing scale (red dashed lines) are compared with each other.
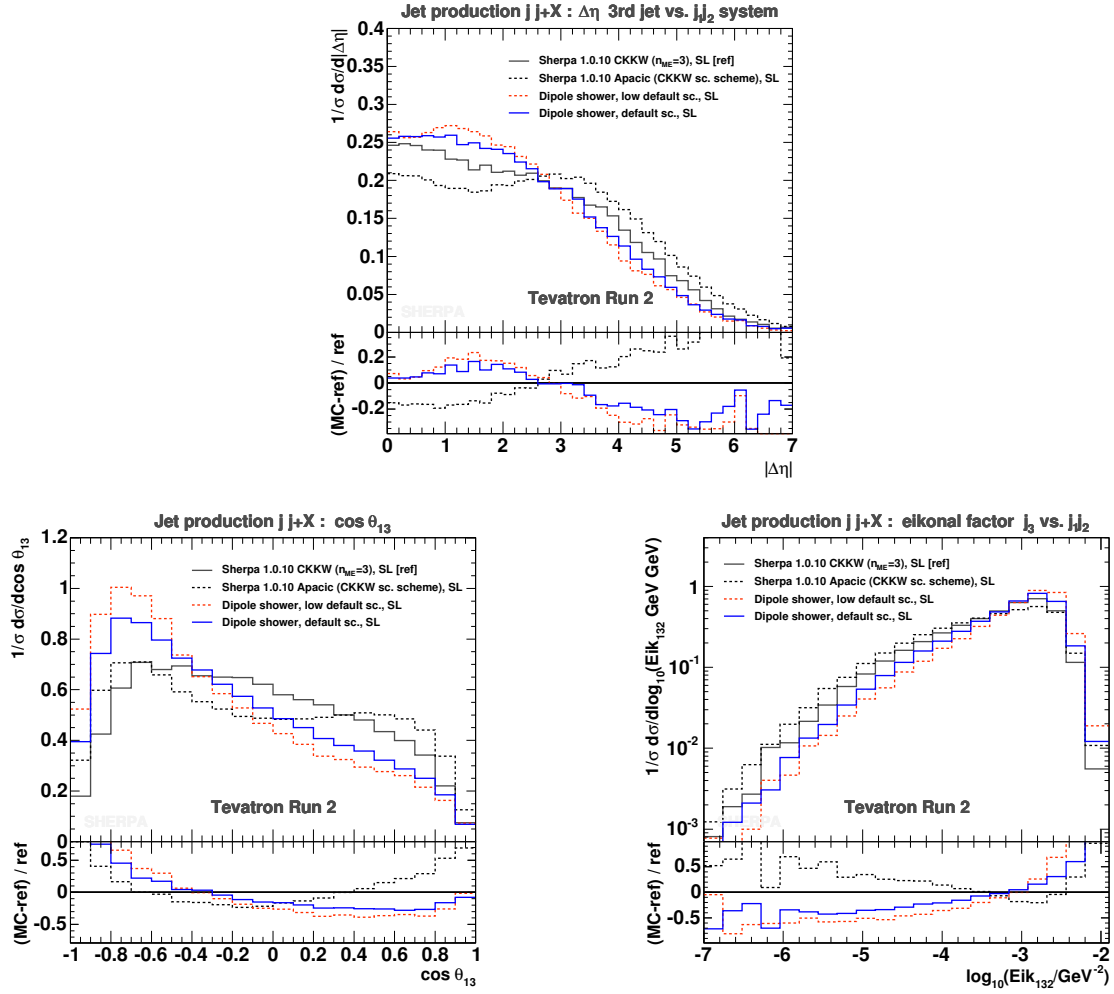
Figure 2.25: Distribution of the modulus of the pseudo-rapidity separation between the third jet and the system made up of the first two jets (top part of figure), $\cos\theta_{13}$ distribution (bottom left) and distribution of the eikonal factor for the first three jets (bottom right), all of which in inclusive QCD jet production at Tevatron Run II. Labelling is as in fig. 2.24.

smaller masses can again be observed for the phase-space restricted dipole showers. This compares quite nicely with the behaviour of the dijet mass distributions of fig. 2.21.

Exclusive three-jet final-state challenge

Recent CDF measurements have found an excess in data of exclusive three-jet events with small ΔR_{23} [134]. So far this is not understood and available tools, such as PYTHIA (Tune A), have problems in describing the data. Of course, this cannot be studied seriously without taking into account the underlying event, nevertheless, to qualitatively get a first impression, the following analysis has been applied:

- Require jet reconstruction according to the cone jet algorithm, use $R = 0.4$,
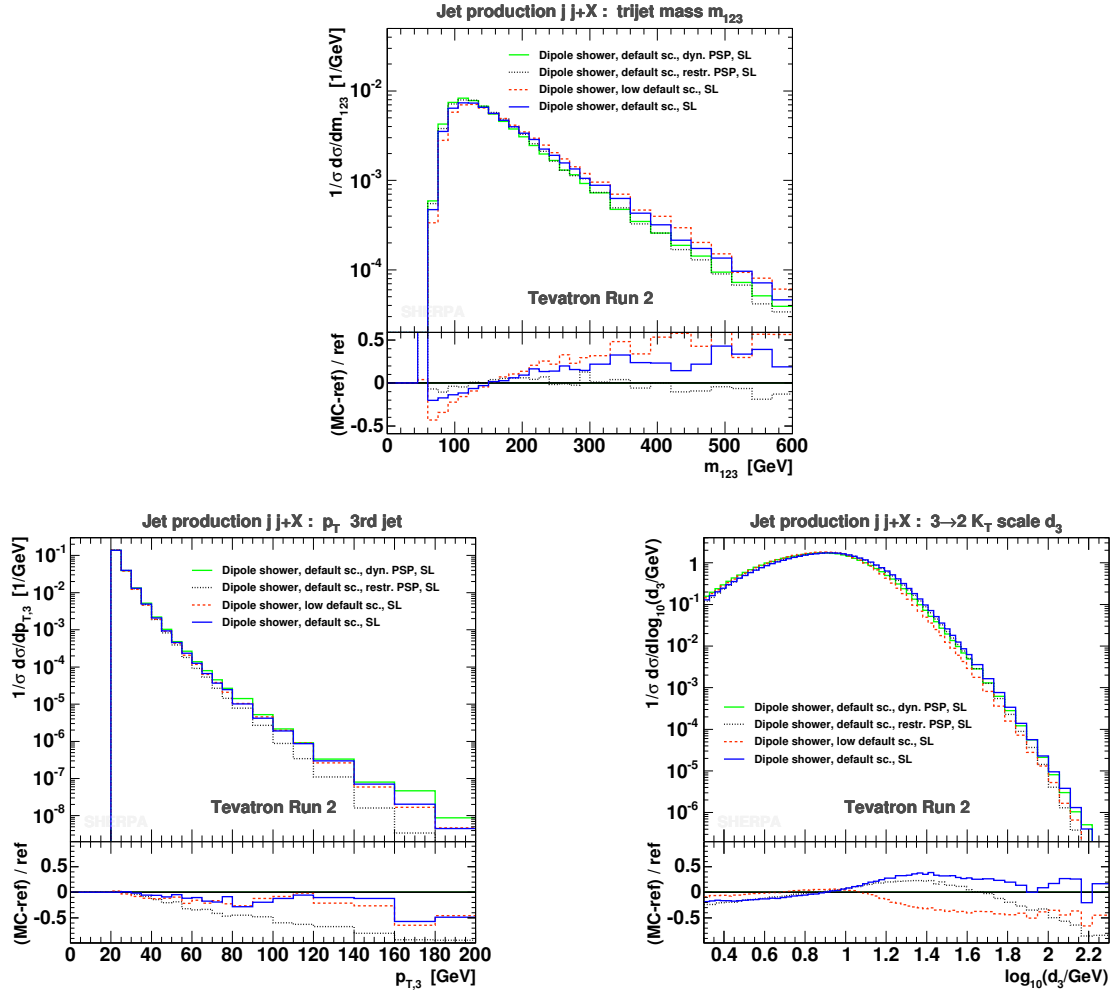
Figure 2.26: Trijet mass distribution for the first three jets (top part of figure), p_T spectrum of the third jet (bottom left) and k_T differential jet rate d_3 (bottom right) in inclusive pure jet production at Tevatron Run II energies. Various dipole shower predictions are shown, the latter two of the legend are as labelled in fig. 2.24, additionally the green solid lines and the black dotted lines exemplify predictions for the dipole shower where $\hat{s}_{\max}$ is set dynamically (cf. the LHC case in sec. 2.6.2) and considerably reduced, respectively.

- use general cuts on jets of $p_{T,i} > 20$ GeV and $|\eta_i| < 2.5$,

- additionally, use $|\eta_1| < 1.0$ for the hardest jet,

- to consider the trigger-jet effect, demand $p_{T,1} > 40$ GeV.

The results are presented in fig. 2.27 and show the pseudo-rapidity spectrum of the third jet together with the ΔR_{23} distribution under debate. Concerning the former, the dipole shower is again found to generate steeper spectra and differences w.r.t. APACIC++ get enlarged for $p_{T,1} > 40$ GeV. Inspecting the latter, the dipole shower that employs the lower

initializing scale already highlights the region of small jet separations without the larger hardest-jet p_T threshold, interestingly, for $p_{T,1} > 40$ GeV, the effect becomes projected out and strongly enhanced for both dipole shower variants, still with more significance for the dipole shower of lower $p_{\perp,\text{ini}}$. Also the APACIC++ prediction starts rising towards smaller separations but stays below the dipole shower curves. Thus, it can be concluded that the dipole shower gives fairly encouraging results showing such an excess at small ΔR_{23} qualitatively. Note that the low default shower may be even re-interpreted as a default shower starting instead from a lower-scale $2 \to 2$ QCD process. In this regard it may be speculated that the dipole shower, if taken to shower the softer $2 \to 2$ QCD processes of the underlying event, would preferably populate the region of small ΔR_{23} separations.

2.7   Conclusions

Here, a new colour-dipole shower model, in particular for hadronic collisions, has been presented in the spirit of the Lund Colour Dipole Model [17, 11]. In this context, great importance has been attached to a novel, perturbative description of initial-state showering, which introduces colour dipoles directly connected to incoming parton lines and leaves the hadron remnants completely outside consideration. The colour-dipole ansatz, formulating QCD emissions mainly in their soft limit, is not new, however the approach proposed here is in clear contrast to the Lund CDM. In summary, throughout the new proposal no kind of initial-state radiation is mapped onto radiation that instead is considered to escape from a pure final-state dipole, none of the suggested dipoles contains an extended colour source and, therefore, is subject to a semi-classically motivated suppression of high $p_\perp$ emissions.

Gluon emissions have been generalized to all kinematic regions appearing in hadronic collisions, including a Lorentz invariant generalization of the definition of the dipole evolution variables. Splitting functions have been derived for dipoles that are spanned along incoming parton lines as well as for such that connect incoming and outgoing ones. Together with the well-known radiation pattern of pure final-state colour dipoles, their utilization in a complete shower algorithm has been presented to describe soft and collinear multiple parton emission. The feasibility of the approach has been shown through its application to electron–positron annihilation into hadrons, inclusive Drell-Yan pair production and inclusive QCD jet production at hadron colliders, all of which delivering first encouraging results in good agreement with other models and with experimental data. It is worth to mention that the feature of generating broader pseudo-rapidity spectra – often mentioned in connection with colour-dipole evolution according to ARIADNE– has not been confirmed by the results of this model, instead, in comparison with inclusive SHERPA CKKW samples for merging one extra jet, in all cases somewhat steeper pseudo-rapidity spectra have been found. Note that, for the first time, results for the inclusive production of jets in a hadronic environment have been obtained from a shower based on the colour-dipole approach and they have been presented in this work.

With the compliance of all requirements for the construction of this shower detailed in the introduction, sec. 2.1, an appealing picture of the cascading has been achieved, where the entire evolution can be seen as a perturbative "explosion" starting from the core process'
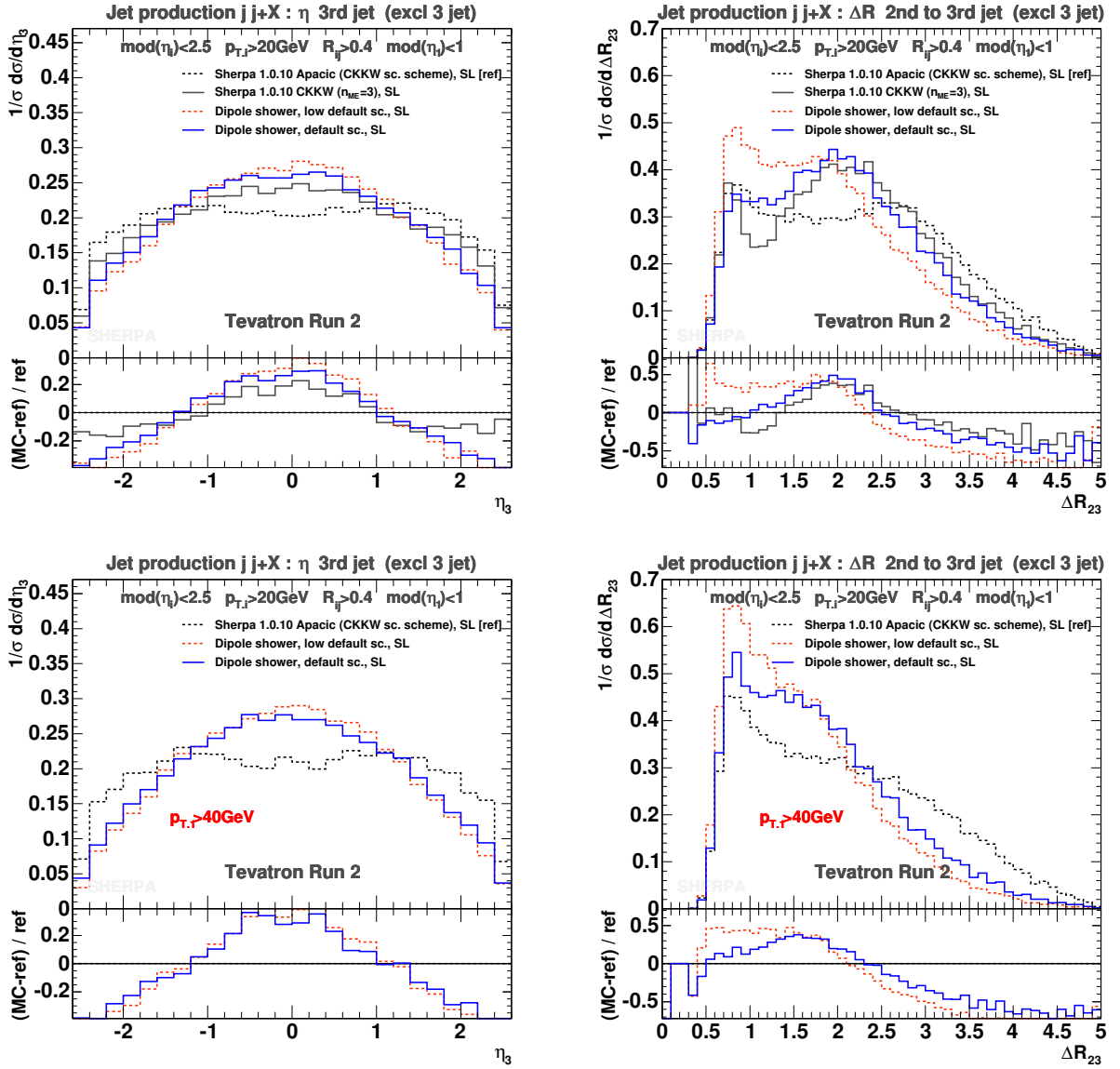
Figure 2.27: Pseudo-rapidity distribution of the third jet and spatial separation between the second and third jet in exclusive three-jet final states for Tevatron Run II energies. The plots at the bottom are obtained requiring a larger jet p_T threshold for the hardest jet to pass. The comparison is for SHERPA and dipole-shower predictions with the labelling as introduced in fig. 2.24.

scale down to a common cut-off scale signalling the onset of hadronization effects. Future work concerns the full incorporation of gluon splittings in the initial and final state, and, the generalization to finite quark masses. In addition, a merging with multi-leg tree-level matrix elements for additional QCD radiation will be addressed, furthermore, a matching with full NLO QCD calculations can be anticipated.

3 A modified cluster-hadronization model

3.1 Introduction

Because of the lack of a detailed understanding of non-perturbative QCD effects, i.e. how confinement forces the coloured quarks and gluons to form colourless bound states, called hadrons, phenomenological models have to be invoked, which parametrize this transition of a coloured partonic system into colourless primary hadrons, which will be subject to further hadron decays. Owing to their underlying principle, Monte Carlo event generators constitute a perfect environment to host hadronization models, which in turn will use the parton-shower final states as their input for the continuation of the development of the event towards lower energy scales as appearing in the real hadron measurements. [1] This exactly is the crucial point rendering hadronization models an important part of the simulation of full scattering processes: experiments observe (jets of) (stable) hadrons and measure their dynamics, but direct access to the underlying (hard) parton dynamics is impossible. Therefore, although of phenomenological origin, (in the context of event generators) hadronization models are mandatory to bridge the gap between experimental data and predictions made by perturbation theory.

On general grounds, hadronization effects are expected giving rise to corrections proportional to $1/E^n$ to quantities that are computable in perturbation theory, for example, in the case of e^+e^- event shapes, the dominant non-perturbative effects have an $1/E$ dependence on the hard-process energy scale E. Hence, soft hadronization mechanisms are favoured, which involve only modest transfers of momentum and/or quantum numbers between neighbouring regions of phase space.

For the intrinsically non-perturbative transition process from the perturbative partonic state to the primary hadrons, different strategies exist and the corresponding Monte Carlo schemes are either based on the Feynman–Field or independent fragmentation [135, 136], on the Lund string [137, 3] (JETSET/PYTHIA) and UCLA [138, 139, 140] models, or on the cluster-hadronization model (HERWIG). The latter concept, [2] initially proposed by Wolfram and Field [149, 150], and further advanced, among others [151, 152, 153], by Webber and Marchesini [154, 155, 15, 156], explicitly rests upon the preconfinement property of QCD [157, 158, 159] and the LPHD (local parton hadron duality) hypothesis [160]. Such cluster models are usually formulated in terms of two phases: cluster formation accom-

---

[1]Once this primary-hadron genesis has been accomplished, all unstable hadrons have to be decayed, and decay chains of various complexity may appear.

[2]Recent developments may be found, e.g. in [19, 141, 142, 143, 144, 145, 146, 147, 148].

plished through the non-perturbative splitting of gluons left by the parton shower into quark–antiquark pairs, and subsequent cluster decays leading to the additional creation of light-flavour pairs. In the $N_C \to \infty$ limit all these quarks and antiquarks can be uniquely formed into colour-singlet clusters, which in their turn mostly undergo simple isotropic decays into pairs of hadrons, chosen according to the density of states with appropriate quantum numbers. Since the parton shower exhibits preconfinement, the mass spectrum of the formed clusters is universal, strongly peaked at low mass and falls off rapidly. But this does not necessarily exclude that clusters of large mass arise after the perturbative phase. Isotropy is not a good approximation for the breakup of massive clusters. Thus, in order to describe the experimental data, one first has to split the high-mass clusters into lower-mass ones employing a longitudinal or string-like mechanism. In this context, one may say that cluster-hadronization models have evolved somewhat in the direction of the string-fragmentation approach.

Here, a modified phenomenological cluster-hadronization model is presented; the basic features of the new model are the following.

Soft colour reconnection is accounted for in the formation and decay of clusters. The flavour-dependent separation of the cluster regime from the region of hadron resonances yields the selection of specific cluster-transition modes. The two regimes are distinguished by comparing the mass of the cluster with the masses of the accessible hadrons matching the cluster's flavour structure. The method for flavour selection is arranged so that the meson and baryon as well as the strangeness and non-strangeness sector can be influenced separately, and their corresponding ratios can be controlled by a baryon- and a strangeness-suppression parameter, respectively. In addition, the set-up of the probabilities of choosing distinct hadron species supports the approximate maintenance of strong-isospin symmetry at the primary-hadron level.

As a case study, the new cluster scheme was implemented for electron–positron annihilation, and, for simplicity, only the light-quark sector was considered. An extension to heavy quarks, although being straightforward, is however not considered here.

The description of this cluster-hadronization model is organized as follows: first, different aspects of cluster formation are discussed in sec. 3.2. Subsequently, in sec. 3.3, the parametrization of light-flavour pair creation is presented. The model's description is concluded by exhibiting cluster transformation and fragmentation processes, which lead to the emergence of primary hadrons, see sec. 3.4. The results, which were obtained with the new hadronization scheme are shown in sec. 3.5 for the process $e^+e^- \to \gamma^*/Z^0 \to d\bar{d}, u\bar{u}, s\bar{s} \to$ hadrons.

3.2   Cluster formation

The parton shower describes multiple parton emission in a probabilistic fashion [2]. By factorizing the full radiation pattern into individual emissions it employs the large N_C limit of QCD. This organizes a binary tree, i.e. a planar structure, of the partons. It also ensures that, once the colour structure of the initial partons from the hard matrix element has been fixed, the colour structure of the partons at the end of the parton shower is unambiguously determined.

After the parton shower has terminated, phenomenological hadronization models set in.

To test their impact on corresponding predictions at the hadron level, they should be constructed such that they can be applied independently of the details of the perturbative phase of event generation. Nevertheless, these details matter, since they influence the optimal choice of parameters of the hadronization model. In the past this led to the simultaneous tuning of perturbative and non-perturbative parameters of various Monte Carlo models [105, 123].

In the proposed model, the non-perturbative transition of coloured partons into primary hadronic matter, clusters, is accomplished by the following steps:

1. To guarantee the independence of the hadronization model from the quark masses eventually used in the parton shower and to account for a gluon mass needed by the model, all partons are brought to their constituent masses [154] of $\mathcal{O}(0.3 \text{ GeV})$, $\mathcal{O}(0.3 \text{ GeV})$ and $\mathcal{O}(0.45 \text{ GeV})$ for u, d and s flavours, and $\mathcal{O}(1 \text{ GeV})$ for the gluon, respectively. For this transition, a numerical method, involving several particles and consisting of a series of boosts and scaling transformations, is employed. However, these manipulations are applied only to parton-shower subsets that are in a colour-singlet state.

2. Since in cluster-hadronization models the clusters consist of two constituents in a colour-neutral state made up of a triplet–antitriplet, the gluons from the parton shower must split (at least) into quark–antiquark pairs [150]. So, a – in principle non-perturbative – transition, $g \to q\bar{q}, \overline{D}D$, into a light quark–antiquark pair $q\bar{q}$ or a light antidiquark–diquark pair $\overline{D}D$ (see sec. 3.3) is enforced for each gluon. The respective flavour composition of the gluon's decay products is obtained with the same mechanism as used for cluster decays; see sec. 3.3. Quarks or diquarks that cannot be produced owing to too high masses are discarded. The kinematical distribution obeys axial symmetry; the energy fraction z of the quark (antiquark) with respect to the gluon is given by a density proportional to $z^2 + (1 - z)^2$, i.e. the gluon splitting function.[3] The limits on z are fixed only after the flavour of the decay products has been selected.

3. In contrast to the original Webber model of cluster fragmentation, this model may also incorporate soft colour reconnection effects[4] by eventually rearranging the colours of the partons forming the clusters. Starting with a simple cascade, fig. 3.1 schematically shows the two options to arrange two colour neutral clusters out of four quarks or diquarks. The first – direct – case corresponds to the usual cluster formation and reflects the leading term in the $1/N_\mathrm{C}$ expansion. The second – crossed – configuration keeps track of subleading terms. Motivated by the well-known colour suppression of non-planar diagrams with respect to planar ones, the relative suppression factor due to the colours is taken to be $1/N_\mathrm{C}^2$.

   However, the results from the W mass reconstruction at LEP2 in $e^+e^- \to W^+W^- \to$ jets have indicated that the effects of reconnections are overestimated when the suppression is taken according to colours merely. The locality assumption of cluster hadronization stemming from space-time picture considerations contradicts pre-

---

[3]Obviously, for antidiquark–diquark pairs, this is a simplistic assumption, since it neglects, at least, the different spin structure of diquark production.

[4]Other soft colour reconnection models are presented, e.g. in [9, 161, 162, 163, 164, 165, 166, 167, 168].
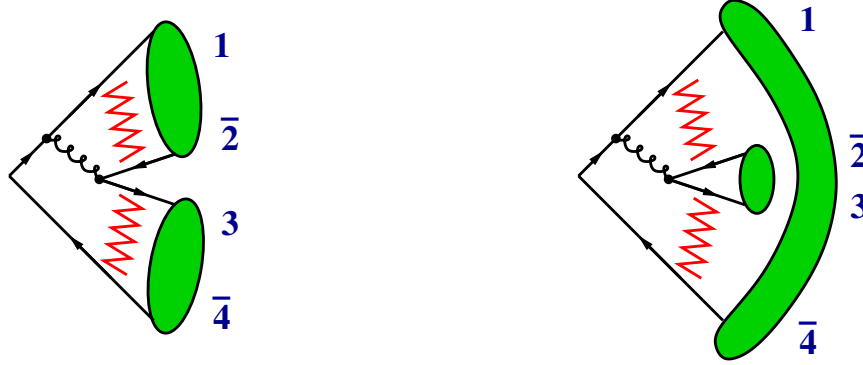
Figure 3.1: Both options of cluster formation for a minimal $qg\bar{q} \to q\bar{q}'q'\bar{q}$ cascade. The zig-zag lines connecting the quark lines symbolize the soft exchange of colour quantum numbers, which is responsible for the colour reconnection.

sumptions, which would enable colour reconnections over a large distance in phase space. Relying on that, a sensible assumption would be that partons close in momentum space are more likely to be colour connected. Therefore, a kinematical weight is applied additionally for each of the two possible cluster pairings. For a pairing ij, kl this weight reads

$$W_{ij,kl} \;=\; \frac{t_0}{t_0 \,+\, (w_{ij} + w_{kl})^2} \,, \tag{3.1}$$

where the quantity t_0, of the order of 1 GeV^2, denotes the scale where the parton-shower evolution stops and hadronization sets in. As a measure, w_{ij} functions such as the invariant mass

$$m_{ij} \;=\; \sqrt{(p_i + p_j)^2} \tag{3.2}$$

of the parton pair (and therefore the cluster), or their relative transverse momentum, similar to the Durham k_T jet scheme [53],

$$p_{\perp ij} \;=\; \sqrt{2 \min\{E_i^2, E_j^2\}(1 - \cos\theta_{ij})} \,, \tag{3.3}$$

might be used. The purely phenomenological ansatz in eq. (3.1) is in line with the idea employed e.g. in the model of Lönnblad [163] where the string "length" between colour-connected partners is minimized. Here a simple weight is chosen ensuring $0 \leq W_{ij,kl} \leq 1$. It compares the hadron squared-mass scale t_0, i.e. an upper limit for this scale, with the squared sum of the measures for the two pairs. If this value is well below that scale, weights greater than $1/2$ are obtained, which in the case of m_{ij} means that the two pairings have masses of the order of $\sqrt{t_0}/2$.

Otherwise the configurations become more and more kinematically suppressed. In essence, any measure, which encodes energy scales of hadronization for the preferred configurations, is suitable for application.

The actual colour configuration of the considered four-parton set is then chosen according to the combined colour and kinematical weight. For the entire system, this reshuffling is iteratively applied to combinations of two successive colour-singlet pairs of partons that have not yet been fixed in the colour-ordered chain.

4. Afterwards, the cluster formation is accomplished by merging two colour-connected partons, quark or antidiquark and antiquark or diquark, into a colourless cluster. In this way, four different cluster types may arise, mesonic ($q_1 \overline{q_2}$ and $\overline{D_1} D_2$), baryonic ($q_1 D_2$), and antibaryonic ($\overline{D_1} \overline{q_2}$) clusters. The total four-momentum of these clusters is just given by the sum of their constituent four-momenta [150].

3.3   Parametrization of light-flavour pair production

In this model the gluon splitting at the beginning of the cluster-formation phase and all cluster decays rely on the emergence of light-flavour pairs, see [150, 154]. During hadronization, which typically sets in at a scale of 1 GeV, there is no possibility for heavy-flavour pair generation [169, 170]. The appearance of baryonic structures is tied to the creation of light diquark–antidiquark pairs.[5] In contrast to the Webber model, here the total diquark spin S is explicitly considered. Thus, $q\bar{q}$ and $\overline{D}_S D_S$ occur as the possible pairs, where

$$q \in \{d,\, u,\, s\}$$

and

$$D_S \in \{dd_1,\, ud_0,\, ud_1,\, uu_1,\, sd_0,\, sd_1,\, su_0,\, su_1,\, ss_1\}\,.$$

Apart from their masses influencing their emergence, the created pair functions as a flavour label only. Furthermore, pair generation is assumed to factorize, i.e. to be independent of the initial flavour configuration. Therefore, interest lies in finding suitable pair-production probabilities, i.e. flavour and spin symmetries should be correctly respected and reasonable hadron multiplicities should be finally obtained in the hadron production.

In this model a phenomenological parametrization of light-flavour pair production is achieved by employing hypotheses leading to a general "flavour dicing" scheme. This scheme is applied to both regimes, cluster formation and decay. The hypotheses are:

1. The emergence of diquarks, which supports baryon generation, is suppressed through a factor $p_\mathcal{B}$ with $0 \leq p_\mathcal{B} \leq 1$.

2. SU(3)$_\mathrm{F}$ symmetry is applied, but is assumed to be broken. This is modelled by a strangeness suppression parameter p_s with $0 \leq p_s \leq 1$, whereas the production of d and u flavours is taken equally likely (strong-isospin symmetry), hence

$$p_{d,u} \;=\; \frac{1 - p_s}{2}\,, \tag{3.4}$$

---

[5]This treatment of static diquark properties resembles to some extent the one employed in the original Lund approach for baryon production [169, 170].

and, as mentioned above, $p_{c,b} \equiv 0$.

3. Spin and flavour weights: the spin-S diquark states ($S = 0, 1$) get a weight proportional to $2S+1$. Additionally, a combinatorial factor of 2 and 1 is applied, depending on whether different or equal flavours constitute the diquark. But, under the assumption of full $\mathrm{SU}(3)_F$ symmetry, the fact that all states in the baryonic $\mathrm{SU}(3)_F$ octet and $\mathrm{SU}(3)_F$ decuplet appear equally likely has to be reproduced. This gives rise to extra weights on the individual diquark types. In particular, the combined diquark weights w_D^S read (neglecting the baryon suppression factor):

$$w_{D=ud,sd,su}^{S=0} \quad = \quad p_D \,, \tag{3.5}$$

$$w_{D=ud,sd,su}^{S=1} \quad = \quad 3\,p_D \,, \tag{3.6}$$

$$w_{D=dd,uu,ss}^{S=1} \quad = \quad 4\,p_D \,, \tag{3.7}$$

where

$$p_D \quad = \quad \frac{p_{d,u}^{2-n_s}\, p_s^{n_s}}{3\,p_s^2 - 2\,p_s + 3} \tag{3.8}$$

and n_s denotes the number of strange quarks in the diquark.

3.4 Cluster transitions into primary hadrons

Once the clusters have been formed, their masses are distributed continuously and independently of the hard process with a peak at low mass. In contrast, the observable hadrons have a discrete mass spectrum and, hence, the clusters must be converted. This is achieved through binary cluster decays and through transformations of individual clusters into single primary hadrons (which probably decay further handled by hadron-decay models). To model the cluster transitions, the following assumptions are employed:

1. Cluster fragmentation is universal, i.e. independent of the hard process and of the parton shower. Apart from the collapse of low-mass clusters into one single hadron, clusters disintegrate locally without impact on other clusters.

2. Cluster transitions, i.e. decays as well as transformations, involve only low momentum transfer, of the order of 1 GeV [154], since hadronization effects are supposed to be sufficiently soft and hadronization corrections to parton-level event shapes such as the mean thrust scale inversely with the centre-of-mass energy.

3. The regime of clusters is separated from the regime of hadrons according to the flavours of the cluster constituents and the accessible hadron masses. Clusters are supposed to be hadrons, if their mass is below a threshold mass. This bound is given by the maximum of the mass associated to the heaviest hadron with identical (valence) flavour content and the sum of the masses of the lightest possible hadron pair emerging in the decay of those clusters.

The last assumption has two consequences, namely that in a first step the newly formed clusters that are already in the hadronic regime have to be transformed into hadrons; in the subsequent binary decays of the remaining clusters, that also the daughter clusters, which fall into the regime of hadron resonances, have to become hadrons immediately. The cluster fragmentation into primary hadrons accordingly occurs in two phases: direct cluster to hadron transitions and two-body cluster decays. In both cases, a definite hadron species $\mathcal{H}$ has to be chosen if needed according to the flavour structure of the considered cluster $\mathcal{C}$. The details are given below.

3.4.1   Hadron selection

Respecting fixed particle properties, the choice is based on hadron wave functions motivated by a non-relativistic quark model. The wave functions are factorized into a flavour- and a spin-dependent part. In our model the flavour part is given for a two-component system in terms of quarks and diquarks. The overlap of this flavour part with the flavour content of the cluster gives rise to a flavour weight. In addition, since spin information is washed out in the clusters [154], the total spin J of the hadron manifests itself as a corresponding weight. The total spin is given through the coupling of the relative orbital momentum L with the net spin S of the valence components. This can be written as $\vec{J} = \vec{L} + \vec{S}$. The contributions of states with different orbital momentum L to the total-spin sum are accounted for by some a-priori weights $\mathcal{P}_L$, which enter as model parameters. Taken together, the total flavour-spin weight $\mathcal{W}$ for a single hadron reads

$$
\mathcal{W}\big(q_1 s_1, \bar{q}_2 s_2 \rightarrow \mathcal{H}^J(q_1 s_1, \bar{q}_2 s_2)\big) \;\; \sim \;\; \frac{\big|\langle \psi_F(\mathcal{H}^J) | q_1 s_1, \bar{q}_2 s_2 \rangle\big|^2}{\sum_{\hat{\mathcal{H}}|\hat{J}=J} \big|\langle \psi_F(\hat{\mathcal{H}}^{\hat{J}}) | q_1 s_1, \bar{q}_2 s_2 \rangle\big|^2}
$$
$$
\times \; \frac{\sum'_{L,S \rightarrow J} \big|\langle S | s_1 s_2 \rangle\big|^2 \, \mathcal{P}_L \, \big|\langle J | LS \rangle\big|^2}{\sum_{\hat{J}} \sum'_{\hat{L},\hat{S} \rightarrow \hat{j}} \big|\langle \hat{S} | s_1 s_2 \rangle\big|^2 \, \mathcal{P}_{\hat{L}} \, \big|\langle \hat{J} | \hat{L}\hat{S} \rangle\big|^2} \; . \quad (3.9)
$$

In contrast to q_1 denoting the quarks, $\bar{q}_2$ stands for antiquarks as well as diquarks. The spins of the two cluster components 1 and 2 are given by $s_1 = s(q_1)$ and $s_2 = s(\bar{q}_2)$, respectively, and $\langle \psi_F(\mathcal{H}^J)|$ denotes the flavour part of the hadron wave function.[6] Moreover, $|\langle j|ls\rangle|^2 = 2j+1/(\sum_{i=|l-s|,\ldots,(l+s)} 2i+1)$ and $\sum'_{L,S \rightarrow J}$ is an abbreviation denoting a summation over $L = 0, 1, \ldots$ and $S = |s_1 - s_2|, \ldots, (s_1 + s_2)$, considering the condition that only those terms contribute, where $|L - S| \leq J \leq (L + S)$ can be fulfilled. Finally, it should be stressed that the second term of eq. (3.9) represents only a static model, which accounts for the correct selection of hadrons according to their total spin.

3.4.2   Single cluster to hadron transitions

When the clusters are formed from colour-connected pairs of quarks and diquarks, some of them, because of their comparably low mass, fall into the hadronic regime. Within this framework these clusters are transformed into single hadrons immediately. In doing so, however, some four-momentum is released and has to be absorbed by other clusters. By

---

[6]For mesons this also includes the possibility of singlet-octet mixing occurring in hadron multiplets.

allowing hadrons with masses lower than the cluster mass only, the momentum transfer is taken to be a mere energy transfer and, therefore, is time-like. This ensures that the absorbing cluster becomes heavier. To fulfil the requirement of low momentum transfer, the already outlined hadron-selection procedure according to the flavour-spin weights $\mathcal{W}$ is modified through the inclusion of an additional – kinematic – weight,

$$\mathcal{W}_{\text{kin.}} = \exp\left[-\left(\frac{Q^2}{Q_0^2}\right)^2\right]. \tag{3.10}$$

In this equation $Q^2 > 0$ denotes the squared momentum (i.e. energy) transfer, and Q_0 is the scale related to the low momentum-transfer demand. The limit Q_0, furthermore, depends on the cluster mass and is also employed in the cluster decays; see below, eq. (3.12). Note that in the original Webber model the clusters being too light to decay are identified to be the lightest hadron with identical flavour structure. In comparison with the Webber scheme, the major difference of this approach in the case of single-cluster transitions is the expansion of the hadron-selection procedure, i.e. the selection is not restricted to the lightest hadron anymore, instead all hadrons with masses lower than the cluster mass are allowed to be selected.

The cluster compensating the residual four-momentum is selected such that it contains the partner that emerged in the same non-perturbative gluon-splitting process as one of the constituents of the transformed cluster. In turn, clusters, which fall into the hadron regime and contain two leading quarks, are always split non-perturbatively into two clusters containing only one leading constituent. In this context leading partons, however, are only those quarks and antiquarks that directly originate from the perturbative phase, and not from the non-perturbative gluon splitting or from the cluster decays. For the resulting single-leading clusters, then, the same considerations as for the direct transformation to hadrons apply. In case a cluster in the hadron regime is made up of a diquark and an antidiquark, which is, in principle, possible, it is forced to specifically decay into two mesons. The kinematics details on both the forced double-leading cluster breakup and the double-diquark cluster decay are the same as will be outlined below, see eq. (3.11).

3.4.3   Two-body cluster decays

Finally all remaining clusters – primary clusters as well as secondary clusters (daughters) – have to be split. The mass categorization outlined above automatically yields one of the modes $\mathcal{C} \to \mathcal{C}_1\mathcal{C}_2$, $\mathcal{C} \to \mathcal{C}_1\mathcal{H}_2$, $\mathcal{C} \to \mathcal{H}_1\mathcal{C}_2$, or $\mathcal{C} \to \mathcal{H}_1\mathcal{H}_2$. These modes involve the creation of an extra flavour pair according to the ideas illustrated in sec. 3.3. Similarly to the cluster-formation phase, then, two flavour configurations for the decay products emerge, namely a direct one and a crossed one; see fig. 3.2. Again, the crossed configuration is suppressed by the colour factor $1/N_{\text{C}}^2$ and the kinematical weight from eq. (3.1) using identical measure functions w and replacing t_0 by Q_0^2, which again depends on the mass of the decaying cluster. Furthermore, the mother-cluster fission kinematics, which makes use of the scale Q_0, is fixed to be anisotropic, and, as already discussed in the introduction, this breaking mechanism is chosen to have string-like characteristics. Starting from a mother cluster with constituent momenta $p_{1,2}^{\mathcal{C}}$ and mass $M_{\mathcal{C}}$, the new momenta of the
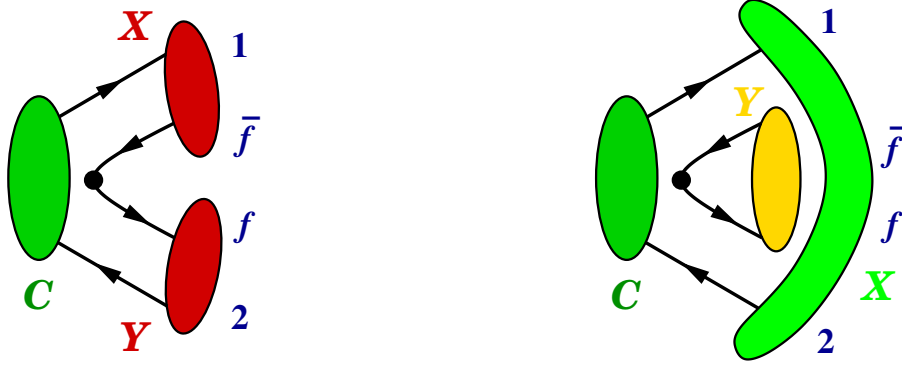
Figure 3.2: Direct and crossed flavour arrangement and colour flow guaranteeing colour neutrality for each final-state configuration in cluster two-body decays.

constituents of the decay products read [154]

$$p_{1,2} = \left(1 - \frac{Q_0}{M_{\mathcal{C}}}\right) p_{1,2}^{\mathcal{C}} \qquad \text{and} \qquad p_{\bar{f},f} = \frac{Q_0}{M_{\mathcal{C}}} p_{2,1}^{\mathcal{C}}, \tag{3.11}$$

where f and $\bar{f}$ label the momenta of the newly created flavour pair. Hence, for the two cluster arrangements (see fig. 3.2) the momenta are given by $P_{\text{dir.}}^{\mathcal{X}} = p_1 + p_{\bar{f}}$, $P_{\text{dir.}}^{\mathcal{Y}} = p_f + p_2$ in the direct, and $P_{\text{cross.}}^{\mathcal{X}} = p_1 + p_2$, $P_{\text{cross.}}^{\mathcal{Y}} = p_f + p_{\bar{f}}$ in the crossed case, respectively. The underlying algorithm, i.e. the mass-categorization idea, for cluster decays implicates the demand that the calculation of the daughter-cluster momenta must not break down for any possible $M_{\mathcal{C}}$. To guarantee well-behaved four-momenta in this fission breaking, i.e. to have well-defined $Q_0/M_{\mathcal{C}}$ fractions with $Q_0 < M_{\mathcal{C}}$, this model uses a parametrization of a running Q_0 increasing monotonously with $M_{\mathcal{C}}$. This running depending on two parameters, $\hat{Q}_0$ and $\hat{M}_0$, with the constraint $\hat{Q}_0 < \hat{M}_0$, can be formulated as

$$Q_0(M_{\mathcal{C}}) = \frac{\hat{Q}_0 M_{\mathcal{C}}}{\hat{M}_0 + M_{\mathcal{C}}} < M_{\mathcal{C}}. \tag{3.12}$$

The ansatz reflects that with increasing mother-cluster masses the momentum transfer in the fission is allowed to be higher. But it also fulfils saturation for very massive clusters, since the dominant scale for hadronization is the QCD scale Λ_{QCD}. From this consideration, the meaning of the two parameters can be found. $\hat{Q}_0$ gives an upper limit on the hadronization-energy scale. In that, it takes over the rôle of the original Q_0 fission constant of the Webber model [154]. The decline towards lower cluster masses can be controlled by the value given to $\hat{M}_0$. Ultimately, both parameters are major tuning parameters of this model, but they are quite natural in the sense that the range is known of meaningful values, which can be given to them and which are of the order of hadronization energies and peak masses of the cluster mass distribution for $\hat{Q}_0$ and $\hat{M}_0$, respectively.

cluster		direct case	crossed case		direct case	crossed case
$q_1\bar{q}_2$	$\xrightarrow{\bar{q}q}$	$q_1\bar{q} + q\bar{q}_2,$	$q_1\bar{q}_2 + q\bar{q}$	$\xrightarrow{D\overline{D}}$	$q_1D + \overline{D}\bar{q}_2,$	$q_1\bar{q}_2 + \overline{D}D$
q_1D_2	$\xrightarrow{\bar{q}q}$	$q_1\bar{q} + qD_2,$	$q_1D_2 + q\bar{q}$	$\xrightarrow{D\overline{D}}$	$q_1D + \overline{D}D_2,$	$q_1D_2 + \overline{D}D$
$\overline{D}_1D_2$	$\xrightarrow{\bar{q}q}$	$\overline{D}_1\bar{q} + qD_2,$	$\overline{D}_1D_2 + q\bar{q}$	$\xrightarrow{D\overline{D}}$	$\overline{D}_1D + \overline{D}D_2,$	$\overline{D}_1D_2 + \overline{D}D$
$\overline{D}_1D_2$	$\longrightarrow$	$q_2\bar{q}_1 + q'_2\bar{q}'_1$		$\longrightarrow$	$q_2\bar{q}'_1 + q'_2\bar{q}_1$	

Table 3.1:   Different cluster types emerging through cluster breakups. Decay channels indicating a four-quark, i.e. two-diquark, system to become a hadron within the modes $\mathcal{C} \to \mathcal{C}_1\mathcal{H}_2$, $\mathcal{H}_1\mathcal{C}_2$, $\mathcal{H}_1\mathcal{H}_2$ are vetoed. The four-quark cluster disintegration into two mesons (see last row of the table) is only available for the mode $\mathcal{C} \to \mathcal{H}_1\mathcal{H}_2$. The occurrence of the two disintegration possibilities is taken to be equally likely.

Having fixed the primary kinematics, via eq. (3.11), and the combination of flavours and momenta to the new clusters, their masses can be deduced from the squares of their total four-momenta. Then, as stated above, the different decay modes $\mathcal{C} \to \mathcal{C}_1\mathcal{C}_2$, $\mathcal{C}_1\mathcal{H}_2$, $\mathcal{H}_1\mathcal{C}_2$, $\mathcal{H}_1\mathcal{H}_2$ are distinguished according to the resulting masses of the daughter clusters. All possible decay channels within each mode are comprehensively summarized in tab. 3.1.

1. For the case of breakups involving clusters only, i.e. for $\mathcal{C} \to \mathcal{C}_1\mathcal{C}_2$, nothing has to be done in addition.

2. If one of the daughter clusters falls into the hadronic regime, i.e. for $\mathcal{C} \to \mathcal{C}_1\mathcal{H}_2$ and $\mathcal{C} \to \mathcal{H}_1\mathcal{C}_2$, a suitable hadron has to be selected such that the hadron will be lighter than the cluster. The selection procedure follows that outlined above for the $\mathcal{C} \to \mathcal{H}$ transformation; the recoil is taken by the daughter system, which belongs to the cluster regime.

3. If both new clusters fall into the hadron regime, i.e. for purely hadronic decays, $\mathcal{C} \to \mathcal{H}_1\mathcal{H}_2$, more severe manipulations are applied. First of all, the newly created flavour pair $f\bar{f}$ is abandoned; instead, two hadrons are chosen directly. Then the combined weight for the selection of such a hadron pair consists of three pieces. The first part accounts for the two flavour-spin contents. The second one includes the correct relation of direct to crossed decay configurations and, furthermore, represents the incorporation of the pair-production rates. The last part considers the phase space of the decay, which is taken to be isotropic in the cluster's rest frame [150, 154]. The combination of the first two weights for the hadron pair is set up as if only complete $SU(3)_F$ multiplets were accessible. Because of the superposition with the phase-space factor, a hadron pair that cannot be produced in a cluster decay owing to its large mass cannot contribute to the selection. [7] The other manipulation,

---
[7]The weight treatment for hadron selection in HERWIG was first modified by Kupčo [171]. By now,

as indicated above, is that once the hadron species are chosen, the cluster decays isotropically in its rest frame into these hadrons.

Two comments are in order here: first of all, this approach takes leading-particle effects into account in the same manner as in Webber's model. This treatment on average enhances the anisotropy of leading-cluster breakups.

Secondly, when considering a cluster consisting of two diquarks, mesons can emerge only by recombining the individual quarks and antiquarks that constitute the diquarks, see tab. 3.1. Since baryons appear in a decay of such clusters through the creation of a quark pair, the diquark recombination is taken to be suppressed by a factor of $p_\mathcal{B}$ with respect to the baryon production, which appears with $1-p_\mathcal{B}$ in this channel. The specific ordering of the quarks into mesons is then done in a fashion similar to the one above, involving hadron pairs. The difference, however, lies in the fact, that Clebsch-Gordan coefficients are additionally employed. These coefficients account for the rearrangement of the product of the diquark and antidiquark spin-S wave function into a double-mesonic basis, since after the breakup the (anti)diquark cannot be regarded as an entity anymore. The treatment, therefore, gives additional constraints on the spins of the emerging mesons. Given that these spins are denoted $S_\mathcal{M}$ and $S_\mathcal{N}$, one has to find the probabilities that their angular-momentum coupling results in the four-quark cluster's net spin, which is initially obtained from the spin coupling of its diquark and antidiquark. Using two-particle spin states $|SS_z\rangle_{12}$, the singlet and triplet vectors written in terms of single-particle spin functions are

$$|00\rangle_{12} \quad = \quad \frac{1}{\sqrt{2}} \left(|{\uparrow_1}{\downarrow_2}\rangle - |{\downarrow_1}{\uparrow_2}\rangle \right), \tag{3.13}$$

$$|1\,{-}1\rangle_{12} \quad = \quad |{\downarrow_1}{\downarrow_2}\rangle, \tag{3.14}$$

$$|10\rangle_{12} \quad = \quad \frac{1}{\sqrt{2}} \left(|{\uparrow_1}{\downarrow_2}\rangle + |{\downarrow_1}{\uparrow_2}\rangle \right), \tag{3.15}$$

$$|11\rangle_{12} \quad = \quad |{\uparrow_1}{\uparrow_2}\rangle. \tag{3.16}$$

Then, according to a $\overline{q_1 q_2} q_3 q_4$ cluster, for the $q_3 \overline{q_1} + q_4 \overline{q_2}$ combination, the, e.g. four-quark cluster spin-vector $|00\rangle_{12}|00\rangle_{34}$ formulated in terms of (anti)diquarks can be re-written as

$$|00\rangle_{12}|00\rangle_{34} \quad = \quad \frac{1}{2} \Big(|11\rangle_{13}|1\,{-}1\rangle_{24} + |1\,{-}1\rangle_{13}|11\rangle_{24} -$$

$$|10\rangle_{13}|10\rangle_{24} + |00\rangle_{13}|00\rangle_{24} \Big). \tag{3.17}$$

This expression already allows to read off the Clebsch-Gordan-like probabilities:

$$C_{00,00} = \frac{1}{4} \qquad \text{and} \qquad C_{00,11} = \frac{3}{4}, \tag{3.18}$$

where the notation $C_{S_{\overline{D}} S_D, S_\mathcal{M} S_\mathcal{N}}$ has been used. The other factors can be obtained in a similar fashion as demonstrated above. Beneficially, up to some change in signs

---

the HERWIG++ group has developed a new, improved, approach [19].

the rearrangement for the other configuration $q_3\overline{q_2} + q_4\overline{q_1}$ yields the same results. Ultimately, one ends up with:

$$C_{01,01} = C_{01,10} = \frac{1}{4} \qquad \text{and} \qquad C_{01,11} = \frac{1}{2}\,; \tag{3.19}$$

$$C_{10,01} = C_{10,10} = \frac{1}{4} \qquad \text{and} \qquad C_{10,11} = \frac{1}{2}\,; \tag{3.20}$$

$$C_{11,00} = \frac{1}{12}\,, \qquad C_{11,01} = C_{11,10} = \frac{2}{12} \tag{3.21}$$

and

$$C_{11,11} = \frac{7}{12}\,. \tag{3.22}$$

3.5 Preliminary results

The performance of the model introduced above is now illustrated by presenting some results for e^+e^- annihilation at the Z^0 pole using only light quarks throughout the event's evolution. The outcomes were obtained with the parton shower of APACIC++ 1.0 [71], the matrix elements were generated by AMEGIC++ 1.0 [56] and combined with this parton shower [36], the primary hadronization was accomplished by the cluster model described above, and the hadron decays were provided through interfacing the corresponding routines of PYTHIA 6.1 [6]. The resulting event generator is the combination of these modules. In the following it is referred to as SHERPAα. The results shown below were all achieved with the same parameter set. Allowing the full colour-reconnection model, all the cluster-model parameters were adjusted only manually through a comparison to the corresponding PYTHIA 6.1 predictions. Tab. 3.2 summarizes the major parameters of the cluster-hadronization model, where those indicated by a star are referred to as the main tuning parameters of the model. The settings of the other module's input variables were mainly taken over from a Z^0 pole tuning of APACIC++ 1.0, together with the full hadronization of PYTHIA 6.1, where the major modification amounted to a change of the parton-shower cut-off, t_{cut}, from $t_{\mathrm{cut}} = 0.5$ GeV^2 to $t_{\mathrm{cut}} = 0.4225$ GeV^2. Since measurements that specifically concentrate on the observation of light-quark characteristics are rarely available, results are mainly compared with those gained from running PYTHIA 6.1 and HERWIG 6.1 [172] both restricted to u, d, s quarks. In doing so, either of the models was run with its default parameter values.

3.5.1 Impact of the colour-reconnection model

In a first step model-internal results are considered. To begin with, the effects of the colour-reconnection model on the cluster-mass distribution, and the statistics of the reconnections in the cluster formation are briefly discussed. Fig. 3.3 illustrates the statement that under the influence of the kinematically re-weighted colour-reconnection model this cluster hadronization tends to produce less massive primary clusters than without the full reconnection procedure. This is in contrast to other colour-reconnection models. However, if one considers the kinematically unweighted model, which uses $w_{ij} \equiv 0$, the

constituent masses			
	$M_{d,u}$	0.30	GeV
	M_s	0.45	GeV
	M_{ud_0}	0.57933	GeV
	M_{dd_1,ud_1,uu_1}	0.77133	GeV
	M_{sd_0,su_0}	0.80473	GeV
	M_{sd_1,su_1}	0.92953	GeV
	M_{ss_1}	1.09361	GeV
*	M_g	1.20	GeV
reconnection squared-mass scale			
	t_0	$M_g^2/4$	
strangeness production probability of pair creation			
*	p_s	0.104	
baryon production probability of pair creation			
*	$p_{\mathcal{B}}$	0.267	
relative orbital-angular-momentum weights			
	$\mathcal{P}_{L=0\dots5}$, $\mathcal{P}_{L>5}$	1.5^{5-L}, 0	
cluster-fission mass scale of Q_0 running			
*	$\hat{Q}_0$	0.84	GeV
steepness regulator of Q_0 running			
*	$\hat{M}_0$	2.10	GeV
gaussian smearing parameter for leading-cluster breakups $\mathcal{C}_\ell \to \mathcal{HH}$			
*	σ_0	0.00077	

Table 3.2: Overview of the parameters and their values used in the cluster-hadronization model of SHERPAα. Major tuning parameters are indicated by "*".

behaviour is completely reversed. Therewith one can conclude (1) that the decrease is especially caused by the kinematic factor, eq. (3.1), where $w_{ij} = p_{\perp ij}$ has been used, and (2) that this factor has rather strong effects on the primary-cluster mass distribution. When considering colour-reconnection sensitive observables, this then might favour the possibility of an isolated tuning of the kinematic factor, i.e. the choice of t_0 given in eq. (3.1). Right now t_0 is set through the gluon constituent mass. For the full (kinematically unweighted) colour-reconnection model in the cluster formation one gets approximately 0.742 (0.689) reconnections per event and, with a frequency of 47.7%, 35.2%, 13.0%, 3.3% (50.3%, 34.5%, 11.8%, 2.8%), and 0.8% (0.6%), one finds 0, 1, 2, 3, and > 3 exchange(s), respectively. Moreover, changing the option full colour reconnection while keeping the parameters (adjusted under the full reconnection model) unchanged yields the following qualitative modifications: for both other options, the number of daughter clusters per event is increased, which results for the reconnection free and the kinematically unweighted model in an enlargement of the mean charged-particle multiplicity of roughly 0.2 and 1.0 charged tracks per event, respectively. In the free case the charged-pion produc-

Primary cluster mass distribution
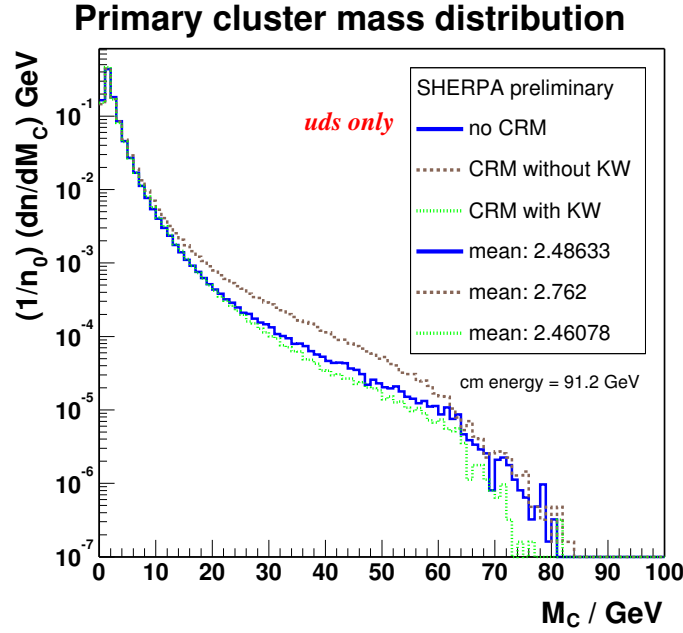
Figure 3.3: Primary cluster-mass distribution in e^+e^- annihilation events evolving into light-quark and gluon jets at the Z^0 pole. The SHERPAα results are shown for three cluster-model cases, the model excluding colour reconnection at all (solid line), the model including the kinematically unweighted colour-reconnection model, i.e. the colour-reconnection model (CRM) without kinematic weight (KW) (dashed line), and, the model including the full colour-reconnection model (dotted line).

tion rate increases, where this is even more enhanced for the kinematically unweighted reconnection model. The charged-kaon rate and the (anti)proton rate decrease for the free model. These two effects are reversed for the reconnection model without kinematic weighting procedure. Furthermore, the charged-particle transverse-momentum distributions are lowered for high $p_\perp^{uds,\text{in/out}}$, where the deviation is smaller for the model with the reconnection option entirely switched off. Again, this is an example, where one may recognize a complete reverse of the full model's behaviour when the kinematic weigthing procedure is not taken into account. In contrast to that, at the same time the scaled-momentum distribution of charged tracks alters only marginally. However, this is not true for the reconnection free model. In this circumstance the scaled-momentum distribution's bump at $x_p^{uds} \approx 0.5$ enhances and the tail of the distribution tends to become harder (see the discussion below and cf. fig. 3.8).

Briefly, the influence of exchanging the $p_{\perp ij}$ with the m_{ij} measure is discussed. In the multiplicity, event-shape, jet-rate and momentum distributions differences are barely noticeable. Modifications can only be reported from the primary-cluster mass distribution, see fig. 3.4. There one may conclude that up to a small region around 10 GeV the m_{ij} model predicts a slightly harder spectrum, however, the trend given by the kinematical weighting is clearly retained. Also this does not seem to have great effects on hadron-level distributions, differences can also be seen in the statistics of the reconnections, since

Primary cluster mass distribution
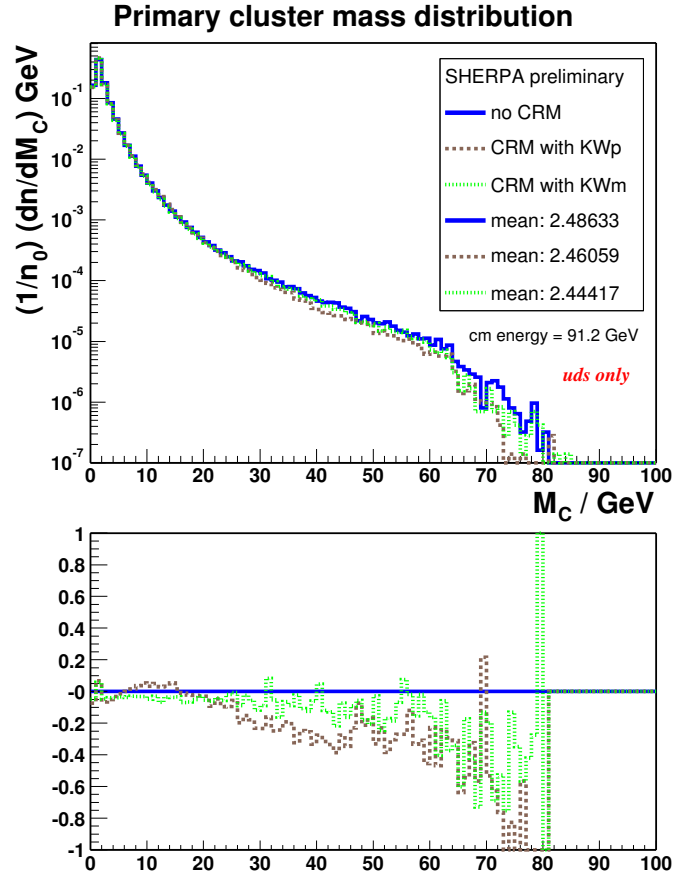
Figure 3.4:   Primary cluster-mass distribution in e^+e^- annihilation events that evolve into light-quark and gluon jets at the Z^0 pole. The SHERPAα results are shown for three cluster-model cases, the model excluding colour reconnection at all (solid line), the $p_{\perp ij}$ model (KWp) (dashed line), and, the m_{ij} model (KWm) (dotted line), both of which considering the complete treatment for colour reconnection. The lower part of the plot shows the normalized difference where the colour-reconnection free model is used as the reference.

in the cluster formation now one gets approximately 0.564 reconnections per event and, with a frequency of 58.1%, 30.3%, 9.1%, 2.0%, and 0.5%, one finds 0, 1, 2, 3, and > 3 exchange(s), respectively. Hence, from the considerations done so far, one cannot judge, which of the two measures is more suitable. In conclusion, the impact of the kinematical weighting has been clearly seen to be very crucial. So, to shed more light on the effects of the reconnection model one has to explore observables that are specifically sensitive to colour reconnection. This then might favour the possibility of an isolated tuning of the kinematic factor, i.e. the choice of t_0 given in eq. (3.1). Right now t_0 is set through 1/4 of the gluon constituent mass squared.
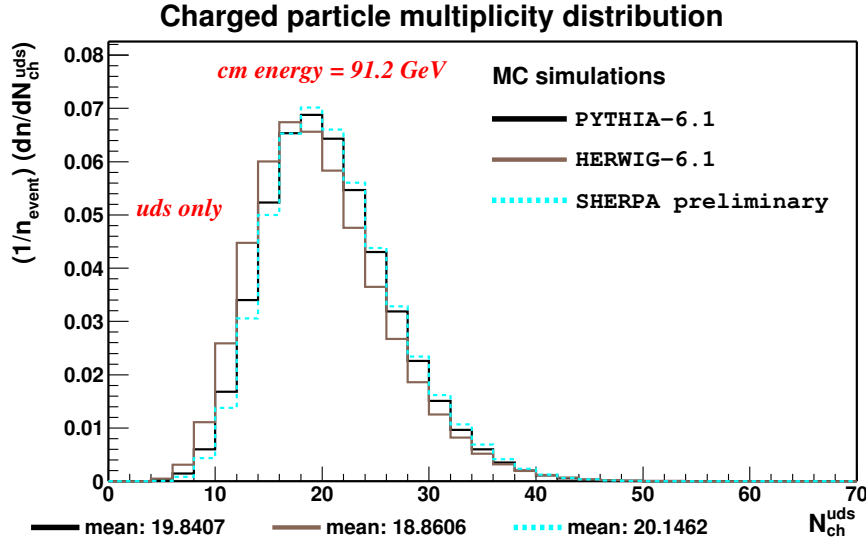
Figure 3.5:   Predicted multiplicity distribution of charged particles in e^+e^- annihilation for light-quark and gluon jets at the Z^0 pole. The SHERPAα result is shown together with the default PYTHIA 6.1(uds) and HERWIG 6.1(uds) predictions.

3.5.2   Model predictions

Now, in the second step, the preliminary predictions of this model under the inclusion of the full colour-reconnection model are discussed. The overall charged-particle multiplicity distribution is presented in fig. 3.5. The shift to higher multiplicities of the SHERPAα curve with respect to the other curves indicates the higher mean value of the SHERPAα prediction. Tab. 3.3 shows mean multiplicities $\langle \mathcal{N}_{\text{ch}}^{uds} \rangle$ as provided by those three fragmentation models in comparison with inclusive measurements. To exemplify the charged-hadron rates, the mean multiplicities for the stable charged hadrons – $\pi^\pm$, $K^\pm$ and $p, \bar{p}$ – are considered and compared with experimental uds results; see also tab. 3.3. To have a comparison with experimental data on charged-particle multiplicity distributions, each event is divided into hemispheres using the plane perpendicular to the thrust axis. The charged tracks per hemisphere are summed for both hemispheres. Then, the average of the two contributions is formed. This procedure yields the hemisphere multiplicity distribution of charged tracks, whereas the forward-backward asymmetry is not taken into account. The resulting SHERPAα distribution is shown in fig. 3.6. There it is compared with experimental data from the OPAL collaboration [178].

In a further test the SHERPAα predictions for the energy dependence of the $\langle \mathcal{N}_{\text{ch}} \rangle$ observable have been considered by using the Z^0 pole adjusted parameters. To do so, the corresponding $\langle \mathcal{N}_{\text{ch}}^{uds} \rangle$ results have been corrected by employing an ansatz

$$\langle \mathcal{N}_{\text{ch}} \rangle \;=\; \langle \mathcal{N}_{\text{ch}}^{uds} \rangle \;+\; f_c\, \delta_c \;+\; f_b\, \delta_b \,, \tag{3.23}$$

which has been quite similarly formulated in [179]. This ansatz exploits the QCD prediction that the difference in charged-particle multiplicity, $\delta_{c,b}$, between heavy- and light-quark events is expected to be almost energy independent [180]. The $f_{c,b}$ are the fractions
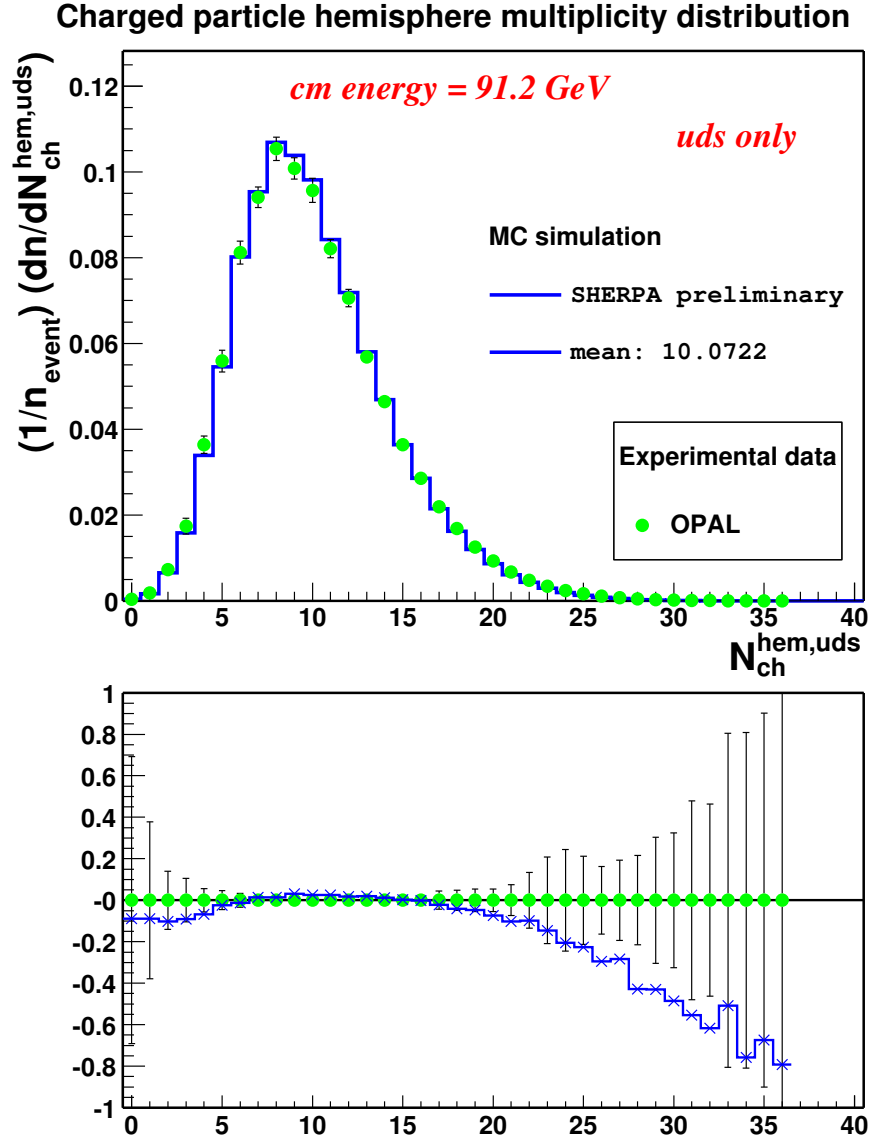
Figure 3.6: Predicted hemisphere multiplicity distribution of charged tracks in electron–positron annihilation for the light-quark sector at the Z^0 pole. The hadron level prediction of SHERPAα is shown in comparison to the corrected distribution of charged-particle multiplicity obtained by OPAL [178]. The total uncertainties are indicated by vertical lines. The lower part of the plot illustrates the normalized difference between the simulation and the data.

|	$\langle \mathcal{N}_{\text{ch}}^{uds} \rangle$	$\langle \mathcal{N}_{\pi^\pm}^{uds} \rangle$	$\langle \mathcal{N}_{K^\pm}^{uds} \rangle$	$\langle \mathcal{N}_{p,\bar{p}}^{uds} \rangle$
PYTHIA 6.1(uds)	19.84	16.72	2.010	0.856
HERWIG 6.1(uds)	18.86	15.37	1.693	1.568
SHERPAα	20.15	16.83	2.018	1.047
OPAL [173]	20.25 ± 0.39			
DELPHI [174]	20.35 ± 0.19			
DELPHI [175]	19.94 ± 0.34	16.84 ± 0.87	2.02 ± 0.07	1.07 ± 0.05
SLD [176]	20.21 ± 0.24			
SLD [177]	20.048 ± 0.316	16.579 ± 0.304	2.000 ± 0.068	1.094 ± 0.043

Table 3.3:   Overall mean charged-particle multiplicity, and production rates of charged pions, charged kaons and (anti)protons in e^+e^- collisions. The values are taken for uds events running at the Z^0 peak centre-of-mass energy. The errors indicated in the table are the total errors of the measurements. More JETSET and HERWIG results on this topic can be found in [175].

of $c\bar{c}, b\bar{b}$ events, which can be obtained from APACIC++ 1.0 when dropping the uds quark restriction. [8] To accomplish the calculation, a weighted average including results from low-energy data, LEP1 and LEP2, $\delta_b = 3.05 \pm 0.19$ [179], has been chosen; $\delta_c = 1.7 \pm 0.5$ has been taken from [180]. These resulting SHERPAα energy behaviour is shown in fig. 3.7, where it is also compared with measurements from various e^+e^- experiments [181].

In view of these comparisons, the conclusion is that the SHERPAα multiplicity results are in reasonable agreement with the PYTHIA 6.1(uds) predictions and with the data.
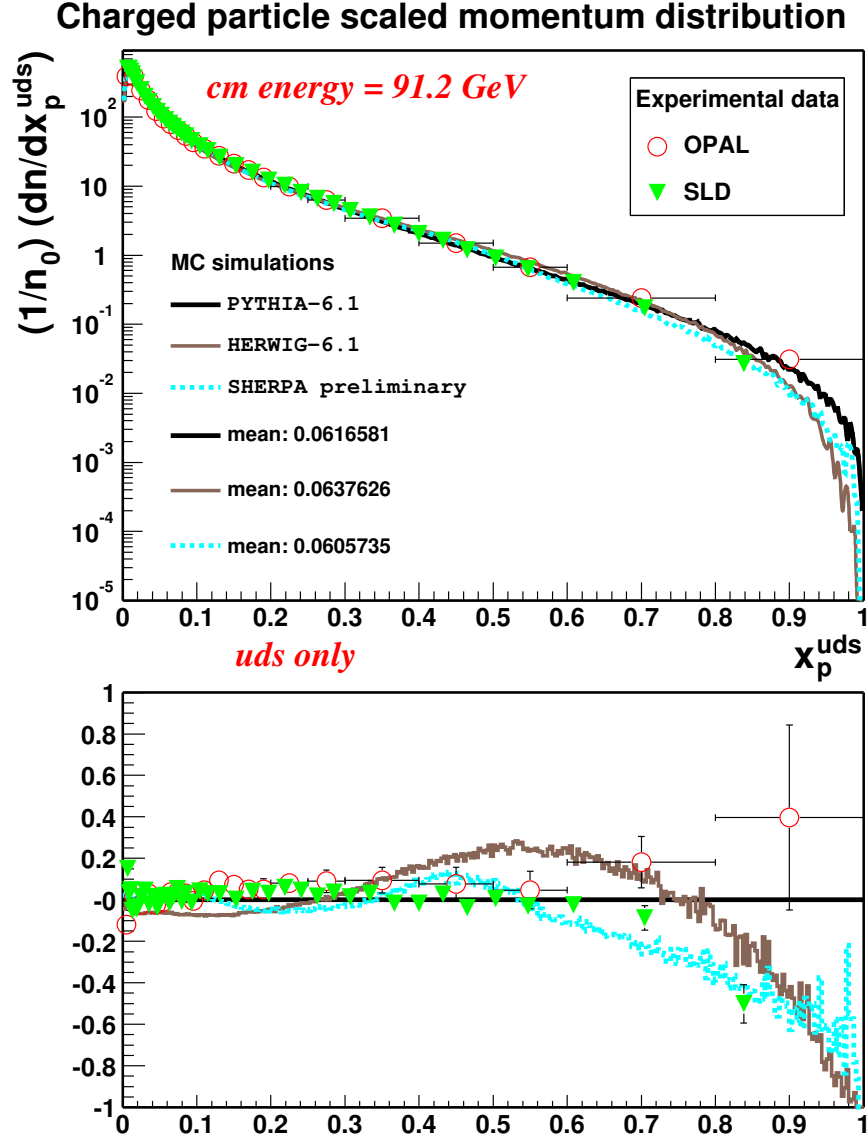
As examples for particle-momentum distributions, the scaled momentum defined as $x_p^{uds} = 2|\vec{p}_{uds}|/E_{\text{cm}}$ and its negative logarithm $\xi_p^{uds} = -\ln x_p^{uds}$ are considered. The x_p^{uds} distribution obtained with SHERPAα is shown in fig. 3.8, together with the predictions of the PYTHIA 6.1(uds) and HERWIG 6.1(uds) event generators. Furthermore, experimental results delivered by the OPAL [173] and SLD [177] collaborations on this differential cross section have been included. Additionally, in fig. 3.9 DELPHI data [175] are compared with the predictions of the fragmentation models under consideration. In order to enhance the significance, a histogram structure being identical to that of the data has been used for

---

[8]In the calculation of the correction of the Monte Carlo result for 10 GeV, the b quark threshold has been assumed to be above that energy, i.e. in this case f_b has been set to zero.
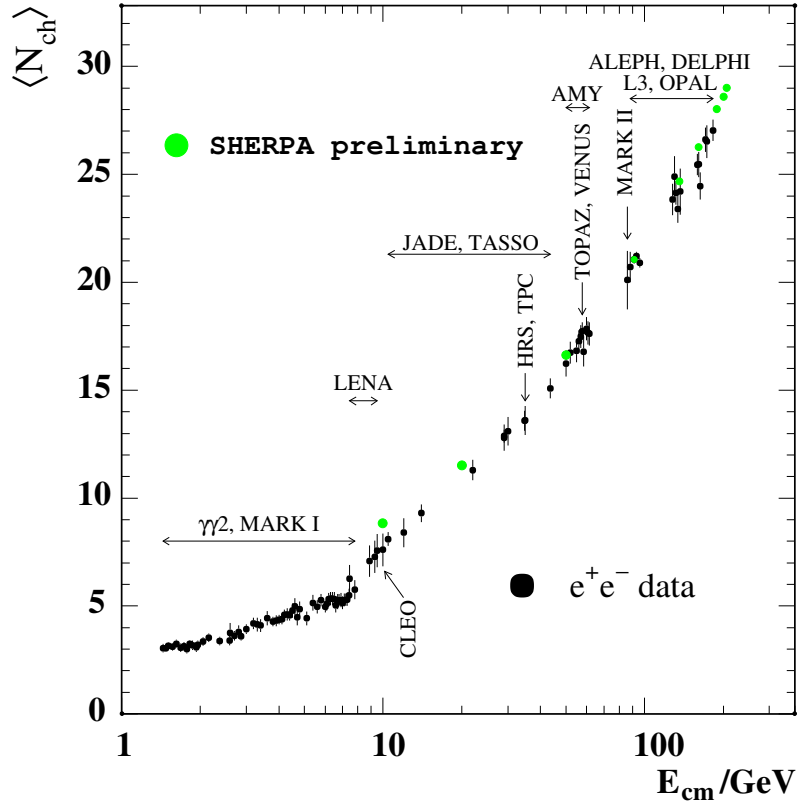
Figure 3.7:   Energy dependence of the mean charged-particle multiplicity in electron–positron annihilation. First predictions of SHERPAα employing a heavy-quark correction are shown in comparison to experimental e^+e^- data [181]. The total uncertainties of the measurements are indicated by vertical lines. The diameter of the SHERPAα points specifies the error due to the correction procedure.

the calculation of the simulated x_p^{uds} values. The PYTHIA 6.1(uds) model is the most consistent with the OPAL and DELPHI data, but it predicts a slightly softer spectrum. Both cluster-hadronization models show quite similar behaviour concerning their deviation from the PYTHIA 6.1(uds) prediction (cf. fig. 3.8). For $x_p^{uds} < 0.7$ they oscillate around this prediction, where both have the tendency to overestimate the data at $x_p^{uds} \approx 0.5$. For $x_p^{uds} > 0.8$ they anticipate a steeper decline, which is quite different from that seen in the OPAL and DELPHI data. In spite of these shortcomings, the agreement of SHERPAα with the DELPHI data is encouraging at least up to x_p^{uds} values of 0.6 (cf. fig. 3.9). Moreover, the recently published SLD results [177] already plotted in fig. 3.8 show a considerably softer high-x_p^{uds} tail. To better judge the performance of the model according to the SLD data, again a histogram structure being identical to the data binning has been used, see fig. 3.10. The soft high-x_p^{uds} tail behaviour then can be described by the new cluster model and by the HERWIG model as well, which is above the former prediction. Nevertheless, in the former case the onset of the rapid fall off is still at scaled-momentum values that are too low. When going towards lower x_p^{uds}, the first bump is truly a deficiency of
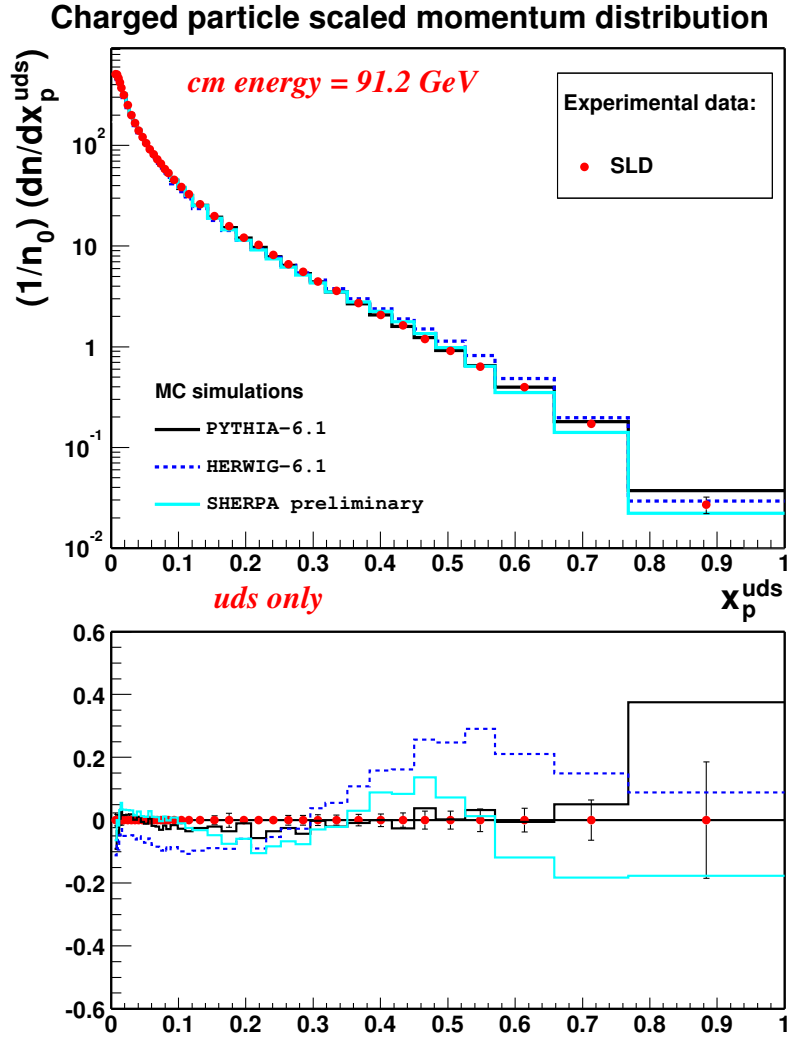
Figure 3.8: Scaled momentum distribution of charged particles for $E_{cm} = 91.2$ GeV in e^+e^- annihilation considering only the light-quark sector. The SHERPAα prediction is compared with experimental light-quark data provided by the OPAL [173] and SLD [177] collaborations. The total uncertainties are represented by vertical error bars, whereas the horizontal lines attached to the OPAL data points indicate the x_p^{uds} range for the corresponding measurement. Also shown are the outcomes of PYTHIA 6.1(uds) and HERWIG 6.1(uds) in their default settings. Concerning the mean value $\langle x_p^{uds} \rangle$ of the distributions, only the HERWIG 6.1(uds) prediction is consistent with the OPAL measurement of $\langle x_p^{uds} \rangle = 0.0630 \pm 0.0003$ (stat.) ± 0.0011 (syst.) [173]. As before, the lower part of the plot represents the normalized difference, however, the PYTHIA 6.1(uds) prediction is now used as the reference curve.
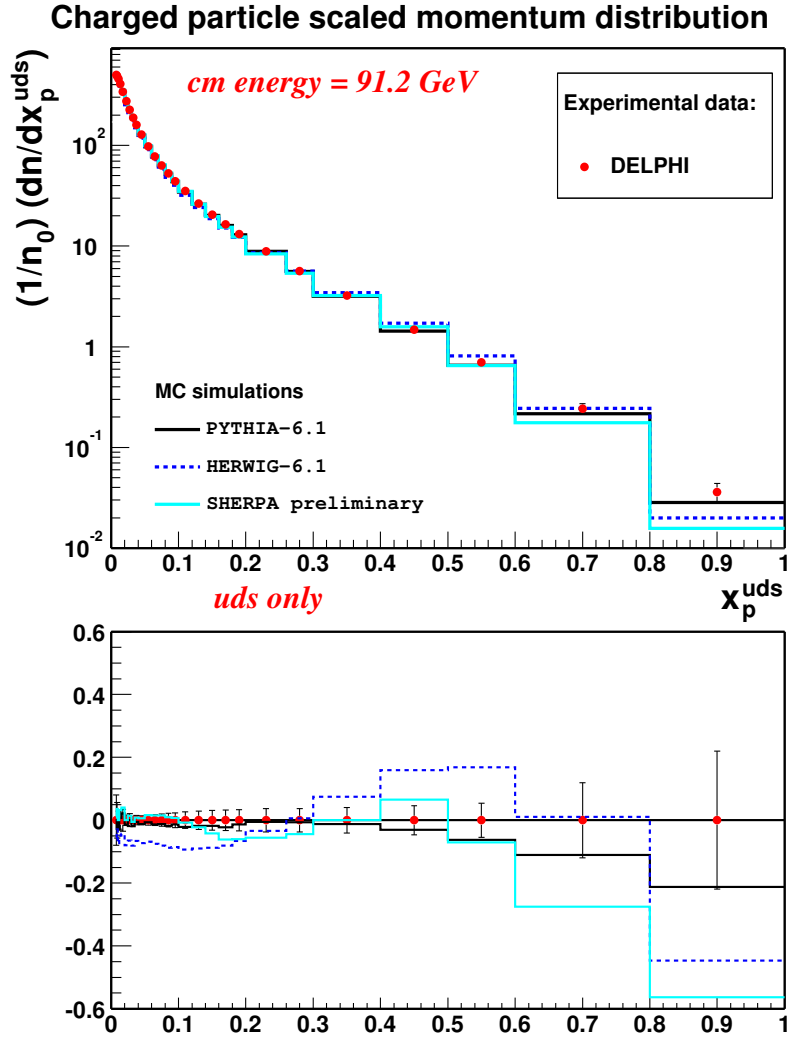
Figure 3.9:   Scaled momentum distribution of charged particles for E_{cm} = 91.2 GeV in electron–positron annihilation considering only the light-quark sector. The SHERPAα prediction is compared with experimental light-quark data provided by the DELPHI collaboration [175]. The total uncertainties are shown by vertical lines. Also included are the predictions of default PYTHIA 6.1(uds) and default HERWIG 6.1(uds). The lower part of the plot again represents the normalized difference between the Monte Carlo models and the data.

cluster approaches. In comparison with the HERWIG 6.1(uds) prediction (see fig. 3.9 and fig. 3.10), the new model yields, however, a smaller bump, and the values for $x_p^{uds} > 0.7$ show a softer decline, i.e. do not fall off as rapidly as the HERWIG 6.1(uds) ones.[9] This slightly better performance might be gained due to the mass-categorization treatment of the cluster transitions, which has been introduced in the new model.

---

[9]Contrary to the old FORTRAN HERWIG, newly published HERWIG++ results on the topic show an improved behaviour which is different to that of HERWIG 6.1(uds) [19].

Figure 3.10:   Scaled momentum distribution of charged particles for $E_{\mathrm{cm}} =$ 91.2 GeV in electron–positron annihilation considering only the light-quark sector. The SHERPAα prediction is compared with experimental light-quark data provided by the SLD collaboration [177]. The total uncertainties are shown by vertical lines. Also included are the predictions of default PYTHIA 6.1(uds) and default HERWIG 6.1(uds). The lower part of the plot again represents the normalized difference between the Monte Carlo models and the data.

All in all, the new model's x_p^{uds} behaviour clearly reflects two symptomatic cluster-model weaknesses, namely (1) that the necessary increase in cluster and, therefore, in hadron multiplicity excessively results in a decrease of large three-momenta of primary clusters, and (2) that the hadronization of events with a small number of primary clusters is not sufficiently modelled yet. Both statements can be seized more properly. In the first case this behaviour does not necessarily have to be wrong, but, surely, one has to carefully tune, in interplay with the overall mean charged-particle multiplicity, the decline towards higher x_p^{uds}. But, unfortunately, there is not only this enhanced decline. Truly a weak
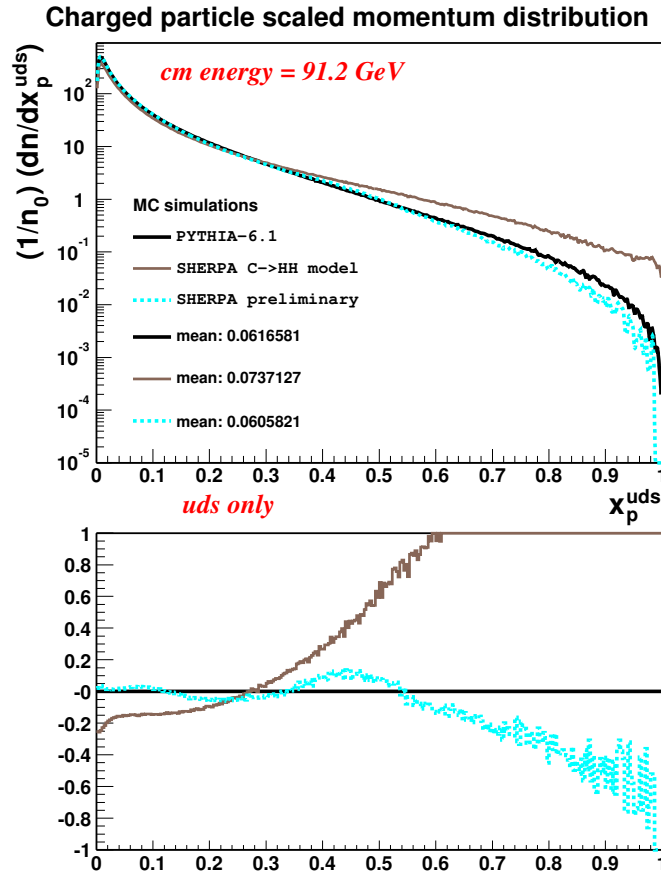
Figure 3.11: Scaled momentum distribution of charged particles for $E_{cm} =$ 91.2 GeV in electron–positron annihilation considering only the light-quark sector. The SHERPAα prediction is compared with the SHERPAα $\mathcal{C} \to \mathcal{H}\mathcal{H}$ model prediction. As the reference curve the result of default PYTHIA 6.1(uds) is included. Then, the lower part of the plot represents the normalized difference between the PYTHIA 6.1(uds) model and the SHERPAα models.

point of the cluster model is the formation of bumps in the x_p^{uds} distribution. This is a sign that the underlying fission kinematics is still not sufficiently adapted to the needs of hadronization, at least when considering the light-quark sector only. To support this statement two different scenarios have been compared and the x_p^{uds} distribution is plotted in fig. 3.11 with the reference curve obtained from PYTHIA 6.1(uds). The pure case of allowing only $\mathcal{C} \to \mathcal{H}_1\mathcal{H}_2$ breakups has been tested against the full SHERPAα model. One gets exactly the expected behaviour, the $\mathcal{C} \to \mathcal{H}_1\mathcal{H}_2$ model is much lower in multiplicity and shows a harder high-x_p^{uds} tail. But up to a small bump at very high x_p^{uds}, its corresponding distribution is free of bumps. This may lead to the conclusion that all the change in the scaled-momentum distribution comes from the cluster-decay kinematics, cf. eq. (3.11). Moreover, the formation of the hadron-level bumps may be explained as follows. In our case of light quarks the leading term for the daughter-cluster masses is the same, $M_{\mathcal{X},Y}^2 \sim Q_0 M_{\mathcal{C}} - Q_0^2$. This then advantages the emergence of quite symmetrical
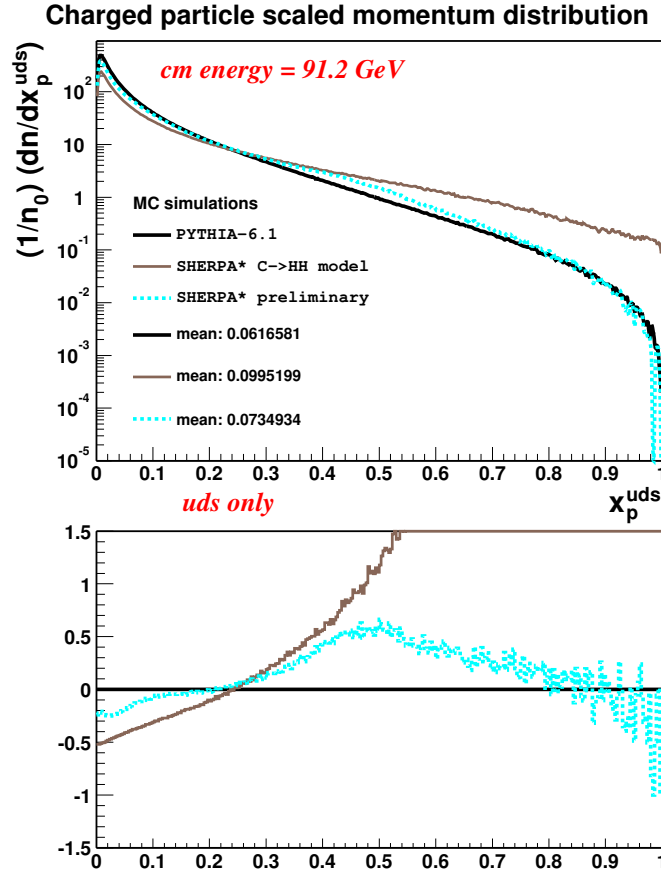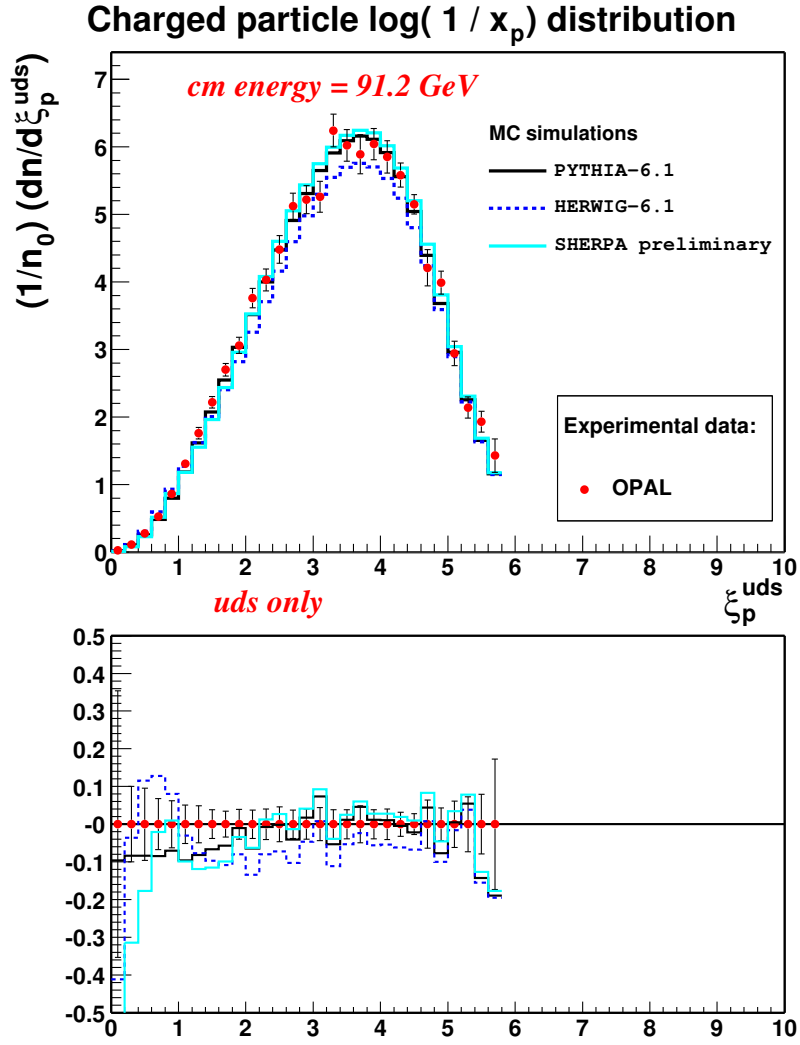
Figure 3.12:   Scaled momentum distribution of charged particles for $E_{\mathrm{cm}} = 91.2$ GeV in electron–positron annihilation for the light-quark sector only. The SHERPA$\alpha*$ prediction is compared with the SHERPA$\alpha*$ $\mathcal{C} \to \mathcal{H}\mathcal{H}$ model prediction. The "$*$" indicates that, for this analysis, only events with a primary-cluster number lower than 7 have been taken into account. The reference curve is given by the default PYTHIA 6.1(uds) outcome. The lower part of the plot represents the normalized difference between the PYTHIA 6.1(uds) model and the SHERPA$\alpha*$ models.

mass configurations for the decay products and, in turn, the $\mathcal{C} \to \mathcal{C}_1\mathcal{C}_2$ and $\mathcal{C} \to \mathcal{H}_1\mathcal{H}_2$ breakups will appear very often. This furthermore translates into the effects that, firstly, scaled-momentum ranges emerge where the kinematics prefers to place the new momenta and, secondly, regions arise where non-purely hadronic decays are very suppressed and therefore the x_p^{uds} behaviour tries to follow the one of the $\mathcal{C} \to \mathcal{H}_1\mathcal{H}_2$ model. This is quite adequately illustrated in fig. 3.12 where, for the SHERPAα model, events with a primary-cluster multiplicity lower than 7 have been explicitly considered. [10] The outcome of this plot clearly puts emphasis on the second statement that especially for events with a low multiplicity in primary clusters the cluster hadronization is still problematic. Taken together, the main problem is the somewhat deficient interplay of the cluster-decay kinematics with the purely isotropic one taken to manage the $\mathcal{C} \to \mathcal{H}_1\mathcal{H}_2$ transitions. In

---

[10]This coincides with the peak position of the primary-cluster multiplicity distribution.

Figure 3.13: $\xi_p^{uds} = \ln(1/x_p^{uds})$ distribution of charged particles for $E_{\mathrm{cm}} = 91.2$ GeV in electron–positron annihilation, considering the light-quark sector only. The SHERPAα prediction is presented together with experimental *uds* data provided by the OPAL collaboration [173], and with results from default PYTHIA 6.1(*uds*) and default HERWIG 6.1(*uds*). The total uncertainties are shown by vertical error bars. The lower part of the plot visualizes the normalized difference between the Monte Carlo simulations and the data.

conclusion, the "decline problem" may be tuned away through carefully tuning the perturbative and non-perturbative parameters simultaneously, whereas the "bump problem" implies to introduce corrections to the cluster-decay kinematics.

In contrast to the x_p^{uds} distribution, the ξ_p^{uds} distribution emphasizes the soft momenta of the spectrum. Fig. 3.13 illuminates the SHERPAα result together with those of the other two QCD Monte Carlo models, and compares them with experimental measurements from the OPAL collaboration [173]. PYTHIA 6.1(*uds*) describes the data over the full ξ_p^{uds} region. Except for the first three data points (the region of hard momenta), SHERPAα can also

reasonably describe the data and is comparable to the PYTHIA 6.1(uds) prediction. It slightly underestimates the region of $1.0 < \xi_p^{uds} < 2.0$. HERWIG 6.1(uds) is low (high) for $2.0 < \xi_p^{uds} < 5.0$ ($0.4 < \xi_p^{uds} < 1.0$). The outcomes of the three Monte Carlo simulations all reproduce a peak position of $\xi_{p,\mathrm{MC}}^{*,uds} = 3.7 \pm 0.1$, which reasonably coincides with the experimental inclusive measurements of the peak position, $\xi_p^{*,uds} = 3.76 \pm 0.02$ (DELPHI [175]) and $\xi_p^{*,uds} = 3.74 \pm 0.22$ (OPAL [173]).

As an example for the group of event-shape observables, the $1 - T^{uds}$ distribution – with T^{uds} being the thrust – of the three aforementioned QCD Monte Carlo event generators with u, d, s quark restriction is presented in fig. 3.14 for light-quark and gluon jets. HERWIG 6.1(uds) accounts on average for more spherical event shapes, which is indicated by a softer decline of the spectrum towards higher values. The SHERPAα prediction, somewhat exceeding the PYTHIA 6.1(uds) result for $0.1 < 1 - T^{uds} < 0.3$, rather resembles the prediction of PYTHIA 6.1(uds), which, owing to the LPHD concept, might be due to the fact that SHERPAα employs a PYTHIA like parton shower.

Lastly the Durham $3 \to 2$ differential jet rate is considered in fig. 3.15. Except for the low-statistics region, the results for the event generators shown in the plot barely exhibit any deviation from one another.

Taken together, the first experiences with the performance of SHERPAα are promising. Reasonable agreement could be achieved in comparisons with PYTHIA 6.1 restricted onto the light-quark sector and, where provided, with experimental data for electron–positron annihilation into light-quark and gluon jets at the Z^0 pole. Keeping in mind that the model has not been extensively tuned, the outcomes have been very encouraging.

3.6 Conclusions

A modified cluster-hadronization model has been presented, modified w.r.t. the long-standing Webber model; the extensions of this approach are the following.

Soft colour-reconnection effects have been included in the cluster formation as well as in the cluster-decay processes. This yields an enhancement of the number of decay configurations. The spin of diquarks has been explicitly accounted for throughout the model. The number of basic cluster species has been enlarged, especially by a new mesonic-cluster type, the four-quark cluster. The significant feature of this approach is the flavour-dependent separation of the cluster and hadron regimes in terms of the mother cluster's mass. This categorization automatically selects the cluster-transition mode. Taken together, these aspects require the set-up of generically new cluster decay channels.

As a case study, this cluster-hadronization model was implemented as a `C++` code. The resulting version has been shown capable of describing electron–positron annihilation $e^+e^- \to \gamma^*/Z^0 \to d\bar{d}, u\bar{u}, s\bar{s}$ into light-quark and gluon jets. Some first tests were passed (see previous section) and the agreement with PYTHIA 6.1(uds) and experimental data is satisfactory. Some cluster-model shortcomings, such as the too low charged-particle multiplicity, could be cured; and the spectrum of the scaled momentum could be improved. The model serves as the starting point for and basis of a more complete model including heavy-quark hadronization. This extended version will be used in the SHERPA event generator.
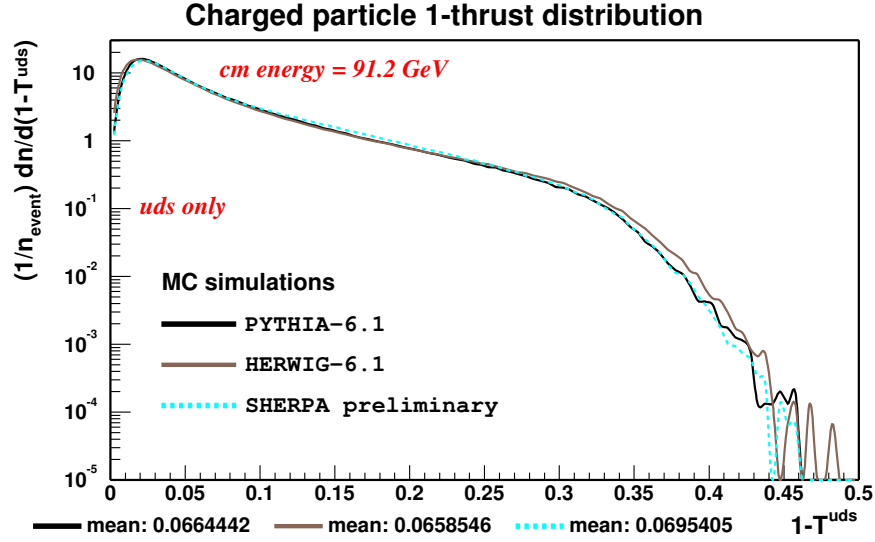
Figure 3.14: $1-T^{uds}$ distribution of charged particles for $E_{\text{cm}} = 91.2$ GeV in e^+e^- annihilation with a restriction on u, d, s and gluon jets. The SHERPAα prediction is compared with predictions of default PYTHIA 6.1(uds) and HERWIG 6.1(uds).
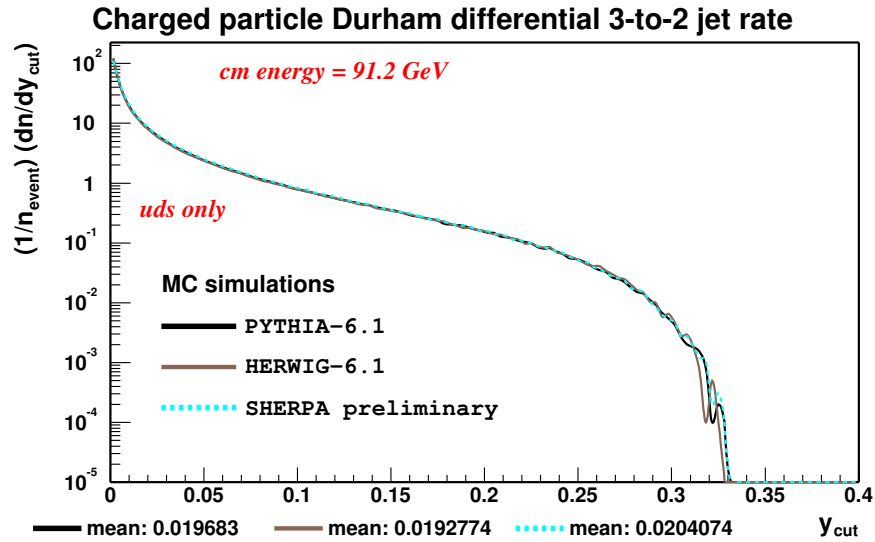
Figure 3.15: The Durham $3 \rightarrow 2$ differential jet rate of charged particles in electron–positron annihilation at the Z^0 pole. Only uds events are taken into account. The SHERPAα result is compared with the results stemming from PYTHIA 6.1(uds) and HERWIG 6.1(uds) performances, both of which run with their default parameters.

4   Summary

This thesis dealt with a number of different aspects as they appear in QCD jet physics at high and low energy scales. QCD dynamics with its basic properties of asymptotic freedom at high scales and multiple parton production and confinement at low scales determines the production, evolution and hadronization of the jets, and different approaches can be used to describe the main physics features in these different domains.

The phenomenological studies presented in the first chapter of this thesis all addressed the aspect of jet production, in conjunction with an improved description of combining it with the subsequent (softer) intra-jet evolution. With these studies the further validation and verification of the CKKW merging procedure as implemented in the event generator SHERPA have been accomplished. The procedure has proven to work successfully in comparison with a variety of predictions made by other merging schemes, as well as, with analytic higher-order calculations and other Monte Carlo tools all aiming at the simulation of additional QCD radiation to production processes that are and will be of enormous relevance for the current and new hadron colliders. The CKKW algorithm correctly merges tree-level matrix elements with the parton shower at leading logarithmic accuracy, with the former constituting the best means to calculate the production of jets, and the latter to handle their evolution. However, in both descriptions the leading logarithms associated to each single emission are encountered and potentially double counted when naively combining the two different calculations. This exactly is avoided by the CKKW approach, such that the good features of both calculations will survive and an improved (leading-order) description of hard multijet configurations together with jet fragmentation is achieved. The studies for validating CKKW thereby triggered refinements of the implementation of the algorithm in SHERPA. The outcomes of the analyses for W+jets and WW+jets, accomplished in the framework of this thesis, clearly have shown the importance of incorporating QCD corrections provided by real-emission matrix elements and, thus, to account for high transverse momenta of jets and correct jet–jet correlations. This cannot be achieved by the sole use of parton showers and, therefore, is of large interest for the experimental analyses to better understand their data and gain good handle of the QCD backgrounds present in all production processes. Therefore, it is fair to conclude that the phenomenological studies of this thesis contributed to the improvement of the event generator SHERPA, which, equipped with its implementation of the CKKW approach, adds valuable contributions to the frontier of current research.

In the second part of this thesis proposals have been presented for new models in describing (1) multiple soft and collinear QCD emission and (2) the hadronization of jets, phenomenologically. Moreover, in the context of Monte Carlo event generation, the models not only have been suggested but also implemented and proven to yield very encouraging results.

The first model is a fully perturbative formulation of a colour-dipole shower in particular for hadronic collisions. Certainly inspired by the colour-dipole model developed by the Lund group, it handles QCD radiation in the initial state of scattering processes in a completely different way, namely in a backward-evolution process involving the parton density functions as in conventional parton showers. In this way, it needs no assumptions of non-perturbative origin and constitutes an unambiguous and clear perturbative approach to multiparton emission in terms of colour dipoles. In contrast to the traditional parton-shower models, which in first approximation resum the leading logarithms associated to the collinear emergence of secondary partons, here, it is the soft limit of QCD radiation that plays the major rôle in the exponentiation of single parton emissions and therefore gives an interesting alternative in constructing the radiation pattern of QCD bremsstrahlung. Owing to its clear formulation in terms of perturbative dipoles and their associated dipole splittings functions, the model features characteristics close to the counterterms used in antenna subtraction methods, it, therefore, seems to have potential in constituting a natural partner to NLO QCD calculations, based on antenna factorization, in the scope of matching them with Monte Carlo showers. The first results that have been obtained with this dipole shower are in very good agreement with existing data of lepton and hadron colliders, and also, predictions made by SHERPA. Additionally, the fact that in this thesis for the first time inclusive QCD jet production at hadron colliders has been simulated with a colour-dipole shower allows the emphasis of a very successful outcome of this work.

The second model presented in this thesis is a phenomenological scheme for cluster hadronization containing a good fraction of modifications w.r.t. the well-established Webber model. It triggered a completely independent first implementation of the new ideas within the event generator SHERPA for the case study of electroweakly produced hadronically decaying vector bosons at the Z^0 pole, certainly a very suitable testbed for the validation of the hadronization corrections induced by the model to perturbative predictions. The model has proven to yield reliable results, where the number of modifications manifests itself in an improvement in the description of LEP data. Therefore, it has been taken to form the basis for the construction of an independent cluster-hadronization model for the event generator SHERPA.

Altogether the work of this thesis reflects the great progress recently achieved in jet physics, addressing questions of current relevance concerning all phases in the description of jets, in particular in the context of Monte Carlo event generation. With the crucial assessment of the CKKW algorithm, the development of a new dipole shower and the preparation of a modified cluster-hadronization model, the accomplishments here contribute to the improvement and extension of the Monte Carlo event generator SHERPA, more than ever rendering it a powerful tool capable of tackling the new challenges of the upcoming experiments at the LHC.

Acknowledgements

Appendix A LHC rates

Here, a number of tables has been collected presenting more results that have been achieved during the comparative study on merging-, factorization- and renormalization-scale variations, with the details in the respective captions of the tables.

The tables clearly show the impact of changing both factorization *and* renormalization scale and, thus, hint at the necessity of varying both in order to obtain a conservative estimate of the theoretical uncertainty. In particular this becomes important, since there is a tendency of the two scales to work in opposite directions.

The tables, tabs. A.1–A.8, are given below.

Code	$\sigma[\text{tot}]$	$\sigma[\geq 1\ \text{jet}]$	$\sigma[\geq 2\ \text{jet}]$	$\sigma[\geq 3\ \text{jet}]$	$\sigma[\geq 4\ \text{jet}]$
ALPGEN, def	**10170**	**2100**	**590**	**171**	**50**
ALpt30	10290	2200	555	155	46
ALpt40	10280	2190	513	136	41
ALpt60	10140	2030	403	93	28
ALscL	10590	2520	790	252	79
ALscH	9870	1810	455	121	33
SHERPA, def	**8803**	**2130**	**574**	**151**	**41**
SHkt15	8840	2260	642	175	45
SHkt30	8970	2020	481	120	32
SHkt40	9200	1940	436	98.5	24
SHkt60	9650	1990	431	86.8	19
SHscL	7480	2150	675	205	58
SHscH	10110	2080	489	118	30
SHasL	9095	2366	677	190	53.2
SHasH	8597	1924	486	122	32.1
SHinL	7208	1918	552	156	43.1
SHinH	10347	2310	584	148	39.3

Table A.1: Cross sections (in pb) for the inclusive jet rates at the LHC, according to the default and alternative settings of the various codes. SHas gives the results for varying in SHERPA the renormalization scales only, in contrast, SHin labels the outcomes when doing a standard variation in the defaults taken for the PDF scales.

Code	$\sigma^{[\geq 1]}/\sigma^{[tot]}$	$\sigma^{[\geq 2]}/\sigma^{[\geq 1]}$	$\sigma^{[\geq 3]}/\sigma^{[\geq 2]}$	$\sigma^{[\geq 4]}/\sigma^{[\geq 3]}$
ALPGEN, def	0.21	0.28	0.29	0.29
ALpt30	0.21	0.25	0.28	0.30
ALpt40	0.21	0.23	0.27	0.30
ALpt60	0.20	0.20	0.23	0.30
ALscL	0.24	0.31	0.32	0.31
ALscH	0.18	0.25	0.27	0.27
SHERPA, def	0.24	0.27	0.26	0.27
SHkt15	0.26	0.28	0.27	0.26
SHkt30	0.23	0.24	0.25	0.27
SHkt40	0.21	0.22	0.23	0.24
SHkt60	0.21	0.22	0.20	0.22
SHscL	0.29	0.31	0.30	0.28
SHscH	0.21	0.24	0.24	0.25
SHasL	0.260	0.286	0.281	0.280
SHasH	0.224	0.253	0.251	0.263
SHinL	0.266	0.288	0.283	0.276
SHinH	0.223	0.253	0.253	0.266

Table A.2: Cross-section ratios for $(n+1)/n$ inclusive jet rates at the LHC, according to the default and alternative settings of the various codes. SHas gives the results for varying in SHERPA the renormalization scales only, in contrast, SHin labels the outcomes when doing a standard variation in the defaults taken for the PDF scales.

$W^+ + n$ jets	$\sigma_{n=0}$ [pb]	$\sigma_{n=1}$ [pb]	$\sigma_{n=2}$ [pb]
$\mu_{\mathrm{F}} = \mu_{\mathrm{R}} = M_W$	11961.5 ± 12.2	3491.1 ± 15.7	1342.5 ± 36.8
$\mu_{\mathrm{F}} = \mu_{\mathrm{R}} = M_T^{(W)}$	11960.1 ± 12.3	3501.8 ± 16.3	1430.4 ± 33.1
$\mu_{\mathrm{F}} = \mu_{\mathrm{R}} = M_W/4$	11122.9 ± 10.2	3947.3 ± 22.3	1969.7 ± 66.1
$\mu_{\mathrm{F}} = \mu_{\mathrm{R}} = 2M_W$	12309.8 ± 13.4	3365.1 ± 13.0	1320.9 ± 35.1
$\mu_{\mathrm{F}} = 2M_W, \mu_{\mathrm{R}} = M_W/4$	12518.8 ± 17.0	4072.9 ± 23.3	1297.3 ± 25.0

Table A.3: Inclusive total cross sections for $W^+ + 0,1,2$ jets at NLO at the LHC, obtained with MCFM and different scale settings. In all cases, the CTEQ6M parton distribution has been used, and jets have been defined through a k_T algorithm with $k_{T,0} = 20$ GeV and $D = 1$. Additional cuts: $|\eta_{j,\ell}| < 5$, $R_{j\ell} = 0.4$, $p_T^\ell > 5$ GeV.

$W^+ + n$ jets	$\sigma_{n=1}/\sigma_{n=0}$	$\sigma_{n=2}/\sigma_{n=1}$
$\mu_{\mathrm{F}} = \mu_{\mathrm{R}} = M_W$	0.291	0.385
$\mu_{\mathrm{F}} = \mu_{\mathrm{R}} = M_T^{(W)}$	0.292	0.408
$\mu_{\mathrm{F}} = \mu_{\mathrm{R}} = M_W/4$	0.355	0.499
$\mu_{\mathrm{F}} = \mu_{\mathrm{R}} = 2M_W$	0.273	0.392
$\mu_{\mathrm{F}} = 2M_W, \mu_{\mathrm{R}} = M_W/4$	0.325	0.319

Table A.4: Ratios of inclusive total cross sections at NLO at the LHC, obtained with MCFM and different scale settings. In all cases, the CTEQ6M parton distribution has been used, and jets have been defined through a k_T algorithm with $k_{T,0} = 20$ GeV and $D = 1$. Additional cuts: $|\eta_{j,\ell}| < 5$, $R_{j\ell} = 0.4$, $p_T^\ell > 5$ GeV.

$W^+ + n$ jets	$\sigma_{n=0}$ [pb]	$\sigma_{n=1}$ [pb]	$\sigma_{n=2}$ [pb]
$\mu_{\mathrm{F}} = \mu_{\mathrm{R}} = M_W$	11960.2 ± 12.3	3439.3 ± 15.3	1298.2 ± 35.6
$\mu_{\mathrm{F}} = \mu_{\mathrm{R}} = M_T^{(W)}$	11960.1 ± 12.3	3436.1 ± 19.1	1337.1 ± 36.6
$\mu_{\mathrm{F}} = \mu_{\mathrm{R}} = M_W/4$	11123.0 ± 10.2	3892.4 ± 23.0	1498.5 ± 114.6
$\mu_{\mathrm{F}} = \mu_{\mathrm{R}} = 2M_W$	12308.5 ± 13.4	3311.2 ± 15.6	1297.0 ± 41.3
$\mu_{\mathrm{F}} = 2M_W, \mu_{\mathrm{R}} = M_W/4$	12518.8 ± 17.0	3988.7 ± 29.0	1641.4 ± 80.4

Table A.5: Inclusive total cross sections for $W^+ + 0,1,2$ jets at NLO at the LHC, obtained with MCFM and different scale settings. In all cases, the CTEQ6M parton distribution has been used, and jets have been defined through a cone algorithm with $E_{T,0} = 20$ GeV and $R = 0.4$. Additional cuts: $|\eta_j| < 4.5$.

$W^+ + n$ jets	$\sigma_{n=1}/\sigma_{n=0}$	$\sigma_{n=2}/\sigma_{n=1}$
$\mu_{\mathrm{F}} = \mu_{\mathrm{R}} = M_W$	0.286	0.377
$\mu_{\mathrm{F}} = \mu_{\mathrm{R}} = M_T^{(W)}$	0.287	0.389
$\mu_{\mathrm{F}} = \mu_{\mathrm{R}} = M_W/4$	0.350	0.385
$\mu_{\mathrm{F}} = \mu_{\mathrm{R}} = 2M_W$	0.267	0.392
$\mu_{\mathrm{F}} = 2M_W, \mu_{\mathrm{R}} = M_W/4$	0.318	0.412

Table A.6: Ratios of inclusive total cross sections at NLO at the LHC, obtained with MCFM and different scale settings. In all cases, the CTEQ6M parton distribution has been used, and jets have been defined through a cone algorithm with $E_{T,0} = 20$ GeV and $R = 0.4$. Additional cuts: $|\eta_j| < 4.5$.

Scale choice (lin)	σ[tot]	jf	$\sigma[\geq 1$ jet]	$\sigma[\geq 2$ jet]	$\sigma[\geq 3$ jet]	$\sigma[\geq 4$ jet]
$f = 1/4, r = 1/4$	**5949**	kt1	**2340 (0.393)**	**1087 (0.465)**	416 (0.383)	88.0 (0.212)
	[6049]	kt.4	2113	924	350	87.4
		cn1	2279	1026	379	76.7
		cn.4	2030	851	310	74.4
$f = 1/2, r = 1/2$	7511	kt1	2527 (0.336)	996 (0.394)	334 (0.335)	74.9 (0.224)
	[7631]	kt.4	2076	746	246	61.7
		cn1	2405	914	294	61.2
		cn.4	1952	671	210	49.5
$f = 1/2, r = 1$	7289	kt1	2175 (0.298)	782 (0.360)	247 (0.316)	50.5 (0.204)
	[7409]	kt.4	1829	612	194	47.1
		cn1	2090	728	221	42.6
		cn.4	1735	556	168	38.1
$f = 1/2, r = 2$	7089	kt1	1904 (0.269)	638 (0.335)	193 (0.303)	36.7 (0.190)
	[7207]	kt.4	1630	516	158	35.5
		cn1	1840	598	175	30.9
		cn.4	1559	470	137	29.6
$f = 1, r = 1/2$	9261	kt1	2892 (0.312)	1051 (0.363)	332 (0.316)	69.8 (0.210)
	[9411]	kt.4	2346	774	241	59.0
		cn1	2757	960	295	57.8
		cn.4	2203	695	207	47.4
$f = 1, r = 1$	**9019**	kt1	**2493 (0.276)**	**826 (0.331)**	240 (0.291)	47.8 (0.199)
	[9166]	kt.4	2086	640	189	43.8
		cn1	2400	768	217	40.8
		cn.4	1975	582	163	35.0
$f = 1, r = 2$	8808	kt1	2201 (0.250)	672 (0.305)	187 (0.278)	32.8 (0.175)
	[8956]	kt.4	1871	539	153	33.0
		cn1	2131	629	168	28.1
		cn.4	1784	493	134	27.4

Table A.7: Cross sections (in pb) and ratios of inclusive jet rates at the LHC for different scale choices (using the prefactors f and r for factorization and renormalization scales, respectively). The CTEQ6M parton distribution has been used, jets are either defined through a k_T algorithm (kt) with $k_{T,0} = 20$ GeV and $D = 1$ or $D = 0.4$, or through a cone algorithm (cn) with $E_{T,0} = 20$ GeV and $R = 1$ or $R = 0.4$. Additional cuts have been applied: $|\eta_{j,e}| < 5$, $R_{j,e} = 0.4$, $p_T^e > 5$ GeV. The total cross section given in square brackets is without lepton cuts.

Scale choice (lin)	$\sigma[\text{tot}]$	jf	$\sigma[\geq 1\ \text{jet}]$	$\sigma[\geq 2\ \text{jet}]$	$\sigma[\geq 3\ \text{jet}]$	$\sigma[\geq 4\ \text{jet}]$
$f=2, r=1/4$	**11297**	kt1	**3602 (0.319)**	**1302 (0.361)**	413 (0.317)	71.6 (0.173)
	[11482]	kt.4	3169	1082	345	71.2
		cn1	3515	1240	380	61.3
		cn.4	3030	996	304	58.6
$f=2, r=1/2$	10919	kt1	3202 (0.293)	1100 (0.344)	330 (0.300)	65.6 (0.199)
	[11094]	kt.4	2570	804	235	55.8
		cn1	3057	1006	290	53.5
		cn.4	2414	714	200	44.3
$f=2, r=1$	10644	kt1	2748 (0.258)	852 (0.310)	237 (0.278)	43.4 (0.183)
	[10815]	kt.4	2286	656	181	39.8
		cn1	2644	794	211	36.6
		cn.4	2160	595	156	32.2
$f=2, r=2$	**10432**	kt1	**2423 (0.232)**	**689 (0.284)**	181 (0.263)	31.2 (0.172)
	[10606]	kt.4	2047	550	148	29.9
		cn1	2345	648	163	26.7
		cn.4	1947	500	129	24.7
$f=4, r=4$	11704	kt1	2336 (0.200)	583 (0.250)	138 (0.237)	20.4 (0.148)
	[11898]	kt.4	1986	475	117	22.3
		cn1	2275	550	125	17.9
		cn.4	1903	436	102	18.0

Table A.8: Cross sections (in pb) and ratios of inclusive jet rates at the LHC for different scale choices (using the prefactors f and r for factorization and renormalization scales, respectively). The CTEQ6M parton distribution has been used, jets are either defined through a k_T algorithm (kt) with $k_{T,0} = 20$ GeV and $D = 1$ or $D = 0.4$, or through a cone algorithm (cn) with $E_{T,0} = 20$ GeV and $R = 1$ or $R = 0.4$. Additional cuts have been applied: $|\eta_{j,e}| < 5$, $R_{j,e} = 0.4$, $p_T^e > 5$ GeV. The total cross section given in square brackets is without lepton cuts.

Appendix B   Parameters of the diboson CKKW study

B.1   Input parameters of SHERPA

All SHERPA studies have been carried out with the CTEQ6L PDF set [125]. The value of α_s has been chosen according to the corresponding value of the selected PDF, namely $\alpha_s = 0.118$. The running of the strong coupling constant is determined by the corresponding two-loop equation, except for the SHERPA `MCFM` comparison. There an one-loop running has been employed for α_s. Jets or initial partons are defined by gluons and all quarks but the top quark; this one is allowed to appear within the matrix elements only through the coupling of the W boson with the b quark. In the SHERPA `MCFM` comparison SHERPA runs, however are restricted to the light-flavour sector, i.e. the g, d, u, s, c sector. In the matrix element calculation the quarks are taken massless, only the shower will attach current masses to them. The shower cut-offs applied are 2 GeV and 1 GeV for the initial and the final state emissions, respectively. If explicitly stated a primordial k_T Gaussian smearing has been employed with both, mean and standard deviation being equal to 0.8 GeV. The Standard Model input parameters are:

$$
\begin{aligned}
&m_W = 80.419 \text{ GeV} , \quad \Gamma_W = 2.06 \text{ GeV}, \\
&m_Z = 91.188 \text{ GeV} , \quad \Gamma_Z = 2.49 \text{ GeV}, \\
&G_\mu = 1.16639 \times 10^{-5} \text{ GeV}^{-2}, \\
&\sin^2 \theta_W = 1 - m_W^2 / m_Z^2, \\
&\alpha_s = 0.118.
\end{aligned}
\tag{B.1}
$$

The electromagnetic coupling is derived from the Fermi constant G_μ according to

$$
\alpha_{\text{em}} = \frac{\sqrt{2}\, G_\mu\, M_W^2\, \sin^2 \theta_W}{\pi} .
\tag{B.2}
$$

The constant widths of the electroweak gauge bosons are introduced through the fixed-width scheme. The CKM matrix has been always taken diagonal.

B.2   Setups for MCFM, MC@NLO and PYTHIA

MCFM

The program version employed is `MCFM v4.0`. The process chosen is `nproc=61`. The investigations have been restricted to the d, u, s, c quark sector. The PDF set used is

CTEQ6L. The default scheme for defining the electroweak couplings has been used and their input values have been adjusted with the corresponding parameter settings given for SHERPA. The renormalization scale and the factorization scale are fixed and set to $\mu_\mathrm{R} = \mu_\mathrm{F} = M_W$.

MC@NLO

The program version used is `MC@NLO 2.31`. The process number is taken as `IPROC=-12850`, so that the underlying event has not been taken into consideration. The two W boson decays into leptons are steered by the two `MODBOS` variables being set to `2` and `3` for the first and the second choice, respectively. The lepton pairs have been generated in a mass window of

$$M_W - 40\,\Gamma_W < m_{l\nu} < M_W + 40\,\Gamma_W \,. \tag{B.3}$$

Again, the CTEQ6L PDF set as provided by `MC@NLO`'s own PDF library is used. The weak gauge boson masses and widths are aligned to the settings used for the previous codes. All other parameters have been left unchanged with respect to their defaults.

PYTHIA

The PYTHIA version used is version 6.214. The process $p\bar{p} \to W^+W^- + X$ is selected through `MSUB(25)=1`. The specific decay modes of the two W's are picked by putting `MDME(206,1)=2` and `MDME(207,1)=3`, where all other available modes are set to zero. The possibility of parton shower emissions right up to the limit, which has been proven to be more convenient for jet production [182], is achieved with `MSTP(68)=2`. This increases the IS shower start scale in PYTHIA to $\sqrt{s} = 1960$ GeV and accounts for a reasonably higher amount of hard QCD radiation. For all comparisons here, the underlying event is switched off, other parameters are left to their default.

B.3   Phase-space cuts

Two different analyses are used for the comparisons of the results obtained throughout this publication. A simple analysis has been taken to verify the pure behaviour of the considered programs. For this case, only jets are analysed utilizing the Run II k_T clustering algorithm defined in [62] with a pseudo-cone size of $R = 1$. The jet transverse momentum has to be greater than 15 GeV.

For more realistic experimental scenarios, an analysis applying jet and lepton cuts has been availed. Then, the pseudo-cone size of the jet algorithm has been set to $R = 0.7$, and the jets have to fulfil the following constraints on the pseudo-rapidity and the transverse momentum,

$$|\eta^{\mathrm{jet}}| < 2.0\,, \quad p_T^{\mathrm{jet}} > 15 \text{ GeV}\,. \tag{B.4}$$

For the charged leptons the cuts on these observables are given by

$$|\eta^{\mathrm{lep}}| < 1.0\,, \quad p_T^{\mathrm{lep}} > 20 \text{ GeV}\,, \tag{B.5}$$

however, a cut on the missing transverse energy has not been introduced. There is a final selection criteria corresponding to the separation of the leptons from each other and from the jets,

$$\Delta R_{\ell\ell} > 0.2\,, \quad \Delta R_{\ell j} > 0.4 \quad .\tag{B.6}$$

Bibliography

[1] Y. L. Dokshitzer, V. A. Khoze, A. H. Mueller and S. I. Troian. Gif-sur-Yvette, France: Ed. Frontieres (1991) 274 p. (Basics of).

[2] R. K. Ellis, W. J. Stirling and B. R. Webber *Camb. Monogr. Part. Phys. Nucl. Phys. Cosmol.* **8** (1996) 1–435.

[3] B. Andersson *Camb. Monogr. Part. Phys. Nucl. Phys. Cosmol.* **7** (1997) 1–471.

[4] T. Sjostrand *Comput. Phys. Commun.* **82** (1994) 74–90.

[5] T. Sjostrand, S. Mrenna and P. Skands *JHEP* **05** (2006) 026 [`hep-ph/0603175`].

[6] T. Sjöstrand *et. al. Comput. Phys. Commun.* **135** (2001) 238–259 [`arXiv:hep-ph/0010017`].

[7] T. Sjöstrand, L. Lonnblad and S. Mrenna `hep-ph/0108264`.

[8] T. Sjöstrand, L. Lönnblad, S. Mrenna and P. Skands `hep-ph/0308153`.

[9] G. Corcella *et. al. JHEP* **01** (2001) 010 [`http://arXiv.org/abs/hep-ph/0011363`].

[10] G. Corcella *et. al.* `hep-ph/0210213`.

[11] L. Lönnblad *Comput. Phys. Commun.* **71** (1992) 15–31.

[12] T. Sjostrand *Phys. Lett.* **B157** (1985) 321.

[13] M. Bengtsson, T. Sjostrand and M. van Zijl *Z. Phys.* **C32** (1986) 67.

[14] H.-U. Bengtsson and T. Sjostrand *Comput. Phys. Commun.* **46** (1987) 43.

[15] G. Marchesini and B. R. Webber *Nucl. Phys.* **B310** (1988) 461.

[16] G. Gustafson *Phys. Lett.* **B175** (1986) 453.

[17] G. Gustafson and U. Pettersson *Nucl. Phys.* **B306** (1988) 746.

[18] B. Andersson, G. Gustafson and L. Lonnblad *Nucl. Phys.* **B339** (1990) 393–406.

[19] S. Gieseke, A. Ribon, M. H. Seymour, P. Stephens and B. Webber *JHEP* **02** (2004) 005 [`hep-ph/0311208`].

[20] S. Gieseke *et. al.* `hep-ph/0609306`.

[21] L. Lonnblad. Prepared for 14th International Workshop on Deep Inelastic Scattering (DIS 2006), Tsukuba, Japan, 20-24 Apr 2006.

[22] T. Sjostrand and P. Z. Skands *Eur. Phys. J.* **C39** (2005) 129–154 [`hep-ph/0408302`].

[23] S. Gieseke, P. Stephens and B. Webber *JHEP* **12** (2003) 045 [`hep-ph/0310083`].

[24] Z. Nagy and D. E. Soper *JHEP* **10** (2005) 024 [`hep-ph/0503053`].

[25] Z. Nagy and D. E. Soper `hep-ph/0601021`.

[26] M. Dinsdale, M. Ternick and S. Weinzierl `arXiv:0709.1026 [hep-ph]`.

[27] S. Schumann and F. Krauss `arXiv:0709.1027 [hep-ph]`.

[28] W. T. Giele, D. A. Kosower and P. Z. Skands `arXiv:0707.3652 [hep-ph]`.

[29] D. A. Kosower *Phys. Rev.* **D57** (1998) 5410–5416 [`hep-ph/9710213`].

[30] A. Gehrmann-De Ridder, T. Gehrmann and E. W. N. Glover *JHEP* **09** (2005) 056 [`hep-ph/0505111`].

[31] S. Frixione and B. R. Webber *JHEP* **06** (2002) 029 [`hep-ph/0204244`].

[32] S. Frixione, P. Nason and B. R. Webber *JHEP* **08** (2003) 007 [`hep-ph/0305252`].

[33] P. Nason. Prepared for 14th International Workshop on Deep Inelastic Scattering (DIS 2006), Tsukuba, Japan, 20-24 Apr 2006.

[34] S. Frixione, P. Nason and C. Oleari `arXiv:0709.2092 [hep-ph]`.

[35] S. Frixione and B. R. Webber `hep-ph/0612272`.

[36] S. Catani, F. Krauss, R. Kuhn and B. R. Webber *JHEP* **0111** (2001) 063–084 [`arXiv:hep-ph/0109231`].

[37] F. Krauss *JHEP* **0208** (2002) 015–031 [`arXiv:hep-ph/0205283`].

[38] L. Lönnblad *JHEP* **05** (2002) 046 [`http://arXiv.org/abs/hep-ph/0112284`].

[39] M. L. Mangano, M. Moretti and R. Pittau *Nucl. Phys.* **B632** (2002) 343–362 [`hep-ph/0108069`].

[40] M. L. Mangano, M. Moretti, F. Piccinini and M. Treccani *JHEP* **01** (2007) 013 [`hep-ph/0611129`].

[41] T. Gleisberg, S. Höche, F. Krauss, A. Schälicke, S. Schumann and J. Winter *JHEP* **0402** (2004) 056 [`arXiv:hep-ph/0311263`].

[42] F. Krauss, A. Schälicke, S. Schumann and G. Soff *Phys. Rev.* **D70** (2004) 114009 [`hep-ph/0409106`].

[43] A. Schälicke and F. Krauss *JHEP* **07** (2005) 018 [`hep-ph/0503281`].

[44] N. Lavesson and L. Lönnblad *JHEP* **07** (2005) 054 [`hep-ph/0503293`].

[45] S. Mrenna and P. Richardson *JHEP* **05** (2004) 040 [`hep-ph/0312274`].

[46] M. L. Mangano, M. Moretti, F. Piccinini, R. Pittau and A. D. Polosa *JHEP* **07** (2003) 001 [`hep-ph/0206293`].

[47] T. Stelzer and W. F. Long *Comput. Phys. Commun.* **81** (1994) 357–371 [`hep-ph/9401258`].

[48] F. Maltoni and T. Stelzer *JHEP* **02** (2003) 027 [`hep-ph/0208156`].

[49] J. Alwall *et. al.* `arXiv:0706.2334 [hep-ph]`.

[50] A. Kanaki and C. G. Papadopoulos *Comput. Phys. Commun.* **132** (2000) 306–315 [`hep-ph/0002082`].

[51] C. G. Papadopoulos and M. Worek *Eur. Phys. J.* **C50** (2007) 843–856 [`hep-ph/0512150`].

[52] J. Alwall *et. al.* `arXiv:0706.2569 [hep-ph]`.

[53] S. Catani, Y. L. Dokshitser, M. Olsson, G. Turnock and B. R. Webber *Phys. Lett.* **B 269** (1991) 432.

[54] S. Catani, Y. L. Dokshitser and B. R. Webber *Nucl. Phys.* **B 406** (1993) 187.

[55] S. Catani, Y. L. Dokshitser and B. R. Webber *Phys. Lett.* **B 285** (1992) 291.

[56] F. Krauss, R. Kuhn and G. Soff *JHEP* **0111** (2002) 044–156 [`arXiv:hep-ph/0109036`].

[57] F. Krauss, A. Schälicke and G. Soff *Comput. Phys. Commun.* **174** (2006) 876–902 [`hep-ph/0503087`].

[58] T. Sjostrand and M. van Zijl *Phys. Rev.* **D36** (1987) 2019.

[59] S. Hoche, F. Krauss and T. Teubner `arXiv:0705.4577 [hep-ph]`.

[60] J.-C. Winter, F. Krauss and G. Soff *Eur. Phys. J.* **C36** (2004) 381–395 [`hep-ph/0311085`].

[61] F. Krauss, A. Schaelicke, S. Schumann and G. Soff *Phys. Rev.* **D72** (2005) 054017 [`hep-ph/0503280`].

[62] G. C. Blazey *et. al.* `hep-ex/0005012`.

[63] G. Gustafson and U. Pettersson *Nucl. Phys.* **B306** (1988) 746.

[64] B. Andersson, G. Gustafson and L. Lönnblad *Nucl. Phys.* **B339** (1990) 393–406.

[65] B. Andersson, G. Gustafson, L. Lönnblad and U. Pettersson *Z. Phys.* **C43** (1989) 625.

[66] L. Lönnblad *Nucl. Phys.* **B458** (1996) 215–230 [`http://arXiv.org/abs/hep-ph/9508261`].

[67] **H1** Collaboration, A. Aktas *et. al. Eur. Phys. J.* **C46** (2006) 27–42 [`hep-ex/0508055`].

[68] L. Lönnblad *Z. Phys.* **C65** (1995) 285–292.

[69] F. Caravaglios, M. L. Mangano, M. Moretti and R. Pittau *Nucl. Phys.* **B539** (1999) 215–232 [`hep-ph/9807570`].

[70] N. Brook, R. G. Waugh, T. Carli, R. Mohr and M. Sutton. Prepared for Workshop on Future Physics at HERA (Preceded by meetings 25-26 Sep 1995 and 7-9 Feb 1996 at DESY), Hamburg, Germany, 30-31 May 1996.

[71] R. Kuhn, F. Krauss, B. Ivanyi and G. Soff *Comput. Phys. Commun.* **134** (2001) 223–266 [`hep-ph/0004270`].

[72] C. Åberg, "Correcting the colour dipole cascade with fixed order matrix elements in deep inelastic scattering." Diploma thesis, Lund preprint LU-TP 04-25.

[73] **D0** Collaboration, B. Abbott *et. al. Phys. Rev. Lett.* **80** (1998) 442–447 [`hep-ex/9708005`].

[74] **CDF** Collaboration, F. Abe *et. al. Phys. Rev. Lett.* **80** (1998) 5275–5280 [`hep-ex/9803015`].

[75] **LEP** Collaboration `hep-ex/0412015`.

[76] **ALEPH** Collaboration, R. Barate *et. al. Phys. Lett.* **B484** (2000) 205–217 [`hep-ex/0005043`].

[77] **OPAL** Collaboration, G. Abbiendi *et. al. Phys. Lett.* **B493** (2000) 249–265 [`hep-ex/0009019`].

[78] **DELPHI** Collaboration, J. Abdallah *et. al. Eur. Phys. J.* **C34** (2004) 127–144 [`hep-ex/0403042`].

[79] **L3** Collaboration, P. Achard *et. al. Phys. Lett.* **B600** (2004) 22–40 [`hep-ex/0409016`].

[80] J. C. Pati and A. Salam *Phys. Rev.* **D10** (1974) 275–289.

[81] R. N. Mohapatra and J. C. Pati *Phys. Rev.* **D11** (1975) 566–571.

[82] R. N. Mohapatra and G. Senjanovic *Phys. Rev.* **D23** (1981) 165.

[83] E. Eichten, I. Hinchliffe, K. D. Lane and C. Quigg *Rev. Mod. Phys.* **56** (1984) 579–707.

[84] K. J. F. Gaemers and G. J. Gounaris *Zeit. Phys.* **C1** (1979) 259.

[85] K. Hagiwara, R. D. Peccei, D. Zeppenfeld and K. Hikasa *Nucl. Phys.* **B282** (1987) 253.

[86] M. S. Bilenky, J. L. Kneur, F. M. Renard and D. Schildknecht *Nucl. Phys.* **B409** (1993) 22–68.

[87] **DELPHI** Collaboration, P. Abreu *et. al. Phys. Lett.* **B459** (1999) 382–396.

[88] **ALEPH** Collaboration, A. Heister *et. al. Eur. Phys. J.* **C21** (2001) 423–441 [`hep-ex/0104034`].

[89] **OPAL** Collaboration, G. Abbiendi *et. al. Eur. Phys. J.* **C33** (2004) 463–476 [`hep-ex/0308067`].

[90] **L3** Collaboration, P. Achard *et. al. Phys. Lett.* **B586** (2004) 151–166 [`hep-ex/0402036`].

[91] **CDF** Collaboration, F. Abe *et. al. Phys. Rev. Lett.* **75** (1995) 1017–1022 [`hep-ex/9503009`].

[92] **D0** Collaboration, S. Abachi *et. al. Phys. Rev.* **D56** (1997) 6742–6778 [`hep-ex/9704004`].

[93] **D0** Collaboration, B. Abbott *et. al. Phys. Rev.* **D58** (1998) 031102 [`hep-ex/9803017`].

[94] **D0** Collaboration, B. Abbott *et. al. Phys. Rev.* **D58** (1998) 051101 [`hep-ex/9803004`].

[95] **CDF** Collaboration, D. Acosta *et. al. Phys. Rev. Lett.* **94** (2005) 211801 [`hep-ex/0501050`].

[96] J. Ohnemus *Phys. Rev.* **D44** (1991) 1403–1414.

[97] S. Frixione *Nucl. Phys.* **B410** (1993) 280–324.

[98] J. Ohnemus *Phys. Rev.* **D50** (1994) 1931–1945 [`hep-ph/9403331`].

[99] A. Pukhov *et. al.* `hep-ph/9908288`.

[100] J. M. Campbell and R. K. Ellis *Phys. Rev.* **D60** (1999) 113006 [`hep-ph/9905386`].

[101] S. Frixione and B. R. Webber `hep-ph/0402116`.

[102] M. Weierstall, "Anpassung und test von fragmentierungsmodellen mit prazisen ereignisform-und einteilchenverteilungen unter besonderer berucksichtigung von identifizierten teilchenspektren."

[103] M. Siebel, J. Drees, K. Hamacher and F. Mandl *Nucl. Phys. Proc. Suppl.* **152** (2006) 7–10.

[104] **OPAL** Collaboration, M. Z. Akrawy *et. al. Z. Phys.* **C47** (1990) 505–522.

[105] **DELPHI** Collaboration, P. Abreu *et. al. Z. Phys.* **C73** (1996) 11–60.

[106] I. G. Knowles *et. al.* `hep-ph/9601212`.

[107] N. Magnussen *et. al.* In *Hamburg 1991, Proceedings, Physics at HERA, vol. 3* 1167-1219. (see HIGH ENERGY PHYSICS INDEX 30 (1992) No. 12988).

[108] A. Banfi, G. Corcella and M. Dasgupta *JHEP* **03** (2007) 050 [`hep-ph/0612282`].

[109] L. Lonnblad and U. Pettersson. LU-TP-88-15.

[110] L. Lonnblad *Nucl. Phys.* **B458** (1996) 215–230 [`hep-ph/9508261`].

[111] E. Fermi *Z. Phys.* **29** (1924) 315–327.

[112] C. F. von Weizsacker *Z. Phys.* **88** (1934) 612–625.

[113] E. J. Williams *Phys. Rev.* **45** (1934) 729–730.

[114] J. M. Campbell, M. A. Cullen and E. W. N. Glover *Eur. Phys. J.* **C9** (1999) 245–265 [`hep-ph/9809429`].

[115] B. Andersson and L. Lonnblad. DESY-92-098.

[116] L. Lonnblad *Z. Phys.* **C65** (1995) 285–292.

[117] R. Kleiss *Phys. Lett.* **B180** (1986) 400.

[118] M. H. Seymour *Nucl. Phys.* **B436** (1995) 443–460 [`hep-ph/9410244`].

[119] U. Pettersson. LU-TP-88-5.

[120] R. D. Field. Redwood City, USA: Addison-Wesley (1989) 366 p. (Frontiers in physics, 77).

[121] A. Daleo, T. Gehrmann and D. Maitre *JHEP* **04** (2007) 016 [`hep-ph/0612257`].

[122] H. Hoeth, "Messung der vierjet-winkelverteilungen und bestimmung der qcd farbfaktoren mit hilfe des apacic++ generators." Diploma thesis, Fachbereich Physik, Bergische Universität Wuppertal, 2003.

[123] K. Hamacher and M. Weierstall `hep-ex/9511011`.

[124] A. Buckley `arXiv:0708.2655 [hep-ph]`.

[125] J. Pumplin *et. al. JHEP* **07** (2002) 012 [`hep-ph/0201195`].

[126] T. Gleisberg, F. Krauss, A. Schlicke, S. Schumann and J. Winter *Phys. Rev.* **D72** (2005) 034028 [`hep-ph/0504032`].

[127] **D0** Collaboration, H. Nilsen D∅ note 5066-CONF.

[128] **CDF** Collaboration, A. A. Affolder *et. al. Phys. Rev. Lett.* **84** (2000) 845–850 [hep-ex/0001021].

[129] **D0** Collaboration, V. M. Abazov *et. al. Phys. Rev.* **D76** (2007) 012003 [hep-ex/0702025].

[130] C. Anastasiou, L. J. Dixon, K. Melnikov and F. Petriello *Phys. Rev.* **D69** (2004) 094008 [hep-ph/0312266].

[131] **D0** Collaboration, V. M. Abazov *et. al. Phys. Rev. Lett.* **94** (2005) 221801 [hep-ex/0409040].

[132] **D0** Collaboration, B. Abbott *et. al. Phys. Rev. Lett.* **82** (1999) 2457–2462 [hep-ex/9807014].

[133] **CDF** Collaboration, F. Abe *et. al. Phys. Rev.* **D50** (1994) 5562–5579.

[134] R. D. Field. private communication, 2007.

[135] R. D. Field and R. P. Feynman *Nucl. Phys.* **B136** (1978) 1.

[136] R. D. Field and R. P. Feynman *Phys. Rev.* **D15** (1977) 2590–2616.

[137] B. Andersson, G. Gustafson, G. Ingelman and T. Sjostrand *Phys. Rept.* **97** (1983) 31.

[138] C. D. Buchanan and S. B. Chun *Phys. Rev. Lett.* **59** (1987) 1997.

[139] S. B. Chun and C. D. Buchanan *Phys. Lett.* **B308** (1993) 153–162.

[140] S. Chun and C. Buchanan *Phys. Rept.* **292** (1998) 239–317.

[141] K. Odagiri *JHEP* **07** (2003) 022 [hep-ph/0307026].

[142] I. Borozan and M. H. Seymour *JHEP* **09** (2002) 015 [hep-ph/0207283].

[143] P. Richardson *JHEP* **11** (2001) 029 [hep-ph/0110108].

[144] F. M. Liu, H. J. Drescher, S. Ostapchenko, T. Pierog and K. Werner *J. Phys.* **G28** (2002) 2597–2616 [hep-ph/0109104].

[145] T. Sjostrand, O. Smirnova and C. Zacharatou Jarlskog *Eur. Phys. J.* **C21** (2001) 93–98 [hep-ph/0104118].

[146] V. Berezinsky and M. Kachelriess *Phys. Rev.* **D63** (2001) 034007 [hep-ph/0009053].

[147] H. J. Drescher, M. Hladik, S. Ostapchenko, T. Pierog and K. Werner *Phys. Rept.* **350** (2001) 93–289 [hep-ph/0007198].

[148] Q. Wang, G. Gustafson and Q.-b. Xie *Phys. Rev.* **D62** (2000) 054004 [`hep-ph/9912310`].

[149] S. Wolfram. Largely based on a talk given at 15th Rencontre de Moriond, Les Arcs, France, Mar 9-21, 1980.

[150] R. D. Field and S. Wolfram *Nucl. Phys.* **B213** (1983) 65.

[151] T. D. Gottschalk *Nucl. Phys.* **B214** (1983) 201.

[152] T. D. Gottschalk *Nucl. Phys.* **B239** (1984) 349.

[153] T. D. Gottschalk and D. A. Morris *Nucl. Phys.* **B288** (1987) 729.

[154] B. R. Webber *Nucl. Phys.* **B238** (1984) 492.

[155] G. Marchesini and B. R. Webber *Nucl. Phys.* **B238** (1984) 1.

[156] B. R. Webber `hep-ph/9912292`.

[157] D. Amati and G. Veneziano *Phys. Lett.* **B83** (1979) 87.

[158] A. Bassetto, M. Ciafaloni and G. Marchesini *Phys. Lett.* **B83** (1979) 207.

[159] G. Marchesini, L. Trentadue and G. Veneziano *Nucl. Phys.* **B181** (1981) 335.

[160] Y. I. Azimov, Y. L. Dokshitzer, V. A. Khoze and S. I. Troian *Z. Phys.* **C27** (1985) 65–72.

[161] T. Sjostrand and V. A. Khoze *Z. Phys.* **C62** (1994) 281–310 [`hep-ph/9310242`].

[162] B. R. Webber *J. Phys.* **G24** (1998) 287–296 [`hep-ph/9708463`].

[163] L. Lonnblad *Z. Phys.* **C70** (1996) 107–114.

[164] J. Rathsman *Phys. Lett.* **B452** (1999) 364–371 [`hep-ph/9812423`].

[165] A. Edin, G. Ingelman and J. Rathsman *Phys. Lett.* **B366** (1996) 371–378 [`hep-ph/9508386`].

[166] A. Edin, G. Ingelman and J. Rathsman *Z. Phys.* **C75** (1997) 57–70 [`hep-ph/9605281`].

[167] G. Ingelman, A. Edin, R. Enberg, J. Rathsman and N. Timneanu *Nucl. Phys. Proc. Suppl.* **B79** (1999) 386 [`hep-ph/9912535`].

[168] R. Enberg, G. Ingelman, A. Kissavos and N. Timneanu *Phys. Rev. Lett.* **89** (2002) 081801 [`hep-ph/0203267`].

[169] B. Andersson, G. Gustafson and T. Sjostrand *Nucl. Phys.* **B197** (1982) 45.

[170] B. Andersson, G. Gustafson and T. Sjostrand *Phys. Scripta* **32** (1985) 574.

[171] A. Kupco `hep-ph/9906412`.

[172] G. Corcella *et. al.* `hep-ph/9912396`.

[173] **OPAL** Collaboration, K. Ackerstaff *et. al. Eur. Phys. J.* **C7** (1999) 369–381 [`hep-ex/9807004`].

[174] **DELPHI** Collaboration, P. Abreu *et. al. Eur. Phys. J.* **C6** (1999) 19–33.

[175] **DELPHI** Collaboration, P. Abreu *et. al. Eur. Phys. J.* **C5** (1998) 585–620.

[176] **SLD** Collaboration, K. Abe *et. al. Phys. Lett.* **B386** (1996) 475–485 [`hep-ex/9608008`].

[177] **SLD** Collaboration, K. Abe *et. al. Phys. Rev.* **D69** (2004) 072003 [`hep-ex/0310017`].

[178] **OPAL** Collaboration, K. Ackerstaff *et. al. Eur. Phys. J.* **C1** (1998) 479–494 [`hep-ex/9708029`].

[179] **OPAL** Collaboration, G. Abbiendi *et. al. Phys. Lett.* **B550** (2002) 33–46 [`hep-ex/0211007`].

[180] B. A. Schumm, Y. L. Dokshitzer, V. A. Khoze and D. S. Koetke *Phys. Rev. Lett.* **69** (1992) 3025–3028.

[181] **Particle Data Group** Collaboration, K. Hagiwara *et. al. Phys. Rev.* **D66** (2002) 010001.

[182] G. Miu and T. Sjostrand *Phys. Lett.* **B449** (1999) 313–320 [`hep-ph/9812455`].

List of publications

Journal publications & eprints

1. J. Alwall *et al.*,
   "*Comparative study of various algorithms for the merging of parton showers and matrix elements in hadronic collisions*",
   arXiv:0706.2569 [hep-ph].

2. T. Gleisberg, F. Krauss, A. Schälicke, S. Schumann and J. Winter,
   "*Studying W^+W^- Production at the Fermilab Tevatron with SHERPA*",
   Phys. Rev. D **72** (2005) 034028 (hep-ph/0504032).

3. T. Gleisberg, S. Höche, F. Krauss, A. Schälicke, S. Schumann and J. Winter,
   "*SHERPA 1.alpha, a proof-of-concept version*",
   JHEP **0402** (2004) 056 (hep-ph/0311263).

4. J. Winter, F. Krauss and G. Soff,
   "*A modified cluster-hadronization model*",
   Eur. Phys. J. C **36** (2004) 381 (hep-ph/0311085).

Proceedings and contributions

1. T. Gleisberg *et al.*, "*New trends in modern event generators*",
   arXiv:0705.4648 [hep-ph].

2. S. Alekhin *et al.*, "*HERA and the LHC - A Workshop on the Implications of HERA for LHC Physics*", hep-ph/0601012 and hep-ph/0601013.

3. T. Gleisberg, S. Höche, F. Krauss, A. Schälicke, S. Schumann and J. Winter,
   "*Event generator for the LHC*",
   Nucl. Instrum. Meth. A **559** (2006) 242 (hep-ph/0508315).

4. T. Gleisberg, S. Höche, F. Krauss, A. Schälicke, S. Schumann, G. Soff and J. Winter,
   "*Predictions for multi-particle final states with SHERPA*",
   Czech. J. Phys. **55** (2005) B529 (hep-ph/0409122).

5. T. Gleisberg, S. Höche, F. Krauss, A. Schälicke, S. Schumann, J. Winter and G. Soff,
   "*Towards a fragmentation model for Sherpa*", published in Proceedings of "International Conference on Linear Colliders, Paris" (2004), hep-ph/0408245.

6. T. Gleisberg, S. Höche, F. Krauss, A. Schälicke, S. Schumann, J. Winter and G. Soff,
   "*New tools for automatic cross section calculation*", published in "Strbske Pleso
   2004, Deep inelastic scattering" 959-962, hep-ph/0407366.

7. T. Gleisberg, S. Höche, F. Krauss, A. Schälicke, S. Schumann, J. Winter and G. Soff,
   "*Monte Carlo models at the LHC*", published in "Strbske Pleso 2004, Deep inelastic
   scattering" 645-650, hep-ph/0407365.

8. A. Schälicke, T. Gleisberg, S. Höche, S. Schumann, J. Winter, F. Krauss and G. Soff,
   "*Event generator for particle production in high-energy collisions*",
   Prog. Part. Nucl. Phys. **53** (2004) 329 (hep-ph/0311270).

Versicherung

Hiermit versichere ich, daß ich die vorliegende Arbeit ohne unzulässige Hilfe Dritter und ohne Benutzung anderer als der angegebenen Hilfsmittel angefertigt habe; die aus fremden Quellen direkt oder indirekt übernommenen Gedanken sind als solche kenntlich gemacht. Die Arbeit wurde bisher weder im Inland noch im Ausland in gleicher oder ähnlicher Form einer anderen Prüfungsbehörde vorgelegt.

Die vorliegende Arbeit wurde am Institut für Theoretische Physik der Technischen Universität Dresden unter wissenschaftlicher Betreuung von Herrn Prof. Dr. Michael Kobel und Herrn Dr. Frank Krauss angefertigt.

Es haben keine früheren erfolglosen Promotionsverfahren stattgefunden.

Hiermit erkenne ich die Promotionsordnung der Fakultät Mathematik und Naturwissenschaften der Technischen Universität Dresden vom 20. März 2000 an.

Dresden, den 28.09.2007   Jan-Christopher Winter